



Impact of Synoptic Wind Variability on the Dynamics and Planktonic Ecosystem of the South Senegalese Upwelling Sector

Pierre Chabert

► To cite this version:

Pierre Chabert. Impact of Synoptic Wind Variability on the Dynamics and Planktonic Ecosystem of the South Senegalese Upwelling Sector. Ocean, Atmosphere. Sorbonne Université, 2023. English. NNT : 2023SORUS096 . tel-04137252

HAL Id: tel-04137252

<https://theses.hal.science/tel-04137252>

Submitted on 22 Jun 2023

HAL is a multi-disciplinary open access archive for the deposit and dissemination of scientific research documents, whether they are published or not. The documents may come from teaching and research institutions in France or abroad, or from public or private research centers.

L'archive ouverte pluridisciplinaire **HAL**, est destinée au dépôt et à la diffusion de documents scientifiques de niveau recherche, publiés ou non, émanant des établissements d'enseignement et de recherche français ou étrangers, des laboratoires publics ou privés.



THÈSE DE DOCTORAT
DE SORBONNE UNIVERSITÉ

Spécialité : Océanographie Physique

École doctorale : 129 - Sciences de l'Environnement d'Île-de-France

réalisée au

Laboratoire d'Océanographie et du Climat
Expérimentations et Approches Numériques
Institut Pierre-Simon Laplace (LOCEAN-IPSL)

présentée par

Pierre CHABERT

pour obtenir le grade de

DOCTEUR DE SORBONNE UNIVERSITÉ

Impact of Synoptic Wind Variability on the Dynamics and Planktonic Ecosystem of the South Senegalese Upwelling Sector

date de soutenance prévue le 6 Février 2023

devant le jury composé de

Pr. Pascale BOURUET-AUBERTOT
Pr. John LARGIER
Pr. Nicolas GRUBER
Pr. Mark D. OHMAN
Dr. Fanny CHENILLAT
Dr. Xavier CAPET
Dr. Vincent ECHEVIN

Sorbonne Université, LOCEAN-IPSL, Paris
UC Davis, Bodega Marine Laboratory, California
ETH Zürich, Switzerland
UCSD, Scripps Inst. of Oceanography, California
Actimar, Brest
CNRS, Sorbonne Université, LOCEAN-IPSL, Paris
IRD, Sorbonne Université, LOCEAN-IPSL, Paris

Présidente
Rapporteur
Rapporteur
Examineur
Examinatrice
Directeur de thèse
Directeur de thèse



Abstract

In addition to the wind seasonal cycle, Eastern Boundary Upwelling Systems undergo fluctuations at shorter synoptic to intraseasonal time scales. This thesis focuses on the impact of synoptic wind intensifications and relaxations with a period of 5-10 days on the dynamics and planktonic ecosystem of the South Senegalese Upwelling Sector (SSUS). This system is located south of the sharp Cape Verde peninsula which acts as an abrupt coastline break and has a particularly shallow continental shelf. We aim to bring additional knowledge on this important coastal upwelling system that has received little attention, especially at synoptic time scales. To investigate this, we develop a modeling framework that involves applying idealized synoptic wind intensification and relaxation to an ensemble of climatological SSUS states. Synoptic fluctuations impact all dynamical variables out of their intrinsic variability range and shape robust anomalies of SSUS-scale and mesoscale spatial patterns. Using a mixed layer heat budget over the shelf, we identify the importance of horizontal processes in the SSUS heat variability and the very localized importance of vertical processes. Plankton biomass are found to oscillate in space and time in response to synoptic wind fluctuations. The atmospheric perturbation is damped during its propagation towards the upper trophic levels of the ecosystem. The response of the planktonic ecosystem is complex and heterogeneous over the shelf, with a distinctive inner shelf behavior. A diatoms budget reveals that their biomass is primarily controlled by primary production, zooplankton grazing and mortality-aggregation. The balance between these processes is responsible for the oscillatory responses of the diatoms biomass to synoptic wind events. All dynamical and biogeochemical variables exhibit modest asymmetries between wind intensification and relaxation responses. This brings support to the hypothesis that synoptic variability has a modest net impact on the climatological mean state. The implications of our results for future research questions are discussed, including the importance of biogeochemical observations and advances in plankton ecosystem modeling.

Keywords : South Senegalese Upwelling Sector, synoptic variability, intrinsic variability, deterministic response, (sub)mesoscale variability, heat budget, planktonic ecosystem, nutrients, plankton.



Résumé

En plus du cycle saisonnier du vent, les systèmes d'upwelling de bord Est des océans subissent des fluctuations à des échelles de temps plus courtes, intrasaisonnières ou synoptiques. Dans cette thèse, nous nous concentrons sur l'impact d'une intensification ou d'une relaxation du vent synoptique sur une période de 5 à 10 jours sur la dynamique et l'écosystème planctonique du secteur d'upwelling du sud Sénégal (SSUS). Ce système possède un plateau continental particulièrement peu profond et est situé au sud de l'abrupte péninsule du Cap-Vert, qui casse la continuité de la ligne de côte. Notre objectif est d'apporter des connaissances supplémentaires sur ce système d'upwelling côtier qui, malgré son importance, a reçu peu d'attention, en particulier aux échelles de temps synoptiques. Pour étudier cela, nous développons une expérience de modélisation qui consiste à appliquer une intensification et une relaxation idéalisées du vent synoptique à un ensemble d'états climatologiques du SSUS. Les fluctuations synoptiques ont un impact sur toutes les variables dynamiques et façonnent des anomalies robustes des structures spatiales à l'échelle du système et à la méso-échelle. En appliquant un bilan de chaleur de la couche mélangée, nous identifions l'importance des processus horizontaux et l'importance très localisée des processus verticaux dans la variabilité du SSUS. Aussi, nous constatons que les biomasses planctoniques oscillent dans l'espace et le temps en réponse aux fluctuations synoptiques. La perturbation atmosphérique est amortie lors de sa propagation vers les niveaux trophiques supérieurs de l'écosystème. La réponse de l'écosystème planctonique est complexe et hétérogène sur le plateau, avec un comportement distinct sur le plateau interne. Un bilan des diatomées révèle que leur biomasse est principalement contrôlée par la production primaire, le broutage du zooplancton et la mortalité-agrégation. L'équilibre entre ces processus est responsable des réponses oscillatoires de la biomasse des diatomées aux événements synoptiques. Toutes les variables dynamiques et biogéochimiques présentent de modestes asymétries entre les réponses d'intensification et de relaxation du vent. Cela supporte l'hypothèse selon laquelle la variabilité synoptique a un impact seulement modeste sur l'état moyen climatologique. Les implications de nos résultats pour les futures questions de recherche sont discutées, notamment l'importance des observations biogéochimiques et les avancées de la modélisation des écosystèmes planctoniques.

Mots-clés : Secteur d'upwelling du sud du Sénégal, variabilité synoptique, variabilité intrinsèque, réponse déterministe, variabilité (sub)mésoéchelle, bilan de chaleur, écosystème planctonique, nutriments, plancton.



Remerciements

Je tiens à remercier grandement mes directeurs de thèse Xavier Capet et Vincent Echevin, pour leurs conseils scientifiques, suivi, patience et qualités humaines. Merci de m'avoir poussé avec bienveillance et avec tant de discussions scientifiques originales, passionnantes et desquelles on ressort grandi. Je remercie mon jury de thèse, John Largier et Nicolas Gruber pour avoir accepté d'évaluer mon manuscrit de thèse; merci à Fanny Chenillat et Mark D. Ohman d'avoir participé à mon jury et pour ces discussions scientifiques si enrichissantes. Merci à mes encadrants de master Francesco d'Ovidio et Mark D. Ohman, qui m'ont permis d'arriver en thèse avec une expérience scientifique et (inoubliable) en mer, et déjà une certaine vision d'un écosystème d'upwelling côtier. Je tiens également à remercier à mon comité de thèse composé de Monique Messié et Lester Kwiatkowski pour leur intérêt et apport scientifique. À ces remerciements s'associe un grand merci à Christophe Hourdin pour tout ce partage de savoir et d'outils pour la facilitation d'usage des modèles. Merci à Olivier Aumont pour ces discussions si riches. Merci à Soeren Thomsen, Siny Ndoye, Alban Lazar, Eric Machu, Renaud Person, Stéphane Pous, François Colas, Mike R. Stukel, Kiefer Forsch pour avoir participé de près ou de loin à ce projet de thèse. Une pensée vient également pour Juliette Mignot, Serge Janicot, Claire Lévy et le groupe Climaction dans sa globalité pour sa sensibilisation sur les enjeux de la transition liée au changement climatique, pour sa démarche éducative et démocratique, pour ses discussions passionnantes, et qui ont aussi permis de garder des débats et un lien durant le premier confinement lié à la crise du covid. Merci à Antoine Nasser pour son aide précieuse sur le calcul; à Gaston Irrmann pour ses conseils en code; à Gina Fifani et Alberto Baudena pour la prise en main du software lagrangien. De chaleureux remerciements à Gina Fifani, George Baaklini, Kenza Himmich pour avoir partagé le bureau 431 avec tant de bonne humeur; Matthis Auger pour tant de discussions depuis des années qui font avancer, mais pas que; merci à Sara Sergi, Clément Haëck, Coraline Lesseure, Léa Olivier, Clovis Thouvenin-Masson, Corentin Clerc, Diego Alaguarda, Yona Silvy, Lucies Vignes, Robin Rolland, Clara Azarian, Cassien Diabe Ndiaye, Marcellin Guilbert, Lea Poli, Linus Vogt, Sara Labrousse, Clément Rousset;

Merci à Baptiste Truchet pour son "divertissement et permettre de revenir reboosté", qui va également à Valentin Raute, Robin Baudino, Marc Lebas, Thomas Rasoloson, Tim Toomey, Antoine Rubel, Marc Pezerat, Gaspard Geoffrey et tous les copains de l'ENSTA Bretagne; Merci à Maxime Brun d'Arre, Jean Rybicki, Ronan Clo, Florian Bahe, Leo Granjon, Simon Hourlier, Vincent Chabin, Leopold David, Claire Couty, Guillaume Débonnaire, Mathieu Ange, Marina Delage, Charlie Ginhoux, Florent Skawinsky et tous les potes de prépa; Merci à Quentin Nicoli, Jean-Baptiste Briot, Constance Thomas, Armelle Phelip, Magali Puidupin, Aude Bobillon, Mathilde Tissier, Katharina Winkler, Jérémie Payan, Félix Gleyze, Valentin Champion, Zoé Feinte et tous les amis de la Croix-Rousse; Merci à mes parents, mon frère, à tous, qui ont toujours été là, merci pour leur soutien, sans qui rien de tout cela n'aurait existé.

"My big fish must be somewhere."
- Ernest Hemingway, *The Old Man and the Sea*

Scientific activities during the PhD

Publications in peer-reviewed scientific journals

Chabert P., V. Echevin, X. Capet (2022) *Bottom-up propagation of synoptic wind intensification and relaxation in the planktonic ecosystem of the South Senegalese Upwelling Sector*, Geophysical Research Letters, to be submitted.

Chabert P., X. Capet, V. Echevin, A. Lazar, C. Hourdin, S. Ndoeye (2022) *Impact of Synoptic Wind Intensification and Relaxation on the Dynamics and Heat Budget of the South Senegalese Upwelling Sector*, Journal of Physical Oceanography, accepted for publication on the 5 December 2022.

Chabert P., d'Ovidio, F., Echevin, V., Stukel M.R., Ohman M.D. (2021) *Cross-Shore Flow and Implications for Carbon Export in the California Current Ecosystem: A Lagrangian Analysis*, JGR: Oceans, DOI : 10.1029/2020JC016611.

Seminars and international conferences

P. Chabert, X. Capet, V. Echevin, A. Lazar *Impact of synoptic wind variability on the dynamics and biogeochemistry of the South Senegalese Upwelling Sector*. EBUS and Humboldt Current 2022 Conference oral session, 2022, online.

P. Chabert, X. Capet, V. Echevin, A. Lazar *Dynamical and biogeochemical responses of the South Senegalese Upwelling System to synoptic wind variability: a modeling approach*. EGU22-3723 oral session, 2022, on-site.

P. Chabert, X. Capet, V. Echevin, A. Lazar *Dynamical response of the South Senegalese Upwelling System to synoptic winds: a modeling approach*. Ocean Science Meeting 2022 - PI01 oral session, 2022, online.

P. Chabert, F. d'Ovidio, V. Echevin, M.R. Stukel, M.D. Ohman, *Cross-Shore Flow and Implications for Carbon Export in the California Current Ecosystem: A Lagrangian Analysis* EBUS Webinar, 2021, online.

P. Chabert, F. d'Ovidio, V. Echevin, M.D. Ohman. *Temporal variability of cross-shore fluxes in the California Current Ecosystem*. Poster presented by a local co-author at OSM (Ocean Sciences Meeting) in San Diego, California, USA, 2019.

Teaching

Introduction to physical oceanography in M1: rotating table experiment and applied problems (24h in 2020 and 2021)

Mathematics applied problems in L1 (30h in 2020 and 2021)

Courses received

Seminar "Impacts du changement climatique", 2022, *LOCEAN* (21h)

Seminar "Changement climatique: science, politique, société", 2020, *Ecole Normale Supérieure*, (21h)

Club de Lecture, 2019-2021, *LOCEAN* (4h)

Modeling training (CROCO), Plouzané, 2019, *Ifremer* (4 days)

Activities in the laboratory

Participation in the organization and animation of the "Month of" (Journal Clubs, seminars and "goûter-débat") of the laboratory (during 2 years, including covid pandemic times; themes: decadal variability, marine biodiversity, ocean modeling, salinity, upwelling).

Oceanographic expeditions

SCOPES cruise: Structuration des COMMunautés PlanctoniquEs en réponse à la dynamique de l'upwelling sud-Sénégalais, 25 days onboard of the *Thalassa*, Senegal, December 2022 - January 2023, *planned*.

Process Cruise P1908: 33 days onboard of the *Atlantis* as a volunteer for the California Current Ecosystem - Long Term Ecological Research (CCE-LTER) program, California, August 2019.



List of Acronyms

ADCP	Acoustic Doppler Current Profiler
AGRIF	Adaptive grid refinement in Fortran
CTD	Conductivity Temperature Depth
CROCO	Coastal and Regional Ocean COmmunity model
CCE	California Current Ecosystem
CCS	California Current System
CTW	Coastal Trapped Waves
CUS	California Upwelling System
EBUS	Eastern Boundary Upwelling System
ECMWF	European Center for Medium-range Weather Forecast
ENSO	El Niño Southern Oscillation
ERA5	ECMWF Re-Analysis 5th generation
GLODAP	Global Data Analysis Project
ITCZ	InterTropical Convergence Zone
PP	Primary Production
NAO	North Atlantic Oscillation
NP	New Production
RP	Regenerated Production
PISCES	Pelagic Interactions Scheme for Carbon and Ecosystem Studies
RMS	Root Mean Square
RMSE	Root Mean Square Error
ROMS	Regional Ocean Modeling System
SML	Surface Mixed Layer

SF Synoptic Forcing

SNR Signal to Noise Ratio

SSH Sea Surface Height

SSUS Southern Senegal Upwelling Sector

SST Sea Surface Temperature

WOA World Ocean Atlas

Table of contents

List of Acronyms	8
Introduction	11
1 Preamble	12
2 Physical structure and dynamics	13
3 Biogeochemical and planktonic ecosystem structure	25
4 Scientific questions of the thesis	34
5 Thesis outline	35
I Methods and preparatory results	37
1 Preamble	38
2 Regional oceanic model CROCO and numerical experiment	39
3 General methods	41
4 Biogeochemical model PISCES and methods	64
II Impact of synoptic wind intensification and relaxation on the dynamics and heat budget	75
1 Preamble	76
2 Impact of Synoptic Wind Intensification and Relaxation on the Dynamics and Heat Budget of the South Senegalese Upwelling Sector: JPO manuscript	77
3 Complementary diagnostics and analyses	112
4 Discussion	126
5 Conclusion	129
III Bottom-up propagation of synoptic wind intensification and relaxation in the planktonic ecosystem	131
1 Preamble	132
2 Bottom-up propagation of synoptic wind intensification and relaxation in the planktonic ecosystem of the South Senegalese Upwelling Sector: GRL draft	133
3 Complementary comments	143
IV Insights into processes shaping the planktonic ecosystem structure	147
1 Preamble	148
2 Nutrients patterns, limitations and control mechanisms	149
3 Light availability	155
4 Control mechanisms of plankton	157
5 Specific inner shelf processes shaping diatoms biomass	167
6 Surface mixed layer and vertical processes	171

7	Discussion	176
8	Conclusion	178
V	Conclusions and perspectives	181
	Appendix A: JGR Oceans publication	189
	Appendix B: Carbon footprint of the PhD	205
	List of Figures	208
	Bibliography	219



Introduction

Contents

1	Preamble	12
2	Physical structure and dynamics	13
2.1	Typical dynamics of EBUS	13
2.2	Sources of variability	15
2.3	Atmospheric synoptic scale variability	16
2.4	Response of coastal upwelling sectors to synoptic wind intensification/relaxation	17
2.5	Asymmetries in climate/ocean physics	18
2.6	Northwest African and South Senegalese Upwelling Sectors	20
3	Biogeochemical and planktonic ecosystem structure	25
3.1	Planktonic ecosystem concepts	25
3.2	Structure, cycles and processes in coastal oceanic upwelling sectors . .	28
3.3	Biogeochemical and planktonic ecosystem structures of Northwest African and South Senegalese Upwelling Sectors	32
4	Scientific questions of the thesis	34
5	Thesis outline	35

1 Preamble

Coastal upwelling systems directly impact societies, humans and the economy by providing substantial fish stocks, that represent 20% of annual world fisheries for 1% of the ocean surface area ([Ryther, 1969](#); [Cushing, 1971](#); and 10% of oceanic new production [Fréon et al., 2009](#)). The Eastern sides of the Atlantic and Pacific basins (Eastern Boundary Upwelling System - EBUS) hold unique and primordial oceanic sectors because of the disproportionate local primary production relative to the area occupied in the global ocean. Alongshore winds push surface waters offshore and create a horizontal divergence such that vertical motions transport cold, subsurface nutrient-rich water upwards. The transport out of the upwelling site is constrained by wind forcing, geomorphological features, source waters and present a remarkable intrinsic variability ([Marchesiello et al., 2003](#)). The massive nutrient supply in the euphotic layer enables a strong primary production and changes in the ecosystem trophic levels along the upwelled waters advection. Along these pathways, larval dispersion and zooplankton hotspots appear downstream ([Messié and Chavez, 2017](#)), followed by pelagic habitats development ([Largier, 2020](#)), top predators and seabirds ([Benoit-Bird and Lawson, 2016](#); [Thompson et al., 2012](#)). These coastal ecosystems are located along highly populated areas of the world (North-West coasts of America and Africa, Peru-Chile and Benguela), and being both vulnerable and socio-economically important, they are of particular interest in the context of climate change ([García-Reyes et al., 2015](#); [Bograd et al., 2023](#)).

2 Physical structure and dynamics

2.1 Typical dynamics of EBUS

At the surface of the Earth, there is an exceeding solar radiation flux at the Equator compared to the poles. This is the first source of atmospheric and oceanic dynamics that redistribute the heat and balance latitudinal heat differences (Cushman-Roisin and Beckers, 2011; Vallis, 2017). On a seasonal basis, the location of trade winds convergence (the InterTropical Convergence Zone - ITCZ) oscillates meridionally and affects the tropical and mid-latitudes atmospheric circulation (associated to Hadley cells circulation). The atmospheric circulation over the four major basins of the globe (north-south Atlantic and Pacific) is structured in a way that equatorward winds blow at subtropical/mid latitudes over the eastern boundaries. Depending on the orientation of the coast, which is mostly meridional at these latitudes for eastern boundaries (West coasts of North and South America and Africa), the season and wind structure, many tropical coastal sectors are subject to alongshore winds.

Upwelling systems are forced by wind stress τ and heat fluxes Q , as shown on the schematic of Fig. 0.1. Because of the rotation of the Earth, these winds induce an offshore drift of surface waters, the Ekman transport (U_{Ek} in Fig. 0.1). The coastal horizontal divergence of this transport is necessarily compensated by vertical velocities (w in Fig. 0.1). The ocean is 10^3 time more dense than the atmosphere, and raising subsurface waters demands an incredible amount of energy. One major property of ocean dynamics is that the ocean is remarkably vertically stratified (Cushman-Roisin and Beckers, 2011) and a major part of the energy is concentrated in the surface mixed layer (SML). Baroclinic conditions caused by the cross-shore pressure gradient and the coastal uplift of isopycnals induce a coastal equatorward jet and a subsurface poleward counter current (indicated respectively by the sea surface elevation $\eta_{++} - \eta_+$; σ_{iso} ; *jet* and *counter current* in the vertical structure of the section of Fig. 0.1). In the case of constant wind, surface waters are constantly expelled offshore and replaced by newly upwelled waters.

Many sector-specific environmental conditions and dynamical processes add up to this schematic view of upwelling systems. For example, Ekman suction drives vertical velocities due to the wind stress curl (smaller w between two different wind τ intensities in Fig. 0.1), and influences the physical and biological structures of these coastal systems (Capet et al., 2004; Rykaczewski and Checkley, 2008; Jacox et al., 2018). Also, in some sectors the structure of the wind induces an alongshore pressure gradient (indicated by $\eta_+ - \eta_-$ in Fig. 0.1) in a way that the Ekman drift is reduced by an onshore geostrophic transport U_{geo} (Marchesiello and Estrade, 2010; e.g. in the Senegalese upwelling system, Ndoye et al., 2017). Upwelling can be enhanced by remote forcing (from remote wind variability) that induce the propagation of coastal trapped waves (CTW in Fig. 0.1, Philander and Yoon, 1982; Polo et al., 2008; Hickey and Banas, 2008). Meso and submesoscales are at the heart of the enhanced intrinsic variability of coastal upwelling systems (Marchesiello et al., 2003; Capet et al., 2008b), with a dominant role of eddies and filaments in shaping the biogeochemical field (Nagai et al., 2015). The contribution of eddy

fluxes, defined as the covariability of a tracer (e.g. heat) and flow fluctuations (deviation from a mean \bar{u} , i.e. $u' = u - \bar{u}$) can be considerable on the circulation, energy transfers and biological activity (Capet et al., 2008b; Colas et al., 2012, 2013; Gruber et al., 2011).

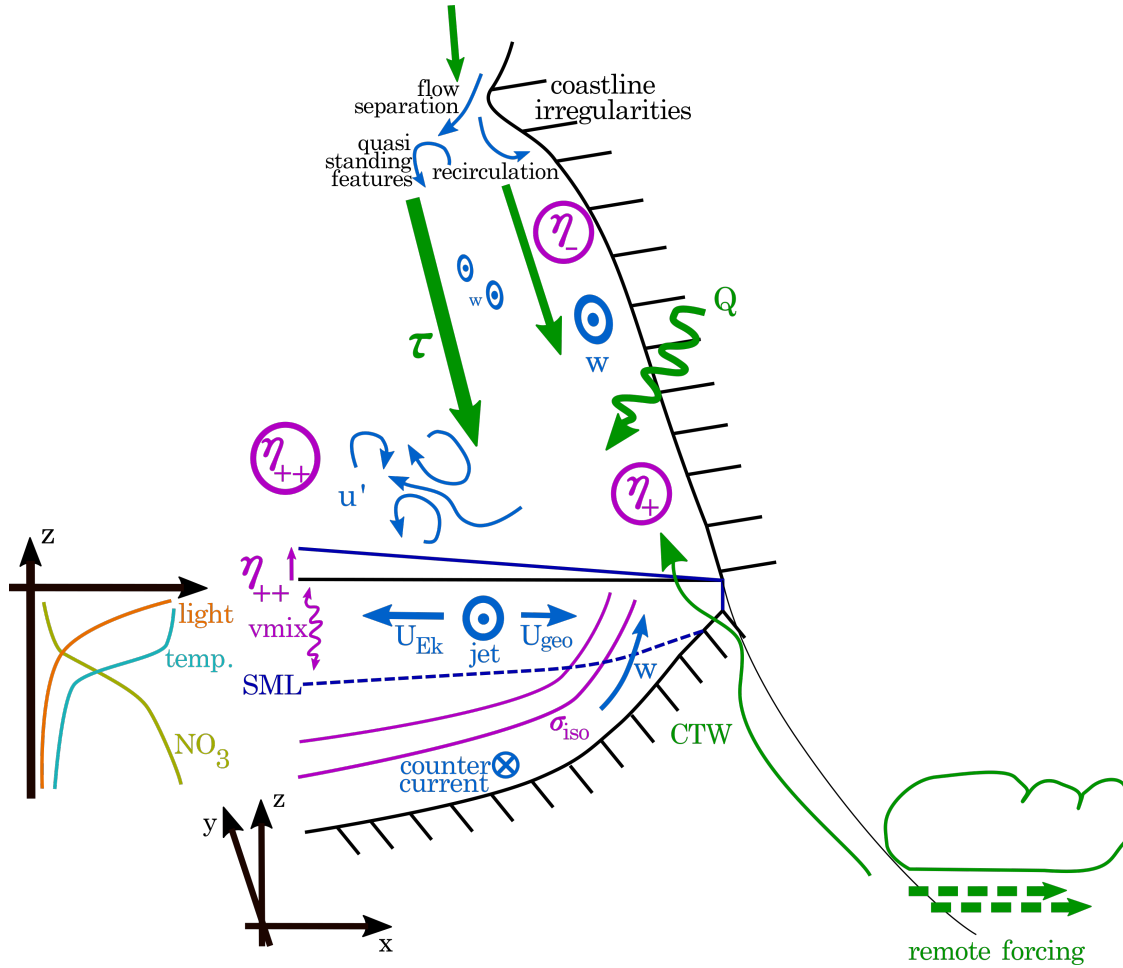


Figure 0.1: Schematic of typical dynamics of a northern hemisphere coastal wind-driven upwelling system. Air-sea heat fluxes (Q , the sinuous arrow indicates the air-sea direction), surface wind stress (τ , straight arrows indicate the wind direction) and coastal trapped waves (CTW, the arrow indicates the direction of propagation) are indicated in green. Dashed green arrows symbolically indicate remote forcing and not a realistic direction. The continuous thick blue arrows indicate the offshore Ekman drift U_{Ek} , the geostrophic onshore flow U_{geo} resulting from the alongshore pressure gradient (indicated in purple by the difference of sea surface heights $\eta_+ - \eta_-$) and the vertical velocities w . The alongshore upwelling *jet* resulting from the cross-shore pressure gradient ($\eta_{++} - \eta_+$) is indicated in blue in the y -axis direction, oppositely to the counter current at greater depth. Sinuous thin blue arrows indicate circulation patterns associated to coastline irregularities and to flow fluctuations $u' = u - \bar{u}$ with \bar{u} the mean flow. The surface mixed layer *SML* depth is indicated in darker blue dashed line. The nearshore rise of isopycnals is indicated with purple lines σ_{iso} and the vertical mixing in the SML with the purple *vmix* sinuous line. The typical vertical profiles of light availability, temperature and nitrate are indicated on the left side in orange, light blue and olive green lines.

Upwelled subsurface source waters typically originate from 50-150 m deep depending on the region (Messié et al., 2009) and have different properties compared to the surface ones, with lower temperature and higher nutrients (e.g. NO_3) concentration (see vertical profiles in

Fig. 0.1). Thus, the wind-driven vertical transport of water brings subsurface cold and nutrient rich waters in the upper layer of the ocean, where light is available for photosynthesis (i.e. the euphotic layer, see the vertical structure of light availability in Fig. 0.1). This triggers primary production, planktonic ecosystem development and increase in trophic levels (Chavez and Messié, 2009; Cushman-Roisin and Beckers, 2011).

2.2 Sources of variability

The strong research interest and enthusiasm for coastal upwelling systems for decades is probably justified by the variety of expressions upwelling dynamics can take depending on the specific traits of a particular sector. Here we describe some important traits of these systems.

Latitude

The first source of variability is the latitude of a coastal upwelling sector. This location dictates environmental conditions like the atmospheric forcing (wind stress and heat fluxes) strength, spatial pattern and temporal variability, surrounding/local hydrographic properties, the origin of waters upwelled (i.e. source waters), the strength of internal mesoscale variability (Marchesiello and Estrade, 2009). The four major EBUS are the California (Current System, CCS; and California Current Ecosystem, CCE), Humboldt Peru/Chile, north-west Africa/Canaries and Benguela systems (see Fig. 0.2). The dynamics, primary production and fish stocks are different in each system and highly variable (Chavez and Messié, 2009; Messié and Chavez, 2017).

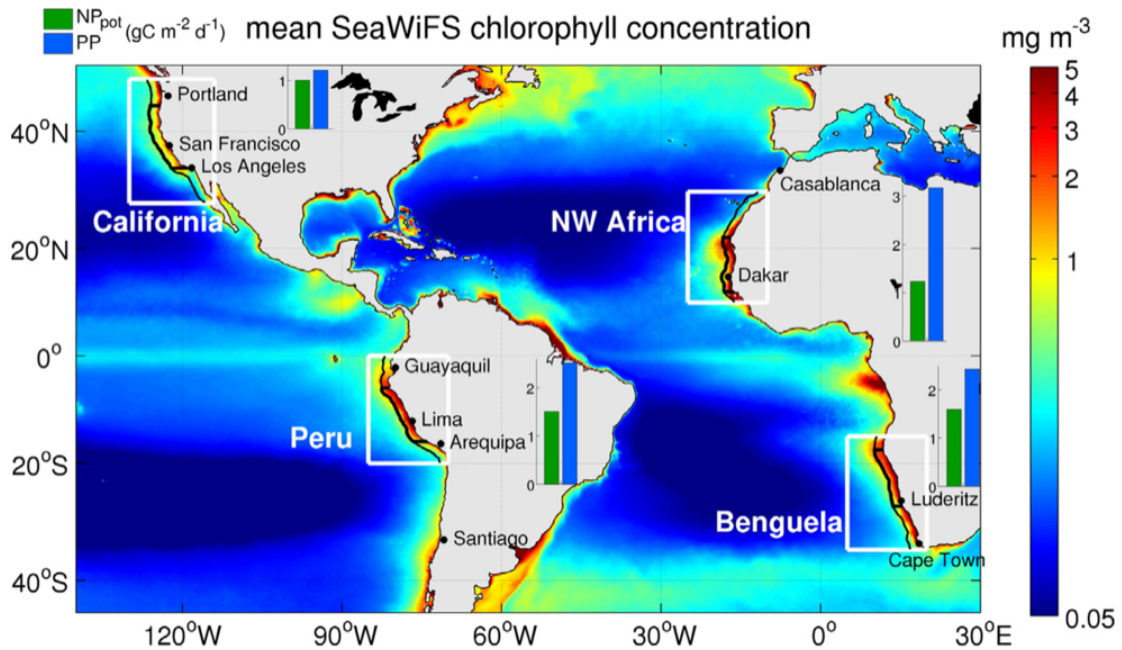


Figure 0.2: Four major Upwelling Systems location and their respective mean chlorophyll concentration, NP_{pot} and PP. From Messié and Chavez (2015).

Geomorphology

The dynamics of wind-driven flows in coastal upwelling systems are constrained by geomorphological aspects of the coast. Water column depth and bathymetry shapes, such as widening

shelves can drastically constrain the flow (Pringle, 2002). Underwater canyons interactions with flow and coastal trapped waves can trigger peculiar circulation (Saldías et al., 2021). The presence of coastline irregularities like capes and bays induce distinct upwelling circulation (Barth et al., 2005; Ramp et al., 2005; Largier, 2020) with intense upwelling cells located off capes (Brink et al., 1981; Jones et al., 1983) and an increased probability of quasi-standing flow features (Narmoussa and Maxworthy, 1989; Marchesiello et al., 2003). Coastline irregularities can also induce flow separation and recirculation processes (Largier, 2020). Also, capes in eastern boundaries sectors are potential drivers of highly constrained flow possibly leading to enhanced retention and associated biogeochemical consequences (Wolanski et al., 1984; Largier, 2020).

Seasonal, intraseasonal and synoptic atmospheric forcing variability

In addition to a strong seasonal cycle in most EBUS (Chavez and Messié, 2009), winds are subject to intraseasonal (10-60 days) and synoptic fluctuations (5-10 days). Usually, these are either intensification or relaxation of wind intensity, but can also be a shift in wind direction. These pulses of wind forcing are a main property of upwelling systems (Largier, 2020). The complexity of wind-driven synoptic events adds up to the EBUS intrinsic mesoscale variability (Marchesiello et al., 2003), given their similarity in terms of time scales.

The importance of better understanding the variability of upwelling systems by investigating the synoptic scale is also related to changes induced by climate change. Upwelling favorable wind patterns are expected to shift poleward with climate change (Rykaczewski et al., 2015), which would result in a reduction of synoptic variability at low latitudes (Aguirre et al., 2019). Changes in the synoptic wind variability, the impact on the physical structure (temperature, stratification, source water, nutrient supply; Rykaczewski and Dunne, 2010) and on marine life (Checkley et al., 2017) remain unclear. This and important uncertainties in projections (Bograd et al., 2023) emphasize the need to better understand the impact of synoptic variability on upwelling systems in the recent period.

In the next sections, we first expose the current knowledge of atmospheric synoptic scale dynamics over North-West Africa, then present the known responses of coastal upwelling sectors to synoptic wind intensification and relaxation and finally focus on the circulation of the Canary and Senegalese sectors.

2.3 Atmospheric synoptic scale variability

In atmospheric sciences, synoptic scales typically refer to horizontal scales of 1000 km and time scales of 5 to 10 days. Here we quickly present the atmospheric dynamics responsible for synoptic wind variability over northwest Africa and especially the Senegalese domain.

Over northwest Africa, wind fluctuations are mostly driven by large scale atmospheric dynamics that generate meridional oscillations of High-Low pressure centers and modify coastal winds (Sultan and Janicot, 2003; Kounta Diop, 2019). Over the Senegalese domain, the dipole between the Azores and Saharo-Libyan high pressure centers (see blue circles in Fig. 0.3, from Kounta Diop, 2019) and land low pressure (heat lows) create a pressure gradient that drives

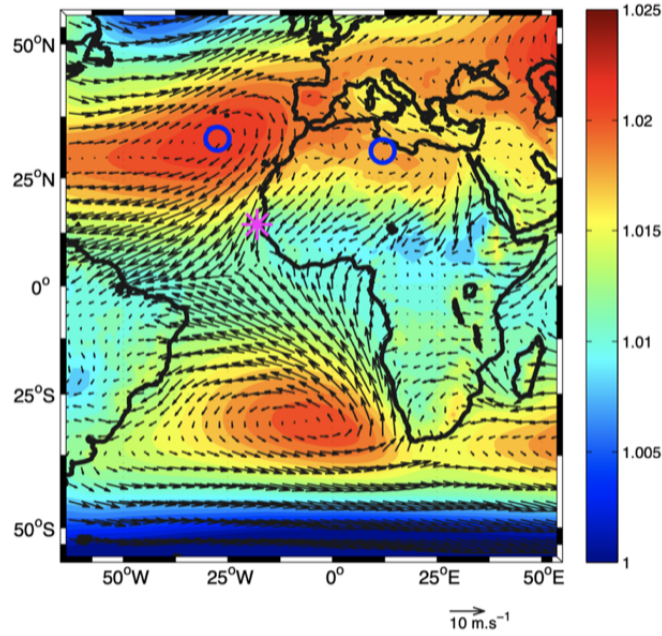


Figure 0.3: Seasonal mean (November-April) of the sea level pressure (colors, in hPa) and 10 m wind speed (arrows), from ERA-Interim 1979-2014 reanalysis, from [Kounta Diop \(2019\)](#) thesis. Average locations of Azores and Saharo-Lybian anticyclones are indicated in blue circles.

alongshore upwelling favorable winds. Composite analysis led by [Kounta Diop \(2019\)](#) has shown that wind intensification over the Senegalese domain is associated with an increased southern extension of the Azores high and a weaker Saharo-Lybian high pressure center. In an opposite manner (but not exactly symmetric), the relaxation of upwelling winds is associated with a northward shift of the Azores high and a stronger Sahara-Lybian high pressure center. These fluctuations in the location and intensity of this dipole drive pressure and thus geostrophic wind anomalies and result in synoptic wind variability.

Meridional oscillations and intensity fluctuations of the pressure dipole are suspected to be linked with the dispersion of mid-latitude Rossby waves created from jet stream instabilities ([Moron et al., 2018](#)), but further research is needed on this topic.

Over the southern tropical band (south of 15-20°N), the ITCZ seasonal migrations determines the upwelling favorable season from November to June ([Roy, 1989](#); [Citeau et al., 1989](#)). Note that the west African monsoon period occurs between July and October. There, easterlies dominate between October and March while westerlies dominate the rest of the season. Easterlies can bring particularly dry air from the Sahara which impacts immensely the total heat flux through enhanced evaporation/latent heat flux ([Thomsen et al., 2021](#)).

2.4 Response of coastal upwelling sectors to synoptic wind intensification/relaxation

Time varying winds drive physical and biogeochemical variability in coastal upwelling systems. Oceanographic instantaneous conditions are largely driven by synoptic scale events ([Zhang et al., 2015](#); [Desbiolles et al., 2014](#); [Aguirre et al., 2021](#)), that also drive changes in carbon fluxes

and biogeochemical, planktonic and ecosystem properties (Torres et al., 1999, 2002; Evans et al., 2015; Bane et al., 2007). Here we describe the known typical responses of coastal upwelling systems to synoptic wind variability, and processes at play during relaxation and intensification.

Stronger winds inject more energy into the ocean, which induces more rapid offshore advection (Botsford et al., 2003), vertical advection and mixing, leading to changes in the upper ocean heat content (Send et al., 1987). In the CCS, modeling studies (Gan and Allen, 2002a) and in situ measurements (Send et al., 1987) have shown that alongshore pressure gradient and alongshore flow are increased during upwelling events. The upper ocean heat content is decreased by vertical advection and entrainment of relatively cool subsurface water into the mixed layer, and in many places by alongshore advection of coastal cold waters.

Weaker winds lead to reduced alongshore advection, reduced vertical advection and mixing, and are associated with changes in the impact of air-sea heat fluxes on the upper ocean heat content (in Bodega Bay in Send et al., 1987). Thus, processes during relaxation differ from those during intensification (Send et al., 1987; Send, 1989). The response of the alongshore pressure gradient (shown in Fig. 0.1) can even lead to a reversal of the flow so that it is orientated poleward (Send et al., 1987). This can modify the circulation and heat balance through the advection of warm waters, the increase of temperature and buoyancy gradients. In the nearshore part, upwelling relaxation may stimulate onshore transport of offshore plankton species through altered frontal activity and recirculation (Shanks et al., 2014). This inshore recirculation of offshore warm waters, along with mixed layer processes (Marchesiello et al., 2003; Ramp et al., 2005) and air-sea heat fluxes (Beardsley et al., 1998) increase the upper ocean heat content.

Overall, there is evidence that upwelling wind intensifications and relaxations influence the coastal ocean dynamics through different and irreversible processes. Asymmetries between the two phases may exist and lead to a rectification/residual effect of the synoptic fluctuations onto the lower-frequency, mean functioning of the system. The notions of asymmetry and rectification effect are at the heart of this thesis and are introduced next.

2.5 Asymmetries in climate/ocean physics

One key aspect of analyzing the impacts of synoptic variability is to assess how the mean oceanic state differs between being forced by symmetric positive and negative wind fluctuations from the mean or only by mean winds. In this context, we illustrate on the schematic in Fig. 0.4 the potential asymmetrical responses, due to rectification effects, of a system forced by symmetrical perturbations ($\delta_f^+ = -\delta_f^-$) in addition to the mean forcing. The system responds asymmetrically if $\delta_r^+ \neq -\delta_r^-$ and the associated net residual effect on the mean state is estimated by $\delta_{res} = \delta_r^+ + \delta_r^-$. In this section, we first present studies of climate physics where advances in our understanding of processes are based on asymmetrical considerations. We then focus on the current knowledge of oceanic synoptic scale asymmetries.

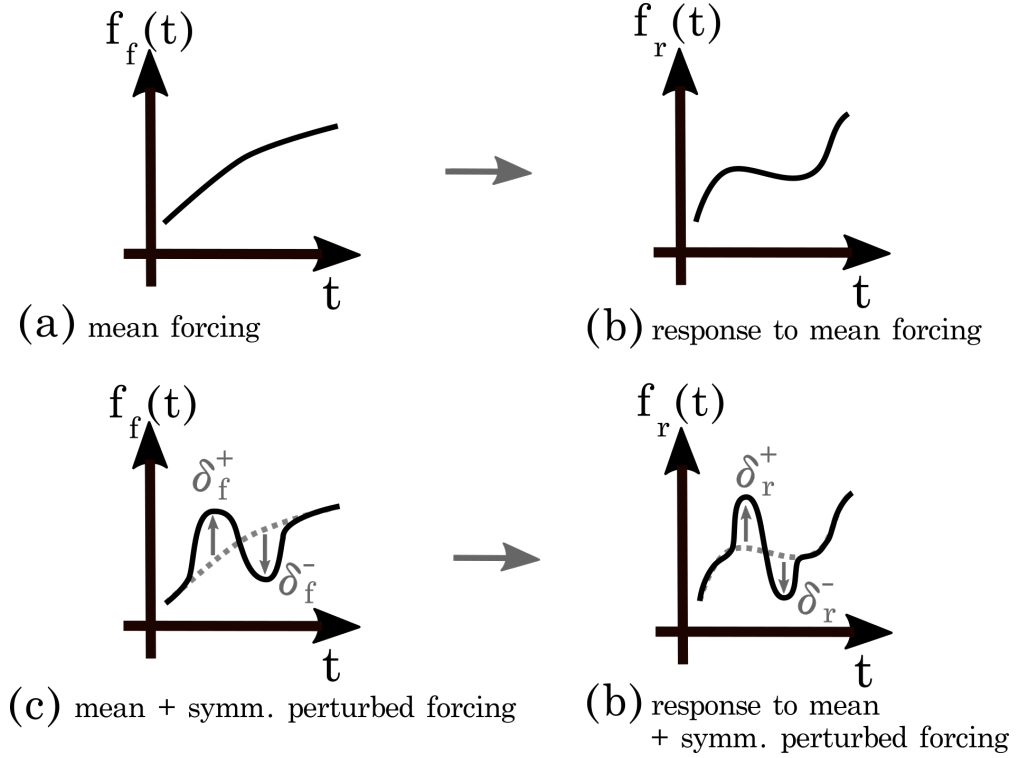


Figure 0.4: Schematic of a system forcing (denoted $f_f(t)$, panels a,c) and response (denoted $f_r(t)$, panels a,c). Positive (δ_f^+) and negative (δ_f^-) symmetrical ($\delta_f^+ = -\delta_f^-$) perturbations in the forcing impact the system response, symmetrically (if $\delta_r^+ = -\delta_r^-$) or not (if $\delta_r^+ \neq -\delta_r^-$).

At the climate scale, asymmetries are observed between positive and negative phases of climate dipole variability. This has been shown for the North Atlantic Oscillation (NAO) for a spatial asymmetry, where the displacement of the Azores high and Icelandic low is more enhanced eastwards during the positive phase (Cassou et al., 2004). For the Indian Ocean Dipole, an asymmetry arises in the amplitude of SST anomalies between negative and positive phases (Hong et al., 2008). Similarly, patterns and duration of El Niño and La Niña events are found asymmetric (Okumura et al., 2017) such that there is a net impact of positive and negative anomalies compared to a mean state.

Spatial asymmetries are also found between hemispheres. For example, asymmetries arise in a transient regime in response to a perturbation in climate forcing (anthropogenic CO₂). Under climate change, the warming rate of the Earth surface is higher in the Northern than in the Southern hemisphere, likely caused by the heat uptake of the Southern ocean and deep vertical mixing (Stouffer et al., 1989; Flato and Boer, 2001). Also, the two hemispheres respond asymmetrically to high latitude sea-ice cover anomalies which can impact the ITCZ displacement (Chiang and Bitz, 2005). Climate change strongly impacts breeding success of seabirds species (considered as ecosystem sentinels) in the northern hemisphere, while this impact is moderate in the south (Sydeman et al., 2021).

In oceanic physics, spatial asymmetries can arise from geomorphological peculiarities. For example, the northern and southern faces of a cape have different alongshore pressure gradient and thus asymmetrical advection properties (Gan and Allen, 2002a). The residual current of barotropic tides is another example of rectification effects (Zimmerman, 1986), like surface

waves/Stokes drift (Curcic et al., 2016). Also, Farneti et al. (2010) highlight the role of mesoscale eddy activity in reducing the oceanic circulation response to atmospheric changes by rectification effects.

In coastal oceanic upwelling systems, the extent to which synoptic scale residual effects influence the mean state is still unclear. Send et al. (1987) argue that processes during relaxation are irreversible (solar heating and mixed layer detrainment) such that they cannot be reversed and induce strong asymmetry with upwelling. Also, the essential importance of synoptic variability has been demonstrated by García-Reyes et al. (2014) who show a better agreement of indices based on cumulative oceanic responses with chlorophyll concentration and zooplankton populations rather than traditional upwelling indices based only on wind intensity. Despite an impact of synoptic scale variability on the upper layer turbulence, eddy kinetic energy and SST alongshore variability compared to monthly climatological simulations, Aguirre et al. (2014) indicate an overall rather linear response of the coastal ocean to synoptic wind intensification and relaxation (in the central Chile upwelling system). These contrasting results highlight the complexity and high variability of coastal upwelling systems.

2.6 Northwest African and South Senegalese Upwelling Sectors

Despite intense synoptic atmospheric variability in the Canary Upwelling System (CUS; Desbiolles et al., 2014; Kounta Diop, 2019; Thomsen et al., 2021; see Senegalese atmospheric variability in Fig. 0.8), little attention has been given to their impact on the northwest African coastal sectors, in contrary to the Iberian part of the system. There, upwelling activity has been linked to circulation weather types in Ramos et al. (2013) and temperature variability during upwelling is assessed by Lopes et al. (2014). Coastal oceanic responses to an upwelling relaxation have been described with in situ observations in the southern (Relvas and Barton, 2005) and northern parts (Cordeiro et al., 2018) of the Iberian peninsula.

Northwest Africa oceanic circulation

Here we present briefly the northern Atlantic eastern basin circulation near the Northwest coast of Africa as shown in Fig. 0.5 from Arístegui et al. (2009). The Canary Current results from the subtropical gyre circulation and flows equatorwards until Cape Blanc ($\sim 20^\circ\text{N}$), where it detaches to flow westwards. The North Equatorial Counter Current ($\sim 9^\circ\text{N}$) flows eastward and separates approaching the African coast. Its northern branch forms the Mauritanian current, that flows northwards until approximatively Cape Blanc and is then deflected westward to merge with the Canary current and form the North Equatorial Current. The weak mesoscale activity in the Canary upwelling system compared to the CCS is due to compensation effects between salinity and temperature that induce differences in stratification (Marchesiello and Estrade, 2009).

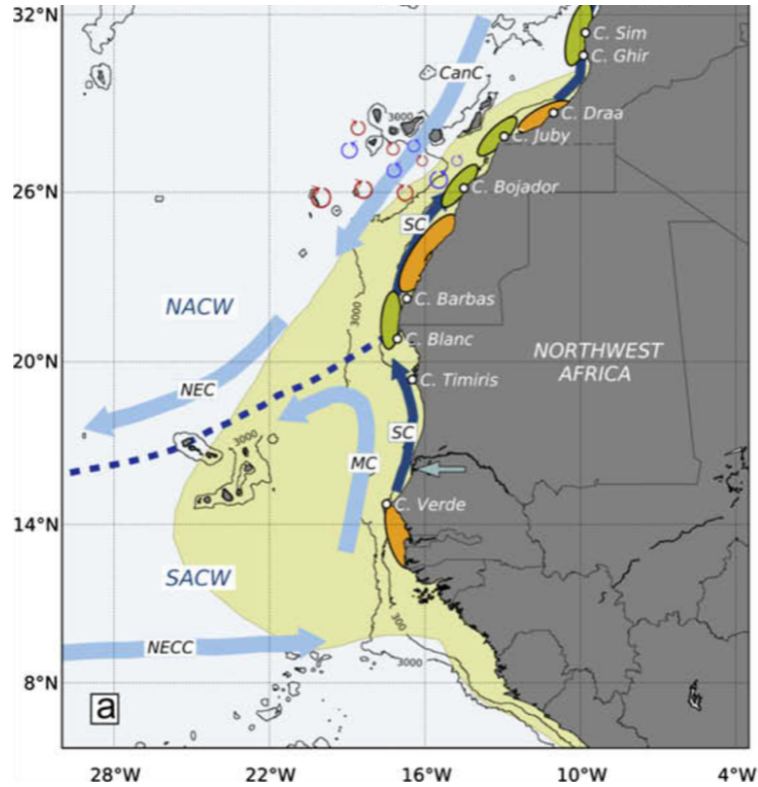


Figure 0.5: Canary Upwelling System circulation. From [Arístegui et al. \(2009\)](#).

South Senegalese Upwelling Sector

The domain of interest of this thesis is the southernmost upwelling sector of the Canary upwelling system, the South Senegalese Upwelling Sector (SSUS - $\sim 12\text{--}15^\circ\text{N}$), on which we aim to increase the general marine environment knowledge. Other west African sectors would deserve a similar attention to better understand the diversity of circulations and their potential important impacts on the Canary system (e.g. Cape Ghir, Western Sahara Bank, Cape Blanc and Arguin Bank; see Fig. 0.7a). Because an important part of the upwelling literature concerns the CCS, we provide a comparison of spatial scales between the Canary and California upwelling systems, and Cape Verde and Monterey Bay sectors in Fig. 0.6. We particularly emphasize the sharpness of Cape Verde and the size of the south Senegalese sector compared to Monterey Bay dimensions. We also took the opportunity to present typical SST patterns, which we will discuss throughout the manuscript.

The SSUS northern limit is the sharp Cape Verde (CV) which hosts the city of Dakar (see Fig. 0.7). The southern limit of the sector is about 300 km south ($\sim 12.5^\circ\text{N}$) and includes Gambian territorial waters (between $13^\circ 35' 35''\text{N}$ and $13^\circ 03' 27''\text{N}$). The system presents two main geomorphological peculiarities: the sharp CV that acts like a coastline break and the shallow and wide continental shelf (the 100 m isobath extends about 50 km offshore, see Fig. 0.7). The SSUS differs from many other upwelling sectors (e.g. CCS) because its surrounding circulation is not equatorward but poleward. This has a direct impact on the boundary conditions of the Senegalese shelf dynamics and the upwelling source waters.

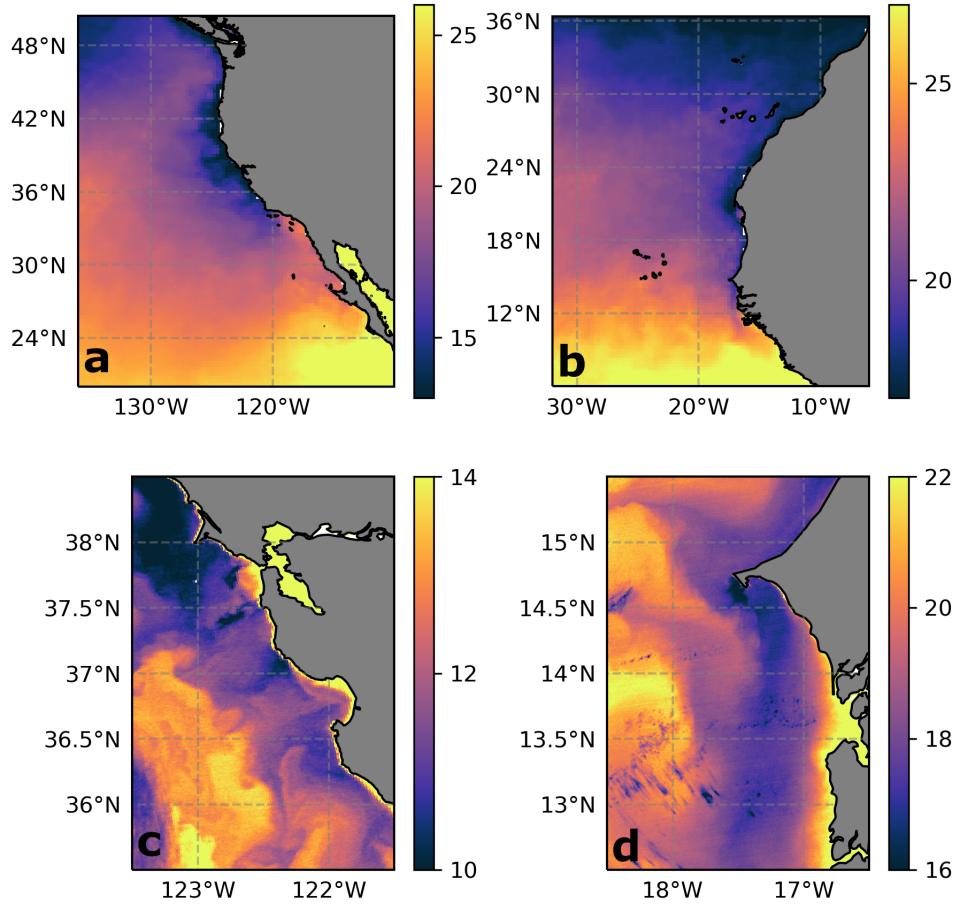


Figure 0.6: West coast of North America (a), Northwest coast of Africa (b), Monterey Bay/ Gulf of Farallones (c) and South Senegalese coast (d). Upper panels are monthly SST averages during August (a) and March (b) 2000, from Copernicus data "Multi Observation Global Ocean ARMOR3D L4" (<https://doi.org/10.48670/moi-00052>) and lower panels are daily SST images of the 23 May 2022 (c) and 1 March 2022 (d), from Nasa AQUA MODIS (<https://oceancolor.gsfc.nasa.gov/>).

As mentioned earlier, the season of upwelling favorable winds is between November and May-June (Roy, 1989). The system is subject to substantial wind fluctuations shown in Fig 0.8a, as for example a major meridional wind intensification in late December 2000 or a relaxation of ~5-10 days during mid February 2001. This time series highlights the high frequency variability of upwelling favorable winds but also net heat flux (Fig 0.8b) during the upwelling season over the SSUS.

During the upwelling season and south of the cape, a quasi-permanent Sea Surface Temperature (SST) minimum area is observed with satellite images (Ndoye et al., 2014) and indicates the probable location of resurgence (Fig. 0.9). This location of resurgence has been identified just south of CV over a very located area thanks to a modeling study of Ndoye et al. (2017).

A cold upwelling plume forms over the shelf and indicates the southwards orientation of the advection of upwelled waters (Ndoye et al., 2014, see Fig. 0.9). The SSUS thus differs from other upwelling sectors where cross-shore transport dominates (e.g. CCS). This structure can be explained by geomorphological features that influence the flow. Waters north of CV are expelled offshore as the cape blocks any alongshore advection. South of CV, the shallowness of the shelf

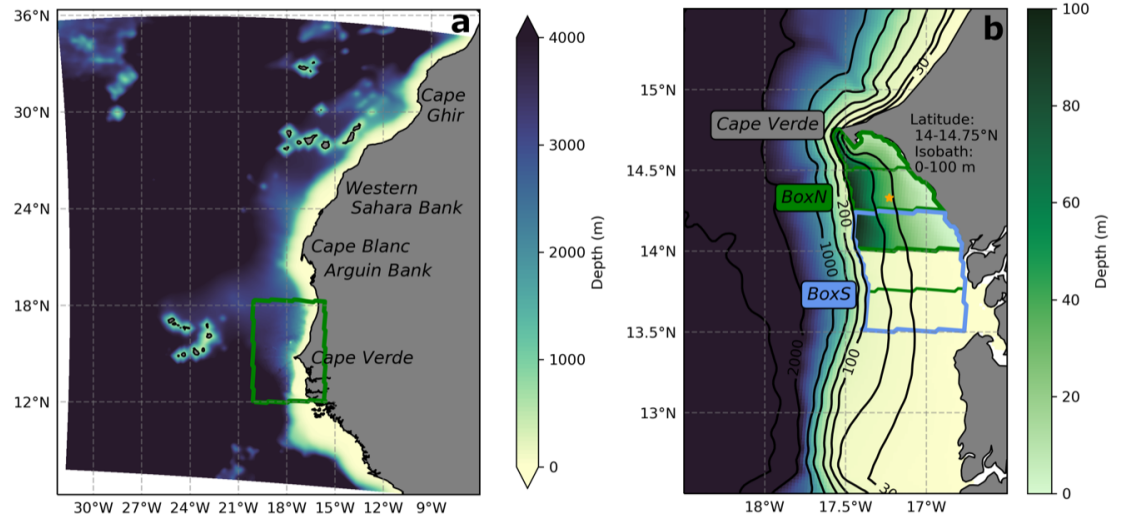


Figure 0.7: Northwest African domains (a) and south Senegalese domain of interest (b). Bathymetry is indicated in colors.

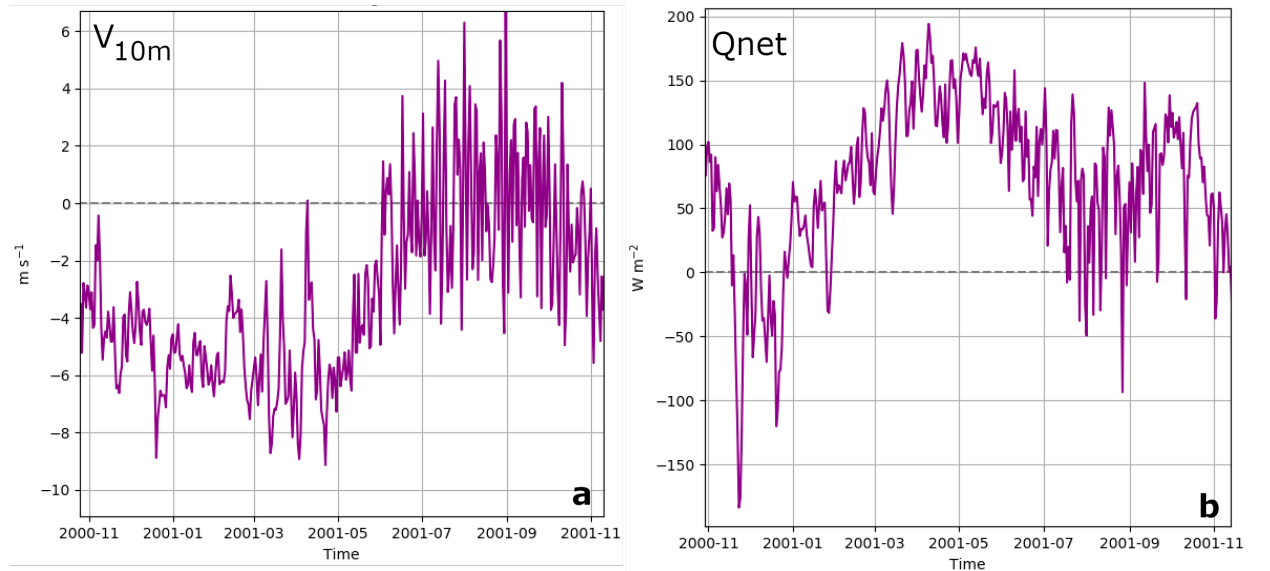


Figure 0.8: Daily averages of (a) the meridional wind speed at 10 m and (b) the net heat flux over south Senegalese waters for the year 2001 from ERA5 reanalysis.

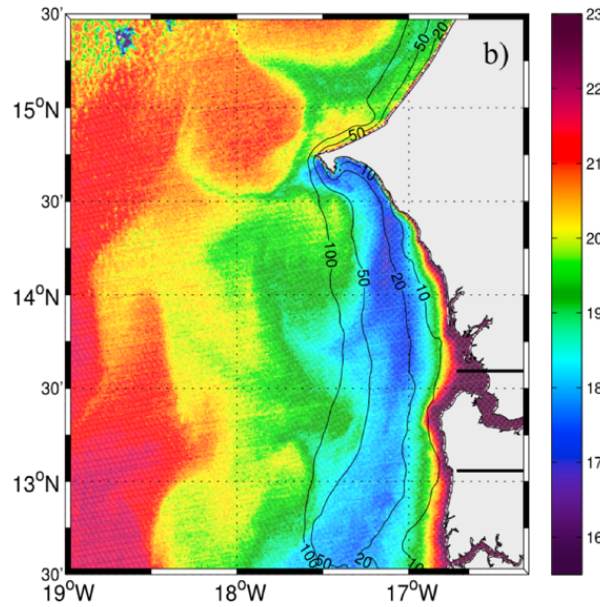


Figure 0.9: Satellite (L2 MODIS) SST instantaneous image during the upwelling season. From [Ndoye et al. \(2017\)](#).

prevents a strong offshore Ekman drift and waters flow along the shelf. Indeed, momentum is mixed over the inner shelf so that wind and bottom friction equilibrate without involving the Coriolis force ([Estrade et al., 2008](#)). In addition, meridional buoyancy gradient (warmer towards the south) and sea surface elevation gradient (sea surface more elevated towards the south) cause a negative alongshore pressure gradient and induce an onshore geostrophic transport that drastically reduces the offshore Ekman transport over this sector ([Ndoye et al., 2017](#)). This highlights the necessity of having a 3D view of this particular system rather than a classical 2D view. Lastly, the widening isobaths increase the transport of mass downstream and favor the entries of water onto the shelf south of CV ([Pringle, 2002](#)).

Another peculiarity of the SSUS is the warm SST nearshore band south of 14.5°N ([Roy, 1998](#)) over a very shallow shelf. Also, the water situated offshore of the cold upwelling plume is warm, more stratified and more subject to stirring by mesoscale features ([Capet et al., 2017](#)). Thorough analysis of a vast SST satellite images dataset ([Ndoye et al., 2014](#)) and intensive measurements ([Capet et al., 2017](#)) revealed strong oceanic variability at synoptic time scales, which will be discussed throughout this thesis.

3 Biogeochemical and planktonic ecosystem structure

In addition to complex dynamics, coastal upwelling systems host a rich ecosystem whose sources of variability can originate from many different environmental, physical or biological processes. In spite of the difficulty to predict the highly variable ecosystem state, progress has been made using long term observations of large scale circulation, productivity and planktonic communities and to create adapted indicators (Di Lorenzo and Ohman, 2013; García-Reyes et al., 2014; Jacox et al., 2018).

In a nutshell, the planktonic ecosystem of an upwelling is a short food chain that transfers rapidly from nutrients supply to pelagic fishes (Rykaczewski and Checkley, 2008; Ohman et al., 2013). High nitrate fluxes from the subsurface into the upper layer where light is available trigger photosynthesis to create organic matter (phytoplankton, e.g. diatoms). The secondary producers that are planktonic animals (zooplankton, e.g. copepods) graze on this phytoplankton biomass and develop. Then, higher trophic levels develop (e.g. small pelagic fish). Plankton biomass are regulated by several biological or physical factors such as nutrients or light limitation, temperature, grazing, predation by upper trophic levels, mortality/aggregation, mixing and advection (Williams and Follows, 2011). In the following section, we briefly develop these biogeochemical concepts in the coastal ocean along with the processes involved. Note that the carbonate cycle and exchanges with the atmosphere, as well as iron and oxygen cycles (the oxygen cycle has been studied by Tall et al., 2021 over the Senegalese shelf) are out of the scope of this thesis.

3.1 Planktonic ecosystem concepts

The phytoplankton is of crucial importance as being the first link of the marine's food chain and responsible for about half of the Earth's primary production (Falkowski et al., 2003). Its relationship with both the nutrients supply and the zooplankton, one trophic level higher, is key to understanding the energy and material transfer from the environment to marine life. In this section we present the general planktonic ecosystem concepts and rely on Fig. 0.10 reproduced from Williams and Follows (2011).

Nutrients and light

At rest, the ocean is vertically stratified: high nutrient concentrations are found at depth and light availability at the surface (see Figs. 0.1 and 0.10a). Thus, for new primary production to occur, a vertical transport that supplies nutrients into the upper layer, where photosynthesis is possible, is needed. This layer is called the euphotic layer, which is defined by the depth at which the photosynthetic available radiation reaches 1% of its surface value (Morel, 1988) and varies depending on light availability and water turbidity.

In the ocean, extra energy is needed to counteract the effect of stratification and produce vertical motions. This could happen with different processes at different scales such as large scale meridional thermocline ventilation (Cox, 1985), basin scale convection (Killworth, 1983),

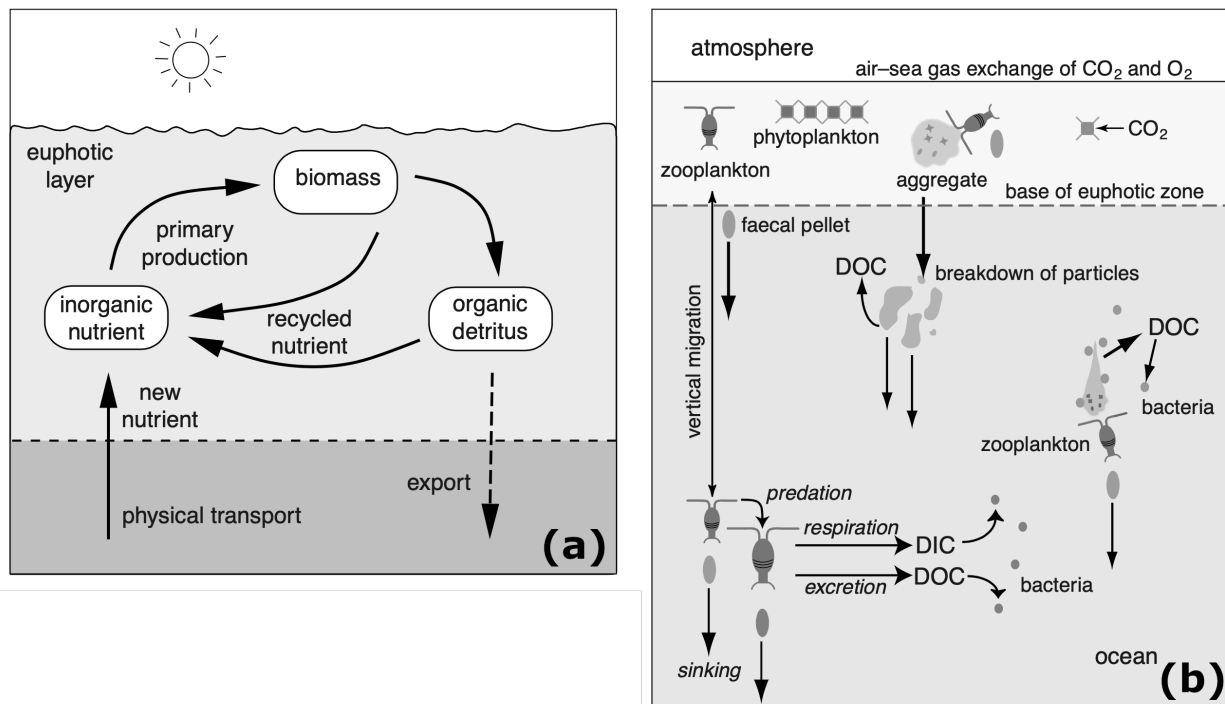


Figure 0.10: Schematics of (a) the fueling of primary production by nutrients and (b) processes regulating the export of organic matter from the euphotic layer to the deep ocean. Those panels are the Figs. 5.15 and 5.17 of [Williams and Follows \(2011\)](#).

mesoscale turbulence ([Lévy, 2008](#)) or submesoscale frontal activities ([Capet et al., 2008c](#)) and intense vertical transport in coastal upwelling systems through wind forcing (e.g. [Chelton, 1982](#)).

The main nutrients necessary for phytoplankton growth are the carbon dioxide (CO_2), nitrate (NO_3), phosphate (PO_4) and silicate (Si) macronutrients and the iron (Fe) micronutrient. They have different sources, rates of bioavailability and oceanic spatial distribution ([Stukel and Barbeau, 2020](#)). The oceanic nitrogen cycle is complex and is hypothesized to be mostly controlled by: nitrogen fixation (metabolic process that converts inert N into biologically available substrates, [Karl et al., 1997](#)), nitrification (transformation of ammonium NH_4 to NO_3 through bacterial activity, [Yool et al., 2007](#)) and denitrification (bacteria through respiration reduce nitrate into molecular nitrogen, [Christensen et al., 1987](#)). Ammonium is preferred to nitrate by phytoplankton, such that ammonium lifetime is short and is mainly concentrated in the upper layer in remineralization areas of organic matter ([Sarmiento and Gruber, 2013](#)). Also, sources of iron are multiple, like the upper (atmospheric deposition), bottom and lateral (sediments in shallow/coastal environments) boundaries of the water column.

The Redfield ratio (C:N:P ratio) in plankton is considered constant to a first approximation ([Takahashi et al., 1985](#)). Its variability depends partly on nutrient availability and can have important ecosystem impacts ([Hutchins and Bruland, 1998](#)), as well as consequences on the upper trophic levels food quality ([Kwiatkowski et al., 2018](#)).

Primary Production

In the euphotic layer, available nutrients and light allow photosynthesis by oceanic primary producers, the phytoplankton (Fig. 0.10a). The total primary production (PP) is separated in the new production term (NP) based on new nutrients (NO_3) and the regenerated production term (RP) based on recycled nutrients (NH_4) such that $PP = NP + RP$. Phytoplanktonic ecosystems can temporarily maintain growth without new nutrients through the regenerated production (Eppley and Peterson, 1979). The relative importance of new versus regenerated production is diagnosed with the ratio: $f - ratio = \frac{NP}{PP}$ (Harrison et al., 1987).

The plankton is initially defined by its inability to counteract the flow. Another essential property of plankton is its amazing diversity, with no consensus from years of research on the number of species (Hutchinson, 1961; Huisman and Weissing, 1999). In spite of this, our knowledge of plankton evolves rapidly with new measurements techniques and increase of sampling effectiveness (Lombard et al., 2019).

Phytoplankton are usually grouped by size, notably in nanophytoplankton (cell size of 2-20 nm) and diatoms (microphytoplankton - larger cells of 20-200 μm). Indeed, the behavior of phytoplankton differs according to their size: a larger (resp. smaller) cell allows a higher nutrient intake in a nutrient rich (resp. poor) environment (Hutchings et al., 1995; Irigoien et al., 2005). Note that as the phytoplankton is a result of photosynthesis, it contains chlorophyll pigments that absorb light in the blue-green bands. Thus, it is common to use the chlorophyll-a concentration (from remote sensing ocean color or in-situ optical measurements) as an indicator of the phytoplankton biomass (e.g. Kahru et al., 2009, 2015; Farikou et al., 2015; Aguirre et al., 2021).

Fate of phytoplankton

The fate of the phytoplankton biomass can be multiple. This organic matter can either die, aggregate, be remineralized by bacterial activity to become recycled nutrients (Fig. 0.10a), sink by gravitation and export carbon towards the bottom of the water column, eventually be buried in the sediments, or be grazed by upper trophic levels (Fig. 0.10b). The relative weight of NP compared to carbon export is diagnosed by the ratio $\frac{NP}{CE}$, that identifies productive waters or carbon export locations (Stukel et al., 2011).

Secondary Production

The second trophic level of the food chain is zooplankton, which have different sizes and food preferences. For example, herbivorous microzooplankton (15-300 μm) only graze on phytoplankton and are smaller than omnivorous mesozooplankton (large cells, i.e. copepods 1-2 mm) which graze phytoplankton, zooplankton and particulate organic matter (Strand et al., 2020).

Like the phytoplankton, size differentiates the behavior of each species in a food rich (in favor of mesozooplankton) or poor (in favor of microzooplankton) environment. For some zooplankton species, diel vertical migration refers to their ability to migrate in the water column between the upper layer during the night and deeper waters during the day (typically between

100-200 m deep when ocean depth is sufficient; [Peterson et al., 1990](#); see Fig. 0.10b). This allows a reduced exposure to upper layer turbulence, sheltering from predators during the day and feeding opportunities during the night ([Peterson et al., 1990](#); [Ohman, 1990](#)).

3.2 Structure, cycles and processes in coastal oceanic upwelling sectors

We presented the leading order planktonic ecosystem concepts. In a dynamically complex coastal upwelling system, biological processes add a source of variability. In different EBUS and coastal subdomains, different factors regulate the biological activity. These causes of variability of planktonic ecosystems are presented in this section at the climatological and synoptic time scales.

Diatoms in upwelling systems

In the heart of coastal upwelling systems, enrichment is strong and waters are cold, such that diatoms are favored and dominate. This is due to their more efficient nutrient uptake (large cells in a nutrient rich environment; [Shannon and Pillar, 1986](#)) and because they have a higher uptake and storage capacity in cold waters ([Lomas and Glibert, 1999](#)) compared to smaller phytoplankton. Large zooplankton consequently dominate in these areas as prey and predator sizes correlate ([Rykaczewski and Checkley, 2008](#)).

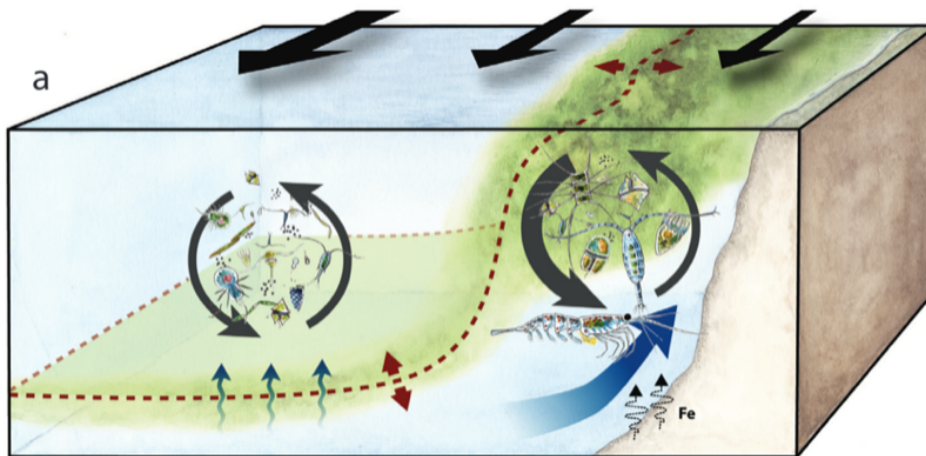


Figure 0.11: Scheme of the cross-shore structure of wind stress (large black arrows), vertical velocities (thick blue arrow represent the strong coastal upwelling and smaller blue arrows the wind stress curl upwelling), nutricline depth (dashed red line) and plankton communities (i.e. large and small plankton; circular arrows represent the intensity of growth and grazing in the nearshore and offshore sectors) in the California Current Ecosystem. From [Ohman et al. \(2013\)](#).

Physical-biogeochemical processes impact on biological structures

Coastal upwelling systems transport waters from different origin, depth and thus different temperature, nutrients and chemical properties ([Hutchings et al., 1995](#); [Jacox et al., 2015](#)). These source waters properties can be modulated by environmental/physical conditions ([Rykaczewski and Dunne, 2010](#)) and directly drive the growth rate of phytoplankton, food qual-

ity and impact upper trophic levels. River discharges can also be a source of nutrients, create density fronts and enhance production, as for example in the Northern end of the CCS (Hickey and Banas, 2008).

Coastline geomorphological features impact the planktonic ecosystem with implications on the dynamics, enrichment and retention of coastal waters (Hickey and Banas, 2008; Largier, 2020). Also, they can define preferential pathways of upwelling (Jacox and Edwards, 2011; Ndoye et al., 2017), which determines the origin of source waters.

The effective vertical transport of nutrients into the upper layer is modulated by the balance between the intensity of vertical velocities, stratification, and nutrient concentration at the base of the mixed layer (Jacox and Edwards, 2011). Vertical velocities induced by the wind cross-shore structure vary spatially and structure planktonic ecosystems. The strongest vertical velocities are found nearshore and colocate with patterns of high plankton biomass and large species (Ohman et al., 2013). Further offshore, slower vertical velocities driven by the wind stress curl colocate with smaller plankton species (Jacox et al., 2016). The wind structure also influences upper trophic levels, especially pelagic fishes (Rykaczewski and Checkley, 2008). Nutricline depth has also a major impact on production (Ohman et al., 2013; Fig. 0.11).¹

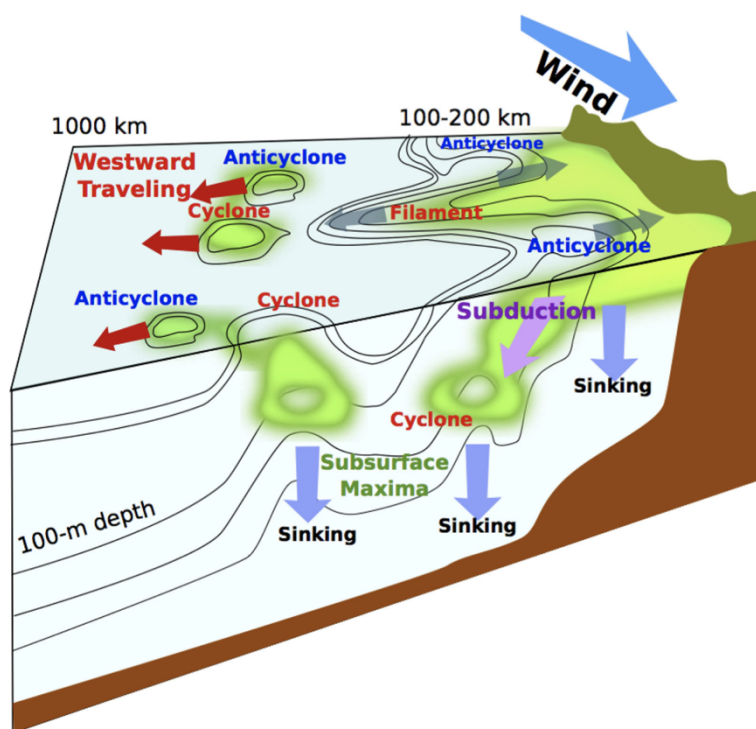


Figure 0.12: Scheme of the main physical and biogeochemical processes at play in the California Current Ecosystem. Wind is indicated with the large blue arrow. The organic matter formed in upwelling waters nearshore is transported offshore by filaments and mesoscale eddies. The westward direction of propagation of both mesoscale cyclones and anticyclones is indicated in the red arrows. Subduction in mesoscale features and sinking in the water column are indicated with purple and blue arrows. From Nagai et al. (2015).

¹and can be responsible for strong interannual variability, for example in the CCS in neutral or ENSO conditions (Chavez et al., 2002; Deutsch et al., 2021).

In a 3D framework, the planktonic ecosystem evolves along the advection paths of upwelled waters. Along these pathways, the nutrient supply precedes phytoplankton blooms, eventually carbon export areas and zooplankton patches (Lasker and Zweifel, 1978; Stukel et al., 2011; Messié and Chavez, 2017). During the offshore advection, mesoscale circulation features have a direct impact on the ecosystem structure (Fig. 0.12). The importance of eddies (both cyclones and anticyclones) and filaments in the offshore transport of carbon and nutrients have been described in the CCE (e.g. Nagai et al., 2015; Chenillat et al., 2016). Also, recirculation can reduce the offshore export. In association with (sub)mesoscale features/eddy effects, subduction reduces the retention of biological material at the coast and in the euphotic layer (Gruber et al., 2011), and is enhanced at mesoscale fronts along with sinking (Stukel et al., 2017). This tends to reduce nearshore productivity and enhance new production in the offshore region where more nutrients are thus available close and below the euphotic layer (Gruber et al., 2011; Kessouri et al., 2020).

Synoptic time scales

As explained in section 2.5, taking into account the synoptic wind variability has been shown to be necessary to predict ecosystem variability (García-Reyes et al., 2014) even though the importance of their impact on the mean state remains unclear.

Still, high frequency wind variability largely modifies coastal upwelling ecosystem properties. Synoptic variability is complex having time scales of the same order as those of the phytoplankton growth. At this scale, upwelling favorable winds either intensify or relax and perturb the state of the oceanic ecosystem. The physical structure of the upwelling changes have been described in section 2.4. Here we aim to present additional coupled physical/biogeochemical processes shaping this response.

Retention of biological material

A fundamental aspect of coastal upwelling ecosystems is the residence time of a recently upwelled water mass in the nearshore area. As mentioned earlier, wind-driven advective and eddy/subduction/frontal processes refrain phytoplankton growth by removing biological material (either nutrients or plankton) out of the nearshore ecosystem/euphotic layer (Largier et al., 2006; Gruber et al., 2011). There is a correspondence between the wind strength and the shelf width, such that offshore losses are reduced and residence time is increased if the wind is weak or if the shelf is wide (Botsford et al., 2003). Sheltered areas increase the nearshore retention such that nutrients concentration and phytoplankton growth are enhanced (Largier, 2020). These areas are also suitable for egg spawning (Bakun and Csirke, 1998). For an effective increase of production, the duration of retention has to be longer than the time of growth of phytoplankton (Botsford et al., 2006). Wind intermittency at the synoptic time scale favors the retention of biological material (in the northern end of the CCS, Hickey and Banas, 2008). Trade-offs between these negative and positive effects define optimal environment windows for maximum production (Cury and Roy, 1989; Jacox et al., 2016).

Effect of synoptic wind intensification and relaxation

The vertical structure of the water column, nutrient availability in the upper layer and thus phytoplankton biomass rapidly change in response to wind fluctuations (Pitcher et al., 1991;

Aguirre et al., 2021), along with zooplankton (Dorman et al., 2005) and crab (Wing et al., 1995) populations. Rectification effects due to biological processes might induce an important impact on the mean state, as for example the postlarvae inshore migration that occurs during relaxation (Morgan et al., 2018).

Intense upwelling winds increase vertical velocities and thus the nutrient supply in the upper layer. However, intense winds might have negative impacts on the primary production. In fact, lower phytoplankton (Aguirre et al., 2021) and zooplankton (Dorman et al., 2005) biomass are observed in response to synoptic upwelling intensification compared to relaxation periods. This could be due to the deepening of the surface mixed layer that dilutes the concentration of biological material and brings a part of it below the euphotic layer, such that primary producers lack light exposure (Largier et al., 2006). Also, strong Ekman transport expels biological material offshore and dilutes nutrients concentration (Largier et al., 2006; Kudela et al., 2006). Dugdale and Goering (1967) argue that this increased advection and turbulence limit the intake of nutrients by phytoplankton during upwelling intensification. In the same way, Evans et al. (2015) hypothesize that the failure of phytoplankton to bloom in response to intense upwelling is caused by their rapid offshore transport and subduction. Intensified cross-shore currents push the highest concentrations of zooplankton further offshore during a wind intensification (Papastephanou et al., 2006).

In an opposite manner, wind relaxation periods enhance residence time and primary production (Botsford et al., 2006), and are essential for marine species to survive and reproduce (Hutchings et al., 1995). Onshore transport (Shanks et al., 2014) and the reduction of the upwelling jet accumulate biological material nearshore, and phytoplankton and zooplankton communities might be colocated nearshore (Spitz et al., 2005; Papastephanou et al., 2006). Despite the general agreement on these typical responses, some studies such as Pitcher et al. (1991) found opposite responses with a high phytoplankton biomass during turbulent and nutrient rich conditions and low biomass during stratified and nutrient depleted conditions.

The combination of events, and especially the succession of an intensification and a relaxation could maximize primary production (Yokomizo et al., 2010). More precisely, observations show that 3 days of upwelling/nutrient supply followed by 3-7 days of relaxed winds/sheltered conditions lead to an increase of production compared to the initial state (Wilkinson et al., 2006). In the same manner, zooplankton concentration increases during and after a relaxation (Dorman et al., 2005) and is hypothesized to be maximal after a 1-5 day upwelling followed by 6-7 days of relaxation (Papastephanou et al., 2006). Recent observations off Peru/Chile (Aguirre et al., 2021) found enhanced phytoplankton biomass after 1-2 days of upwelling wind relaxation. All these observations support the same optimal window environment: plankton biomass is maximum after a succession of upwelling-relaxation events (i.e. nutrient pulse-sheltered conditions) of several (1-7) days.

Trophic amplification

In addition to modifying the planktonic ecosystem structure, another aspect of the impact of atmospheric perturbations is their propagation towards the upper levels. This propagation is defined by how much each variable is perturbed as a consequence of the atmospheric perturbation. The characteristics of this propagation towards the upper trophic levels is also a key

facet of understanding planktonic ecosystem properties. For example, analysis of the propagation up the food web of the perturbation in the start date of the upwelling season shed light on remineralization and grazing impacts on the plankton biomass (Chenillat et al., 2013).

This is also of particular interest under a changing climate, which induces warmer surface waters and enhanced stratification (Bakun et al., 2015). It has been shown that a bottom-up perturbation (i.e. a warmer and more stratified ocean) induces a negative amplification of biomass changes (i.e. zooplankton losses are stronger than phytoplankton losses) at the climate scale (Chust et al., 2014).

3.3 Biogeochemical and planktonic ecosystem structures of Northwest African and South Senegalese Upwelling Sectors

Observing the highly variable and diverse planktonic ecosystem with an adequate spatial and temporal coverage is a great challenge (Lombard et al., 2019). Only a few coastal areas in the world are covered with a sufficiently long time series to identify causes of interannual variability and trends, for example in the CCE (Kahru et al., 2009; Di Lorenzo and Ohman, 2013). In fact, much of the progress in our understanding of coastal ecosystems has come from intense efforts on long term observations and original studies in the CCE. On the northwest coast of Africa, only a small number of in situ biogeochemical observations have been made. Mauritanian coastal waters are relatively well observed with recurrent measurements (between 2005 and 2016 in Klenz et al., 2018). South Senegalese shelf observations are rare and mostly recent (Cury and Roy, 1989; Capet et al., 2017; Machu et al., 2019; Tall et al., 2021).

The seasonal cycle of the chlorophyll concentration in the Northwest African sector varies along the coast (Lathuilière, 2008). In the northern part of the domain (24-33°N) weak chlorophyll seasonality is observed and associated to persistent high chlorophyll nearshore (see an example of monthly mean chlorophyll concentration in Fig. 0.13). In the Cape Blanc region (19-24°N) the chlorophyll concentration also has a weak seasonal cycle and high values are also found further offshore (Lathuilière et al., 2008). In the southernmost region (10-19°N), chlorophyll concentration is high between February and May Lathuilière (2008), consistent with the wind regime during this season (Kounta Diop, 2019). Over the Northwest African sector, the highest surface chlorophyll concentration variability is found over this southernmost region.

The typical structure of chlorophyll concentration over the Northwest African sector is shown in Fig. 0.13 (monthly average chlorophyll concentration during March 2010 from satellite observations, Gohin et al., 2002). The latitudinal variation of chlorophyll concentration highlights the importance of the Senegalese sector and sheds light on the alongshore plume south of Cape Verde at 14.5°N.

Overall, primary production estimates are greater along the northwest African coast than along the western American coast (Lachkar and Gruber, 2011; Messié and Chavez, 2015; Chavez and Messié, 2009). In the Northwest African system, light and temperature are believed to play a minor role on the production that is mostly regulated by the nutrient supply (Messié and Chavez, 2015). Depending on the subdomain, this new nutrient supply occurs either vertically through upwelling or laterally through meridional advection (Auger et al., 2016). In certain ar-

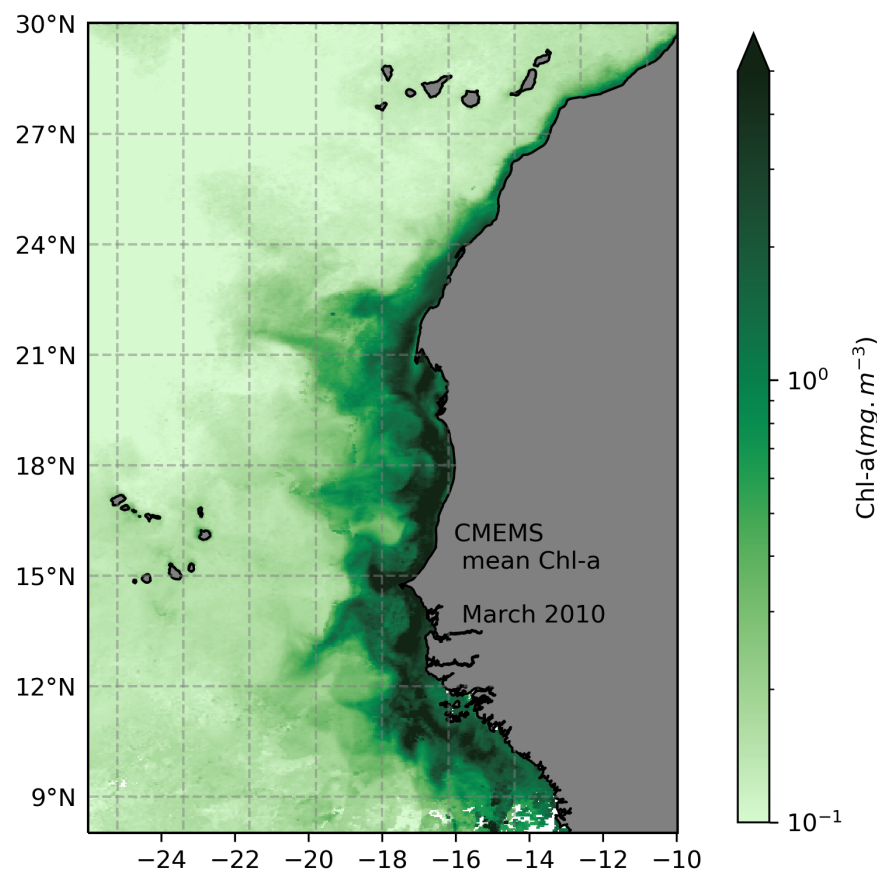


Figure 0.13: Monthly average of March 2010 near surface chlorophyll-a concentration, satellite observation from Copernicus (Gohin et al., 2002).

eas, regenerated production is also believed to drive most of the production (Auger et al., 2016). Depending on the eastern/western orientation of winds, high atmospheric iron deposition by Saharan dust prevents Fe limitation.

Over the South Senegalese upwelling system, remote sensing analyses and in situ measurements brought evidence of the dominance of diatoms during the upwelling season and nanophytoplankton in non upwelling seasons (Farikou et al., 2015, Hadjal Medjid and Eric Machu, 2016, unpublished). Farikou et al. (2015) show that zooplanktonic species are more abundant (but less diverse) during the upwelling season, particularly mesozooplankton. Despite a high variability, the analysis of in situ measurements of Hadjal Medjid and Eric Machu (2016, unpublished) allows to describe a snapshot of the SSUS planktonic ecosystem. The authors show that diatoms are mostly found in shelf cold waters and nanophytoplankton in off-shore warm waters during the upwelling season; and that the production is believed to be first limited by nitrate, then phosphate, silicate being a priori in excess.

The rich ecosystem of the south Senegalese shelf is also a sheltered region for fisheries (Brochier et al., 2018). In Senegal, the upwelling has a strong socio-economic impact for over 600 k people with over 400 k tons of fish catches per year, mostly of *Sardinella aurita* (FAO 2012, Garibaldi, 2012).

4 Scientific questions of the thesis

The general question investigated in this thesis concerns the impact of symmetrical synoptic wind fluctuations on the physical and planktonic ecosystem of a highly variable coastal upwelling sector. Generally, we hypothesize that synoptic fluctuations have modest asymmetrical responses and thus a modest impact on the mean state. We also aim to provide additional knowledge of the important and little studied Senegalese coastal upwelling system.

First, we wish to identify the impacts of synoptic wind intensification and relaxation on the dynamics of the SSUS. The first focus of this thesis is to assess the impact (i) on the physical structure, (ii) on horizontal and vertical velocity fields, mesoscale and submesoscale variability, (iii) asymmetrical responses and (iv) processes driving heat changes over the shelf surface mixed layer.

Second, we aim to shed light on the properties of the planktonic ecosystem as a whole in response to synoptic fluctuations. The second focus of this thesis is on (i) the overall impact on the structure of the biogeochemical and planktonic fields, (ii) the spatial and temporal shapes of the responses, (iii) the relative degree of propagation of the atmospheric perturbation in the ecosystem levels, (iv) asymmetrical responses, and (v) the spatial heterogeneity, e.g. the behavior of the inner shelf in comparison to the whole shelf.

Third, we aim to identify the processes at play in the planktonic ecosystem responses. The third axis of this thesis relies on (i) the identification of physical or biological processes at play controlling the nitrate, phytoplankton and zooplankton concentrations, (ii) a particular focus on processes responsible for the diatoms concentration changes as the dominant species of the ecosystem, (iii) assessing favorable wind conditions (intensification or relaxation) for primary production and plankton biomass.

5 Thesis outline

To answer these questions, we design a modeling framework in which idealized synoptic wind anomalies (intensification and relaxation) force an ensemble of climatological initial states. The ensemble run strategy is used to reduce uncertainties induced by intrinsic variability. A particular focus is made on the asymmetries between intensification and relaxation twin simulations because they are indicative of rectification effects associated with synoptic variability. We support our analysis with an evaluation of the model against in situ measurements. The modeling developed in this thesis does not pretend to recreate the real ocean variability. It aims to reproduce typical physical processes and to propose a certain view of planktonic ecosystem properties. The data, methods, description and advantages of such a numerical experiment will be developed in chapter [I](#), along with preparatory results. The impacts of synoptic fluctuations on the SSUS dynamics are presented in the form of an article accepted for publication in JPO (Journal of Physical Oceanography) in chapter [II](#) along with complementary results. Properties of the planktonic ecosystem model in response to a synoptic atmospheric perturbation are presented in chapter [III](#) in the form of an article (draft to be submitted to Geophysical Research Letters, GRL) along with complementary results. A process oriented analysis of this biogeochemical response is presented in chapter [IV](#), before the final conclusions and perspectives.

We also present the results of a study started during the masters and finished during the early PhD, in which we analyzed ecosystem properties along the advection pathways of upwelled water masses in the CCE. This JGR Oceans publication ([Chabert et al., 2021](#)) (Journal of Geophysical Research: Oceans) is presented in Appendix [V](#) and helped the interpretation of the SSUS biogeochemical model analysis. Note that an estimation of the energy/carbon cost of this PhD project is presented in Appendix [V](#).

Methods and preparatory results

Contents

1	Preamble	38
2	Regional oceanic model CROCO and numerical experiment	39
3	General methods	41
3.1	Model settings and simulations	41
3.2	ERA5 reanalysis dataset	43
3.3	Idealized synoptic events	44
3.4	Spatial averaging	53
3.5	Complementary details	53
3.6	Ensemble experiment	55
3.7	Residual effect	57
3.8	Heat budget	58
3.9	Lateral heat transport along box sections	60
3.10	Melax buoy data	61
4	Biogeochemical model PISCES and methods	64
4.1	Biogeochemical model PISCES	64
4.2	Model evaluation against biogeochemical observations	68
4.3	Budget on biological tracers	72
4.4	Weight of perturbation diagnostic	73

1 Preamble

In this chapter, we present the datasets, methods and some preparatory results of the thesis analyses. First, the regional oceanic model CROCO used in our analyses is described. Then, the methods sections of the JPO manuscript of chapter II are presented here and enriched with preprocessing and complementary details. Advanced budget techniques are presented. Next, we present the marine biogeochemistry model PISCES and the evaluation of our physical-biogeochemical simulations against observations. This chapter aims to provide keys to better interpret the results of the following chapters and apprehend the global approach of this thesis.

2 Regional oceanic model CROCO and numerical experiment

In this thesis, we use the Coastal and Regional Ocean Community hydrodynamic model (CROCO, from <https://www.croco-ocean.org/>; Hilt et al., 2020), which is an evolution of the Regional Ocean Modeling System (ROMS; Shchepetkin and McWilliams (2005, 2009).

CROCO resolves the following set of equations and hypotheses that are the Primitive Equations. The momentum balance is written in Eqs. I.1, I.2 (variables listed below the set of equations), the temporal evolution of a tracer (e.g. temperature) in Eq. I.3 and the equation of state in Eq. I.4. The hydrostatic hypothesis balances the vertical pressure gradient with the buoyancy force and the Boussinesq hypothesis ignores density differences except when they affect the buoyancy and give Eq. I.5. The fluid is incompressible such that the velocity divergence is null and gives Eq. I.6.

$$\frac{\partial u}{\partial t} + \vec{\nabla} \cdot (\vec{v} u) - f v = -\frac{\partial \phi}{\partial x} + \mathcal{F}_u + \mathcal{D}_u \quad (\text{I.1})$$

$$\frac{\partial v}{\partial t} + \vec{\nabla} \cdot (\vec{v} v) + f u = -\frac{\partial \phi}{\partial y} + \mathcal{F}_v + \mathcal{D}_v \quad (\text{I.2})$$

$$\frac{\partial C}{\partial t} + \vec{\nabla} \cdot (\vec{v} C) = \mathcal{F}_C + \mathcal{D}_C \quad (\text{I.3})$$

$$\rho = \rho(T, S, P) \quad (\text{I.4})$$

$$\frac{\partial \phi}{\partial z} = -\frac{\rho g}{\rho_0} \quad (\text{I.5})$$

$$\vec{\nabla} \cdot \vec{v} = \frac{\partial u}{\partial x} + \frac{\partial v}{\partial y} + \frac{\partial w}{\partial z} = 0 \quad (\text{I.6})$$

with the diffusive terms $\mathcal{D}_u, \mathcal{D}_v, \mathcal{D}_C$; forcing terms $\mathcal{F}_u, \mathcal{F}_v, \mathcal{F}_C$; traditional Coriolis parameter $f(x, y) = 2\Omega \sin \phi$; acceleration of gravity g ; dynamic pressure $\phi(x, y, z, t)$; (x, y, z) components of vector velocity (u, v, w) .

CROCO (and ROMS) presents several advantageous numerical properties. Consistency, accuracy and stability are improved through the splitting of baroclinic slow mode and barotropic fast mode resolutions (Shchepetkin and McWilliams, 2005). The vertical coordinates on sigma levels (stretched terrain-following) allow finer surface and bottom spatial resolutions. The use of high order numerical schemes favors computational performance and accuracy. Vertical mixing in boundary layers is represented through the non local boundary layer parameterization (K profile parameterization - KPP) that has been demonstrated to consistently reproduce observed mixed layers properties (Large et al., 1994). The adaptive grid refinement (in Fortran, AGRIF; Debreu et al., 2008) allows the resolution of both the regional scale and subdomains local scale circulations. We use it in its two-way mode in which the child grid (higher resolution) receives boundary condition information from its parent grid and feedbacks onto it (lower resolution; upscaling).

ROMS and CROCO are commonly used in regional configurations of coastal upwelling systems in California (e.g. [Capet et al., 2008b](#); [Colas et al., 2012](#); [Lachkar and Gruber, 2011](#)), Peru-Chile ([Echevin et al., 2018](#); [Hauschildt et al., 2021](#)), northwest Africa ([Marchesiello and Estrade, 2009](#); [Lachkar and Gruber, 2011](#); [Auger et al., 2016](#)) and Benguela ([Veitch et al., 2010](#)).

General principle of our numerical experiment

In a nutshell, we develop a set of original modeling experiments based on the fact that the strong intrinsic variability exhibited by climatological simulations ([Marchesiello et al., 2003](#)) can be smoothed out by ensemble averaging. The idea is to force an ensemble of initial states with idealized wind intensification and relaxation anomalies and compare with twin simulations forced by climatological fields. Comparison of the ensemble averages of the perturbed and unperturbed twin simulations gives access to the forced oceanic response. The post-processing of the simulation and plots were done using Python unless specified.

3 General methods

We develop a modeling framework that involves idealized synoptic wind intensification and relaxation. Their specific spatio-temporal patterns are chosen based on composite analyses presented below. The resulting forcing is applied to a five member climatological SSUS ensemble simulations carried out using CROCO.

3.1 Model settings and simulations

We use the Coastal and Regional Ocean COmmunity model (CROCO, from <https://www.croco-ocean.org/>; Hilt et al. (2020)), derived from Regional Ocean Modeling System (ROMS; Shchepetkin and McWilliams (2005, 2009)). The model configuration presented in Ndoye et al. (2017) takes advantage of the AGRIF grid refinement capability (Debreu and Blayo, 2008). A parent grid covers most of the Canary current system with a spatial resolution of ~ 10 km. A child domain spans the Senegalese ocean with finer resolution ~ 2.5 km (Fig. I.1a). The grid has 50 terrain-following vertical levels. The two grids are run alongside using two-way coupling (Debreu et al., 2012). For the sake of simplicity and coherency with future biogeochemical coupling, we do not use the diurnal shortwave cycle. The general model approach relies on two classes of simulations.

First, a 10-year long climatological simulation is run to obtain 1) an ensemble of physical initial states on which to apply synoptic experiments and 2) model climatological average fields (noted with subscript $climM$) used for heat flux restoring to climatological SST (see Appendix A). The climatological simulations are produced using monthly climatological surface heat fluxes from the International Comprehensive Ocean Atmosphere Data Set (COADS; noted Q_{climO} ; years 1854-1992; spatial resolution $\Delta x = 0.5^\circ$; Worley et al. (2005)), SST from the Moderate Resolution Imaging Spectroradiometer (MODIS; noted SST_{climO} ; years 2002-2018; $\Delta x = 5$ km; NASA (2014)) for SST restoring, wind stress from the Scatterometer Climatology of Ocean Winds (SCOW; noted $\tau_{x|climO}$; $\tau_{y|climO}$; 1999-2009; $\Delta x = 0.25^\circ$; Risien and Chelton (2008)) and open boundary conditions from the Simple Ocean Data Assimilation (SODA over the period 2000-2008 Carton and Giese (2008)).

Second, a series of shorter synoptic runs (45 days) is performed for three different types of surface wind and air-sea heat flux anomalies: synoptic wind intensification, relaxation, and no anomaly (reference), respectively denoted SF^+ , SF^- and SF^0 . Subscript SF (resp. SF^\pm) refers to any synoptic forcing condition in $\{SF^+; SF^-; SF^0\}$ (resp., in $\{SF^+; SF^-\}$). The construction of forcing anomalies is described in the subsequent sections.

The standard vertical mixing scheme we use is the K-Profile Parameterization (KPP, Large et al., 1994) but we also explore the sensitivity of our results by carrying some runs with the k- ϵ (Rodi, 1987) parameterization (chapter II section 2.6.1).

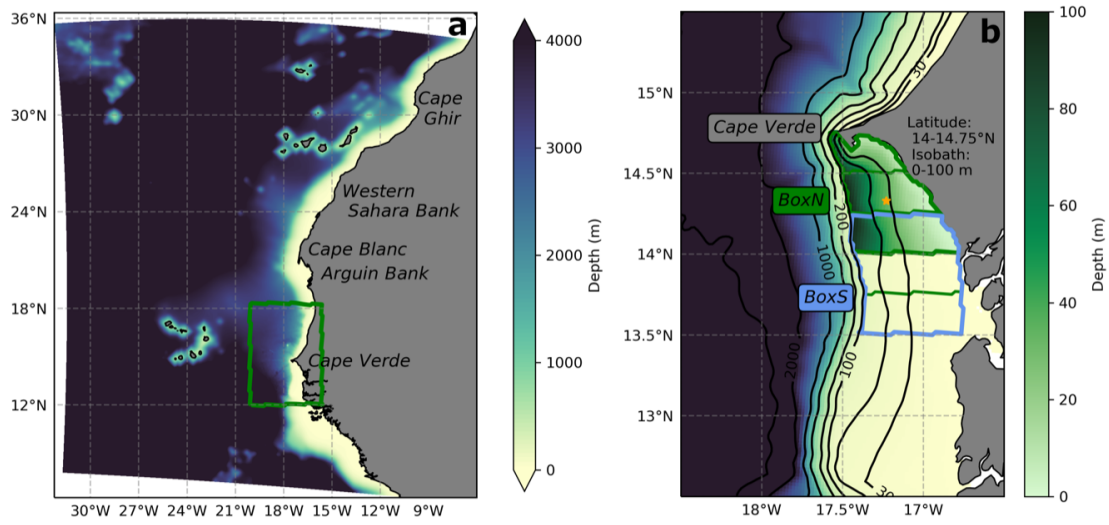


Figure I.1: Grid configuration used in the study. It consists of a parent domain encompassing most of the Canary current system with a zoom at 2.5 km horizontal resolution over the the Senegalese waters (green rectangle in panel a; see text for details). The study area located south of Cape Verde (SSUS) and various averaging boxes (green and blue solid lines) are shown in panel b, as well as the Melax buoy location (orange star).

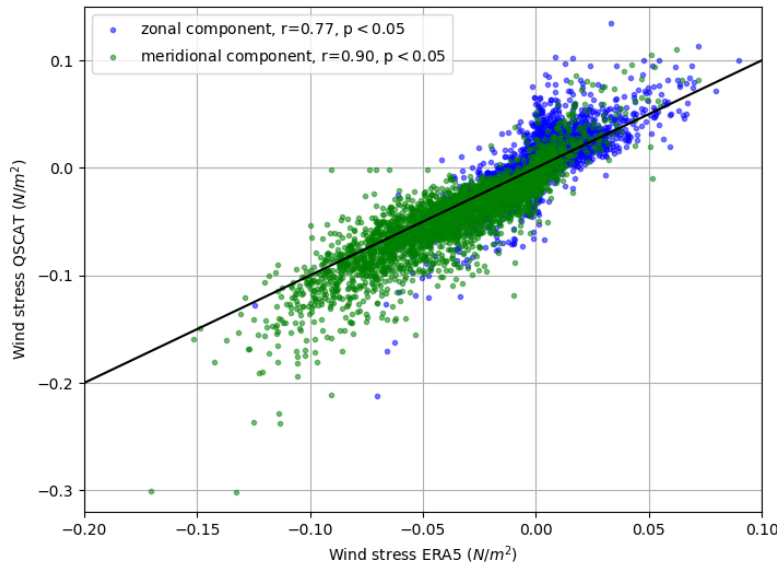


Figure I.2: Daily averages of zonal (blue) and meridional (green) QSCAT (y-axis) and derived from ERA5 (x-axis) and their correlation.

3.2 ERA5 reanalysis dataset

We aim to initiate a perturbation in the climatological physical forcing to analyze the response of the coastal ocean. To do so, we build idealized synoptic wind intensification and relaxation events by compositing the ERA5 reanalysis dataset.

Initially, we constructed the physical forcing anomalies with QSCAT winds (from Ndoye PhD thesis work, interpolated on model grids, initially from QuickSCAT L2B; <https://podaac.jpl.nasa.gov/>). By applying the anomalies of wind stress in preliminary simulations, we obtained a small effect on the surface mixed layer depth. Because this was qualitatively inconsistent with observations, we decided to also include synoptic perturbations of air-sea heat fluxes which are known to be substantial (Ndoye et al., 2017; Capet et al., 2017; Thomsen et al., 2021).

Thus, atmospheric synoptic conditions are expressed in terms of wind stress but also of net heat fluxes. As for other upwelling systems, the latter plays a noticeable role on the SSUS dynamics (Ndoye et al., 2017; Capet et al., 2017). We use the ERA5 dataset from the European Centre for Medium-Range Weather Forecasts (ECMWF: ‘ERA5 hourly data on single levels from 1979 to present’; Hersbach et al. (2018); $\Delta x = 0.25^\circ$) to compute synoptic wind stress and heat flux anomalies. We choose the temporal coverage between 2000 and 2010 to match the time period of the climatological wind stress we use (see section 3.1) to force our model and obtain climatological physical states. We use the following variables: zonal and meridional wind speed at 10 m; short and longwave radiation, sensible and latent heat fluxes which are combined to provide net air-sea heat flux (Barnier et al., 1995). Wind stress is obtained from wind speed with the formula: $\tau = \rho_a C_D U_{10}^2$ with $\rho_a = 1.22 \text{ kg m}^{-3}$ the air density and $C_D = 0.0013$ the momentum transfer coefficient. This is in agreement with recent findings of Strub and James (2022) that recommend to compute wind stress from wind speed fields in ERA5 in coastal areas to prevent errors induced by interpolation. For use in the compositing, a monthly climatology is built for wind stress and net heat flux, over the period 2000-2010. Fig. I.2 indicates a good agreement between QSCAT and ERA5 zonal and meridional wind stress over the region of interest. Given their relative agreement between them and with in situ wind measurements (Ndoye et al., 2014); their common use (Hersbach et al., 2018), as well in coastal regions (Desbiolles et al., 2014; Ndoye et al., 2014; Strub and James, 2022), we have confidence in our use of these products.

3.3 Idealized synoptic events

Zonal and meridional wind stress ($\tau_x; \tau_y$) and net heat flux (Q) forcing fields are built as the sum of two separate terms (generically written for a field ϕ):

$$\phi_{SF^\pm}(x, y, t) = \phi_{clim}(x, y, t) + f(t) \times \phi'_{SF^\pm}(x, y). \quad (\text{I.1})$$

Posing $\phi'_{SF^0} = 0$, Eq. (I.1) is also valid for SF^0 . ϕ_{clim} is as described in section 3.1 for wind stress (see below and Appendix A for heat flux). By construction, synoptic anomalies have a spatial structure that is fixed in time ϕ'_{SF^\pm} and a temporal modulation of their amplitude $f(t)$. ϕ'_{SF^\pm} are defined based on ERA5 compositing.

3.3.1 Composites fields $\phi'_{SF^\pm}(x, y)$

The composite analysis is restricted to the upwelling season defined as the period ranging from late October to late May. We consider that the ERA5 daily meridional wind stress (τ_y) is representative of the alongshore upwelling favorable winds over the SSUS (Tall et al., 2021). We average τ_y over the SSUS subdomain (-19°E; -16.5°E to 12.5°N; 15.5°N) and remove the seasonal cycle (blue line in Fig. I.3b) obtained with a low pass Butterworth filter (with a threshold period of 115 days) to obtain the subseasonal wind stress anomaly $\delta\tau_y$ (red line in Fig. I.3).

Upwelling intensification (resp. relaxation) events are defined as the days during which $\delta\tau_y$ is below (resp. above) minus (resp. plus) one $\delta\tau_y$ standard deviation. We select ($\tau_x; \tau_y$) and (Q) fields at these dates and remove the corresponding climatological monthly average (section 3.2) to obtain an anomaly field. Finally, we construct an unique upwelling season anomaly ϕ'_{SF^+} (resp. ϕ'_{SF^-}) by averaging over all identified intensification (resp. relaxation) events (Figs. I.8a-d)¹.

The wind stress and heat flux anomalies present smooth regional scale patterns all over western Africa (Figs. I.8c,d). Wind anomalies become weak south of 12°N so there will be little room for remotely generated SSUS upwelling/downwelling at synoptic scale (Philander and Yoon, 1982).

The decomposition of the idealized events into short and long wave radiation, sensible and latent heat flux are informative about atmospheric conditions during upwelling wind intensification or relaxation. The latent heat flux anomaly dominates the net heat flux anomaly: there is less (resp. more) evaporation, thus more heat loss (resp. more heat gain), during intensification (resp. relaxation) events (see LH and Q_{net} anomalies in Fig. I.6), in agreement with previous studies describing atmospheric synoptic patterns (Garstang, 1967; Desbiolles et al., 2014). We show their spatial structure (in absolute) in Fig. I.5c. Note that we found very similar results using QSCAT wind time series for the events detection.

Because relaxation and intensification anomalies are quite similar (with opposite signs, see Fig. I.6) and because it is convenient to use perfectly symmetric structures, we choose to ignore the composites obtained for relaxation events and define: $\phi'_{SF^-}(x, y) = -\phi'_{SF^+}(x, y)$.

¹Northeasterly and Northwesterly wind events were separated at an early stage of the study but produced similar ocean responses so this distinction is ignored, although described concisely in the following section.

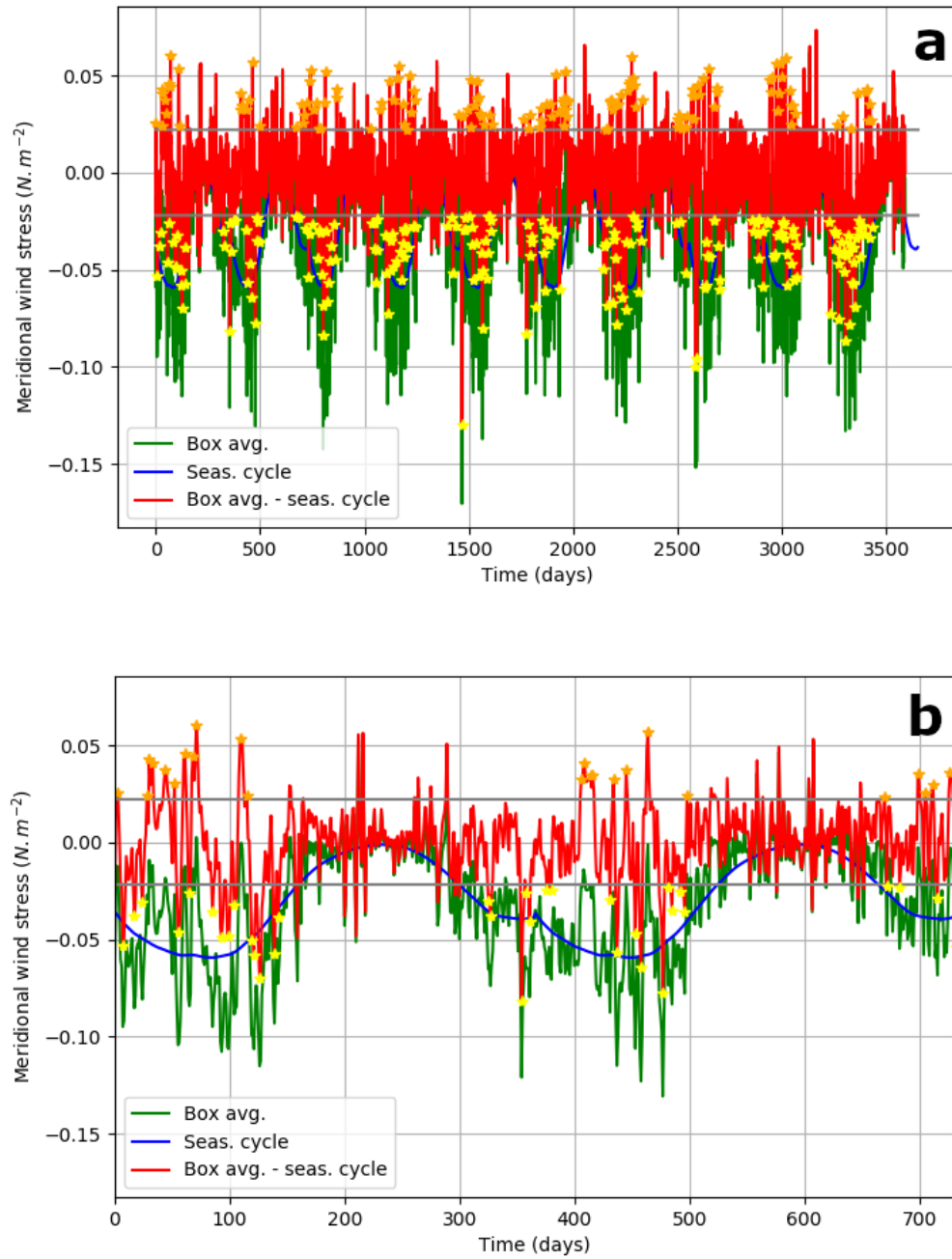


Figure I.3: Time series over the 10 years studied (2000-2010): the green line indicates the meridional wind stress from ERA5 averaged over the SSUS, the blue line indicates the seasonal cycle of the latter signal, the red line indicates the detrended signal. Upwelling intensification (yellow stars) and relaxation events (orange stars) are detected during the upwelling season (November-May), with the standard deviation threshold (grey lines). Panel (a) is the 10 years time interval and panel (b) shows a zoom on the two first years.

Westerlies vs Easterlies

We initially explored the variety of wind events over the system during the upwelling season from November to May. One aspect of this is the precise orientation of wind during intensification events, i.e. whether they are westerlies or easterlies. Despite the wind being mostly orientated meridionally, the zonal orientation has direct implication on the different properties of air transported over the system: relatively humid air from the west (Atlantic ocean) and dry air from the east (African continent/Sahara), potentially drastically impacting the air-sea heat exchange through latent heat flux (Thomsen et al., 2021). The particularly high variability of net heat fluxes over Senegalese waters are shown in Fig. 0.8b. From November to May, eastern wind events shift towards western wind events with a transition around April (see Fig. I.4).

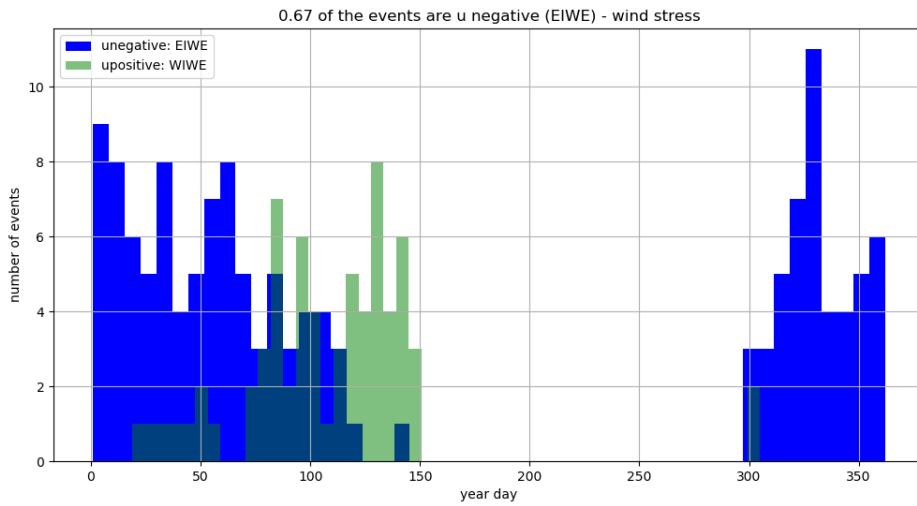


Figure I.4: Distribution of easterlies and westerlies events along the November-May upwelling season with ERA5 reanalysis.

We show the westerlies and easterlies events decomposed into different heat fluxes in Fig. I.5a,b. Westerlies events are more frequent towards the summer time such that the short wave radiation is higher than during eastern events (Fig. I.5). The other heat fluxes are similar during western and eastern events; we do not find dramatic values in the sensible heat flux as in Thomsen et al. (2021). The total heat flux is thus weaker during eastern wind events. As they are more frequent, the heat fluxes during easterlies intensification events resemble those that do not differentiate easterlies and westerlies events. However, in anomalies relative to the monthly mean climatological field, the difference is negligible. The meridional wind stress and total heat flux anomalies are similar during eastern and western events. For this reason, and because initial simulations with westerlies and easterlies events showed small differences in the oceanic response, we decided not to differentiate them.

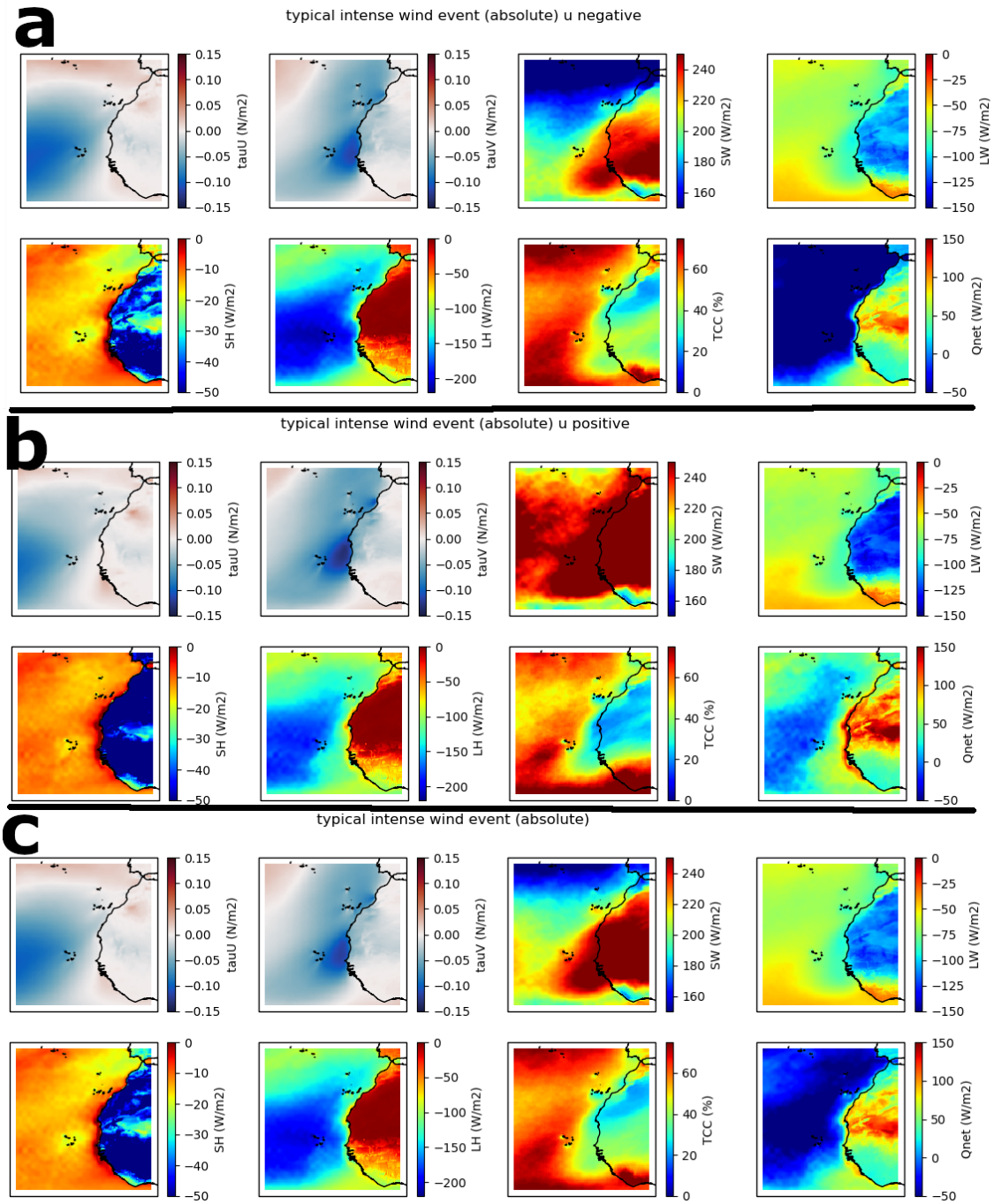


Figure I.5: Composites of zonal and meridional wind stress (τ_U , τ_V), short and long wave radiation (SW, LW), sensible and latent (SH, LH), total cloud coverage (TCC) and total heat fluxes (Qnet). The two upper lines (a) are composites of eastern wind events, the two middle lines (b) of western events and the two lower lines (c) show the composites without zonal differentiation.

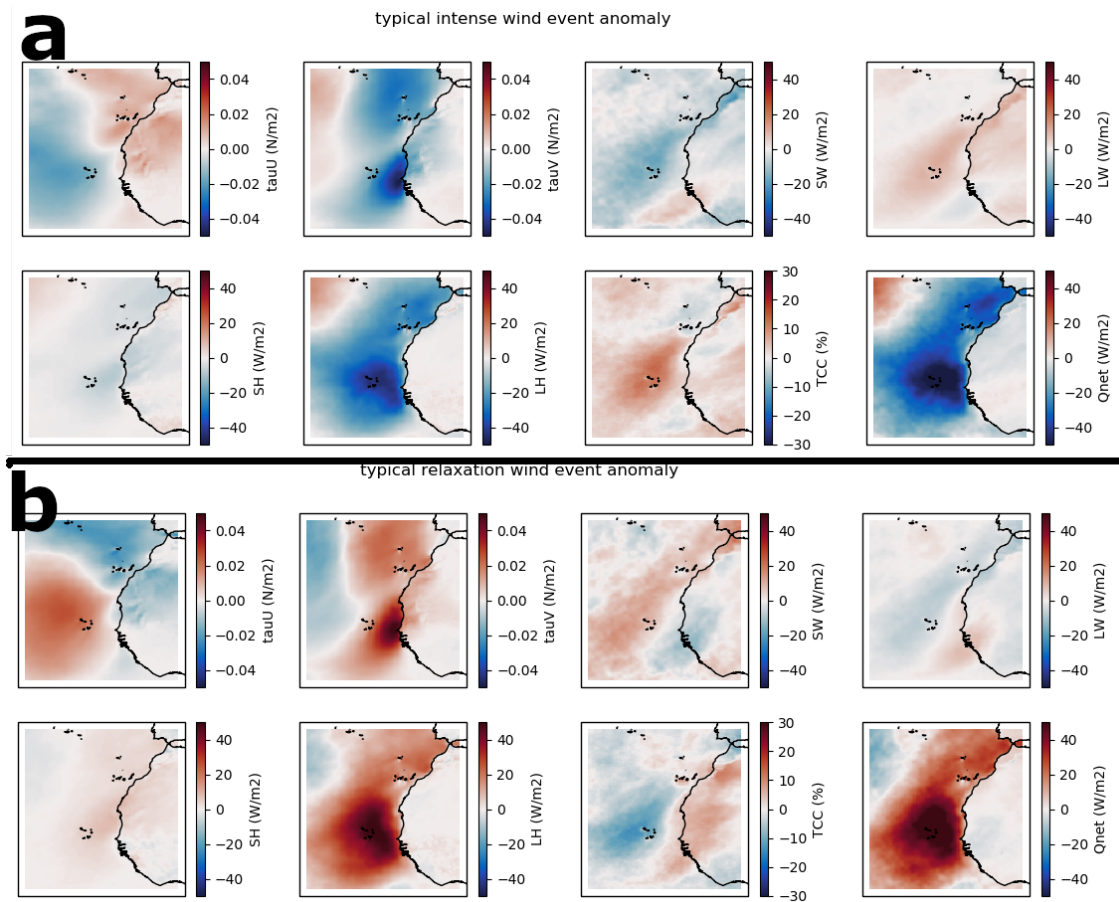


Figure I.6: Same as Fig. I.5 in anomaly relative to monthly mean climatological values. The two upper lines (a) show the anomalies during intensification events and the two lower during relaxation events (b).

3.3.2 Amplitude modulation $f(t)$

We now define the time modulation of amplitude $f(t)$. For simplicity we take $f(t)$ of the following form: two linear ramps, one upward and one downward with duration T_r each, and a plateau with constant wind stress anomaly between them with duration T_p . The choices made for T_r and T_p are key because they set the frequencies at which the SSUS dynamics will be perturbed. To provide general guidance a spectral analysis of the SSUS-averaged meridional wind stress (ERA5) was performed for 9 upwelling seasons (defined between late October and late May of the following year). The mean spectrum does not reveal any synoptic time scale energetic peak but presents a distinctly shallower slope over the time range 10-12 days compared to longer time scales (not shown). In the following, we present simulations with $T_r = 3$ days, $T_p = 5$ days and thus $T_{syn} = 2 \times T_r + T_p = 11$ days. Note that initial explorations for $T_{syn} = 6$ days produced dynamical and thermodynamical responses qualitatively similar to those with $T_{syn} = 11$ days but with smaller amplitude. As mentioned above, the wind stress direction is weakly affected by the synoptic fluctuation so little energy feeds near-inertial motions despite T_r being commensurate with the inertial frequency in the SSUS ($T_f = 2$ days). The idealized events are applied from 2 to 11 March included (hereinafter day 1 to day 10) in the middle of the upwelling season (Roy, 1989), a period of particular interest (Capet et al., 2017; Machu et al., 2019).

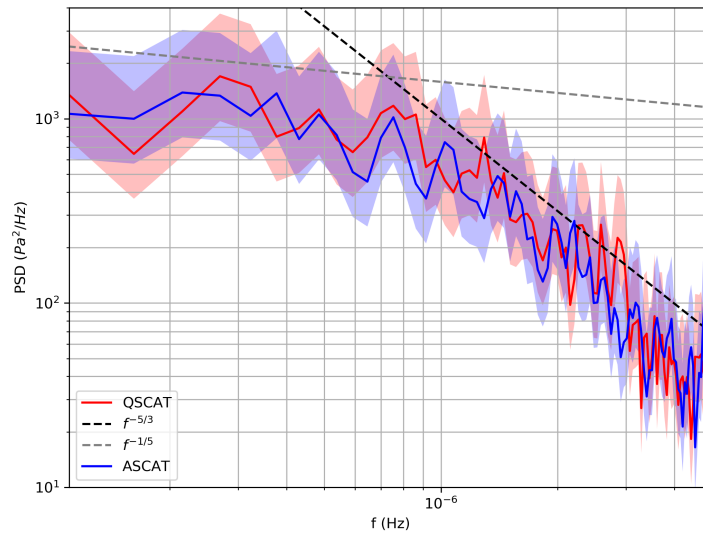


Figure I.7: Power Spectral Density of daily meridional wind stress time series of QSCAT (red) and ASCAT (blue), using Welch's method.

To complement this, we show the Power Spectrum Density of the QSCAT daily meridional wind time series in Fig. I.7. It uses Welch's method and the error interval is obtained by the χ^2 method (Pearson, 1900). No highest energy peak appears in this frequency analysis. However, the slope of the spectrum changes from $f^{-1/5}$ to $f^{-5/3}$ at $f \approx 10^{-6}$ i.e. $T_f \approx 10$ days. In test simulations with a shorter time period (5 days), the variables were perturbed but were less outside of their range of intrinsic variability. We consider that longer perturbations are not relevant because a period of 10 days is sufficient for the variables to reach a stabilized state (see further discussion on this in chapter II sections 2.4.3 and 3.6). Thus, we consider that 10 days is a reasonable typical time scale of synoptic events (see $f(t)$ in Fig. I.8).

3.3.3 Net heat flux forcing implementation

The heat flux forcing in the synoptic runs writes

$$Q_{SF}(x, y, t) = Q_{clim}(x, y, t) + f(t) \times Q'_{SF}(x, y). \quad (I.2)$$

The construction of appropriate air-sea heat fluxes modulated during wind intensification and relaxation to force the synoptic simulations was made so as to respect three objectives/constraints: avoid artificial restoring to climatological SST during the synoptic runs; keep Q_{clim} close to the net air-sea heat flux diagnosed from our climatological run Q_{climM} and, in particular, prevent discontinuities at the restart time of the synoptic runs; have Q_{SF} independent of online model SST so that different members of an ensemble have the exact same Q forcing. The exact definition of $Q_{SF}(t)$ and more details are given in the following paragraph (Appendix A of the JPO manuscript). The modulation of heat fluxes by synoptic events averaged over the SSUS is shown in Fig. I.8. The evolution of Q_{clim} during that period of the year is also noticeable. The magnitude of $Q'_{SF}(t)$ is $\sim 40 \text{ W m}^{-2}$ at peak anomaly but a sensitivity to doubling Q'_{SF} is also presented (chapter II section 2.6). Choosing a symmetric form for Q'_{SF} is broadly consistent with the ERA5 composite analysis (which would yield a value 5 W m^{-2} smaller for the relaxation perturbation)² and facilitates the identification of asymmetries/synoptic rectification effects. Note that a minor pre-processing error led to an imperfect symmetry of the heat flux synoptic anomalies (Fig. I.8). In BoxN (see Fig. I.1b and section 3.4), the typical effect of the erroneous heat flux (-5 W m^{-2} on average between days 1 and 15) on surface mixed layer temperature is estimated to be $\sim 0.07^\circ\text{C}$ and subsequently neglected (more details can be found in chapter II section 3.2).

Complement on the net heat flux forcing implementation (Appendix A JPO)

As large uncertainties remain on local and regional heat fluxes, model climatological simulations are often performed using online SST restoring to correct for heat flux bias (e.g. Ndoye et al., 2017) using the formulation proposed by Barnier et al. (1995):

$$Q_{climM}(t) = \overbrace{Q_{climO}}^{(m_1)} + \overbrace{\frac{dQ}{dSST}(SST_{onlineM}(t) - SST_{climO})}^{(m_2)}, \quad (I.3)$$

where $SST_{onlineM}$ denotes model SST computed at every time step. Time dependency is omitted for variables that follow a smooth seasonal cycle.

Eq. (I.3) is the formulation used to perform our multi-year climatological run. Using more elaborate bulk formulation to compute heat fluxes instead has not led to any improvement in the representation of SST and SML depth (not shown). In the synoptic simulations, using Eq. (I.3) would produce an artificial feedback because the development of model SST synoptic anomalies would modify Q_{climM} , typically $\pm 30 \text{ W m}^{-2}$ for $\mp 1^\circ\text{C}$ anomaly. To circumvent this, SST_{climO} in Eq. (I.3) could be replaced by a prescribed SST field taking account of the synoptic

²In other upwelling regions surface heat fluxes may also be an important contributor to asymmetries (Send et al., 1987)

forcing on SST. But this would require an *a priori* knowledge of the ocean SST response which we do not have. In addition, formulation of m_2 in Eq. (I.3) would lead to different net air-sea heat fluxes for different ensemble members. Therefore, we choose to shift to a different formulation for Q_{clim} that does not involve any online restoring to SST, has a minimal effect in Eq. (I.3)'s version of Q_{clim} , and ensures that all ensemble runs will be identically forced. To do so, we replace m_2 with m_{2adj} defined as follows:

$$m_{2adj} = \frac{dQ}{dSST}(SST_{climM} - SST_{climO}), \quad (\text{I.4})$$

$$Q_{clim} = m_1 + m_{2adj}. \quad (\text{I.5})$$

In m_{2adj} , SST_{climM} is the SST diagnosed from the climatological simulations. Replacing $SST_{onlineM}$ with SST_{climM} ensures that m_2 and m_{2adj} are identical when sufficient averaging is performed, e.g. formulatiin Eq. (I.3) averaged over a large number of ensemble runs is equivalent to formulatiin Eq. (I.5). Eq. (I.5) adjusted heat fluxes are applied on initial states obtained from climatological simulations run with Eq. (I.3) (see section 3.3). To preserve exact continuity of Q_{clim} at restart time (14 Feb.), we create a transition period to smoothly shift from Eq. (I.3) to Eq. (I.5). This transition is performed using two linear ramps f_{down} (from 1 to 0) and f_{up} (from 0 to 1) respectively applied to m_2 and m_{2adj} between 15 February and 1 March. The same method is used for the surface freshwater flux formulation during synoptic simulations. For heat flux, the complete formulation includes the synoptic anomaly and writes:

$$Q_{SF}(t) = m_1 + f_{down}(t)m_2 + f_{up}(t)m_{2adj} + f(t)Q'_{SF}. \quad (\text{I.6})$$

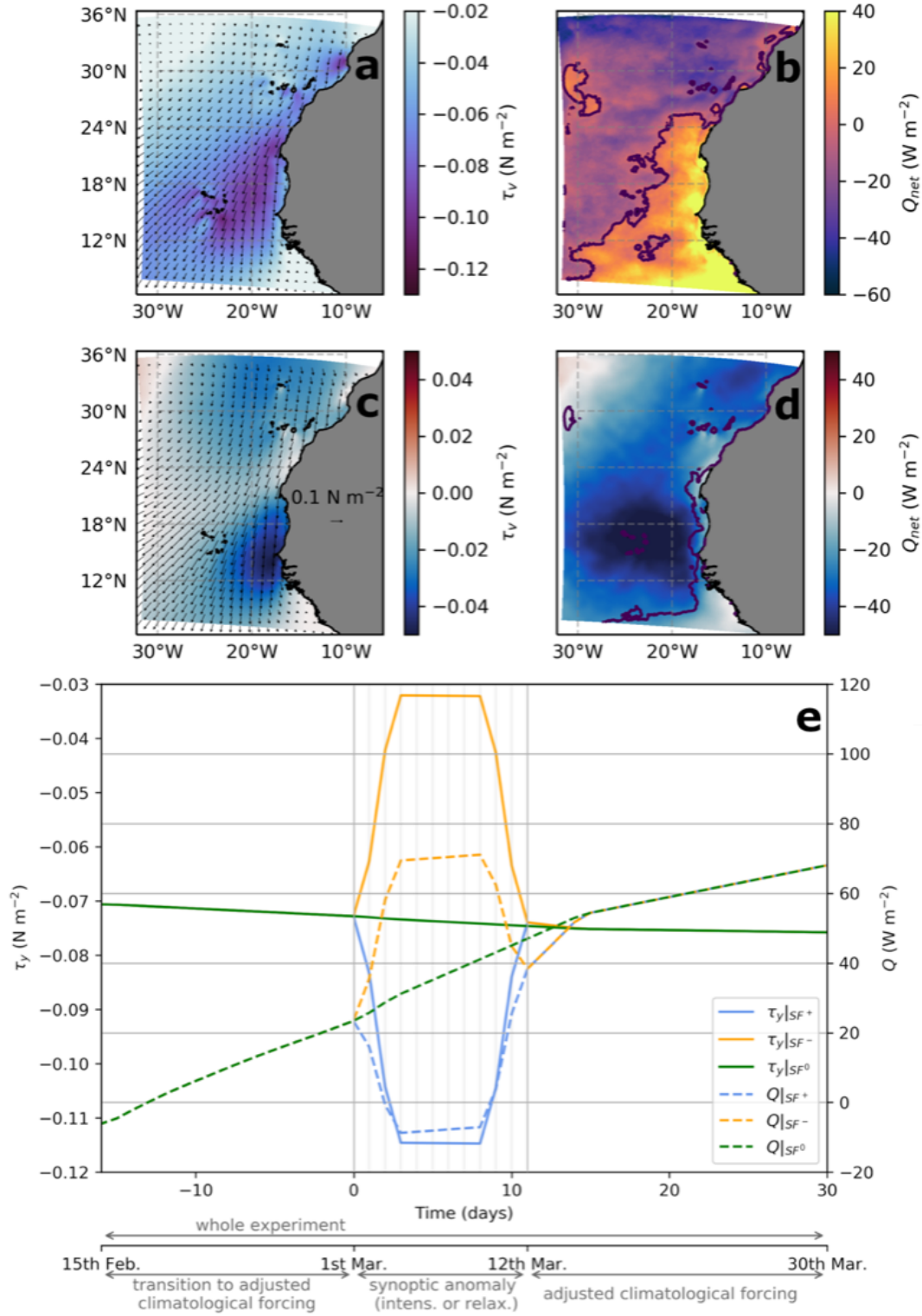


Figure I.8: Canary current meridional wind stress (a, c) and net heat fluxes (b, d) climatological (a,b; SF⁰) and SF⁺ anomaly (c,d) fields at the peak of the synoptic intensification. Anomalies for SF⁻ are the opposite of those for SF⁺. The experimental timeline is presented in panel e. Continuous (resp. dashed) lines indicate the evolution of the meridional wind stress (resp. net heat flux) averaged over the SSUS. Green (resp. blue and orange) lines are for climatological (resp. wind intensification and relaxation) forcings. A slight deviation from perfect SF⁺-SF⁻ symmetry can be seen for heat fluxes, due at a small error. Its impact on simulated upper ocean temperature is negligible (see section 3.3.)

3.4 Spatial averaging

Various forms of spatial averaging are used to identify responses to synoptic events. In particular, we define a northern (BoxN; see Fig. I.1b) and a southern box (BoxS) in which we expect contrasted dynamics to occur. Their East-West delimitations are the coast and the 100 m isobath, respectively. We expect upwelling to mostly take place in BoxN delineated by the latitude 14.75°N (i.e., the Cape Verde peninsula) and 14°N (see Fig. 2a in Ndoye et al. (2017), and our Fig. II.8). The southern box, in which lateral advection likely dominates, is delineated by latitudes 14.25°N and 13.5°N. Alongshore averaging involves a simple remapping from longitude to water column depth with 5 m bins. It is performed over the gray area shown in Figs. II.7 and II.8 (chapter II), in the center of BoxN.

3.5 Complementary details

We show in Fig. I.9 the latitudinal values of wind stress before (day 0) and during (day 3) the wind intensification along the 100 m isobath (in absolute and anomaly between day 0 and day 3). Here we underline the weak anomaly over the southernmost area (south of 10°N), which is the only source possible of remote forcing (we use climatological boundary conditions). Thus, SF^{\pm} ability to generate anomalous remote forcing is very limited.

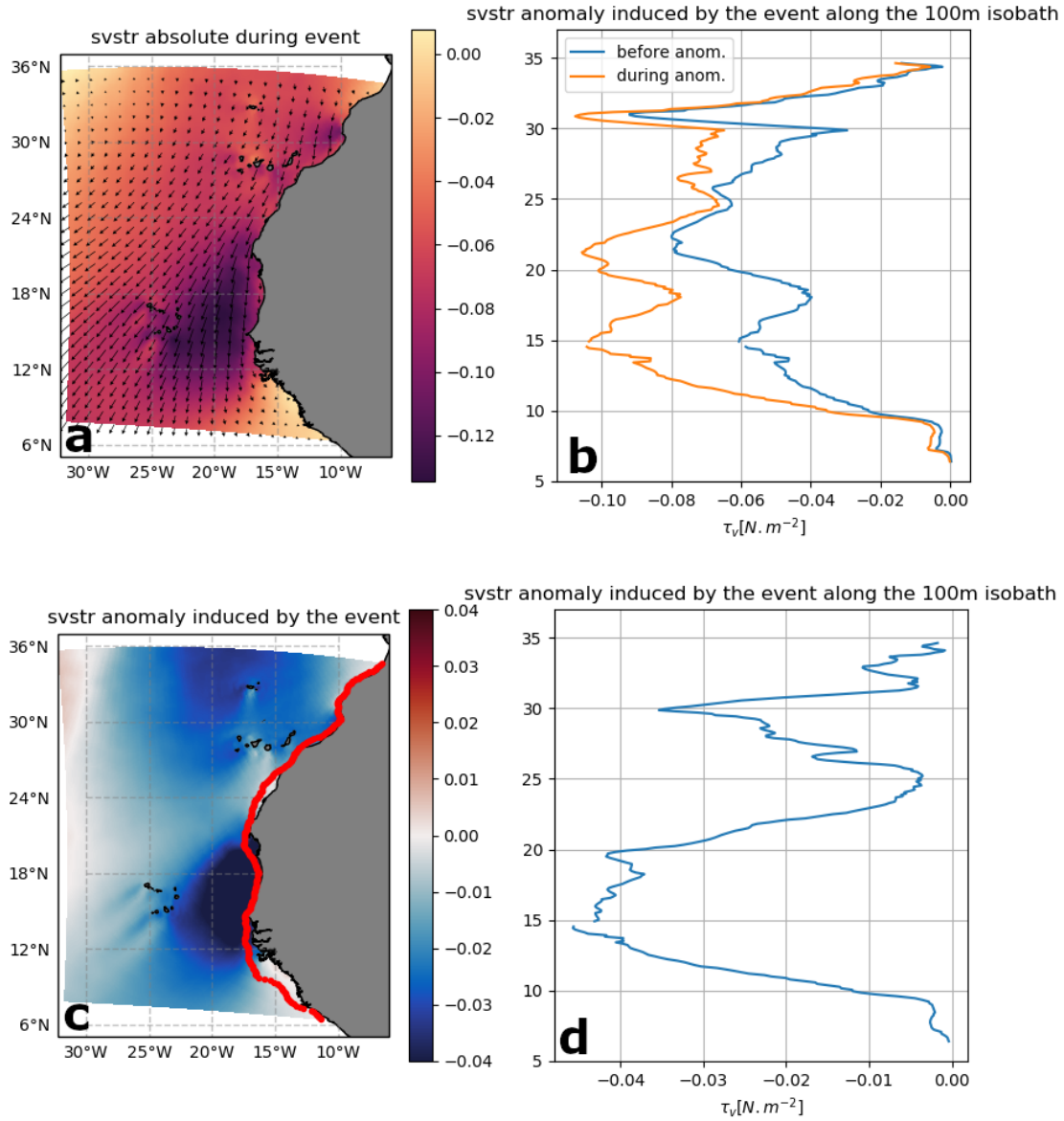


Figure I.9: Meridional wind stress spatial pattern during the anomaly at day 3 (a) and along 100 m isobath before and during the wind intensification anomaly at days 0 and 3 (b). Panels (c,d) indicate the anomalies between days 0 and 3. The 100 m isobath is indicated with the red line on panel c.

3.6 Ensemble experiment

3.6.1 Ensemble approach

Separating the oceanic response to synoptic atmospheric anomalies from intrinsic (primarily mesoscale) variability can be demanding in terms of available flow statistics (Marchesiello et al., 2003; Colas et al., 2013). We use an ensemble modeling approach to mitigate the effect of intrinsic variability and thus ascertain the SSUS deterministic response to synoptic wind events. Each ensemble run member (e) provides an independent system state vector evolution $X^{(e)}(x, y, z, t)$.

The ensemble average is X_{SF} :

$$X_{SF} = \frac{1}{N_e} \sum_{e=1}^{N_e} X_{SF}^{(e)}(x, y, z, t) \quad (\text{I.7})$$

with $(e) \in \{1; \dots; N_e\}$ the members on the ensemble. Mean synoptic anomalies are defined as the difference between synoptic and climatological ensemble averages ΔX_{SF^\pm} :

$$\Delta X_{SF^\pm} = X_{SF^\pm} - X_{SF^0} \quad (\text{I.8})$$

For each member, the deviation to the ensemble average $\delta X_{SF}^{(e)}$, i.e., the intrinsic variability part, is defined by:

$$X_{SF}^{(e)} = X_{SF} + \delta X_{SF}^{(e)} \quad (\text{I.9})$$

By injecting Eq. (I.9) in Eq. (I.8), we obtain:

$$\Delta X_{SF^\pm} = X_{SF^\pm}^{(e)} - \delta X_{SF^\pm}^{(e)} - (X_{SF^0}^{(e)} - \delta X_{SF^0}^{(e)}) \quad (\text{I.10})$$

or also:

$$\Delta X_{SF^\pm} = \underbrace{X_{SF^\pm}^{(e)} - X_{SF^0}^{(e)}}_{\Delta X_{SF^\pm}^{(e)}|_f} - \underbrace{(\delta X_{SF^\pm}^{(e)} - \delta X_{SF^0}^{(e)})}_{\delta X_{SF^\pm}^{(e)}|_i} \quad (\text{I.11})$$

The mean forced response ΔX_{SF^\pm} due to synopticity can thus be written as the sum of a deterministic forced term $\Delta X_{SF^\pm}^{(e)}|_f$ plus a term due to intrinsic variability $\delta X_{SF^\pm}^{(e)}|_i$, and this equation is valid for each ensemble run. The intrinsic variability part would vanish when averaging over a sufficiently large ensemble but we wish to choose a relatively small N_e for environmental/energy consumption reasons. The fact that we use identical initial conditions for the SF^\pm and reference climatological runs SF^0 is helpful in that regard because it limits the random scrambling due to turbulence compared to a situation where the initial states would be inconsistent between each other. In other words, we expect to have minimized the magnitude of $\delta X_{SF^\pm}^{(e)}|_i$ relative to the magnitude of each term in its definition. To corroborate this, we show the RMS of the different terms in Eq. (I.11) for $X = \text{SST}$ in the shelf BoxN as a function of time (Fig. I.10a). For each ensemble run, $RMS(\delta X_{SF^+}^{(e)}|_i)$ grows from 0 at $t=0$ days (when SF^+ and SF^0 simulations are identical) to $\approx \sqrt{2} RMS(\delta X_{SF^+}^{(e)}) \approx \sqrt{2} RMS(\delta X_{SF^0}^{(e)})$ at $t=7$ days (this is also true when averaging over all ensemble members). Therefore, comparing synoptic and climatological twin simulations with identical initial conditions ameliorates the signal ($\Delta X_{SF^\pm}^{(e)}|_f$) to noise

$(\delta X_{SF^\pm}^{(e)} | i / \sqrt{N_e})$ ratio during the early part of the SF^\pm experiments, until day 11-12 for SF^+ and day 7 for SF^- as readily seen in Fig. I.10b (see below chapter II section 2.4.4 on this SF^+ / SF^- distinction). In practice choosing $N_e = 5$ appears appropriate to identify SSUS-scale evolutions (see Fig. I.10b). More localized responses will be considered insofar as they emerge from noise with this relatively small ensemble, which guarantees that they are part of the first-order ocean response.

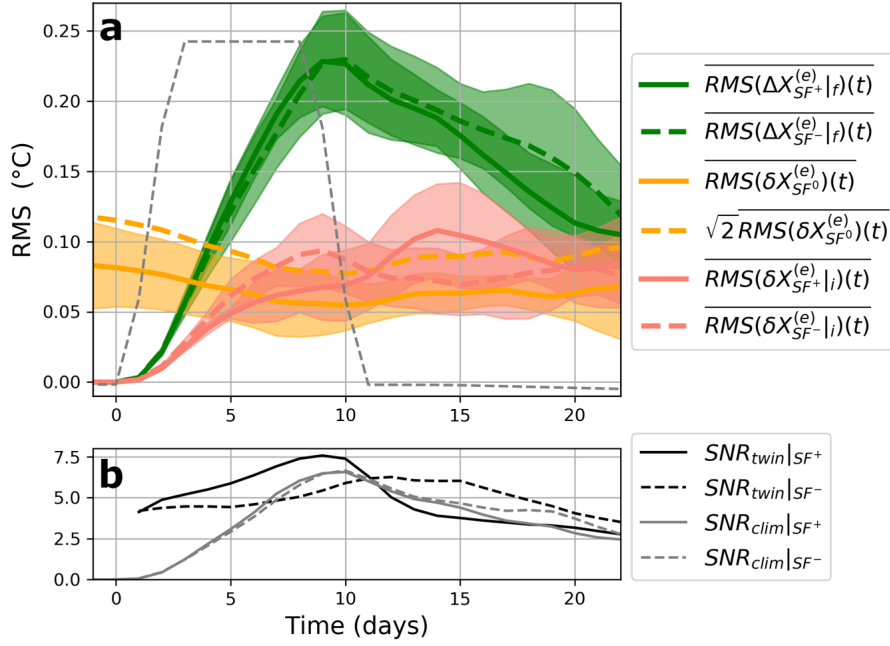


Figure I.10: a) Time series of the ensemble averages of spatial RMS for various quantities computed for $X=SST$ (panel a); see text in section 3.6 and Eq. I.11). The grey dashed line represents the amplitude modulation of the synoptic anomaly $f(t)$. b) Signal to Noise Ratios (SNR) as defined in section 3.6.

3.6.2 Robustness of the diagnosed forced ocean response

At any given location, the anomalous response to synoptic forcings revealed by ensemble averaging will be considered robust if the following criterion is met:

$$\left| \sum_{e=1}^{N_e} \text{sign}(X_{SF^\pm}^{(e)} - X_{SF^0}^{(e)}) \right| = 5, \quad (\text{I.12})$$

that is if the synoptic anomaly is of the same sign in all ensemble members. When time and ensemble averaging are combined (e.g., to produce Figs. II.6 and II.7 in chapter II), the criterion must hold for each individual day of the time averaging window, which makes the criterion as stringent as possible.

3.7 Residual effect

In our idealized setting, we will infer the residual effect produced by synoptic variability as:

$$RES_{SF}(X) = \frac{1}{2}(X_{SF^+} + X_{SF^-}) - X_{SF^0} \quad (\text{I.13})$$

for any oceanic variable X . We are also interested in the quantity:

$$\mathcal{R}_{SF}(X) = \frac{RES_{SF}(X)}{X_{SF^0}} = \frac{\frac{1}{2}(X_{SF^+} + X_{SF^-})}{X_{SF^0}} - 1 \quad (\text{I.14})$$

which quantifies the relative importance of the asymmetry. \mathcal{R}_{SF} will systematically be computed after ensemble and time averaging between day 3 and 8, i.e., during the plateau of SF^\pm forcing anomaly.

3.8 Heat budget

The clearest manifestation of synoptic variability is SST modulation. Based on vertical velocity fields shown in [Ndoye et al. \(2017\)](#) (see also our Fig. II.8 in chapter II) and the minimum SST zone, we suspect that the role of vertical advection may be weak outside the northern sector of the SSUS. We perform an online heat budget to confirm this and more generally clarify the importance of the different processes at play in the temperature changes in the SML (as in [Cambon 2008](#); [Jullien et al. 2012](#); [Echevin et al. 2018](#)). The SML heat budget equation is:

$$\underbrace{\langle \partial_t T \rangle}_{\text{RATE}} = - \underbrace{\langle \partial_x u T \rangle - \langle \partial_y v T \rangle}_{\text{HADV}} - \underbrace{\langle \partial_z w T \rangle}_{\text{VADV}} + \underbrace{\langle D_l(T) \rangle}_{\text{HMX}} + \underbrace{\langle D_z(T) \rangle}_{\text{VMIX+ENTR}} + \underbrace{\langle F(z) \rangle}_{\text{FORC}} \quad (\text{I.15})$$

where T is the model potential temperature, the left term is the heating rate, (u, v, w) are the three dimensional currents components. The right-hand side terms correspond to the advection in flux form (the total advection is noted $ADV = HADV + VADV$), horizontal and vertical mixing, entrainment/detrainment and heating/cooling due to surface heat fluxes. $\langle X \rangle = (1/h) \int_{-h}^0 X dz$ is the vertical averaging of the state vector X over the time-dependent mixed layer depth (h) range.

A particular focus will be on advection because it is presumably important in driving the heat changes in the SSUS. Unfortunately, the interpretation of individual advection terms can be made difficult by the strong compensations between them ([Gan and Allen, 2005a](#); [Colas et al., 2013](#)). Incidentally, the non divergence of the flow, (i.e. $\partial_x u + \partial_y v + \partial_z w = 0$) implies that advection terms can be rewritten as follows:

$$-(\partial_x u T + \partial_y v T + \partial_z w T) = -(\partial_x u (T - T_0) + \partial_y v (T - T_0) + \partial_z w (T - T_0)) \quad (\text{I.16})$$

with T_0 any arbitrary function of time only. A judicious choice for T_0 when studying the heat budget over a control volume \mathcal{V} is ([Lentz, 1987](#); [Montgomery, 1974](#)):

$$T_0(t) = \frac{1}{V} \iiint_{\mathcal{V}} T(x, y, z, t) dV \quad (\text{I.17})$$

This is because, when volume averaging, every RHS term of Eq. (I.16) can be rewritten as a flux of tracer $(T - T_0)$ across \mathcal{V} interfaces, hence advection terms only contribute to the heat budget if/where they transport temperature anomalies. Compensations between the three terms are thus strongly reduced (see the end of this section). Advection terms of the volume average budgets described in chapter II section 2.5.2 are computed following this procedure.

This technique allows a reduction of compensations between the three advection terms. In many circumstances, strong compensation arises between the two lateral advection terms present in a tracer evolution Equation, with each separate term being much bigger than their sum. Although the two cases are distinct, this is true whether advection is expressed in flux form or not. To illustrate this in the former case, consider the two coastal flow configurations in Fig. I.11. In panel a), the coastline is rectilinear and so is the flow. Assuming alongshore invariance (T and u independent of x) and v identically 0, each horizontal advection term in the temperature tendency equation (Eq. I.15) for the control area is identically zero. In panel b) the

coastline makes a right angle and we assume that the flow simply rotates by 90° without any divergence/convergence in the control area nor any change in temperature ($T=T_0$) between the inflow at $x = -L_x$ and the outflow at $y = L_y$.

Tendency due to advection writes:

$$-\int_{-L_x}^{L_x} \int_{-L_y}^{L_y} (\partial_x u T + \partial_y v T) dx dy = -[uT]_{-L_x}^{+L_x} - [vT]_{-L_y}^{+L_y} = uT|_{-L_x} - vT|_{+L_y} \quad (\text{I.18})$$

where we have assumed that $2L_x = 2L_y = 1$ so that metric factors can be ignored. Each term in the final RHS expression is zero but the two terms exactly cancel each other. The distinction between situations a) and b) reflects a difference in the flow geometry but it obscures the fact that, from a heat advection perspective, they are essentially (trivially) similar.

To prevent this kind of unnecessary complication, we work with tracer anomaly relative to its control average value $T - T_0$ (as done by [Lentz, 1987](#) and [Montgomery, 1974](#)). This does not change anything for case a). On the other hand, for case b) we now have:

$$\begin{aligned} -\int_{-L_x}^{L_x} \int_{-L_y}^{L_y} (\partial_x u (T - T_0) + \partial_y v (T - T_0)) dx dy &= -[u(T - T_0)]_{-L_x}^{+L_x} - [v(T - T_0)]_{-L_y}^{+L_y} \\ &= u(T - T_0)|_{-L_x} - v(T - T_0)|_{+L_y} \end{aligned} \quad (\text{I.19})$$

In the final RHS expression we recognize fluxes at the open boundaries of the control area but these flux terms now only contribute insofar as the water transported by the flow have properties different from those of the control area. In the situation b) where inflow and outflow are characterized by the same temperature $T=T_0$ both terms are identically zero, just as for case a).

Note that the introduction of this T_0 term was done offline on advection terms. This involved the rewriting and modifications of CROCO advection terms calculations in Fortran into Python functions.

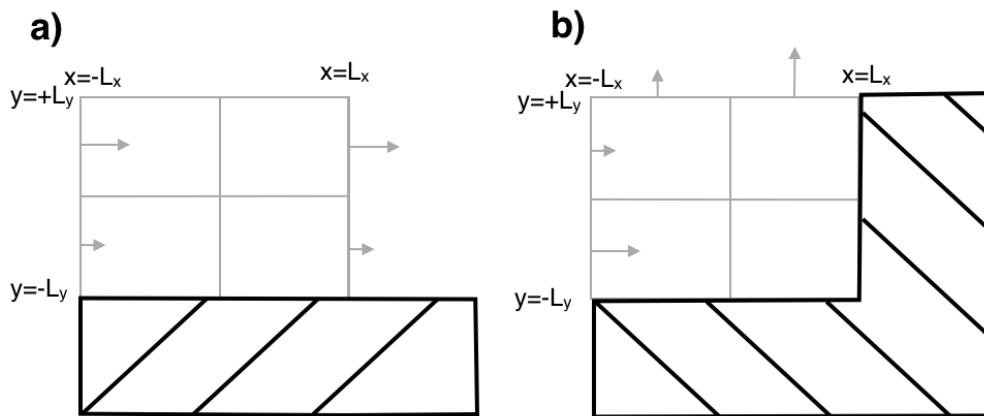


Figure I.11: Examples of flow geometry in which both horizontal advection terms (expressed in flux form) are identically zero (case a) or not (case b) despite the similarity of the situation from the perspective of heat budget in the control area ($x=\pm L_x, y=\pm L_y$). Schematic by Xavier Capet.

3.9 Lateral heat transport along box sections

Our budget technique allows the identification of oceanic processes over the SSUS. In this approach, we interpret the $HADV$ term as a process averaged inside a box (first RHS term in Eq. I.15). However, this interpretation misses the role of each boundary as an entry or exit of transport material over the sector. Thus, we fill this gap by computing the lateral transport along each boundary (LHS terms in Eq. I.20). The equivalence between this alternative technique and the advection terms of the box averaged heat budget (Eq. I.15) is shown using Green's theorem in Eq. I.20 (with U either u or v the current orthogonal to each model grid cell of the section, $x_1; x_2$ and $y_2 : y_2$ the BoxN horizontal limits, V the BoxN SML volume).

$$\begin{aligned} & \frac{1}{V} \int \int_{l;z}^{0:SML} U(T - T_0) dl dz + \frac{1}{V} \int \int_{x_1;x_2}^{y_2:y_2} w(T - T_0) dx dz \\ &= \frac{1}{V} \int \int \int_{BoxN;SML} (\partial_x u T + \partial_y v T + \partial_z w T) dx dy dz \end{aligned} \quad (I.20)$$

This leads to an alternative interpretation of the budget that can be analyzed with fluxes at its boundaries. Especially, we distinguish the heat transport along the three box boundaries, that are the Northern, Western and Southern sections (see Fig. I.12). With the help of the PAGO algorithm (Barrier et al., 2015; Deshayes et al., 2014, available at <http://pypago.nicolasbarrier.fr/>), we compute the heat transport anomaly integrated over the SML along the sections, that writes $\frac{1}{h} \int_{z=h}^0 U(T - T_0) dz$. This technique helps the interpretation of the SML heat budget and is discussed in the JPO manuscript (chapter II section 2.5.2) and in section 3.5.

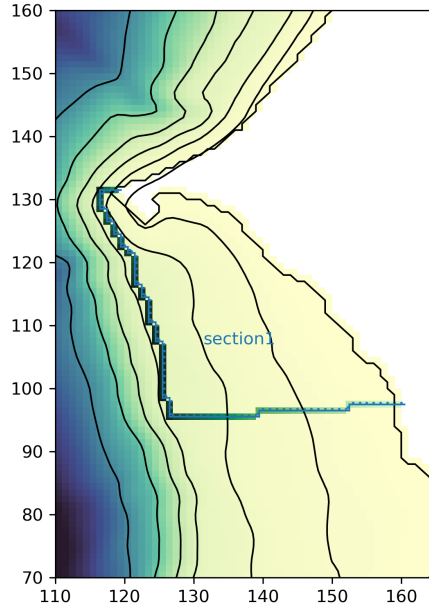


Figure I.12: Sections of the lateral boundaries of the integration box.

3.10 Melax buoy data

In order to evaluate the model ability to reproduce shelf dynamics at seasonal and sub-seasonal time scales, we use in situ measurements from Melax (meaning lightning in Wolof) mooring located over the shelf in ~ 35 m water depth at $14^{\circ}20.8'N$ - $17^{\circ}13.68'W$. An array of thermistors measured temperature every 30 s, at 11 depths (exactly at {1; 4; 6; 8; 10; 12; 14; 18; 21; 24; 28} meters), i.e. every 2 m and every 3.5 m in the upper and lower halves of the water column. An upward looking ADCP measured bottom temperature and horizontal current vertical profiles every 90 min with a vertical resolution of 1 m. The time series analyzed in this work extends from 11 February 2015 to 26 April 2016. Note that some preprocessing has been needed, e.g. filling missing values in the bottom thermistor (replaced by ADCP temperature sensor data). For the sake of simplicity and given our interest in time scales of at least a few days, we degrade the temporal resolution of the data to 1 day. More details on data processing/availability and mooring characteristics are provided in the next sections (Appendix B of the JPO manuscript) and in [Tall et al. \(2021\)](#), respectively. Section 3.10.2 (also Appendix B of the JPO manuscript) justifies our approach in chapter II section 2.3.2 about model evaluation with Melax observations.

3.10.1 Melax data processing (Appendix B of the JPO manuscript)

We are not concerned with high-frequency (e.g., intradaily) variability. The temporal resolution of Melax data is degraded to 1 day. This is done with a straightforward daily averaging for ADCP currents and atmospheric variables. A more complex processing is chosen for temperature because its vertical profile is modulated by the diurnal shortwave cycle and generation of warm surface layers whereas model temperature is not. To limit model-data discrepancies arising from this difference, the most vertically mixed temperature profile at Melax is selected for every day of interest. The maximum mixing criterion is based on the temperature difference between 1 m and 10 m deep: $T(z)|_{\min(T(z=1m)-T(z=10m))}$. We choose 10 m as it is a commonly used depth of reference for SMLs ([de Boyer Montégut et al., 2004](#)). This procedure typically amounts to choosing nighttime Melax in situ profiles because near-surface diurnal warming effects are then absent.

3.10.2 Melax temperature vertical profiles (Appendix B of the JPO manuscript)

The Melax data set comprises a limited number of upwelling wind intensification and relaxation events (Fig. II.4c). For each of them, the real ocean initial state and wind forcing history (before and during the event) differ from our idealized simulations (see Fig. II.5). Therefore, pending more observations, model evaluation can only be done qualitatively. We have selected the upwelling intensification and the relaxation events whose wind history appeared most consistent with our synthetic forcings. The level of agreement for the wind prior to the event is better for the relaxation than for the intensification. In the latter, the observed initial state (first three days) is characterized by a relaxed wind which certainly contributes to enhancing the amplitude of the synoptic temperature response (\approx a factor two larger in the observations than in the model runs with synthetic forcing anomalies). Model-data agreement is much better for the relaxation except toward the end of the event, but this is presumably again related to the fact

that the meridional wind in the selected observed event and in our synthetic forcings behave quite differently (compare Figs. II.5d and h). Overall, qualitative agreement between observed and modeled vertical temperature profiles shows the ability of our simulations to reproduce real ocean processes.

3.10.3 Melax SML

In addition, we present a few findings concerning the observed vertical structure of the water column. The time series of Melax thermistors (Fig. I.13) shows the seasonal cycle with waters below 20°C between February and May both in 2015 and 2016. In this period, the water column is well mixed with less than 2°C surface/bottom temperature difference. This difference is increased during the rest of the time period, especially between July and October 2015 with differences reaching more than 10°C. Fig. I.13 also shows the high frequency variability (T~5-10 days) of the vertical temperature profiles.

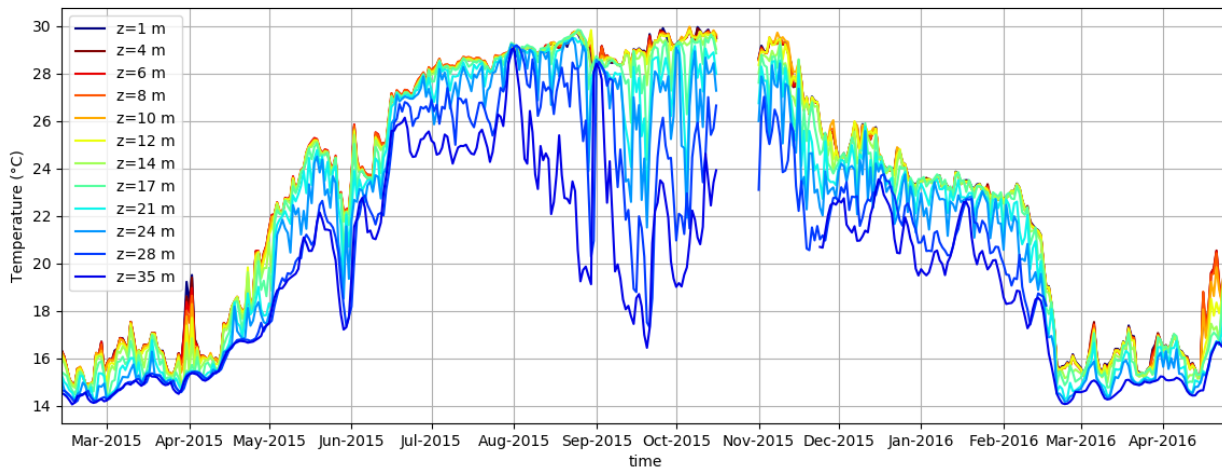


Figure I.13: Time series of Melax thermistors data from 11 February 2015 to 26 April 2016.

Given the limited time period, it is difficult to build climatological averages to evaluate climatological simulations. However, we attempted to quantitatively validate the SML depth using thermistors data. We use the SML criterion of $|\theta - \theta_{10m}| > 0.2^\circ\text{C}$ (de Boyer Montégut et al., 2004) and we use 5 day averages to smooth the signal without filtering intra-annual variability. The model SML (with KPP and GLS) roughly reproduces the Melax observations in terms of seasonal cycle and mean value between February and May: 18 m with KPP vertical mixing, 17 m with GLS and 16 m with KPP vertical mixing and chlorophyll shading (see section 4.1; Echevin et al., 2021; note that this was not used in simulations of chapter II) against 14 m in Melax observations (see Fig. I.14). Also, the model SML temporal variability is consistent with observations with changes of the order of 5 m in 10 days.

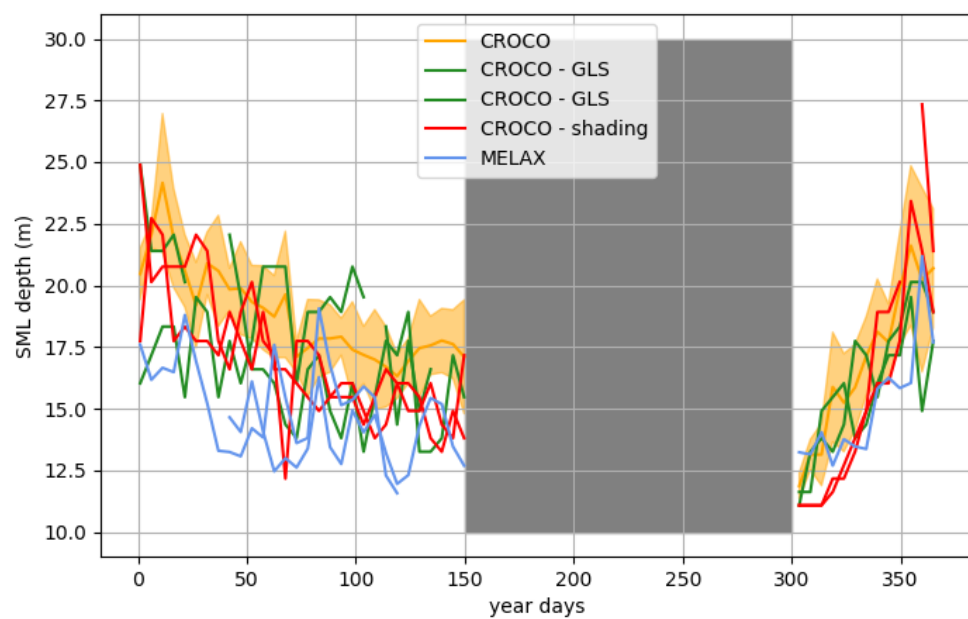


Figure I.14: Surface Mixed Layer depth time series (only between November-May during the upwelling season) observed at Melax (blue lines), of 9 years of CROCO KPP (orange lines and the shaded orange area indicates the standard deviation), two individual years with $k-\epsilon$ vertical mixing scheme (green lines) and chlorophyll shading (red lines) simulations. Note that times when the water column is fully mixed are masked.

4 Biogeochemical model PISCES and methods

4.1 Biogeochemical model PISCES

We use the biogeochemical model PISCES (Pelagic Interactions Scheme for Carbon and Ecosystem Studies, available at <https://www.pisces-community.org/>, Aumont et al., 2015) whose schematic diagram is shown in Fig. I.15.

PISCES is a model based on discrete plankton sizes (Chisholm, 1992). It is built on two trophic levels, each separated into two size classes, i.e. into 4 biological living compartments: 2 phytoplankton: nanophytoplankton (cell size of 2-20 μm) and diatoms (microphytoplankton - 20-200 μm); and 2 zooplankton: microzooplankton (20-200 μm) and mesozooplankton (large cells, i.e. copepods 200 μm -2 mm, Strand et al., 2020). Only diatoms use Si for growth. Note that a fifth planktonic group can be used by activating the QUOTA version, which adds a picophytoplankton compartment and allows the stoichiometric variability. Growth rates of phytoplankton are based on Monod equations (Monod, 1942) for N, P and Si (the Redfield ratio is constant and growth depends on nutrient external availability) and on a quota approach for Fe (the Fe/C ratio can vary based on the external availability of the limiting nutrient).

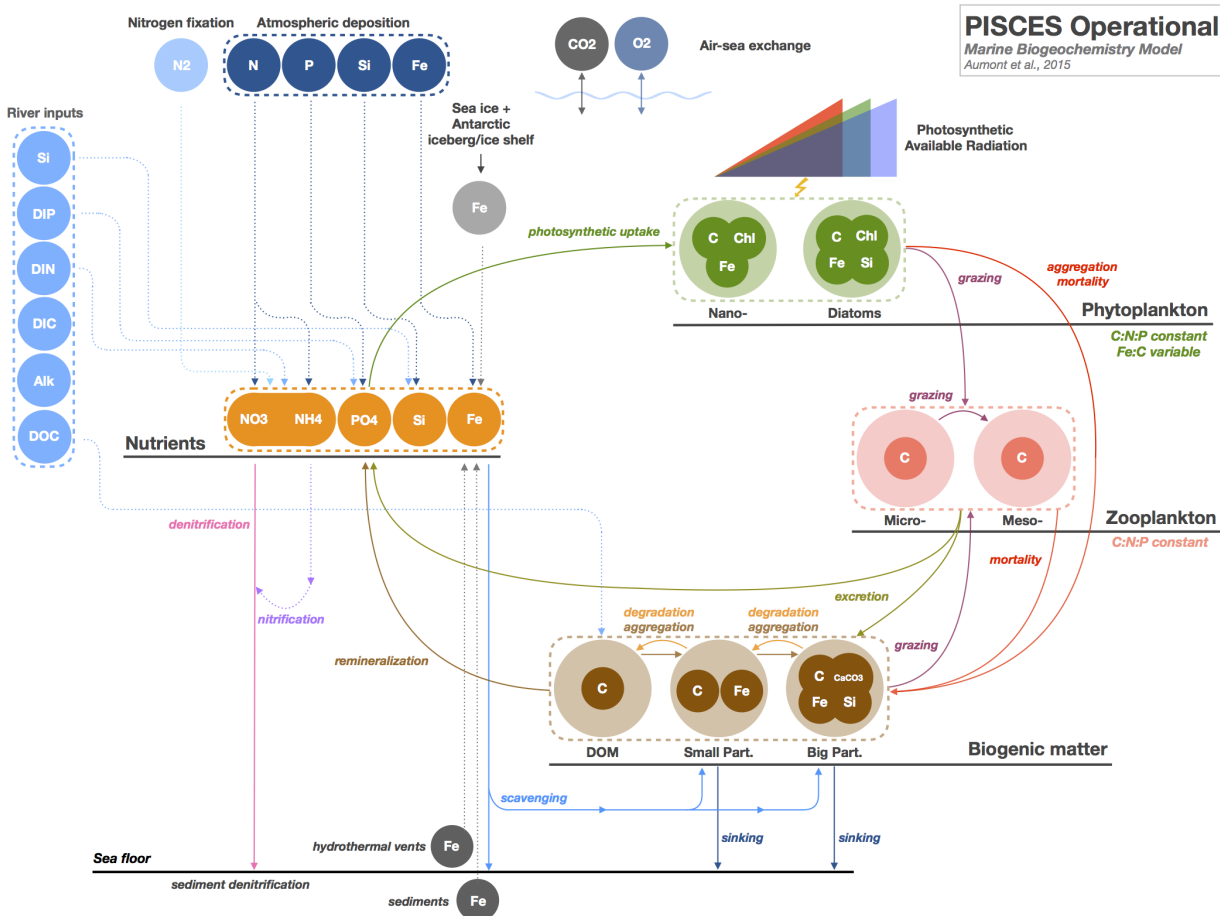


Figure I.15: Schematic of PISCES Operational Marine Biogeochemistry Model from <https://www.pisces-community.org/index.php/model-description/>; Aumont et al. (2015).

In PISCES, microzooplankton graze only phytoplankton (herbivorous) and mesozooplankton graze phytoplankton, smaller zooplankton and particulate organic matter (omnivorous). Grazing functions are based on Michaelis-Menten parameterizations (Michaelis and Menten, 1913). Their growth rate is constrained by linear, natural mortality but also by a quadratic mortality term that represents the stress induced by unrepresented processes like the predation by upper trophic levels or viral diseases. The model uses daily averages for PP and does not represent the diurnal cycle. It does not represent diel vertical migration (Peterson et al., 1990; Aumont et al., 2015), even though its parameterization has been recently proposed by Gorgues et al. (2019).

The phytoplankton biomass is controlled both by bottom-up effects (light and nutrients limitation of production) but also top-down controls by zooplankton grazing. As an example, we show the rate of change of the diatoms biomass D , given by Eq. I.1 using PISCES notations (Aumont et al., 2015).

$$\frac{\partial D}{\partial t} = (1 - \delta^D) \mu^D D - m^D \frac{D}{K_m + D} D - sh \times w^D D^2 - g^Z(D) Z - g^M(D) M \quad (\text{I.1})$$

with the right hand side (RHS) terms as follows: μ^D growth rate (corrected by the exudation term δ^D), m^D linear (natural) mortality rate (K_m is the half-saturation constant for mortality), aggregation (sh is the shear rate and w^D the minimum quadratic mortality of phytoplankton), and grazing by microzooplankton and mesozooplankton (with g^Z and g^M their respective grazing rates; and Z , M their biomass).

Several features of PISCES should be noted, especially concerning Iron chemistry (PISCESv2 has noticeably increased the complexity of the iron cycle) and boundary conditions. The dust deposited at the air-sea boundary contains 3.5% of particulate iron and sinks into the ocean at a given velocity. During its sinking, the particulate iron turns into dissolved iron (solubility constant rate is 0.01% per day) and becomes available for phytoplankton intake (bioavailable). In addition, other external sources of nutrients into the system ocean are river deposits, sea ice and hydrothermal vents (Aumont et al., 2015). Note that over the Northwest coast of Africa, high atmospheric iron deposition by Saharan dust prevents Fe limitation.

Another aspect to note about boundary conditions in the context of coastal studies is the interaction with the bottom boundary. A portion of the particulate organic carbon that reaches the seafloor is permanently buried at a specific rate. The degradation rate of the remaining organic matter by denitrification and oxic processes at the sediment interface finally gives the nitrate, oxygen and ammonium concentrations (enhanced in shallow waters, Christensen et al., 1987). The treatment of Si at the bottom boundary differs from this, especially because the part of Si not buried is instantaneously dissolved in the water column.

In this thesis, PISCES is coupled with the CROCO configuration described earlier. For biogeochemical open boundary conditions, we use the World Ocean Atlas (WOA) climatology for nitrate, phosphates, silicates and oxygen (Garcia et al., 2018) and Global Data Analysis Project (GLODAP) for dissolved inorganic and organic carbon (Key et al., 2004). We use the dust deposition of Tegen and Fung (1994) as atmospheric forcing.

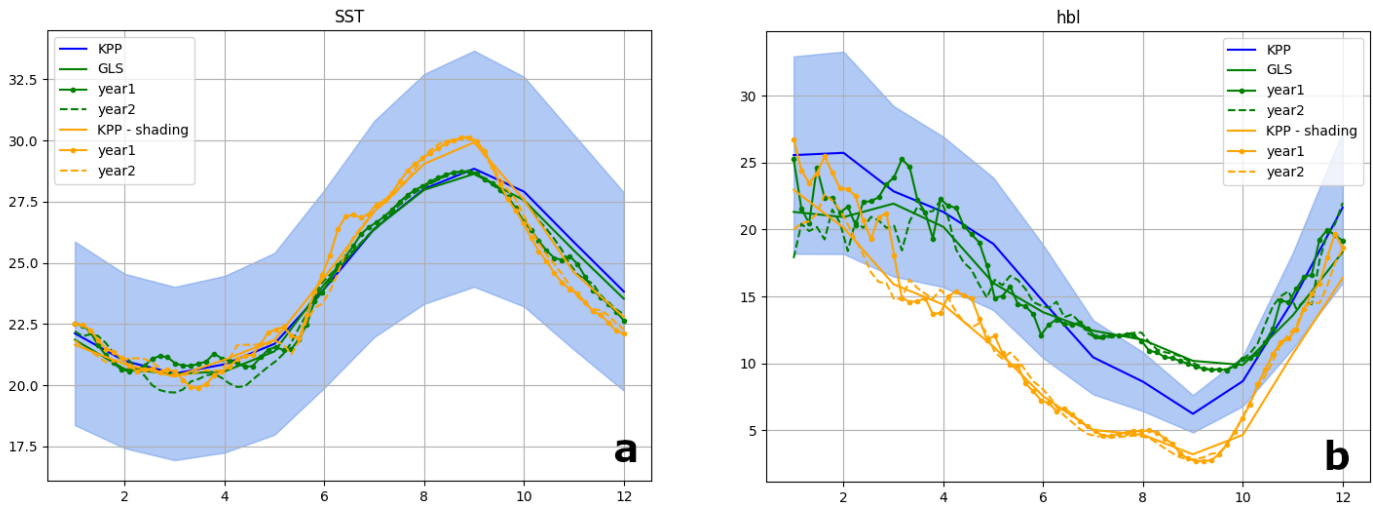


Figure I.16: Time series of the SST (a) and SML depth (b) seasonal cycle for CROCO-KPP (blue lines), $k-\epsilon$ (green) and KPP with chlorophyll shading (orange), daily averages between $(-18, -17^\circ\text{E}$ and $14, 14.6^\circ\text{N}$). Blue shaded areas indicate the standard deviation to the mean of the variables.

This regional configuration reaches an important numerical complexity by combining the CROCO-AGRIF PISCES features. Concerning the configuration and the heat and tracer budgets that we will present later, it involved some time of solving numerical issues. This was also done with the help of a support team, which was highly valuable for this project (Christophe Hourdin, Renaud Person and Stéphane Pous). Still, we encountered persistent numerical issues, especially concerning CROCO-AGRIF-PISCES with the $k-\epsilon$ vertical scheme, with unresolved bugs that seemed to concern Message Passing Interface (MPI)/AGRIF core issues. Given the limited time of the PhD, we choose to focus on simulations with the KPP vertical mixing scheme.

In standard CROCO-PISCES configurations, the coupling is one way, so the biogeochemical feedback on ocean dynamics is not considered. However, in highly productive areas as EBUS, high planktonic biomass in the euphotic zone may impact solar energy penetration into the ocean. [Echevin et al. \(2021\)](#) describe this effect in the Peru-Chile Upwelling System and propose a feedback loop on the ocean model to adjust the fluxes into the ocean. This "shading" concentrates solar energy where chlorophyll is high and thus modifies the distribution of solar energy in the vertical. Fig. I.16 indicates that the SST and SML depth seasonal cycles are slightly modified with shading: weak increase of SST at its maximum values in september and up to a 5 meters shallower SML depth in september (and 2 m in average between February and May as described in section 3.10.3).

We run 7 years of climatological simulations to obtain an ensemble of initial states. The average nitrate concentration off Senegal up to 200 m deep is at near-equilibrium after 2 years (Fig. I.17), after which we consider the spin-up time of the area of interest to be over. We thus take the last 5 climatological 1 February initial states to start our synoptic experiments.

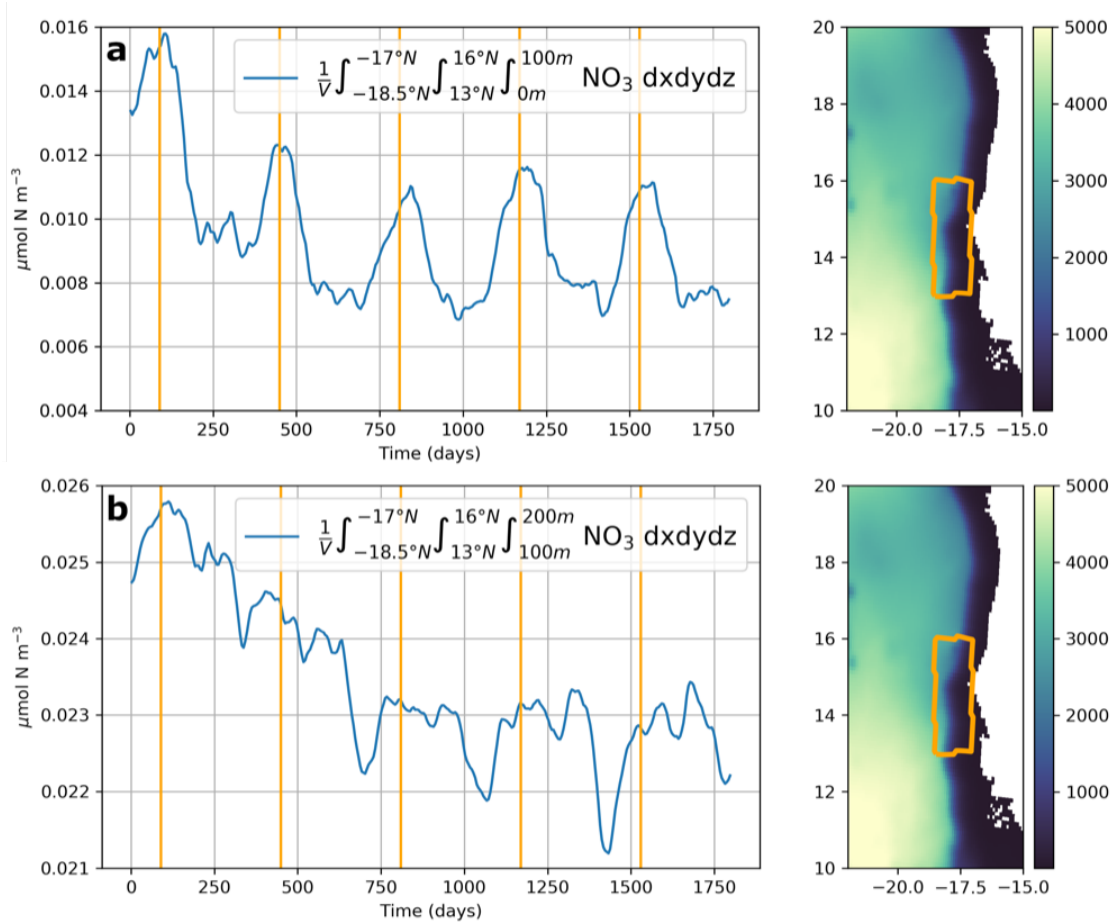


Figure I.17: Time series of the averaged nitrate concentration in coastal Senegalese waters (the averaging box is shown in orange on panels on the right), between depths 0-100 m (a) and 100-200 m (b). The time period is 5 years of climatological simulations.

4.2 Model evaluation against biogeochemical observations

We evaluate the model climatological simulations against available biogeochemical observations. We use the near surface chlorophyll concentration derived from satellite observations. We compare the climatological fields of the last 5 years of our simulations to two products: the CMEMS (Gohin et al., 2002) (dataset "dataset-oc-glo-bio-multi-l4-chl_4km_monthly-rep") and SOMNVA (from Khassoum Correa and Eric Machu) datasets. The surface nitrate is evaluated with the World Ocean Atlas climatological fields (Garcia et al., 2018) and its vertical structure near the SSUS with the available profiles in the World Ocean Database (at <https://www.ncei.noaa.gov/products/world-ocean-atlas>).

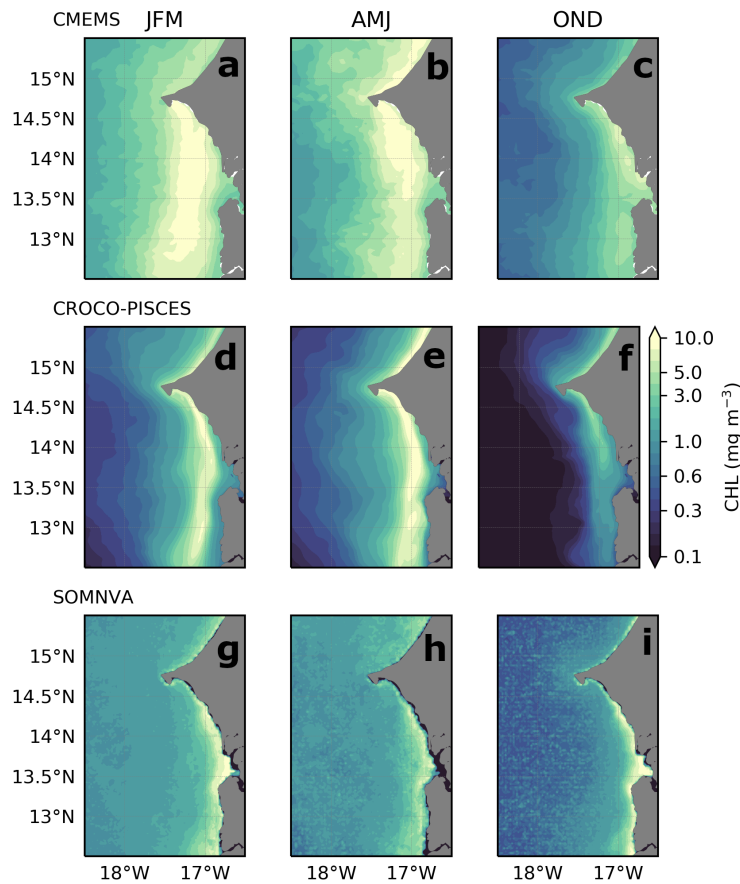


Figure I.18: Climatological seasonal averages of surface chlorophyll-a concentration of satellite CMEMS observations (a-c), CROCO-PISCES simulations (d-f) and SOMNVA observations (g-i).

During January-February-March (JFM), the CMEMS product exhibits a tongue-like structure of chlorophyll with maximum intensity beyond 10 mg m^{-3} (Figure I.18a) and the SOMNVA a maximum intensity at the coast just below 10 mg m^{-3} (Figure I.18g). These major differences between the two observation products show the difficulty to evaluate our model. Even if we do not know if this structure is realistic, our model reproduces the tongue-like cross-shore structure of chlorophyll of the CMEMS product (Figure I.18d) but underestimates its width of about 50 km. Also, the model underestimates offshore values by about 2 mg m^{-3} (compared to both SOMNVA and CMEMS, this bias depends on the distance to shore), even though it overesti-

mates it during March only (not shown). Our simulations reproduce the seasonal cycle with a maximum of chlorophyll in January-February-March (JFM) and a reduced concentration in October-November-December (OND). July-August-September (JAS) is not shown because of very low chlorophyll values in all three datasets.

The seasonal cycle of nitrate is reproduced in the model with a maximum in JFM and a minimum in JAS-OND, in agreement with the seasonal cycle of chlorophyll. The surface nitrate concentration near Senegal ($\sim 15^\circ\text{N}$) is roughly reproduced ($\approx 5 \text{ } \mu\text{mol L}^{-1}$). Over a wider spatial range, the model underestimates the nitrate concentration, especially offshore (e.g. nearly depleted in the model against $\approx 5 \text{ } \mu\text{mol L}^{-1}$ in the observations at $\sim 18^\circ\text{W}$, see Fig. I.19 panels a,e). This nitrate bias in our model could explain the bias in chlorophyll. It is difficult to conclude on quantitative bias because of the limited number of observations (see Fig. I.19 panels i-l). Note that the seasonal cycle of the standard deviation of the nitrate is also qualitatively reproduced (Fig. I.19 panels m-p and q-t).

We compare the vertical nitrate structure of the model with the few available observations from the World Ocean Database first during JFM. Based in Fig. I.20a, we find that the model tends to underestimate the nitrate concentration at the surface and that the vertical structure is roughly correct. The following seasonal evolution is reproduced by the model (Fig. I.20b-d): more stratification during April-May-June (AMJ); surface depletion and reduced stratification during JAS; reduced stratification during OND. The model vertical structure is more diffuse than the more stratified observed one, which agrees with SML depth physical biases. However given the number of observations (64 in total over the area, with ≈ 60 only at the surface), a quantitative estimation of nutrients concentration biases is limited.

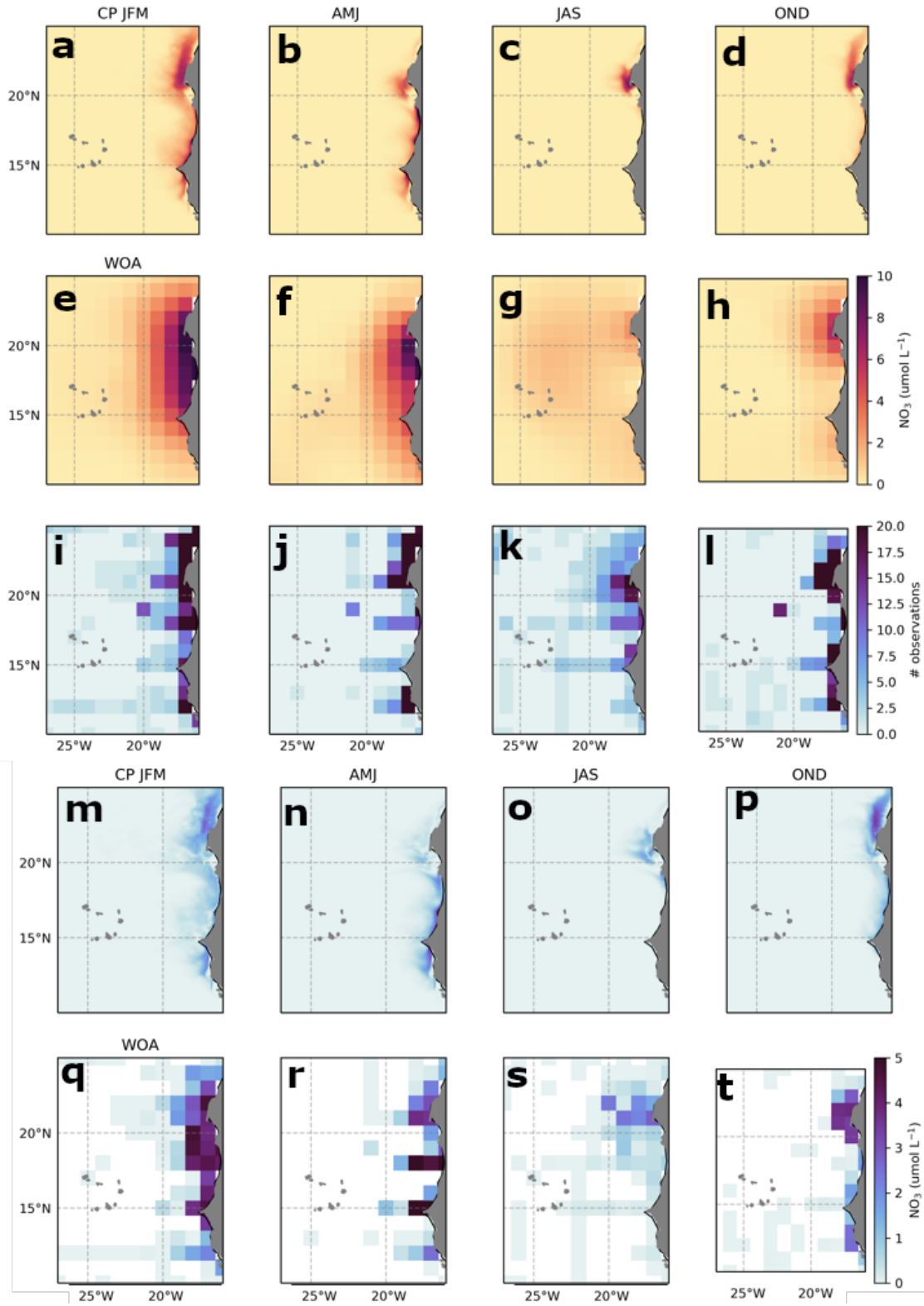


Figure I.19: Climatological seasonal averages of surface nitrate concentration of CROCO-PISCES (CP) simulations (a-d), World Ocean Atlas observations (e-h) and the number observations it uses (i-l); standard deviation of CROCO-PISCES simulations (m-p) and World Ocean Atlas observations (q-t).

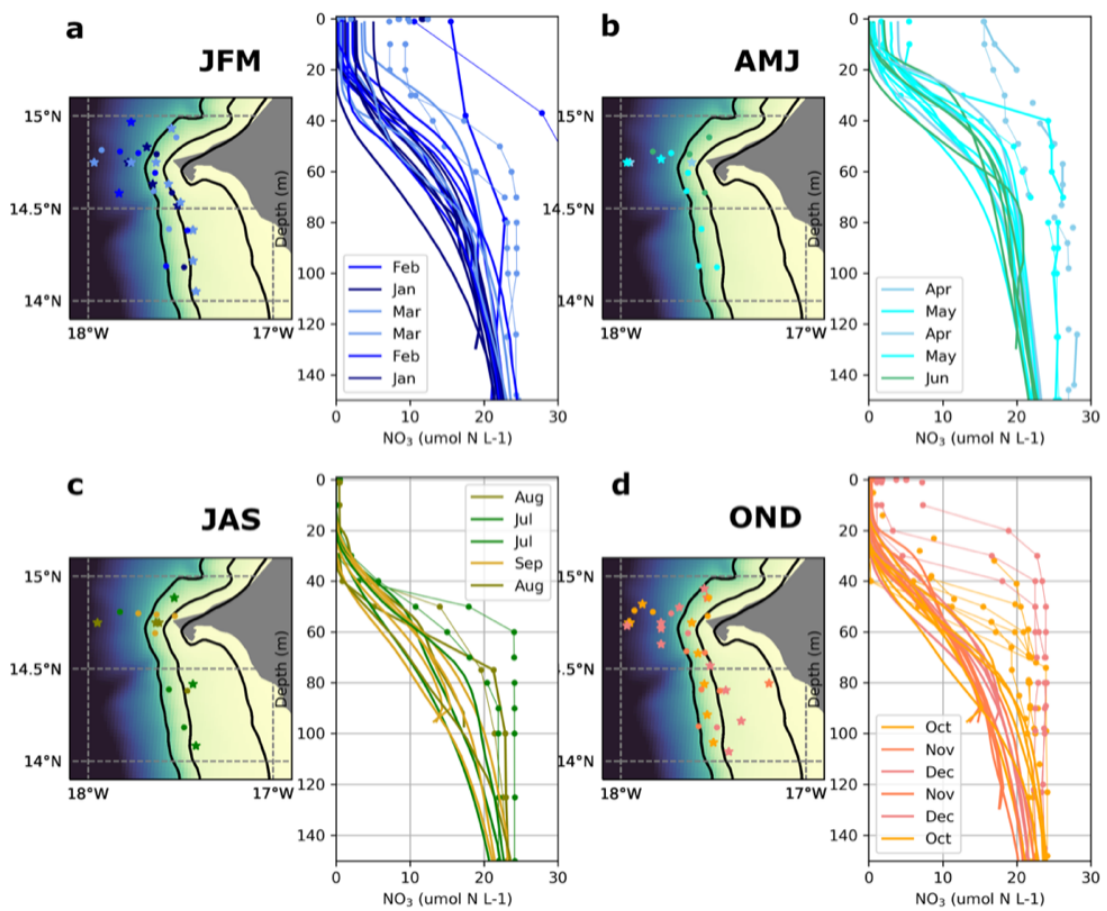


Figure I.20: Seasonal World Ocean Database (dotted lines) and model (continuous lines) locations and vertical profiles of NO_3 in the Cape Verde sector.

4.3 Budget on biological tracers

We perform a budget on biological (phytoplankton and zooplankton) and biogeochemical (nitrate) tracers. Especially, a detailed budget on diatoms (D) is performed in which each term will be analyzed. To do so, we use the PISCES "diabio" functionality which enables us to output separate biological terms (Aumont et al., 2015), that we modify to extract the right diagnostics for the budget. This involved a verification of the budget closure at each grid cell. Then, by integrating in the SML, a residual term appears between the rate and the sum of physical and biological terms, that is the entrainment/detrainment term. In the simplest case, we integrate the budget over the whole water column such that the vertical terms disappear and we combine zonal and meridional advection into the horizontal term.

Using the diatoms Eq. I.1 of PISCES, the budget on the diatoms concentration (ensemble averages) is thus given by Eq. I.2. We grouped together mortality and aggregation as they both represent a sink out of the direct trophic chain.

$$\begin{aligned} \partial_t D = & \underbrace{\overbrace{\partial_x u D + \partial_y v D + \partial_z w D}^{adv} + \overbrace{h_{mix} + v_{mix} + entr/detr}^{mix}}_{phy} \\ & + \underbrace{PP - mort/aggreg - micrograz - mesograz}_{bio} \end{aligned} \quad (I.2)$$

with $D = DIA(x, y, z, t)$ in $\mu \text{ mol C L}^{-1}$. For the sake of simplicity, no notation indicates daily average and ensemble averages. Also, information about the vertical integration is not indicated if it is over the whole water column and indicated if over the SML (e.g. $|_{SML}$).

4.4 Weight of perturbation diagnostic

We diagnose the weight of a perturbation in a given variable X with $\mathcal{W}^{\pm 0}(X)$ defined in Eq. I.3. Intermediary quantities are drawn in Fig. I.21.

$$\mathcal{W}^{\pm 0}(X) = \max_t \left(\frac{X_{SF^{\pm}} - X_{SF^0}}{X_{SF^0}} \right) \quad (\text{I.3})$$

Note that, mathematically, if we substitute the *max* with a temporal average, the half sum of the weight diagnostic for SF^+ and SF^- is equivalent to the residual diagnostic defined in section 3.7 as writes Eq. I.4.

$$\begin{aligned} \frac{1}{2}(\mathcal{W}^{+0} + \mathcal{W}^{-0}) &= \frac{1}{2} \left(\frac{X_{SF^+} - X_{SF^0}}{X_{SF^0}} + \frac{X_{SF^-} - X_{SF^0}}{X_{SF^0}} \right) \\ &= \frac{\frac{1}{2}(X_{SF^+} + X_{SF^-})}{X_{SF^0}} - 1 \\ &= \mathcal{R}_{SF}(X) \end{aligned} \quad (\text{I.4})$$

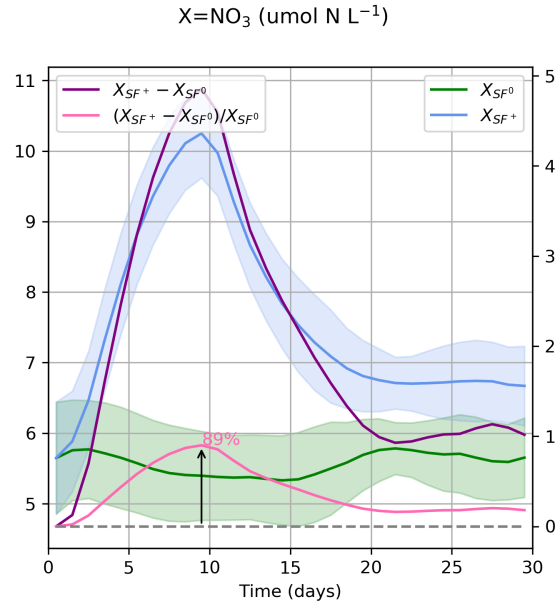


Figure I.21: Time series of intermediate quantities to reach the weight of perturbation diagnostic $\mathcal{W}^{\pm 0}(X)$, here with $X = \text{NO}_3$.

Impact of synoptic wind intensification and relaxation on the dynamics and heat budget

Contents

1	Preamble	76
2	Impact of Synoptic Wind Intensification and Relaxation on the Dynamics and Heat Budget of the South Senegalese Upwelling Sector: JPO manuscript	77
2.1	Introduction	77
2.2	Methods*	80
2.3	Model evaluation with in situ buoy measurements	88
2.4	Synoptic SSUS dynamics	90
2.5	Mixed layer heat budget	100
2.6	Sensitivity tests and limitations	106
2.7	Discussion	108
2.8	Conclusions	109
3	Complementary diagnostics and analyses	112
3.1	Spatial structure anomalies: JPO Supplementary Material	112
3.2	Details on a minor pre-processing error	114
3.3	Spatial and temporal dependence of the deterministic response	115
3.4	Additional dynamical aspects of the SSUS dynamics	117
3.5	Heat transport along the box boundaries	123
3.6	Sensitivity tests	124
4	Discussion	126
4.1	Ensemble approach	126
4.2	General discussion	127
5	Conclusion	129

1 Preamble

This chapter presents the impact of synoptic wind intensification and relaxation on the dynamics and heat budget of the SSUS. It is composed first of a paper accepted for publication in JPO (reformatted for the thesis manuscript) where methods and results are described before the discussion. A second section presents complementary diagnostics and interpretations and helps gaining a global view of all aspects of the response. A third section discusses the main results and their implications. **Note that the entire section 2.2, indicated with an *, can be skipped for those who have read chapter I.**

2 Impact of Synoptic Wind Intensification and Relaxation on the Dynamics and Heat Budget of the South Senegalese Upwelling Sector: JPO manuscript

Pierre Chabert¹, Xavier Capet¹, Vincent Echevin¹, Alban Lazar¹, Christophe Hourdin¹, Siny Ndoye²

Abstract

In addition to their well-known seasonal cycle, Eastern Boundary Upwelling Systems (EBUS) undergo modulation on shorter synoptic to intraseasonal time scales. Energetic intensifications and relaxations of upwelling favorable winds with 5-10 days typical time scales can impact the EBUS dynamics and biogeochemical functioning. In this work the dynamical effects of wind-forced synoptic fluctuations on the South Senegalese Upwelling Sector (SSUS) are characterized. The region geomorphology is unique with its wide continental shelf and a major coastline discontinuity at its northern edge. The ocean response to synoptic events is explored using a modeling framework that involves applying idealized synoptic wind intensification or relaxation to a five-member climatological SSUS ensemble run. Model evaluation against sparse mid-shelf in situ observations indicates qualitative agreement in terms of synoptic variability of temperature, stratification and ocean currents, despite a moderate but systematic bias in current intensity. Modeled synoptic wind and heat flux fluctuations produce clear modulations of all dynamical variables with robust SSUS-scale and mesoscale spatial patterns. A mixed-layer heat budget analysis is performed over the continental shelf to uncover the dominant processes involved in SSUS synoptic variability. Modulations of horizontal advection and atmospheric forcing are the leading-order drivers of heat changes during either wind intensification or relaxation while vertical dynamics is of primary importance only in a very localized area. Also, modest asymmetries in the oceanic responses to upwelling intensification and relaxation are only identified for meridional velocities. This brings partial support to the hypothesis that synoptic variability has a modest net effect on the climatological state and functioning of upwelling systems dynamics.

2.1 Introduction

Eastern Boundary Upwelling System (EBUS) dynamics are driven by alongshore upwelling favorable winds generating vertical transport of nutrients in the euphotic layer and primary production. Winds undergo a strong seasonal cycle in most EBUS (Chavez and Messié, 2009) but they are also subjected to shorter intraseasonal (10-60 days) and synoptic fluctuations (5-10 days), typically in the form of wind intensity modulations (i.e., relaxations and intensifications),

¹Sorbonne Université, CNRS, IRD, MNHN, Laboratoire d'Océanographie et du Climat: Expérimentations et Approches Numériques (LOCEAN-IPSL), Paris, France

²Ecole Supérieure des Sciences et Techniques de l'Ingénieur (ESTI), Université Amadou Mahtar Mbow, BP 45927, Dakar, Senegal

but also shifts in wind direction. Synoptic variability can have large effects on the variability of ocean physical and biogeochemical properties (e.g., off central Chile: [Aguirre et al. \(2014\)](#); [Torres et al. \(1999, 2002\)](#) and off US West Coast: [Zhang et al. \(2015\)](#); [Shanks et al. \(2014\)](#); [Evans et al. \(2015\)](#); [Bane et al. \(2007\)](#)). As climate change may induce a reduction of synoptic variability in the low latitude portions of EBUS ([Aguirre et al., 2019](#)), it would also be useful to better understand its impact on the coastal ocean dynamics.

Since [Send et al. \(1987\)](#) (see also [Send \(1989\)](#)) it is known that intensification and relaxations phases may not have symmetric effects on ocean properties. The effects of relaxations do not, in general, reverse those of intensifications. Thus, rectification by eddy-like terms (i.e. residual effects) are associated with synoptic fluctuations and the mean/climatological state and functioning of upwelling regions are distinct from what they would be in the absence of these fluctuations. Other forms of rectification effects include those due to mesoscale eddies on the general ocean or atmospheric circulation ([Farneti et al., 2010](#)), to ENSO in the Pacific ocean ([Okumura et al., 2017](#)), to barotropic tides ([Zimmerman, 1986](#)), and surface waves (i.e., the so-called Stokes drift, [Curcic et al. \(2016\)](#)). Synoptic forcing rectification (or lack thereof) is tracer and location dependent ([Kuebel Cervantes and Allen, 2006](#); [Largier et al., 2006](#)). An important cause of asymmetry for upper ocean heat content is the fact that vertical processes (advection and mixing) are large cooling terms during intense upwelling events, but get merely turned off during relaxation. For upper ocean heat content in the Point Reyes - Bodega Bay upwelling sector ([Send et al., 1987](#)) the asymmetry also arises from the differential behavior of surface heat fluxes and alongshore heat advection. The latter is generally believed to be an important source of asymmetry wherever coastline and bathymetric irregularities (e.g., capes and bays) produce complex time- and space-variable alongshore temperature gradients ([Send et al., 1987](#)), and quasi-standing flow features ([Barth et al., 2005](#); [Ramp et al., 2005](#); [Narimousa and Maxworthy, 1989](#)).

Biogeochemical tracers (e.g. dissolved oxygen, [Send and Nam \(2012\)](#); [Aguirre et al. \(2021\)](#)) and marine organisms (e.g. phyto- and zooplankton [Pitcher et al. \(1991\)](#); [García-Reyes et al. \(2014\)](#)) are also subjected to rectification. The biological response of the latter to synoptic fluctuations ([Dorman et al., 2005](#); [Wing et al., 1995](#); [Morgan et al., 2018](#)) may produce additional ecosystem asymmetries.

All this has important implications, including for interannual variability. For instance, it contributes to decoupling low-passed time-averaged upwelling indices and ecosystem functioning indicators such as enrichment in nutrients, and primary/secondary production ([García-Reyes et al., 2014](#)). But other studies indicate a rather linear response of the ocean to upwelling wind intensifications and relaxations ([Aguirre et al., 2014](#)), hence little rectification associated with synoptic-scale wind variability. Coexistence of these contrasting results may be the consequence of distinct oceanographic and geomorphological contexts but progress is needed on this topic. Having mesoscale turbulence time scales comparable to those of synoptic variability further complicates the problem ([Marchesiello et al., 2003](#)).

Despite the intensity of synoptic wind fluctuations in the Canary current system (Desbiolles et al., 2014; Kounta Diop, 2019), their effect on the ocean has received limited attention, except in the northern part of the system (Ramos et al., 2013; Cordeiro et al., 2018; Relvas and Barton, 2005; Lopes et al., 2014).

We strive to fill this gap for the southern Senegal upwelling sector situated at the southern end of the system and, thereby, increase the general knowledge on the subject. Other West African sectors would certainly deserve a similar attention (e.g. Cape Ghir, Western Sahara Bank, Cape Blanc and Arguin Bank; see Fig. II.1a).

In a nutshell, upwelling winds along West Africa are driven by the pressure gradient between the North Atlantic Subtropical Anticyclone, named Azores high, and heat lows present on land. South of 15-20°N, the position of the ITCZ is also determinant. Their seasonal evolutions are such that the SSUS upwelling season is mainly from November to June (Roy, 1989) (with the July-Oct. interruption being characterized by a monsoon regime). Atmospheric extra-tropical Rossby wave activity has been linked to wind synoptic variability but the mechanisms at play would need further clarification (Sultan and Janicot, 2003; Kounta Diop, 2019).

The SSUS northern limit is the sharp Cape Verde (hereinafter CV) which hosts the city of Dakar. Its southern limit is somewhat arbitrarily chosen at 12.5°N so that it also includes Gambian territorial waters. During the upwelling season, the major geomorphologic irregularity at CV (coastline and bathymetry, see Fig. II.1) is responsible for a quasi-permanent sea surface temperature (SST) pattern composed of a cold upwelling tongue emanating from CV that is predominantly oriented north-south (Ndoye et al., 2014); and a warm inshore SST strip south of approximately 14.5°N (Roy, 1998). Numerical simulations have revealed the extreme concentration of upwelling in the northern part of the SSUS and the importance of alongshore/-southward transport in the system (Ndoye et al., 2017). SSUS synoptic fluctuations have been documented using satellite observations (Ndoye et al., 2014) and in situ measurements (Capet et al., 2017). It is hypothesized in the latter study that alongshore advection is key to explain mid-shelf heat content synoptic fluctuations.

To make progress, we design a set of original numerical experiments in which synthetic synoptic forcing anomalies (intensifications and relaxations) are applied to the realistic regional model of Ndoye et al. (2017). We describe and analyze various aspects of the forced SSUS dynamical response, including submesoscale activity and surface mixed layer (hereafter SML) heat content. Direct comparison between intensification and relaxation twin simulations (i.e. with similar initial state) offers a simple way to examine the natural leading order source of synoptic rectification (but leaves aside effects due to complex wind histories, i.e., succession of intensifications and relaxations of variable duration). An ensemble run strategy is used to reduce uncertainties induced by intrinsic quasi-balanced activity. A particular focus is on intensification/relaxation asymmetries because they are indicative of rectification effects associated with synoptic variability.

The paper is organized as follows. Material and methods are presented in section 2. A brief model evaluation is proposed in section 3. The SSUS forced response to synoptic atmospheric fluctuations is presented in section 4. Mixed layer heat budget analyses are performed in section 5. Some sensitivity tests and model limitations are presented in section 6. We finish with a discussion and some concluding remarks in sections 7 and 8.

2.2 Methods*

We develop a modeling framework that involves idealized synoptic wind intensification and relaxation. Their specific spatio-temporal patterns are chosen based on composite analyses presented below. The resulting forcing is applied to a five member climatological SSUS ensemble simulations carried out using CROCO.

2.2.1 Model settings and simulations

We use the Coastal and Regional Ocean COMMunity model (CROCO, from <https://www.croco-ocean.org/>; Hilt et al. (2020)), derived from Regional Ocean Modeling System (ROMS; Shchepetkin and McWilliams (2005, 2009)). The model configuration presented in Ndoye et al. (2017) takes advantage of the AGRIF grid refinement capability (Debreu and Blayo, 2008). A parent grid covers most of the Canary current system with a spatial resolution of ~ 10 km. A child domain spans the Senegalese ocean with finer resolution ~ 2.5 km (Fig. II.1a). The two grids are run alongside using two-way coupling (Debreu et al., 2012). For the sake of simplicity and coherency with future biogeochemical coupling, we do not use the diurnal shortwave cycle. The general model approach relies on two classes of simulations.

First, a 10-year long climatological simulation is run to obtain 1) an ensemble of physical initial states on which to apply synoptic experiments and 2) model climatological average fields (noted with subscript *clim*) used for heat flux restoring to climatological SST (see Appendix A). The climatological simulations are produced using monthly climatological surface heat fluxes from the International Comprehensive Ocean Atmosphere Data Set (COADS; noted Q_{climO} ; years 1854-1992; spatial resolution $\Delta x = 0.5^\circ$; Worley et al. (2005)), SST from the Moderate Resolution Imaging Spectroradiometer (MODIS; noted SST_{climO} ; years 2002-2018; $\Delta x = 5$ km; NASA (2014)) for SST restoring, wind stress from the Scatterometer Climatology of Ocean Winds (SCOW; noted $\tau_{x|climO}; \tau_{y|climO}$; 1999-2009; $\Delta x = 0.25^\circ$; Risien and Chelton (2008)) and open boundary conditions from the Simple Ocean Data Assimilation (SODA over the period 2000-2008 Carton and Giese (2008)).

Second, a series of shorter synoptic runs (45 days) is performed for three different types of surface wind and air-sea heat flux anomalies: synoptic wind intensification, relaxation, and no anomaly (reference), respectively denoted SF^+ , SF^- and SF^0 . Subscript SF (resp. SF^\pm) refers to any synoptic forcing condition in $\{SF^+; SF^-; SF^0\}$ (resp., in $\{SF^+; SF^-\}$). The construction of forcing anomalies is described in the subsequent sections.

The standard vertical mixing scheme we use is the K-Profile Parameterization (KPP, Large et al. (1994)) but we also explore the sensitivity of our results by carrying some runs with the k- ϵ (Rodi, 1987) parameterization (section 2.6.1).

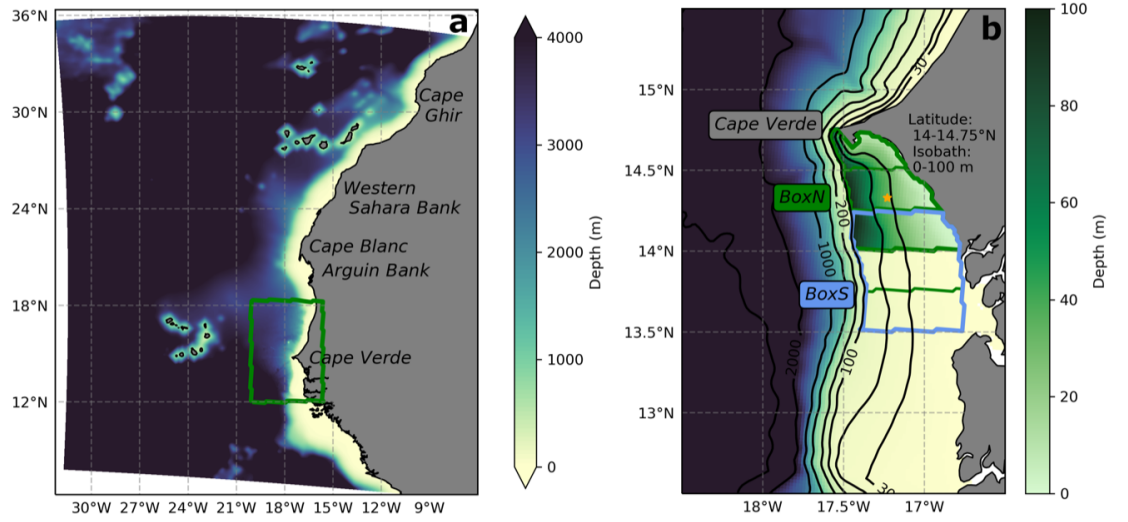


Figure II.1: Grid configuration used in the study. It consists of a parent domain encompassing most of the Canary current system with a zoom at 2.5 km horizontal resolution over the the Senegalese waters (green rectangle in panel a; see text for details). The study area located south of Cape Verde (SSUS) and various averaging boxes (green and blue solid lines) are shown in panel b, as well as the Melax buoy location (orange star).

2.2.2 ERA5 reanalysis dataset

Atmospheric synoptic conditions are expressed in terms of wind stress but also of net heat fluxes. As for other upwelling systems, the latter plays a noticeable role on the SSUS dynamics (Ndoye et al., 2017; Capet et al., 2017). We use the ERA5 dataset from the European Centre for Medium-Range Weather Forecasts (ECMWF: ‘ERA5 hourly data on single levels from 1979 to present’; Hersbach et al. (2018); $\Delta x = 0.25^\circ$) to compute synoptic wind stress and heat anomalies. We choose the temporal coverage between 2000 and 2010 to match the time period of the climatological wind stress we use (see section 2.2.1) to force our model and obtain climatological physical states. We use the following variables: zonal and meridional wind speed at 10 m; short and longwave radiation, sensible and latent heat fluxes which are combined to provide net air-sea heat flux (Barnier et al., 1995). Wind stress is obtained from wind speed with the formula: $\tau = \rho_a C_D U_{10}^2$ with $\rho_a = 1.22 \text{ kg m}^{-3}$ the air density and $C_D = 0.0013$ the momentum transfer coefficient. For use in the compositing, a monthly climatology is built for wind stress and net heat flux, over the period 2000-2010.

2.2.3 Idealized synoptic events

Zonal and meridional wind stress ($\tau_x; \tau_y$) and net heat flux (Q) forcing fields are built as the sum of two separate terms (generically written for a field ϕ):

$$\phi_{SF^\pm}(x, y, t) = \phi_{clim}(x, y, t) + f(t) \times \phi'_{SF^\pm}(x, y). \quad (\text{II.1})$$

Posing $\phi'_{SF^0} = 0$, Eq. (II.1) is also valid for SF^0 . ϕ_{clim} is as described in section 2.2.1 for wind stress (see below and Appendix A for heat flux). By construction, synoptic anomalies have a spatial structure that is fixed in time ϕ'_{SF^\pm} and a temporal modulation of their amplitude $f(t)$. ϕ'_{SF^\pm} are defined based on ERA5 compositing.

Composites fields $\phi'_{SF^\pm}(x, y)$

The composite analysis is restricted to the upwelling season defined as the period ranging from late October to late May. We consider that the ERA5 daily meridional wind stress (τ_y) is representative of the alongshore upwelling favorable winds over the SSUS (Tall et al., 2021). We average τ_y over the SSUS subdomain (-19°E; -16.5°E to 12.5°N; 15.5°N) and remove the seasonal cycle obtained with a low pass Butterworth filter (with a threshold period of 115 days) to obtain the subseasonal wind stress anomaly $\delta\tau_y$.

Upwelling intensification (resp. relaxation) events are defined as the days during which $\delta\tau_y$ is below (resp. above) minus (resp. plus) one $\delta\tau_y$ standard deviation. We select $(\tau_x; \tau_y)$ and (Q) fields at these dates and remove the corresponding climatological monthly average (section 2.2.2.2) to obtain an anomaly field. Finally, we construct an unique upwelling season anomaly ϕ'_{SF^+} (resp. ϕ'_{SF^-}) by averaging over all identified intensification (resp. relaxation) events (Figs. II.2a-d)³.

The wind stress and heat flux anomalies present smooth regional scale patterns all over western Africa (Figs. II.2c,d). Wind anomalies become weak south of 12°N so there will be little room for remotely generated SSUS upwelling/downwelling at synoptic scale (Philander and Yoon, 1982).

The decomposition of the idealized events into short and long wave radiation, sensible and latent heat flux are informative about atmospheric conditions during upwelling wind intensification or relaxation. The latent heat flux anomaly dominates the net heat flux anomaly: there is less (resp. more) evaporation, thus more heat loss (resp. more heat gain), during intensification (resp. relaxation) events (not shown), in agreement with previous studies describing atmospheric synoptic patterns (Garstang, 1967; Desbiolles et al., 2014).

Because relaxation and intensification anomalies are quite similar and because it is convenient to use perfectly symmetric structures, we choose to ignore the composites obtained for relaxation events and define: $\phi'_{SF^-}(x, y) = -\phi'_{SF^+}(x, y)$.

Amplitude modulation $f(t)$

We now define the time modulation of amplitude $f(t)$. For simplicity we take $f(t)$ of the following form: two linear ramps, one upward and one downward with duration T_r each, and a plateau with constant wind stress anomaly between them with duration T_p . The choices made for T_r and T_p are key because they set the frequencies at which the SSUS dynamics will be perturbed. To provide general guidance a spectral analysis of the SSUS-averaged meridional wind stress (ERA5) was performed for 9 upwelling seasons (defined between late October and late

³Northeasterly and Northwesterly wind events were separated at an early stage of the study but produced similar ocean responses so this distinction is ignored.

May of the following year). The mean spectrum does not reveal any synoptic time scale energetic peak but presents a distinctly shallower slope over the time range 10-12 days compared to longer time scales (not shown). In the following, we present simulations with $T_r = 3$ days, $T_p = 5$ days and thus $T_{syn} = 2 \times T_r + T_p = 11$ days. Note that initial explorations for $T_{syn} = 6$ days produced dynamical and thermodynamical responses qualitatively similar to those with $T_{syn} = 11$ days but with smaller amplitude. As mentioned above, the wind stress direction is weakly affected by the synoptic fluctuation so little energy feeds near-inertial motions despite T_r being commensurate with the inertial frequency in the SSUS ($T_f = 2$ days). The idealized events are applied from 2 to 11 March included (hereinafter day 1 to day 10) in the middle of the upwelling season (Roy, 1989), a period of particular interest (Capet et al., 2017; Machu et al., 2019).

Net heat flux forcing implementation

The heat flux forcing in the synoptic runs writes

$$Q_{SF}(x, y, t) = Q_{clim}(x, y, t) + f(t) \times Q'_{SF}(x, y). \quad (\text{II.2})$$

The construction of appropriate air-sea heat fluxes modulated during wind intensification and relaxation to force the synoptic simulations was made so as to respect three objectives/constraints: avoid artificial restoring to climatological SST during the synoptic runs; keep Q_{clim} close to the net air-sea heat flux diagnosed from our climatological run Q_{climM} and, in particular, prevent discontinuities at the restart time of the synoptic runs; have Q_{SF} independent of online model SST so that different members of an ensemble have the exact same Q forcing. The exact definition of $Q_{SF}(t)$ and more details are given in Appendix A. The modulation of heat fluxes by synoptic events averaged over the SSUS is shown in Fig. II.2. The evolution of Q_{clim} during that period of the year is also noticeable. The magnitude of $Q'_{SF}(t)$ is $\sim 40 \text{ W m}^{-2}$ at peak anomaly but a sensitivity to doubling Q'_{SF} is also presented (section 2.6). Choosing a symmetric form for Q'_{SF} is broadly consistent with the ERA5 composite analysis (which would yield a value 5 W m^{-2} smaller for the relaxation perturbation)⁴ and facilitates the identification of asymmetries/synoptic rectification effects. Note that a minor pre-processing error led to an imperfect symmetry of the heat flux synoptic anomalies (Fig. II.2). In BoxN (see Fig. II.1b and section 2.2.2.4), the typical effect of the erroneous heat flux (-5 W m^{-2} on average between days 1 and 15) on surface mixed layer temperature is estimated to be $\sim 0.07^\circ\text{C}$ and subsequently neglected.

2.2.4 Spatial averaging

Various forms of spatial averaging are used to identify responses to synoptic events. In particular, we define a northern (BoxN; see Fig. II.1b) and a southern box (BoxS) in which we expect contrasted dynamics to occur. Their East-West delimitations are the coast and the 100 m isobath, respectively. We expect upwelling to mostly take place in BoxN delineated by the latitude 14.75°N (i.e., the Cape Verde peninsula) and 14°N (see Fig. 2a in Ndoye et al. (2017), and our Fig. II.8). The southern box, in which lateral advection likely dominates, is delineated by lati-

⁴In other upwelling regions surface heat fluxes may also be an important contributor to asymmetries (Send et al., 1987)

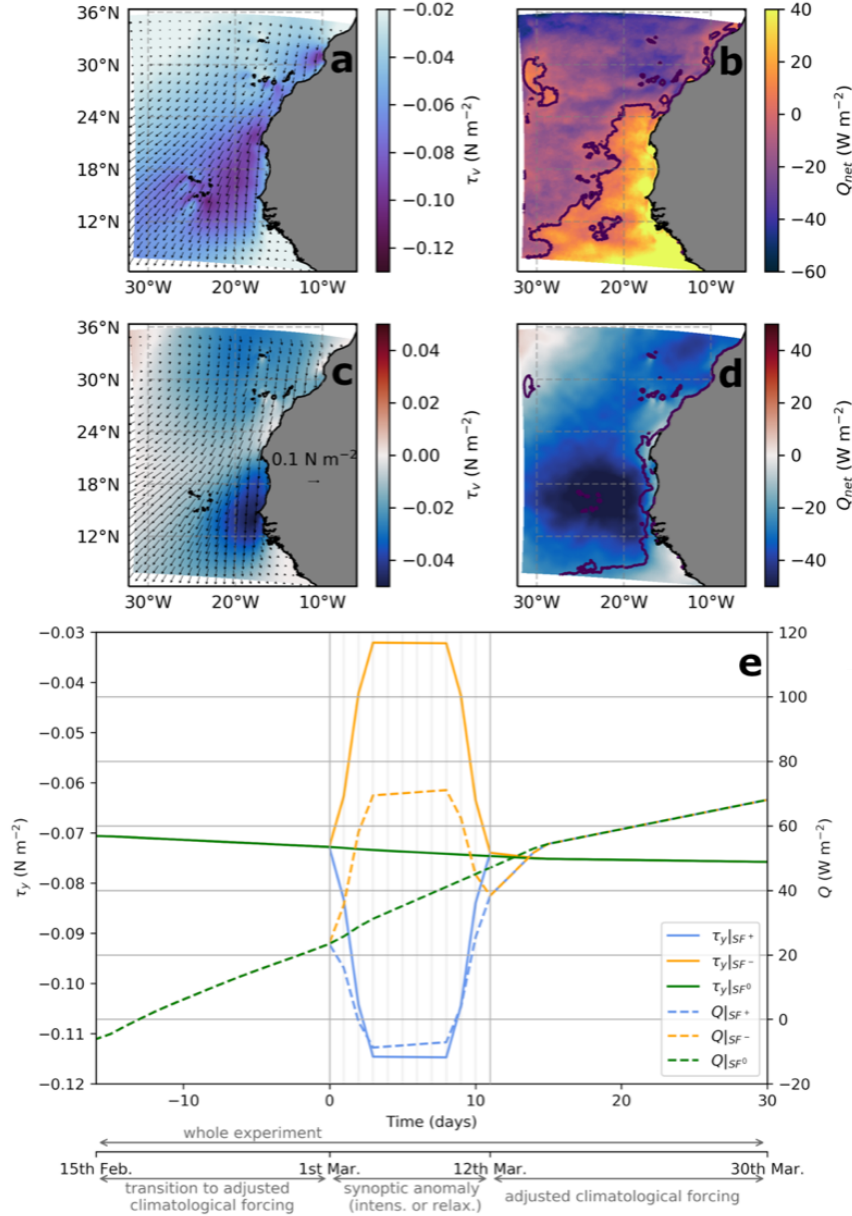


Figure II.2: Canary current meridional wind stress (a, c) and net heat fluxes (b, d) climatological (a,b; SF^0) and SF^+ anomaly (c,d) fields at the peak of the synoptic intensification. Anomalies for SF^- are the opposite of those for SF^+ . The experimental timeline is presented in panel e. Continuous (resp. dashed) lines indicate the evolution of the meridional wind stress (resp. net heat flux) averaged over the SSUS. Green (resp. blue and orange) lines are for climatological (resp. wind intensification and relaxation) forcings. A slight deviation from perfect $\text{SF}^+ - \text{SF}^-$ symmetry can be seen for heat fluxes, due at a small error. Its impact on simulated upper ocean temperature is negligible (see section 2.2.3.)

tudes 14.25°N and 13.5°N. Alongshore averaging involves a simple remapping from longitude to water column depth with 5 m bins. It is performed over the gray area shown in Figs. II.7 and II.8, in the center of BoxN.

2.2.5 Ensemble experiment

Ensemble approach

Separating the oceanic response to synoptic atmospheric anomalies from intrinsic (primarily mesoscale) variability can be demanding in terms of available flow statistics (Marchesiello et al., 2003; Colas et al., 2013). We use an ensemble modeling approach to mitigate the effect of intrinsic variability and thus ascertain the SSUS deterministic response to synoptic wind events. Each ensemble run member (e) provides an independent system state vector evolution $X^{(e)}(x, y, z, t)$.

The ensemble average is X_{SF} :

$$X_{SF} = \frac{1}{N_e} \sum_{e=1}^{N_e} X_{SF}^{(e)}(x, y, z, t) \quad (\text{II.3})$$

with $(e) \in \{1; \dots; N_e\}$ the members on the ensemble. Mean synoptic anomalies are defined as the difference between synoptic and climatological ensemble averages ΔX_{SF^\pm} :

$$\Delta X_{SF^\pm} = X_{SF^\pm} - X_{SF^0} \quad (\text{II.4})$$

For each member, the deviation to the ensemble average $\delta X_{SF}^{(e)}$, i.e., the intrinsic variability part, is defined by:

$$X_{SF}^{(e)} = X_{SF} + \delta X_{SF}^{(e)} \quad (\text{II.5})$$

By injecting Eq. (II.5) in Eq. (II.4), we obtain:

$$\Delta X_{SF^\pm} = X_{SF^\pm}^{(e)} - \delta X_{SF^\pm}^{(e)} - (X_{SF^0}^{(e)} - \delta X_{SF^0}^{(e)}) \quad (\text{II.6})$$

or also:

$$\Delta X_{SF^\pm} = \underbrace{X_{SF^\pm}^{(e)} - X_{SF^0}^{(e)}}_{\Delta X_{SF^\pm}^{(e)}|_f} - \underbrace{(\delta X_{SF^\pm}^{(e)} - \delta X_{SF^0}^{(e)})}_{\delta X_{SF^\pm}^{(e)}|_i} \quad (\text{II.7})$$

The mean forced response ΔX_{SF^\pm} due to synopticity can thus be written as the sum of a deterministic forced term $\Delta X_{SF^\pm}^{(e)}|_f$ plus a term due to intrinsic variability $\delta X_{SF^\pm}^{(e)}|_i$, and this equation is valid for each ensemble run. The intrinsic variability part would vanish when averaging over a sufficiently large ensemble but we wish to choose a relatively small N_e for environmental/energy consumption reasons. The fact that we use identical initial conditions for the SF^\pm and reference climatological runs SF^0 is helpful in that regard because it limits the random scrambling due to turbulence compared to a situation where the initial states would be inconsistent between each other. In other words, we expect to have minimized the magnitude of $\delta X_{SF^\pm}^{(e)}|_i$ relative to the magnitude of each term in its definition. To corroborate this, we show

the RMS of the different terms in Eq. (II.7) for $X = \text{SST}$ in the shelf BoxN as a function of time (Fig. II.3a). For each ensemble run, $RMS(\delta X_{SF^+}^{(e)}|_i)$ grows from 0 at $t=0$ days (when SF^+ and SF^0 simulations are identical) to $\approx \sqrt{2} RMS(\delta X_{SF^+}^{(e)}) \approx \sqrt{2} RMS(\delta X_{SF^0}^{(e)})$ at $t=7$ days (this is also true when averaging over all ensemble members). Therefore, comparing synoptic and climatological twin simulations with identical initial conditions ameliorates the signal ($\Delta X_{SF^\pm}^{(e)}|_f$) to noise ($\delta X_{SF^\pm}^{(e)}|_i / \sqrt{N_e}$) ratio during the early part of the SF^\pm experiments, until day 11-12 for SF^+ and day 7 for SF^- as readily seen in Fig. II.3b (see below section 2.4.4 on this SF^+ / SF^- distinction). In practice choosing $N_e = 5$ appears appropriate to identify SSUS-scale evolutions (see Fig. II.3b). More localized responses will be considered insofar as they emerge from noise with this relatively small ensemble, which guarantees that they are part of the first-order ocean response.

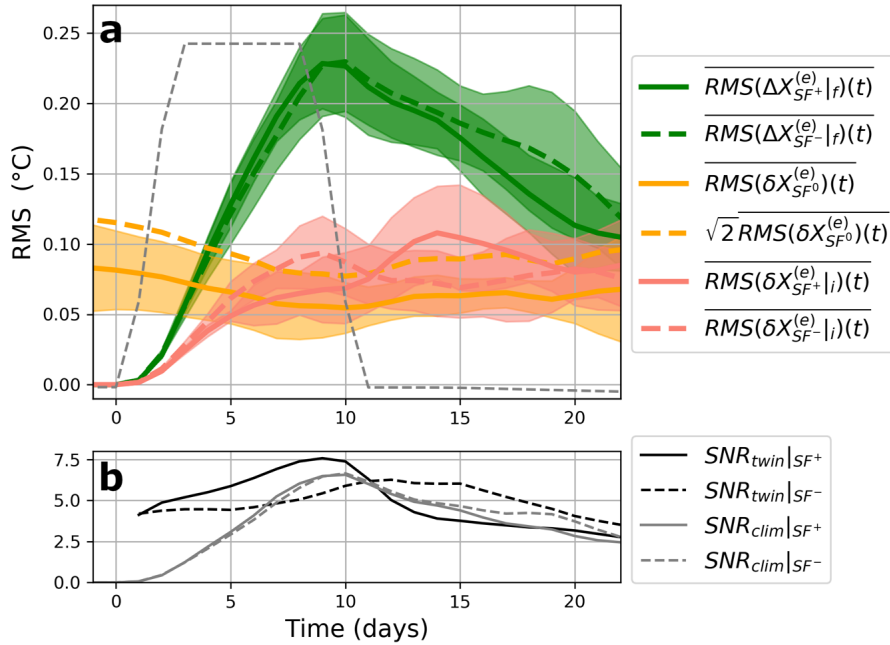


Figure II.3: a) Time series of the ensemble averages of spatial RMS for various quantities computed for $X=\text{SST}$ (panel a); see text in section 2.2.5 and Eq. II.7). The grey dashed line represents the amplitude modulation of the synoptic anomaly $f(t)$. b) Signal to Noise Ratios (SNR) as defined in section 2.2.5.

Robustness of the diagnosed forced ocean response

At any given location, the anomalous response to synoptic forcings revealed by ensemble averaging will be considered robust if the following criterion is met:

$$\left| \sum_{e=1}^{N_e} \text{sign}(X_{SF^\pm}^{(e)} - X_{SF^0}^{(e)}) \right| = 5, \quad (\text{II.8})$$

that is if the synoptic anomaly is of the same sign in all ensemble members. When time and ensemble averaging are combined (e.g., to produce Figs. II.6 and II.7), the criterion must hold for each individual day of the time averaging window, which makes the criterion as stringent as possible.

2.2.6 Residual effect

In our idealized setting, we will infer the residual effect produced by synoptic variability as:

$$RES_{SF}(X) = \frac{1}{2}(X_{SF^+} + X_{SF^-}) - X_{SF^0} \quad (\text{II.9})$$

for any oceanic variable X . We are also interested in the quantity:

$$\mathcal{R}_{SF}(X) = \frac{RES_{SF}(X)}{X_{SF^0}} = \frac{\frac{1}{2}(X_{SF^+} + X_{SF^-})}{X_{SF^0}} - 1 \quad (\text{II.10})$$

which quantifies the relative importance of the asymmetry. \mathcal{R}_{SF} will systematically be computed after ensemble and time averaging between day 3 and 8, i.e., during the plateau of SF^\pm forcing anomaly.

2.2.7 Heat budget

The clearest manifestation of synoptic variability is SST modulation. Based on vertical velocity fields shown in Ndoye et al. (2017) (see also our Fig. II.8) and the minimum SST zone, we suspect that the role of vertical advection may be weak outside the northern sector of the SSUS. We perform an online heat budget to confirm this and more generally clarify the importance of the different processes at play in the temperature changes in the SML (as in Cambon 2008; Jullien et al. 2012; Echevin et al. 2018). The SML heat budget equation is:

$$\underbrace{\langle \partial_t T \rangle}_{\text{RATE}} = - \underbrace{\langle \partial_x u T \rangle + \langle \partial_y v T \rangle}_{\text{HADV}} - \underbrace{\langle \partial_z w T \rangle}_{\text{VADV}} + \underbrace{\langle D_l(T) \rangle}_{\text{HMIX}} + \underbrace{\langle D_z(T) \rangle}_{\text{VMIX+ENTR}} + \underbrace{\langle F(z) \rangle}_{\text{FORC}} \quad (\text{II.11})$$

where T is the model potential temperature, the left term is the heating rate, (u, v, w) are the three dimensional currents components. The right-hand side terms correspond to the advection in flux form (the total advection is noted $ADV = HADV + VADV$), horizontal and vertical mixing, entrainment/detrainment and heating/cooling due to surface heat fluxes. $\langle X \rangle = (1/h) \int_{-h}^0 X dz$ is the vertical averaging of the state vector X over the time-dependent mixed layer depth (h) range.

A particular focus will be on advection because it is presumably important in driving the heat changes in the SSUS. Unfortunately, the interpretation of individual advection terms can be made difficult by the strong compensations between them (Gan and Allen, 2005a; Colas et al., 2013). Incidentally, the non divergence of the flow, (i.e. $\partial_x u + \partial_y v + \partial_z w = 0$) implies that advection terms can be rewritten as follows:

$$-(\partial_x u T + \partial_y v T + \partial_z w T) = -(\partial_x u (T - T_0) + \partial_y v (T - T_0) + \partial_z w (T - T_0)) \quad (\text{II.12})$$

with T_0 any arbitrary function of time only. A judicious choice for T_0 when studying the heat budget over a control volume \mathcal{V} is (Lentz, 1987; Montgomery, 1974):

$$T_0(t) = \frac{1}{V} \iiint_{\mathcal{V}} T(x, y, z, t) dV \quad (\text{II.13})$$

This is because, when volume averaging, every RHS term of Eq. (II.12) can be rewritten as a flux of tracer $(T - T_0)$ across \mathcal{V} interfaces, hence advection terms only contribute to the heat budget if/where they transport temperature anomalies. Compensations between the three terms are thus strongly reduced (see supplementary material section 1). Advection terms of the volume average budgets described in section 2.5.2 are computed following this procedure.

2.2.8 Melax buoy data

In order to evaluate the model ability to reproduce shelf dynamics at seasonal and sub-seasonal time scales, we use in situ measurements from Melax mooring located over the shelf in ~ 35 m water depth at $14^\circ 20.8' \text{N}$ - $17^\circ 13.68' \text{W}$. An array of thermistors measured temperature at 11 depths every 30 s. An upward looking ADCP measured bottom temperature and horizontal current vertical profiles every 90 min with a vertical resolution of 1 m. The time series analyzed in this work extends from 11 February 2015 to 26 April 2016. For the sake of simplicity and given our interest in time scales of at least a few days, we degrade the temporal resolution of the data to 1 day. More details on data processing/availability and mooring characteristics are provided in Appendix B and in Tall et al. (2021), respectively.

2.3 Model evaluation with in situ buoy measurements

2.3.1 Depth averaged currents

The model climatological and synoptic simulations are evaluated against in situ measurements at Melax. Following McCabe et al. (2015), we start by the simple comparison between modeled and observed daily depth averaged horizontal currents in March. The direction and intensity of the model currents is qualitatively consistent with observations (Fig. II.4). Moderate biases are nevertheless noticeable, most conspicuously the lack of flow variability when climatological forcings are used. Including synoptic forcings leads to a much improved data/model agreement, as expected. Another bias is the overly intense southward flow in the model. Despite the fact that synoptic events do not change the averaged forcing, their incorporation also reduces (but does not entirely remove) this mean flow bias, for reasons that we clarify in section 2.4.4. Importantly, note that wind relaxation appears necessary to produce barotropic poleward flows in CROCO (compare Figs. II.4a and II.4b) but not in the ocean at Melax. This discrepancy may arise from the fact that: relaxation and upwelling conditions are less easily separated than in our idealized setting; our simulations ignore oceanic variability remotely generated outside our model grid. This being said, model and in situ data exhibit considerable variability in along-shore velocity for relaxation and intensification conditions (e.g., velocities $\approx -0.3 \text{ m s}^{-1}$ during relaxations).

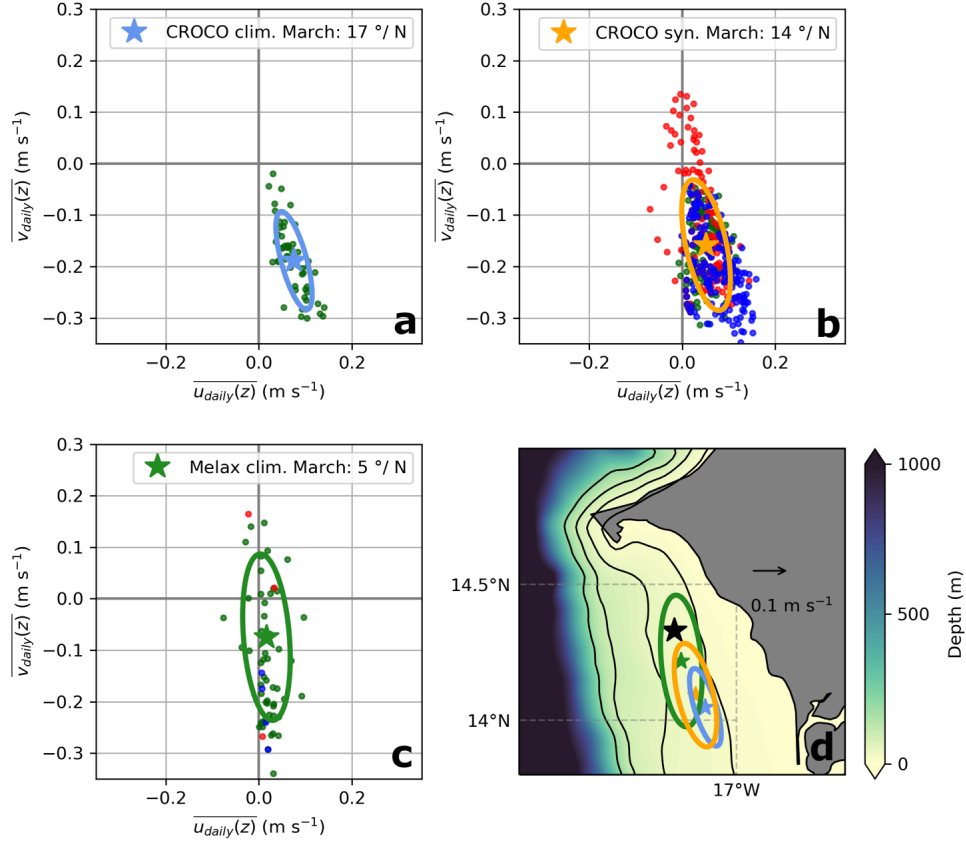


Figure II.4: (u, v) depth averaged currents in: a) CROCO climatological simulations, b) CROCO synoptic simulations and, c) Melax (2015-2016 observations). Each dot corresponds to one daily mean (5 days mean in panel a) current value for the month of March. The center of each ellipse materialized with a star indicates the mean current averaged over each available day while its semi-axes indicate the maximum and minimum variance. The angle between the ellipse major axis and North is indicated on top of each panel. In b) and c), blue (resp. red) dots correspond to daily currents at wind intensification (resp. relaxation) times. Ellipses are all repeated for comparison in panel d, with the location of Melax (black star) as the origin ($u = v = 0$).

2.3.2 Temperature vertical structure during synoptic events

The compositing method applied to ERA5 (see section 2.2.2) is applied to Melax data. Wind measurements are used to identify synoptic relaxations and intensifications. Because we run idealized simulations, the model lacks variability and cannot reproduce the complexity of the real ocean. None exactly resembles our idealized events and most differ in important ways. Thus, we limit ourselves to a qualitative assessment of the model resemblance to observations during one intensification and one relaxation having wind anomaly extrema consistent with those of our synthetic forcings (Fig. II.5). Noticeable model/data differences are found in terms of overall wind forcing history (pre-intensification winds below average for the selected intensification event; absence of return to average wind conditions for the selected relaxation event),

and initial ocean stratification. However, we note qualitative model-data agreement on synoptic thermal evolution including SML depth, and even on the magnitude of the temperature response to the first part of the relaxation event. Note that SML mean depth and its seasonal variability in our climatological simulations (~ 18 m; Feb.-May) is roughly consistent with Melax observations (~ 14 m; note that including chlorophyll shading (Echevin et al., 2021) reduces the model SML depth to 16 m; not shown).

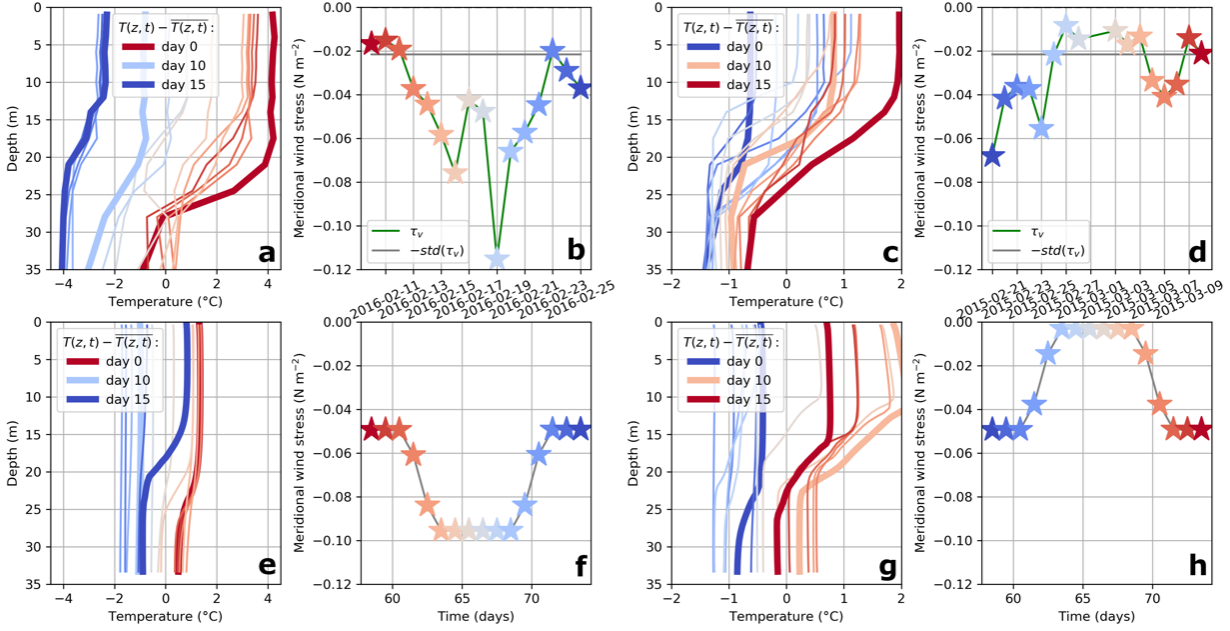


Figure II.5: Temperature anomaly profiles (panels a, c, e, g) and wind evolution (panels b, d, f, h) during intensification (panels a, b, e, f) and relaxation events (panels c, d, g, h). The upper (resp. lower) row corresponds to Melax observations during two carefully chosen events (resp. to ensemble averaged model solutions at Melax). The color codings of temperature profiles and of the wind time series are identical, which provides a time information to the former.

2.4 Synoptic SSUS dynamics

The circulation and thermohaline structure of the SSUS in response to synoptic forcing is not completely reorganized but important modulations are found in terms of horizontal patterns and vertical structure. A careful evaluation of temporal evolutions also reveals asymmetrical responses between SF^+ and SF^- . The impact on the submesoscale variability is assessed.

2.4.1 Surface patterns of change

Patterns of change are generally consistent with expectations from theory. Over the southern Senegalese shelf, stronger (resp. weaker) winds lead to decreasing (resp., increasing) SSH and SST, and increasing southward (resp. decreasing southward or even reversing) flow (Figs. II.6, II.7). SSH and SST patterns of change are very robust except SST's during relaxation

over the deeper part of the shelf. Over most of the shelf the SSH field has returned to near-climatological conditions for the period corresponding to days 19-22. This is less true for SST which exhibits anomalies whose magnitude remains comparable to that found during days 6-9, in particular for the relaxation experiments.

Examination of Figs. II.6,II.7 (see also Figs. S2-3) also reveals the presence of mesoscale circulation features. In all simulations, an anticyclonic circulation tends to dominate the area just southwest of Cape Verde. This circulation is being reinforced during the active period of SF^+ (days 6-9) but this is a transient feature that is no longer visible at later times, hence is not associated with a coherent structure. On the other hand, SF^+ and SF^- each lead to the development of a relatively robust cyclonic eddy-like structure. For SF^+ , the cyclonic feature becomes visible at days 14-15. It remains centered around 13.5°N while progressively drifting offshore. This cyclone carries upwelled shelf waters and brings them offshore (see Fig. II.7b). For SF^- , the cyclonic structure is already visible at days 6-9. Its center is located at 17.6°W-14.25°N, near where the above-mentioned anticyclonic circulation is generally located. This cyclone is associated with an offshore flow between Cape Verde and 14.5°N. It subsequently drifts northward and hugs the Cape Verde peninsula around day 10, i.e., when normal upwelling winds resume. It is then absorbed/incorporated in the ensuing negative SSH anomalies and is transported offshore.

Examination of each individual SF^+ and SF^- run confirms this tendency to form cyclones made of recently upwelled shelf water and shed them offshore when winds relax, i.e, in the early part of SF^- and in the late part of SF^+ but with noticeable variations between ensemble runs. Shape, intensity and exact offshore and alongshore location of these cyclonic features vary depending on the eddy field configuration over the continental slope and their evolution during the synoptic experiment. When large mesoscale features are present off the SSUS the formation of cyclones can even be inhibited. Cyclones produced in SF^- tend to be smaller, less robust, and more frequently absent in the different runs (compare robustness information in Figs. II.6b and f). We relate this to the fact that there must be more available potential energy (i.e., cold upper ocean water) in SF^+ shortly after the upwelling wind intensification than there is in SF^- at the beginning of the relaxation. This description of the mesoscale field is helpful to understand some of the fine-scale features present in the SST field (see Figs. S2-3).

Vertical velocities at the base of the SML is an instructive field indicative of where upwelling takes place. Fields shown in Fig. II.8 are quite noisy because averaging is performed over periods of a few days only. Nevertheless, the region within 25-50 km of Cape Verde systematically emerges as the place where largest vertical velocities occur (in agreement with Ndoye et al. (2017)), and also where the modulation of their intensity by SF^+ and SF^- is most noticeable.

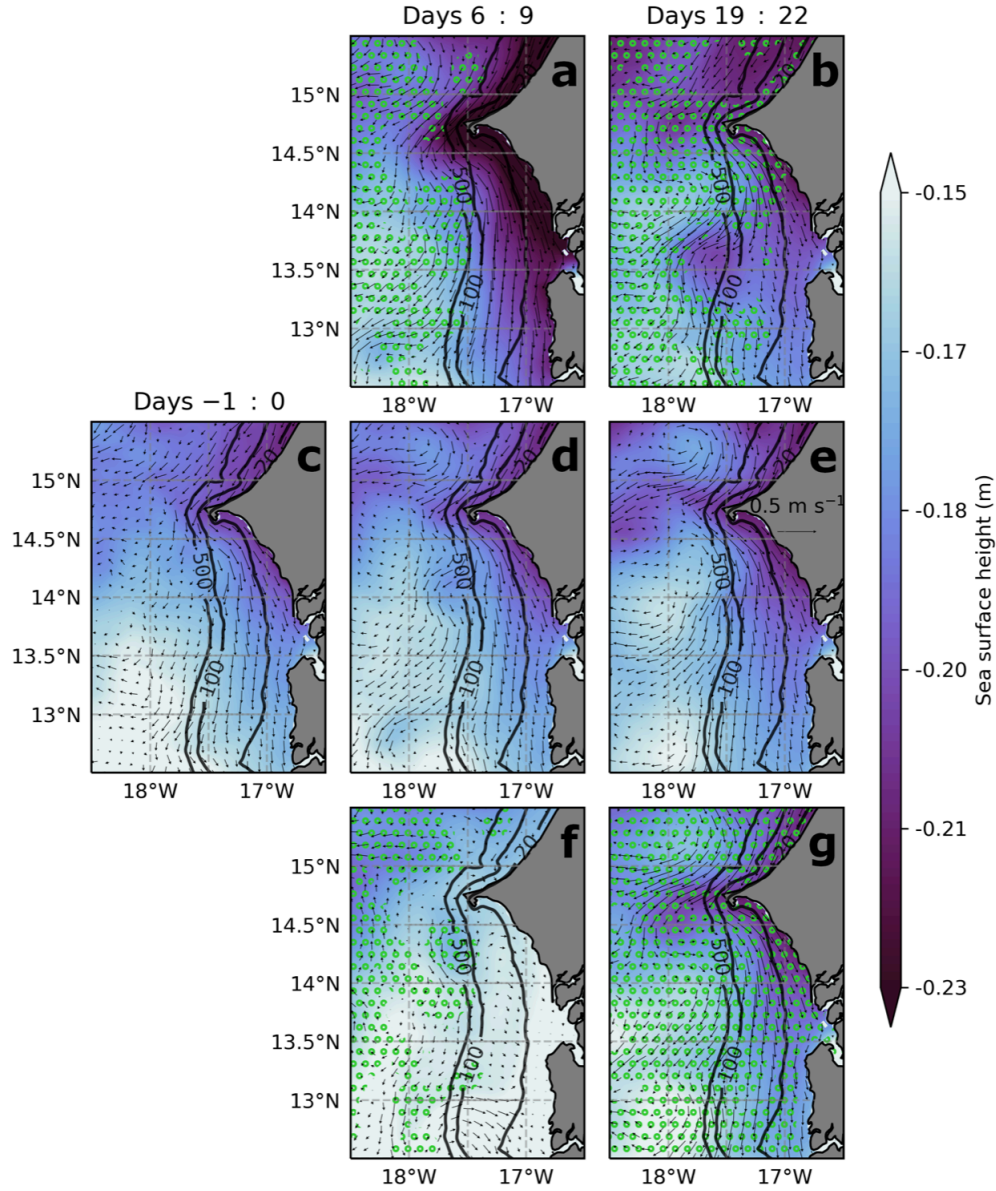


Figure II.6: Ensemble averaged fields of SSH (color) and surface velocity (arrows) for SF^+ (upper row), SF^0 (middle row) and SF^- (lower row). From left to right, the three columns correspond to the three periods before (average of day -1 to day 0; see timeline and date reference in Fig. II.2e), during (days 6 to 9 included) and after (days 19 to 22 included) the synoptic event. For SF^+ and SF^- panels, light green circles indicate locations where not all ensemble members agree on the sign of the SSH anomaly relative to SF^0 (see section 2.2.5).

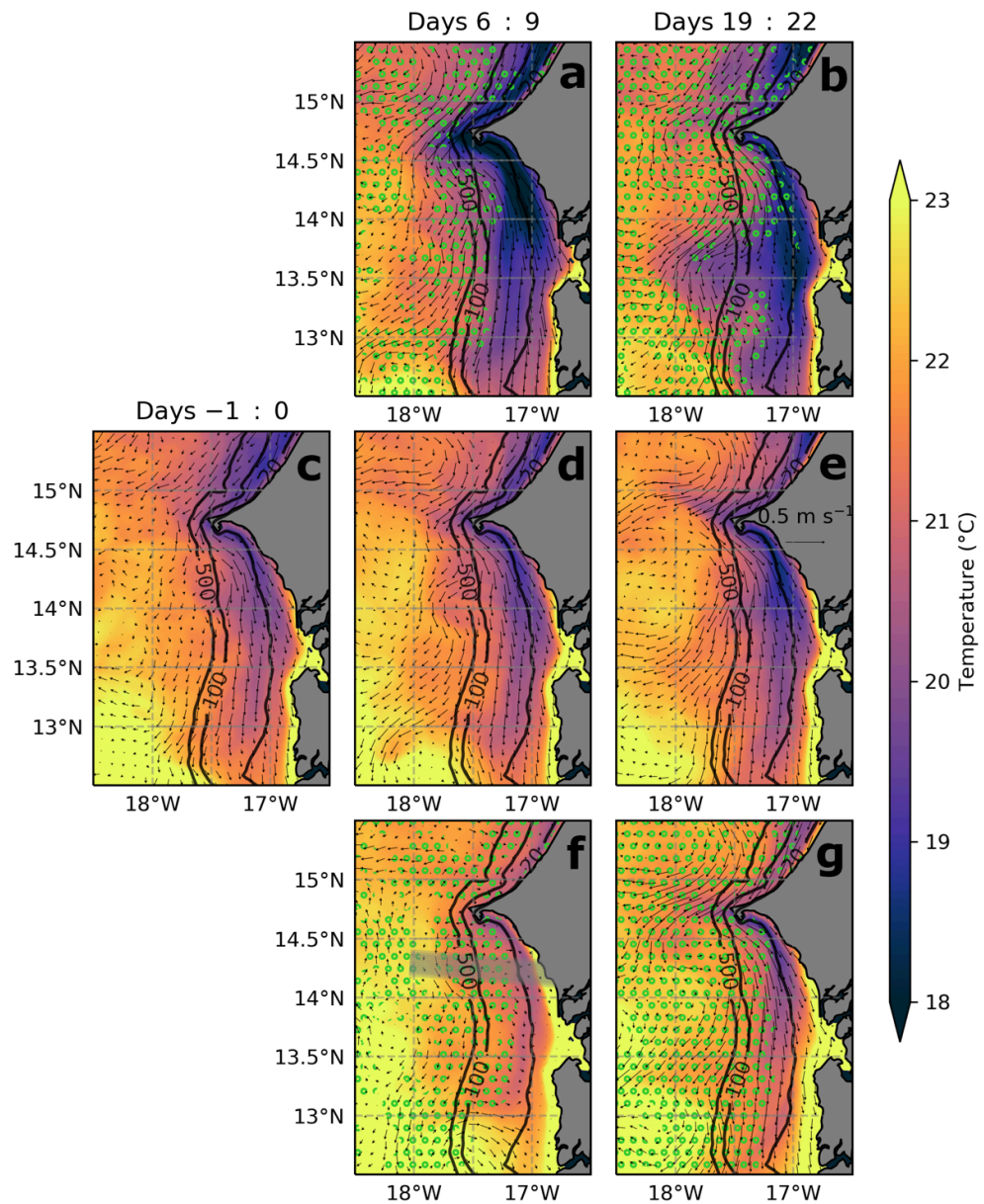


Figure II.7: Similar to Fig. II.6 but for SST. The grey shading in panel f represents the sector over which along-isobath averaging is performed to obtain Fig. II.9.

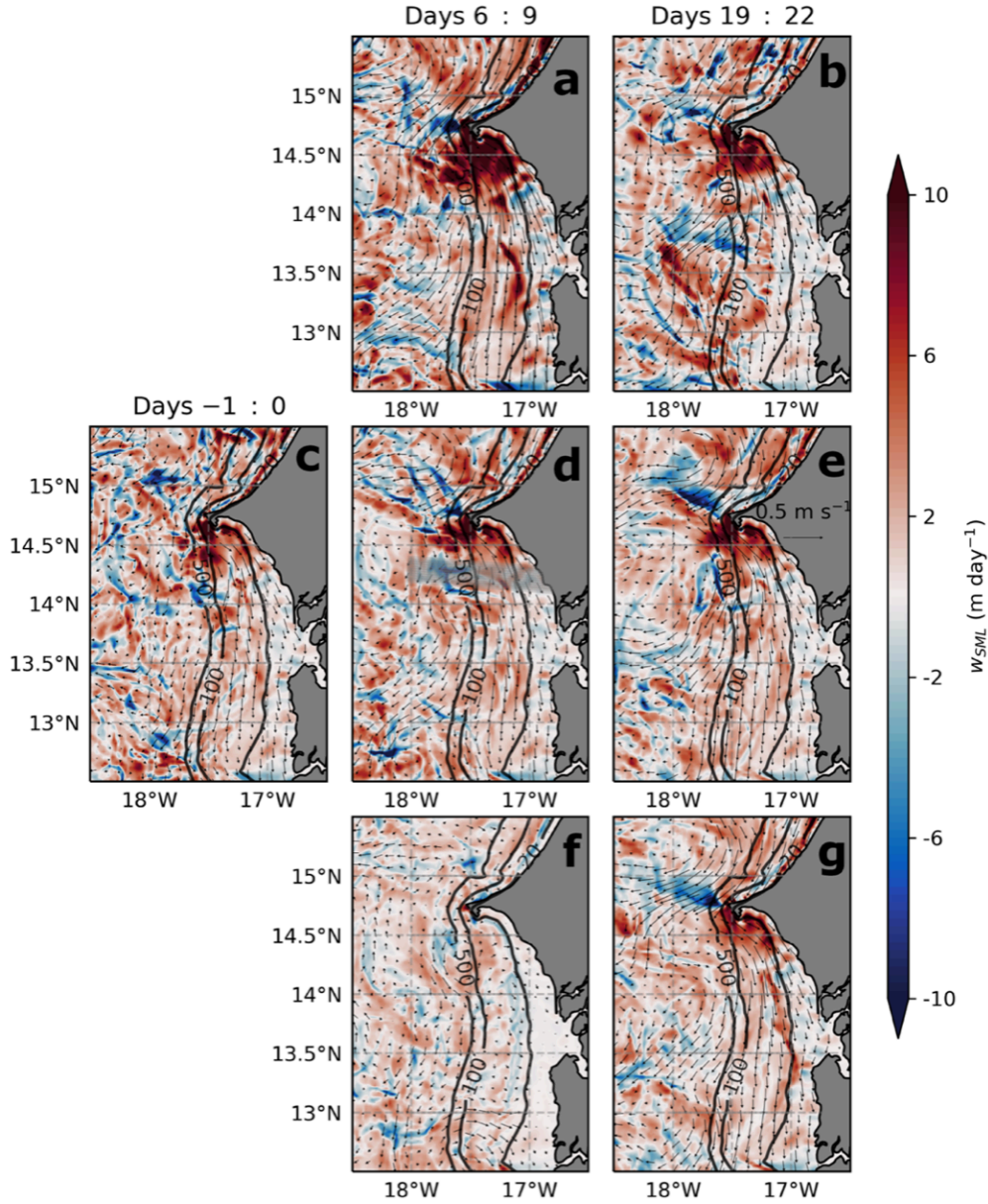


Figure II.8: Same as Fig. II.6 for vertical velocities at the mixed layer depth.

2.4.2 Vertical structure

The vertical structure of the dynamical response is described using cross-shore transects of temperature and meridional velocity (ensemble and alongshore averages, Fig. II.9). We start with a brief characterization of the climatological state: SML depth ~ 30 m thick; offshore and coastal SST $\sim 21^\circ\text{C}$ and 19.5°C , respectively (Fig. II.9c); shoaling of isopycnals from offshore to nearshore of the order of 30 m; extension of the offshore equatorward upwelling jet (defined by the 0.1 m s^{-1} isotach) from the coast to ~ 60 km offshore (near 17.5°W); presence of a subsurface poleward current located offshore of 17.4°W and below ~ 40 m depth; positive vertical velocities ($v \sim 2 \text{ m day}^{-1}$) below the SML. All this illustrates the relative weakness of the southern Senegal upwelling in comparison to other well-known sectors where isopycnal tilts, across-shore temperature/density contrasts, and vertical velocities can be much greater (e.g. Renault

2. Impact of Synoptic Wind Intensification and Relaxation on the Dynamics and Heat Budget of the South Senegalese Upwelling Sector: JPO manuscript

et al. (2021) in the California upwelling system). Our average synoptic intensification SF^+ (resp. relaxation SF^-) has a moderate influence on thermohaline structure and circulation: temperature decreases (resp., increases) by 1.5°C ; the SML deepens to 35 m (resp. shoals to 20 m; see Figs. II.9a and f); the upwelling jet extension deepens and expands offshore ~ 80 km (resp. shoals and contracts inshore).

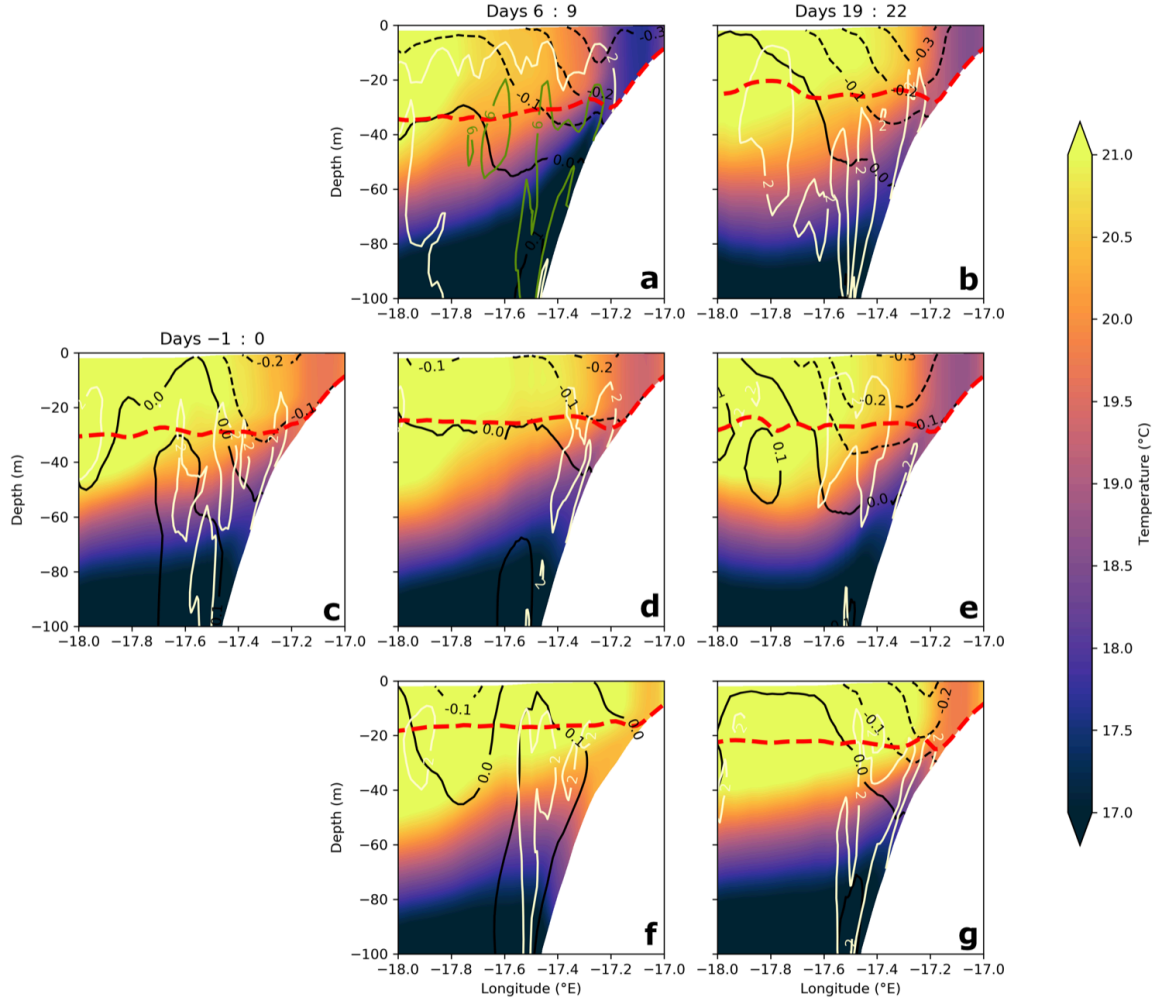


Figure II.9: Across-shore vertical section of temperature (color), surface mixed layer depth (red dashed line), meridional currents (black contours, in m s^{-1}) and vertical velocities (white and green lines indicate isolines 2 and 6 m day^{-1}). Fields are ensemble, alongshore and time averaged. Alongshore averaging is carried out in the grey box represented in Fig. II.7f using a regridding from longitude to ocean depth. SF^+ (upper row), SF^0 (middle row) and SF^- (lower row) evolutions are shown.

As for vertical velocities, their change for SF^+ is substantial with a 100% increase to $\sim 6 \text{ m day}^{-1}$ (Fig. II.9a) and the presence of upward velocities all the way to 18°W . A reduction of w during SF^- exists but it is more difficult to evaluate in Fig. II.9f because the alongshore averaging sector is at the edge of the upwelling/large w patch (see Fig. II.8d).

The inner shelf is typically defined as the region where the surface and bottom boundary layers are coalesced and the water column is fully mixed. The outer edge of the inner shelf is important dynamically and also for the ecosystem. Its location varies from 17.2°W at days 6-9 during SF^+ to 17.1°W at days 6-9 during SF^- .

2.4.3 SSUS-scale temporal evolutions

Quantities represented in Fig. II.10 (SST, SML depth, w at the mixed layer base, and u, v at the ocean surface) are spatially averaged over BoxN (see section 2.2.4, Fig. II.1b) where upwelling dynamics is prevalent. Some findings presented above in relation to Fig. II.9 are also visible in Fig. II.10 (e.g. magnitude of changes in SST $\sim \pm 1.5^\circ\text{C}$) but the latter provides detailed insight in the system temporal responses, e.g., the precise SSUS-scale changes in SML depth (~ 3 m with an asymmetry between SF^+ and SF^- discussed below) or the major changes in surface velocity magnitude during the synoptic events. In agreement with the study of Gan and Allen (2002a), these velocity changes are associated with important modifications in alongshore pressure gradient (not shown).

We note a clear distinction between SST, which seems still away from equilibrium state toward the end of SF^\pm (day 8) and all the other variables which exhibit plateaus between day 3 and 8, albeit less clearly so for u_{surf} and SML depth. This particularity reflects the long inertia of thermal exchange processes. In sensitivity runs with a longer synoptic intensification plateau (16 instead of 6 days for T_p) SST does not decrease after day 10. This is a useful information on the time scale of the system thermal response which is thus ~ 10 days. Momentum adjustments typically need ~ 1 inertial period T_f (2 days) and are therefore faster, as confirmed by Figs. II.10d,e.

SST response is also specific in that the rate of change is larger during the spin-up (peak reached in ~ 7 days) than during the spin-down phase (near-return to climatology in ~ 12 days), particularly for SF^- . We will return to this point in sections 2.4.2.4.4, 2.6 and 2.7. Also, note that the return to climatology of v_{surf} is ambiguous toward day 22 when a small downward trend is still visible. We interpret this as a consequence of the climatological wind evolution during the month of March (see Fig. II.2e). Except for SML depth, intrinsic variability is systematically less than the forced response at its peak during SF^\pm .

2.4.4 Intensification-relaxation asymmetries and the net effect of synoptic wind events

Quantifying the asymmetries between intensification and relaxation is an important objective of this study because it provides useful insight into the rectification effects induced by synoptic variability of wind forcings (note that modeling studies have frequently been performed using monthly climatological forcing devoid any synopticity, e.g. Marchesiello et al. (2003); Penven et al. (2005)).

The relative importance of the asymmetry \mathcal{R}_{SF} (see section 2.2.6) is indicated for each variable plotted in Fig. II.10. SST presents rather minor asymmetries that develop after the peaks of forcing anomalies (Fig. II.10a). They concern the time of peak ocean anomaly (day 9 for intensification and day 10 for relaxation) and time to near-return to climatology (\sim day 20 and beyond day 22, respectively). The latter asymmetry is observed at late times when climatological air-sea heat fluxes have changed substantially (see Fig. II.2e).

Despite noticeable $\text{SF}^+ - \text{SF}^-$ asymmetries in SML depth anomaly (resp. $+2$ and -4 m), \mathcal{R}_{SF} remains limited (6%). This is because the SML depth synoptic anomalies are much smaller than the climatological signal ($\text{SML}_{SF^0} \sim 17$ m). Asymmetries in w_{SML} (3%) and u_{surf} (8%) are

2. Impact of Synoptic Wind Intensification and Relaxation on the Dynamics and Heat Budget of the South Senegalese Upwelling Sector: JPO manuscript

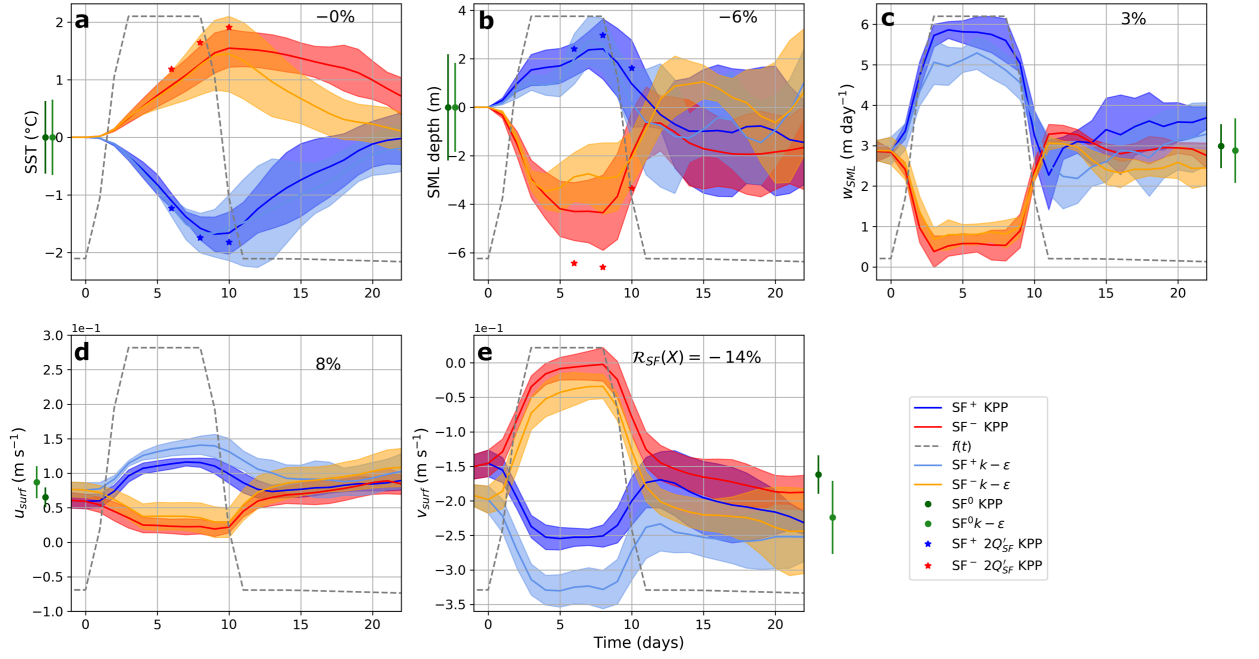


Figure II.10: Time series of a) SST anomaly b) SML depth anomaly c) vertical velocity at the base of the SML d) surface zonal and e) meridional velocity for SF^+ and SF^- runs. Variables are ensemble and spatially averaged (over BoxN; see Fig. II.1b). Blue (resp. red) lines correspond to SF^+ (resp. SF^-). Dark (resp. light) tones are for KPP (resp. GLS $k-\epsilon$) ensembles. Anomalies are relative to SF^0 . Red and blue stars in panels a) and b) indicate values found at days 6, 8, and 10 for the simulations forced with double heat flux anomalies ($2 Q'_{SF}$). Green dots and bars left or right of the figure box represent respectively the averages and the intrinsic variability levels computed as plus/minus the maximum standard deviation (std) between day -1 and day 22 in the ensemble run SF^0 . Dark (resp. light) green is for simulations with KPP (resp. GLS $k-\epsilon$) turbulence submodel. SML depth is diagnosed based on a density threshold for simulations with GLS $k-\epsilon$. It is computed internally when using KPP but using the same threshold-based method only makes minute differences. Shaded envelopes represent the standard deviation computed each day from the different ensemble members. The grey dotted line represent the shape of synoptic forcing anomaly (i.e., $f(t)$; see section 2.2.3). Percentages in the upper right corner of each panel indicate the relative importance of the asymmetry between SF^+ and SF^- , $\mathcal{R}_{SF}(X)$ (see definition in section 2.2.6). Note that the amplitude of the y-axis range is similar in panels d and e.

also limited. The largest SF^+ - SF^- asymmetry is found for meridional surface velocities whose anomalies are respectively 10 and 15 cm s^{-1} (see Fig. II.10), which yields $\mathcal{R}_{SF} = -14\%$. Underlying processes are discussed in section 2.7.

In Fig. II.11, we show the spatial structure of the $RES_{SF}(v)$ field at the ocean surface and that for a cross-shore vertical section (with some alongshore averaging, see section 2.2.4). Between CV and 14.25°N, quasi barotropic poleward residual currents with magnitude $\sim 0.05\text{--}0.1 \text{ m s}^{-1}$ are manifest. Their tendency is to oppose the southward climatological flow which improves the comparison with observations (section 2.3).

A more subtle class of asymmetries concerns the robustness of the ocean response (i.e., the relative importance of forced deterministic versus intrinsic response), which we describe for SST and SSH. During SF^+ intensification phase, SSH/SST patterns are robust over most of the shelf (excluding limited areas near the shelf break for SST) while this is only true for SSH during the SF^- relaxation phase. For SST, relaxation is associated with more ensemble run variability

except over the inner shelf (compare Figs. II.7a,f). At later times ($t > \text{day } 9$), the robustness of the SSH patterns decreases more rapidly for SF^- than for SF^+ (Figs. II.6a,b versus II.6f,g). The evolution is opposite for SST (Figs. II.7a,b versus II.7f,g), i.e., the ocean response appears more deterministic for SF^- than for SF^+ , in agreement with Fig. II.3b. All this reveals the importance of intensifying winds (during the early part of SF^+ and the late part of SF^-) in deterministically organizing the SST field, and thus contribute to asymmetries.

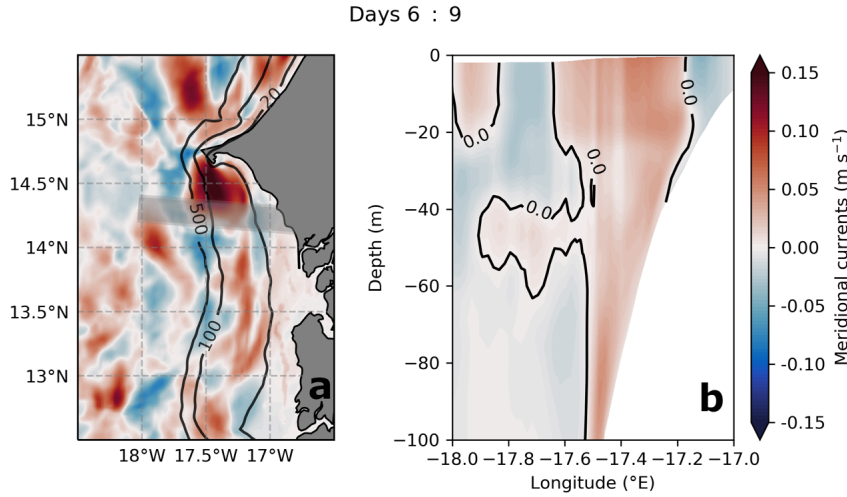


Figure II.11: Surface slice (a) and vertical-across-shore section (b) of ensemble, alongshore, and time averaged meridional current residual $RES_{SF}(v)$ (see definition in section 2.4.4). Time (resp. alongshore) averaging is performed between days 6 and 9 included (resp. over the sector shaded in grey in panel a).

2.4.5 Impact on the submesoscale variability

Frontal processes (i.e., submesoscales) have typical time scales of the order of a few days (McWilliams, 2016). This is similar to the time scales associated with our synoptic fluctuations. Moreover, proximity to the coastline and rapid changes in bathymetry make identification of submesoscale through spatial filtering challenging. It is thus impractical to extract synoptic modulations of the submesoscale activity by applying spatio-temporal filters on quantities like density or lateral velocities, e.g., as done in Capet et al. (2008b). Instead, we diagnose the RMS vertical velocities w_{SML}^{RMS} , a well-known faithful indicator of submesoscale (Lévy et al., 2001; Lapeyre and Klein, 2006; Capet et al., 2008b). This quantity is computed over the southern box (see BoxS in Fig. II.1b). Excluding the northern part of the SSUS ensures that upwelling vertical velocities are absent so that w_{SML}^{RMS} is considered a proxy for submesoscale turbulence. The strength of surface fronts and submesoscale activity is generally enhanced when conditions favor intense baroclinic instability, i.e., in the presence of strong regional-scale density contrasts and, most importantly, of deep SML (Fox-Kemper et al., 2008). This is also true over continental shelves, except for their shallowest part where bottom friction damps submesoscales very effectively (Capet et al. (2008a); see also Hetland (2017); Kobashi and Hetland (2020) in the context of river plumes).

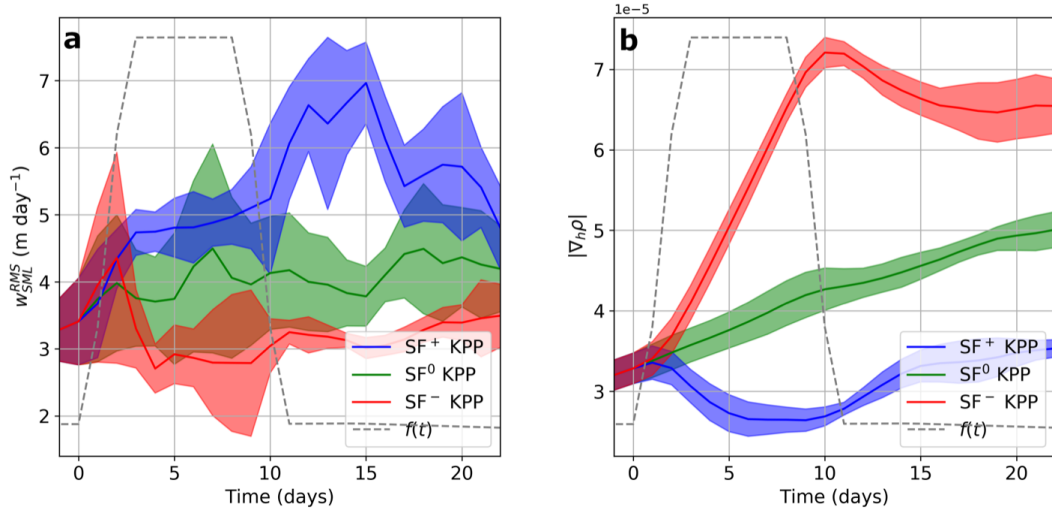


Figure II.12: a): Vertical velocities at the base of the SML. b): horizontal density gradient magnitude $|\nabla_h \rho|$. Both quantities are averaged over BoxS (see Fig. II.1b) and represented for SF⁺ (blue), SF⁰ (green) and SF⁻ (red). Shaded envelopes indicate the ensemble standard deviation.

A reduction $\sim 30\%$ of w_{SML}^{RMS} is observed during SF⁻ (the small initial increase at days 0-3 also found in SF⁰ is not considered statistically meaningful). Conversely, submesoscale activity is increased by $\sim 20\%$ during SF⁺ compared to climatological conditions (Fig. II.12a). Even larger departures are found at later times with a peak $\sim +100\%$ at day 15 and w_{SML}^{RMS} significantly above the climatological values until day 22.

The early part is consistent with changes in SML depth but the later part is not. Examination of w_{SML} fields at day 15 of individual runs reveals an alternating positive-negative w pattern, as typically associated with frontal intensification by mesoscale stirring (Wang, 1993). It is moreover systematically located at the northern edge of the mesoscale cyclone described in section 2.4.1 and thus intimately tied to the lateral offshore export of cold upwelling water that follows SF⁺. Likewise, the weaker cyclone produced during SF⁻ also leads to enhanced w_{SML} in its vicinity, albeit with less sharp structures. All this illustrates the subtlety of the relationships between forcings and fine-scale coastal ocean response, and in particular the possible existence of time lags of a few days between their respective evolutions. Another subtlety concerns the apparent SSUS scale decoupling between the evolutions of w_{SML}^{RMS} and $|\nabla_h \rho|$ (compare Figs. II.12a and b). We attribute this to the overwhelming importance of temperature contrasts in the inshore band where friction inhibits the classical expression of frontogenesis. Specifically, we find that, in BoxS, averaged $|\nabla_h \rho|$ is ~ 3 times stronger inshore of the 15 m isobath compared to offshore. The heat budget analysis presented below adds further support to the fact that, despite the noticeable response of w_{SML}^{RMS} after SF⁺, the modulation of SSUS submesoscale by synoptic events is modest.

2.5 Mixed layer heat budget

Considering the vertical velocities, surface current and SST patterns, we hypothesize that the northern part of the shelf (BoxN in Fig. II.1b) is the preferential location where upwelling of cold waters occurs (Ndoye et al., 2017). To qualify this and more generally gain insight into the respective roles of the different processes in warming/cooling during synoptic events, we carry out a SML heat budget (see section 2.2.7) over various areas of the shelf. In all simulations (SF^\pm and SF^0), vertical mixing and entrainment are of secondary importance. Our focus is thus on air-sea heat exchanges (FORC), advection terms ($ADV=HADV+VADV$) and the heat rate of change (RATE) which is approximately equal to the sum.

2.5.1 Spatial structure

Figs. II.13-II.15 show FORC, ADV and RATE for SF^0 , SF^+ and SF^- respectively. In all three cases, the inner shelf is characterized by robust FORC (resp. ADV) warming (resp. cooling) contributions, albeit less so for SF^+ (resp. SF^- , note the weak warming patch between 13.5-14°N for days 6-9, see Fig. II.15a). This contrasts with the situation found over the mid- and outer shelf where tendency terms are uniformly small (FORC) or spatially variable (ADV). The FORC warming pattern is due to the spatial structure of the air-sea heat flux forcing field (not shown), and not to spatial differences in how shortwave heat flux is distributed vertically between the mixed layer and the subsurface. Note that nearshore air-sea heat flux warming arises from the SST bias correction terms m_2 and m_{2adj} present in Eq. (I.6). Our experience at sea in the region suggests that this may be a realistic feature associated with coastal wind drop off that is absent in existing wind reanalyses products; not accounted for in large scale air-sea heat flux products such as COADS used in m_1 ; but recovered thanks to the bias correction terms.

During the intensification part of SF^+ , FORC is, by construction, reduced compared to climatological conditions (see Fig. II.2b). However, the cooling tendency observed in RATE at days 6-9 is dominated by changes in ADV, which becomes strongly negative over most of the shelf. After the intensification, ADV cooling is restricted to a small inshore portion of the shelf while ADV warming has a major influence on the heat budget between 13.5-14.75°N. However, this warming tendency at days 19-22 is also found in SF^0 , and to a lesser extent SF^- (in which the latitudinal extent of the warming patch is much reduced). Thus, this warming pattern in SF^+ reflects not only a post-synoptic event adjustment but also the spring seasonal warming trend present in the climatology of air-sea heat fluxes (Fig. II.2e).

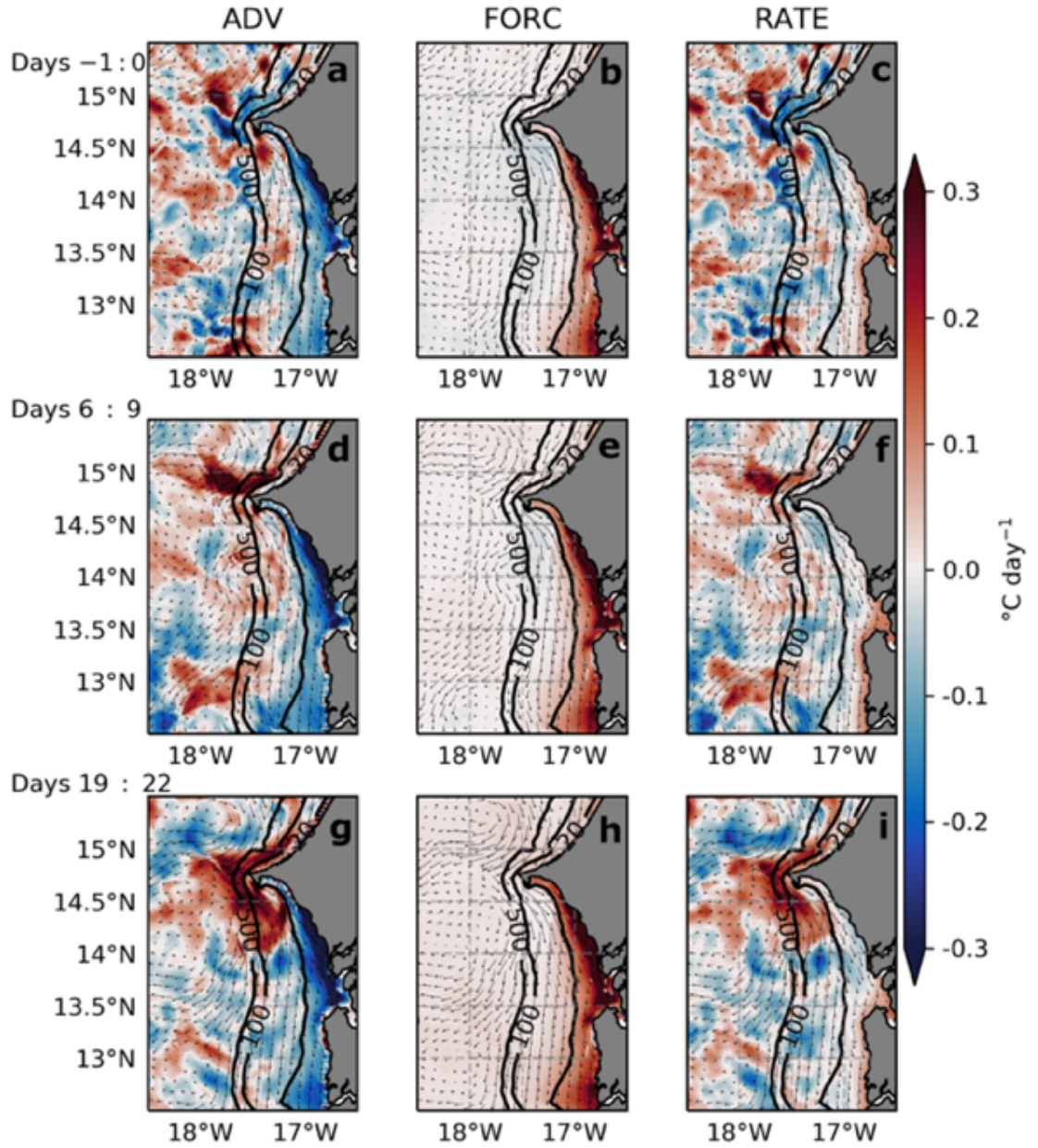


Figure II.13: Ensemble averaged SF^0 advection (left column), atmospheric forcing (middle column) and heating rate (right column) terms as defined in Eq. II.11 (in $^{\circ}\text{C day}^{-1}$). Surface velocities are also shown (arrows). The three rows are for the same three time windows used in Fig. II.6 and II.7 (days -1 to 0, 6 to 9 and 19 to 22 from top to bottom).

During the relaxation, advection brings heat over most of the shelf except for a tiny inshore sector (Fig. II.15a, 14-14.6°N) where ADV cooling persists. There, the SML is strongly warmed by the atmospheric forcing (Figs. II.15b,e). When the relaxation stops, heating from the atmosphere slightly decreases but advection is the dominant cooling driver (Fig. II.15d) that brings SML temperature back to climatological conditions.

A contribution due to restratification by submesoscales is presumably hidden in ADV (except over the inner shelf where frontal processes are strongly damped). But we do not find any indication that it differs between SF^+ and SF^- , in agreement with the modest response of the submesoscale presented in section 4e.

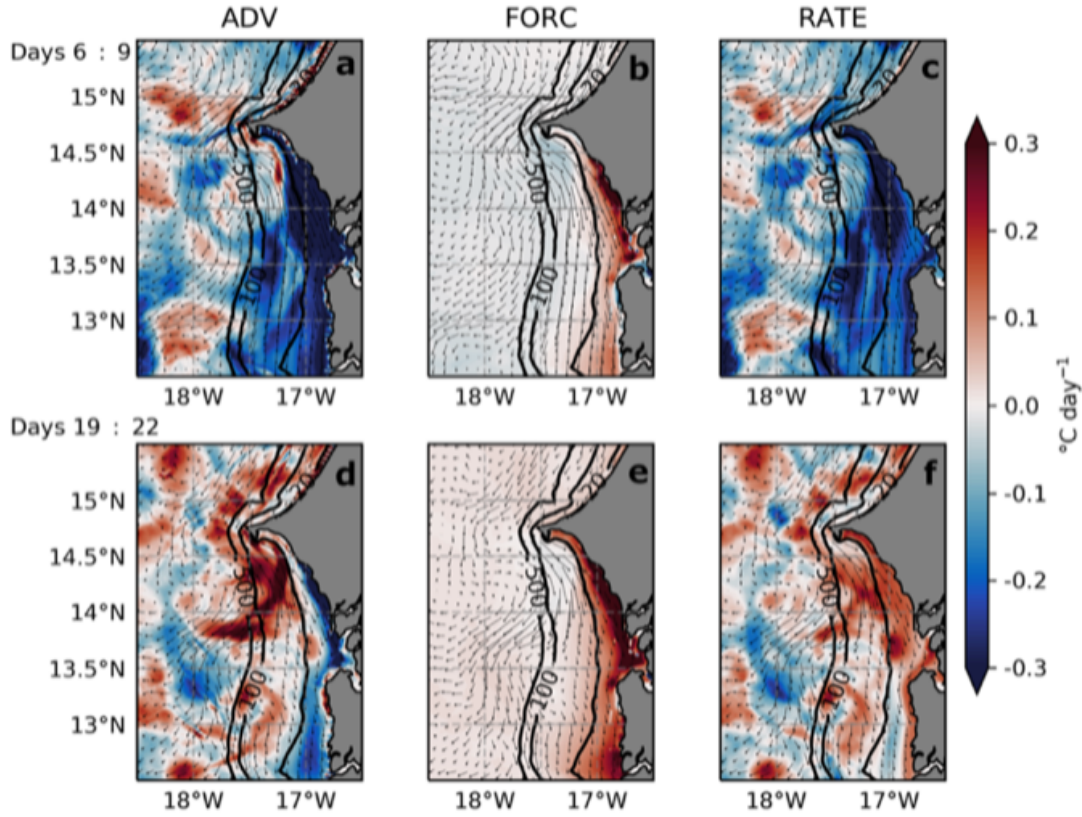


Figure II.14: Same as Fig. II.13 for SF^+ . Averages over the time window before the synoptic anomaly (days -1 to 0) is as for SF^0 and is therefore not repeated (see Fig. II.13 upper row).

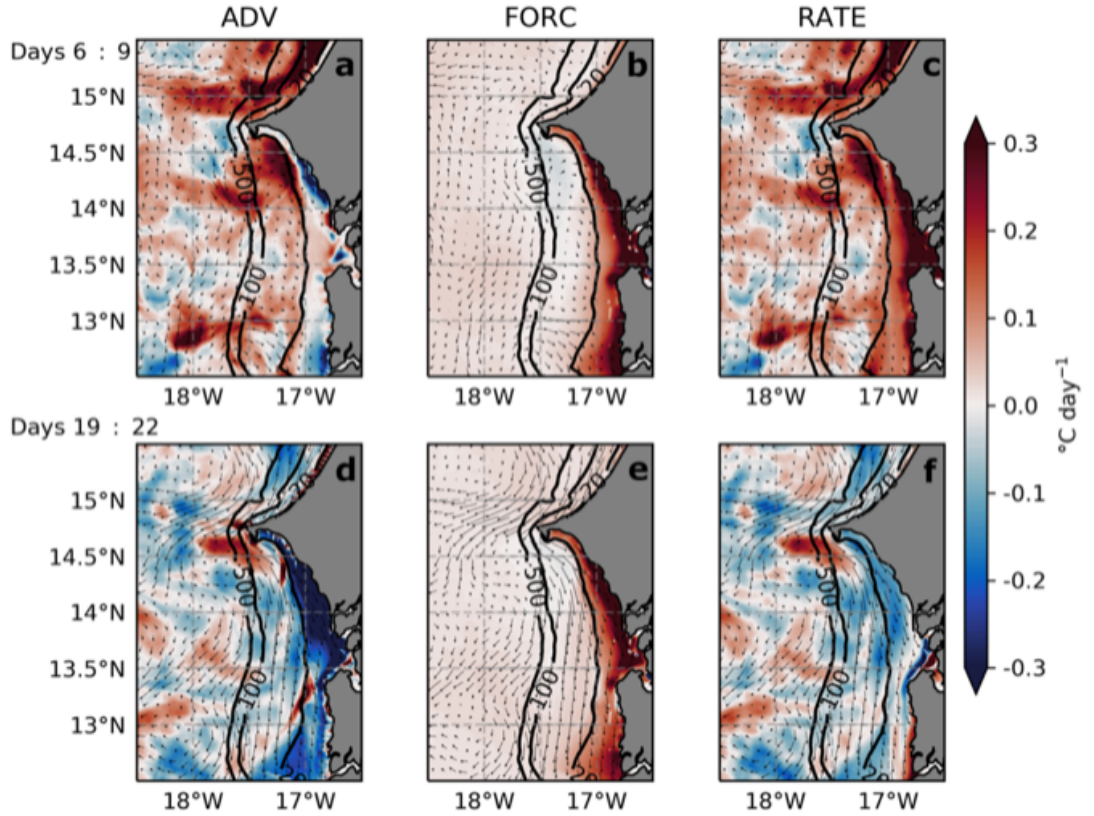


Figure II.15: Same as Fig. II.14 for SF^- .

2.5.2 Box averaged heat budget

A more in-depth analysis is now given thanks to horizontal averaging, introduction of a reference temperature T_0 , and separation of the horizontal versus vertical advection terms (see section 2.2.7). First, averaging of the SML heat budget terms is done over the northern part of the shelf (BoxN in Fig. II.1b). We start with SF^0 in which RATE is consistent with expectations (positive and increasing slightly over time, Fig. II.16a) but the relative contributions of lateral and vertical advection appear counter-intuitive for an upwelling region. Indeed, we find that lateral advection tends to cool the SML ($\sim -0.1^{\circ}C \text{ day}^{-1}$) while vertical advection is nearly zero.

During the intensification period of SF^+ (Fig. II.16b), the same general remark applies although horizontal advection cooling is intensified (to $\sim -0.2^{\circ}C \text{ day}^{-1}$) and vertical advection is weakly (but robustly) negative ($\sim -0.05^{\circ}C \text{ day}^{-1}$). Overall, RATE is dominated by HADV between days 3 and 8.

SML warming (RATE) changes rapidly toward the end of the intensification period and reaches $+0.2^{\circ}C \text{ day}^{-1}$ at day 11. An oscillatory behavior is manifest at later times. It is due to HADV and partly compensated by VADV. Examination of the lateral heat transport anomalies at the boundaries of BoxN with the help of the PAGO software (Deshayes et al., 2014; Barrier et al., 2015) (available at <http://pypago.nicolasbarrier.fr/>) reveals synoptic modulations

in the relative rates of warm water ($T > T_0$) import into and export out of BoxN. Import predominantly takes place through the northern part of the offshore boundary, whereas export predominantly takes place through the southern part of the offshore boundary and through the southern boundary (not shown). Both import and export of heat are impacted by the evolutions of the mesoscale eddy field described in section 2.4.1, which gives rise to the oscillations of RATE observed after the wind intensification period.

In first approximation, SML heat content modulation during SF^- are opposite to those found in SF^+ : increasing HADV and VADV during the relaxation part; rapid return to negative HADV around day 9-11; reduced magnitude of VADV compared to HADV. On the other hand, close examination reveals some differences in behavior: a change in the sign of VADV at day 6; relative weakness of the oscillations that follow the relaxation phase compared to those seen after the intensification in SF^+ ; differences in RATE and HADV extrema during active part of SF^+ ($-0.3^\circ\text{C day}^{-1}$ for RATE) and SF^- ($+0.2^\circ\text{C day}^{-1}$ for RATE); increase in intrinsic variability observed between days 5 to 10 (i.e., toward the end of the relaxation period) versus between days 8 to 12 in SF^+ .

The surprisingly small role played by vertical advection (Figs. II.16a,b,c) deserves further elaboration. To the readers familiar with more energetic upwelling sectors, e.g., offshore of central California or Chile, we remind that vertical velocities are weak in the SSUS, typically a few meters per day (see Fig. II.8 and also discussion in Capet et al. 2017), and do not dramatically increase with strong winds. This being said, the shape of the SSUS upwelling tongue (Fig. II.7) and the fact that the Cape Verde peninsula is effective at interrupting the alongshore flow of cold upwelling water strongly suggests that a heat sink (i.e., a source of cold water) must cool the SML south of Dakar. To confirm this and estimate the importance of this sink, we perform heat budget analyses for several BoxN-like control domains that differ by the latitude lat of their southern edge, varied from 13.5°N to 14.5°N with 0.25° increments. The northern and offshore edges of the control volumes remain fixed at 14.75°N and at the 100 m isobath respectively, as for BoxN. These boxes are designated by \mathcal{S}_{lat} (so that BoxN is \mathcal{S}_{14}) and their area is denoted S_{lat} . HADV and VADV contributions to the heat budget equation are denoted with a subscript lat and represented as a function of control volume extension in Fig. II.17.

VADV cooling is important in SF^+ and SF^0 but it is very concentrated in the northernmost part of the SSUS ($-0.1^\circ\text{C day}^{-1}$ in $\mathcal{S}_{14.5}$ for SF^+), where HADV is, conversely, a heat source (SF^- and SF^0) or negligible heat sink (SF^+). As the domain extension increases southward the magnitude of the VADV (resp. HADV) contribution is reduced (resp., increased). Precisely, HADV becomes dominant between 14.25 and 14.5°N . The negligible role of VADV cooling occurring south of 14.5°N in SF^+ is demonstrated by comparing its mean effect in $\mathcal{S}_{14.25}$ and \mathcal{S}_{14} to the effect obtained by “diluting” the VADV contribution in $\mathcal{S}_{14.5}$. Precisely Fig. II.17 shows $VADV_{14.5} \times \frac{S_{14.5}}{S_{14.25}}$. A minor contribution of VADV is still present between 14.25 and 14.5°N but most of the cooling in $\mathcal{S}_{14.25}$ (82%) actually takes place in the northernmost ocean sector $\mathcal{S}_{14.5}$. Because $VADV_{14.5} \times \frac{S_{14.5}}{S_{14.0}} < VADV_{14}$, we infer that vertical advection must overall warm the SML between 14.25 and 14°N (with an absolute magnitude equal to 25% of the cooling found in

$\mathcal{S}_{14.25}$). South of 14°N changes become small except for the role of HADV during SF^+ which keeps decreasing all the way to 13.50°N , reflecting the southward expansion of the upwelling tongue.

In the northern part of the SSUS, VADV is found to have a significant warming contribution in SF^- . Despite the limited role of frontal processes in our SSUS simulations (section 2.4.5) we see this as an evidence of baroclinic instability processes, i.e., of correlations between temperature and vertical velocity fluctuations.

Fig. II.17 also reveals the asymmetric roles played by lateral and vertical advection. The largest $RES_{SF}(VADV)$ value is found in the smallest northern box where SF^+ (resp. SF^-) has little (resp. a large) effect on VADV compared to the climatological reference (see Fig. II.17b). HADV asymmetry is distinct in behavior but also decreases as the control volume gets bigger. A modest level of asymmetry is found for $\mathcal{S}_{13.5}$. This is in apparent contrast with the results of Send et al. (1987) but consistent with the importance of alongshore heat advection in the SSUS, even during sustained upwelling conditions. Overall, our analysis demonstrates that asymmetry and rectification are strongly domain dependent.

These findings are in part dependent on the choices made when designing the idealized forcings and in particular the magnitude of air-sea heat flux anomalies (section 2.2.3), i.e., they reflect moderate amplitude spring-time synoptic events (see section 2.7 for further elaboration).

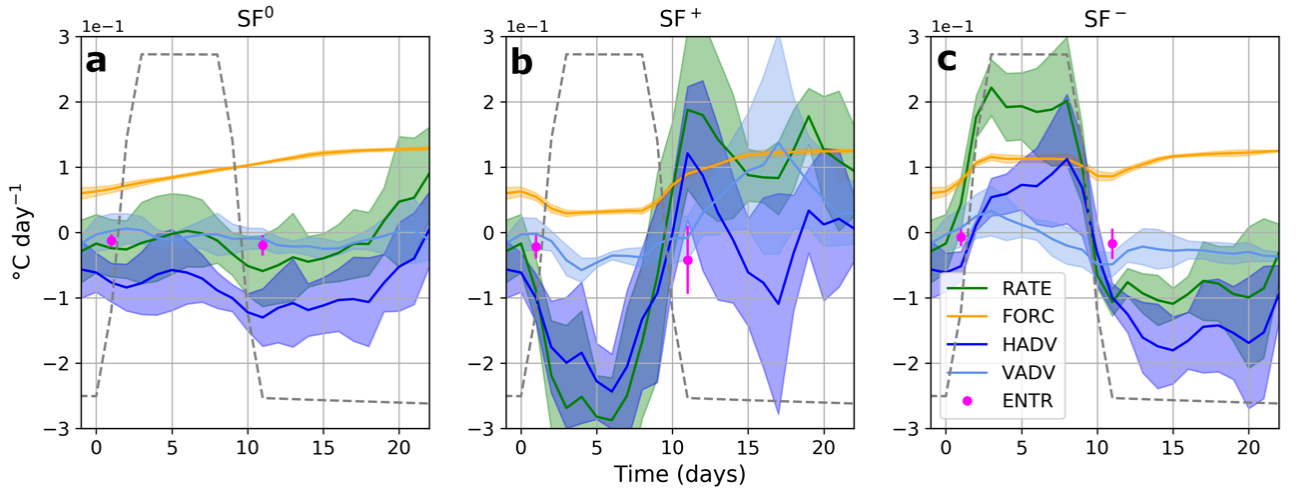


Figure II.16: Time series of ensemble and BoxN (see Fig. II.1b) spatially averaged heat budget tendency terms. Color coding of the different terms is indicated in panel c). Shaded envelopes represent the ensemble standard deviation. Panels (a,b,c) correspond respectively to SF^0 , SF^+ and SF^- . Magenta dots located at $t = 1$ day (resp. $t = 11$ days) provide entrainment (ENTR) values time averaged between day 0 and 9 (resp. day 10 and 22). The associated magenta bar represents the maximum value of the ensemble standard deviation over the corresponding time window.

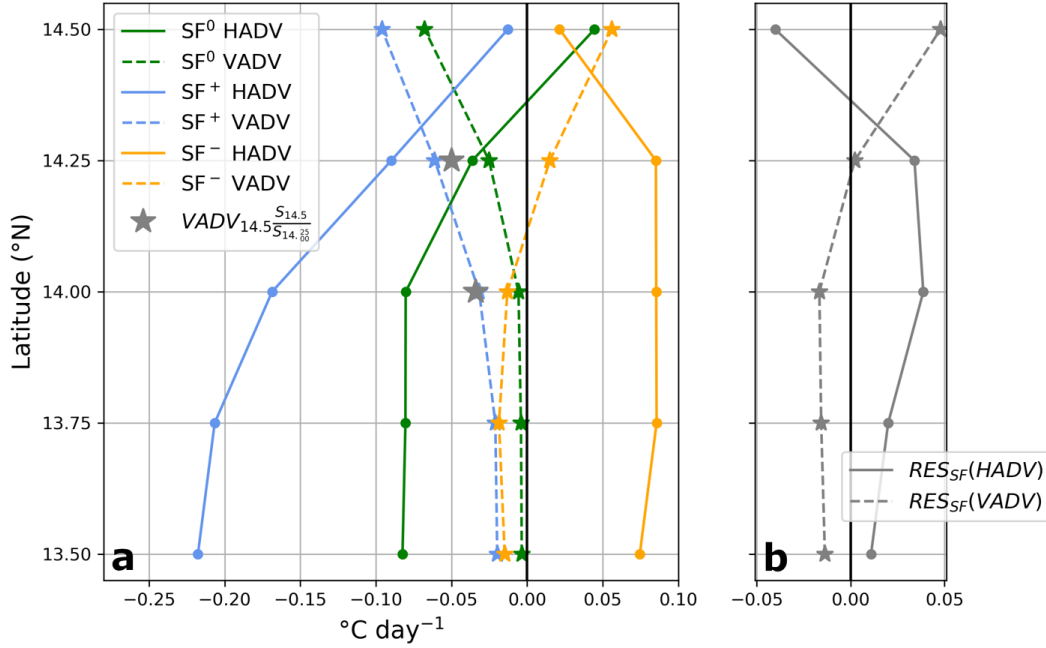


Figure II.17: a) Horizontal (solid lines) and vertical (dashed lines) heat advection tendencies as a function of the location of the averaging box southern boundary (which varies from 13.50 to 14.50°N). Five averaging boxes are used (indicated with dots and stars superimposed on lines). Each tendency value is ensemble and time averaged (between days 6 and 9, i.e., at the end of the synoptic anomaly if any). Green, blue and orange lines indicate respectively SF⁰, SF⁺, and SF⁻. Isolated grey stars represent the outcome of diluting the SF⁺ vertical advection tendency found north of 14.50°N in the boxes with southern extension at 14.25°N and 14.00°N. b) SF⁺/SF⁻ asymmetry (i.e., synoptic residual) $RES_{SF}(X)$ associated with the domain averaged horizontal (solid) and vertical (dashed) advection tendency terms shown in panel a.

2.6 Sensitivity tests and limitations

2.6.1 Vertical mixing scheme

Previous studies have shown the sensitivity of coastal dynamics to the particular choice made for the turbulence closure scheme (Wijesekera et al., 2003; Van Roekel et al., 2018). Here we explore this sensitivity by comparing the reference simulations using K-Profile Parameterization (Large et al., 1994) with simulations computed with the General Length Scale (GLS) k- ϵ (Fearon et al., 2020; Umlauf and Burchard, 2003). GLS k- ϵ surface mixed layer depths (computed using a threshold condition on density change from surface to mixed layer base equal to 0.01 kg m⁻³; see de Boyer Montégut et al. (2004)) tend to be smaller (~ 2 m, not shown) than those obtained when using KPP.

The synoptic anomalies of SML depth generated by both schemes are quite similar for SF^+ . The differences are more pronounced for SF^- , with less shoaling (resp. more deepening) during the active part (resp. the return to climatological conditions) when using GLS $k-\epsilon$. From this ensues visible differences in SST during the late period of SF^- when GLS $k-\epsilon$ yields a faster return to climatological SST values (Fig. II.10a).

The most dramatic sensitivity is found for zonal and meridional currents. The currents are systematically weaker with KPP than with GLS $k-\epsilon$ and the difference is amplified as wind (and currents) get stronger (Figs. II.10d,e). The treatment of bottom friction is identical in all runs (linear drag with friction coefficient equal to $3 \times 10^{-4} \text{ m s}^{-1}$). We thus attribute this sensitivity to differences in momentum mixing intensity and indeed have verified that KPP yields viscosity coefficients near the shelf bottom that are 3-5 times stronger than found in GLS $k-\epsilon$ (differences over the inner shelf are even more pronounced). Although changing the vertical mixing scheme does not fundamentally alter our results, exploring this sensitivity further and determining which scheme is most realistic would be useful (but note that the flow bias at Melax shown in section 2.3.1 would be even stronger with GLS $k-\epsilon$).

2.6.2 Doubling air-sea heat flux synoptic anomalies Q'_{SF}

As in other upwelling systems (Thomsen et al., 2021), net air-sea heat flux is quite variable at synoptic and intra-seasonal time scales in the SSUS (e.g. at Melax, S. Faye personal communication). To explore this sensitivity, simulations with doubled Q'_{SF} ($\mp 80 \text{ W m}^{-2}$ in SF^\pm) were carried out. In terms of magnitude, sensitivity of SST is moderate (+10% - resp. 30% - SST anomaly at day 8 in SF^+ - resp. SF^- ; Fig. II.10a) and that of SML depth is a bit stronger (+25% - resp. 50% - SML depth anomaly at day 8 in SF^+ - resp. SF^- ; Fig. II.10b).

The asymmetry found between SF^+ and SF^- is consistent with the fact that thermodynamic effects are amplified when the momentum forcing (wind) is weak. But overall, these sensitivity runs confirm that wind forcing is the dominant driver. A different conclusion would presumably be reached for isolated synoptic events taking place in November-January when easterly winds from the Sahara can be responsible for Q'_{SF} anomalies reaching several hundred watts per m^2 (Thomsen et al., 2021).

2.6.3 Study limitations

There are several important limitations to the insight provided by our study. Firstly, the idealizations we made ignore the complexity of the wind and air-sea heat flux history (succession of synoptic events of various duration and intensity) and of the associated ocean response.

It has been known for a long time that coastal upwelling can be generated by remote winds whose effect is then transmitted (poleward along an eastern boundary) by coastal trapped waves (Philander and Yoon, 1982). Synoptic wind anomalies have a regional imprint (Fig. II.2c) which is very weak south of 12°N , i.e., our domain of interest is close to the southern limit of the synoptic fluctuation pattern. Consistently, we find very limited signs of propagation of remote synoptic signals in the SSUS (e.g., in v_{surf} and SSH) but this may be otherwise for some of the real world synoptic events. Using climatological boundary conditions for all runs, we also ignore the synoptic modulations of the West African boundary current (WABC) system that are

generated outside our computation domain (i.e., remote forcing south of $\sim 6^\circ\text{N}$). SSH altimeter data (Polo et al., 2008) and tropical Atlantic simulations (Polo et al., 2008; Kounta Diop, 2019) indicate that coastal trapped waves generated by seasonal and intraseasonal wind fluctuations along West Africa can propagate from as far as the Gulf of Guinea to the SSUS.

Also note that we suspect a spring bias in the intensity of the WABC based on SST/ocean color satellite image analyses (Ndoye et al., 2014), but lack current observations to confirm this. Having an overly weak poleward WABC could limit the ability of wind relaxations to trigger continental shelf flow reversals (Tall et al., 2021) and thus also explain the flow bias at Melax (see section 2.3.1). Finally, spatial horizontal resolution is only marginally submesoscale-permitting (Dong et al., 2020) so frontal processes must be less energetic in our model than in the real ocean, which could have consequences on the SML heat budget and its synoptic modulations.

2.7 Discussion

Cape Verde is a major geomorphological irregularity with implications on the surrounding ocean flow. As shown in Gan and Allen (2002a), we also find that alongshore pressure gradients tend to be of opposite sign north and south of the Cape. On the other hand the details of the circulation differ from those presented for the well-studied Point Reyes, Point Arena (Gan and Allen, 2002a), and Cape Blanco (Barth et al., 2000).

In the typology established by Largier (2020) the SSUS geometry/flow configuration would fall in between two categories relevant to other ocean sectors: i) smooth and broad embayment with no flow separation (e.g. Sonoma Coast in California and Antofagasta bay in Chile) and ii) abrupt coastline deflection associated with a flow separation and shelf recirculation (e.g. Gulf of Farallones in California and St Helena bay in South Africa). Although Cape Verde also seems rather sharp, and a flow separation is manifest (Fig. II.6), no recirculation occurs in normal/-climatological conditions. In the model simulations we presented, this remains true during strong upwelling and relaxation conditions, albeit with some robust flow modifications induced in part by mesoscale features. We attribute this relative stability of the flow to the strong constraint associated with the shelf enlargement south of Cape Verde and to the associated onshore flow needed to satisfy the mass balance (Pringle, 2002).

One manifestation of this stability is the importance of the deterministic response to forcing synoptic modulations relative to intrinsic turbulent variability. SSUS flow modifications generated when the system is subjected to upwelling wind intensifications or relaxations are indeed largely independent of the initial state at onset of the synoptic event. To leading order, they are also spatially homogeneous over the continental shelf. As for time scales, our analyses of synoptic modulation and return to climatological conditions demonstrate that the SSUS circulation and dynamics is constrained by the forcing history over a relatively short period of ~ 10 days (see Fig. II.3a), i.e., memory effects are quite limited in time. Both the persistence in time of SF effects and the spatial heterogeneity of the ocean response to SF are significantly bigger for the open ocean (not shown). All this is consistent with the prevalence of a wind forcing-bottom friction balance in the momentum equations.

Given the design of our experiments, any asymmetry between the ocean response to SF^+ and SF^- forcing anomalies provides insight into residual effects generated by wind synoptic variability. Diagnosed asymmetries (Fig. II.10 and II.11) are small for SST, SML depth, w at the mixed layer base and a bit stronger for currents, particularly meridional ones. In the spirit of Gan and Allen (2002a) the possibility that alongshore pressure gradients at the offshore edge of our domain be responsible for asymmetry found for the latter was examined. Alongshore sea level gradient diagnosed over the 100 m isobath between 14 and 14.6°N reveal negligible asymmetry ($\mathcal{R}_{SF}(X) = 3\%$, not shown). Reasons underlying asymmetry in v were not explored further given their limited importance overall. Bottom drag which was chosen to have a linear formulation cannot produce asymmetries alone but its interplay with near-bottom mixing could. Note that more asymmetry would presumably arise from employing quadratic/nonlinear bottom drag.

The intriguing SST asymmetry taking place after the period of anomalous synoptic forcing (Fig. II.10) is sensitive to the employed mixing scheme. The longer persistence of SST and SML depth anomalies with KPP mixing may point to erroneous hysteresis effects but a more in-depth investigation would be needed to confirm this.

A well-known source of asymmetry is thermal/density advection in the bottom boundary layer which behaves differently in upwelling and downwelling conditions (Beckmann, 1998). Because we find little asymmetry in bottom temperature/density, as estimated using the synoptic residual RES_{SF} (not shown), the importance of this effect must also be small.

The reader familiar with the California current literature may be surprised by the limited asymmetry revealed by our surface mixed layer heat budgets. We relate this to the importance of alongshore advection, not just during relaxation but also during sustained wind conditions. This may be due to the shelf flow regime and its control by friction. Also note that we find significant asymmetry of the vertical and horizontal advection terms for the northern part of the SSUS, i.e., a control volume of size not much smaller than the one considered by Send et al. (1987). This underscores the domain dependence of synoptic rectification effects.

The degree to which the circulation responds deterministically is also noticeably different between SF^+ and SF^- , with significantly more robust SST responses in the former case as long as the synoptic wind anomaly is present (compare Figs. II.7a,f; see also Fig. II.3b until day 11). This is perhaps not unsurprising that stronger forcing is associated with larger signal-to-noise but it has, to our knowledge, not been noted before in this context. At later times when the wind has returned to climatological conditions, the opposite is true (compare Figs. II.7b,g; see also Fig. II.3b after day 11), which seems consistent with more energy being available in SF^+ to feed turbulent processes.

2.8 Conclusions

In this study we shed light into the upper ocean SSUS heat balance. At the time of year we focus on (the heart of the upwelling season) air-sea heat flux is the only significant source of heat. This heat input compensates cooling by advection which arises from the horizontal flow except in the immediate vicinity south of Cape Verde where vertical advection dominates. All this is broadly consistent with the localization of vertical velocities found in Ndoye et al. (2017)(see

also Fig. II.8).

However, the main study focus is the effect of atmospheric fluctuation in the synoptic range. In upwelling systems, such fluctuations can strongly modulate the ocean dynamics and have been implicated in anomalous biogeochemical events of high significance⁵. By means of idealized ensemble runs we have strived to characterize the ocean response of a West African upwelling sector to atmospheric synoptic fluctuations.

During upwelling intensification the dominant SSUS upwelling pathway identified in climatological conditions (Ndoye et al., 2017) remains in place and most of the upwelling takes place within 20-30 km from the Cape Verde peninsula. During wind relaxations, upwelling is nearly halted (although the wind is not) and the horizontal flow is modified with weak equatorward currents over the shelf and even surface poleward flow about the shelf break. The associated changes in SST (or mixed layer temperature) are smooth in time, spatially modulated by (sub)mesoscale turbulence with magnitude reaching $\pm 1.5^{\circ}\text{C}$. The synoptic modulations of the underlying heat budget are characterized by major disruptions of the heat tendency terms with a near doubling (resp. complete reversal) of the horizontal and vertical advection tendency terms north of 14.25°N during SF^{+} (resp. SF^{-}). Air sea heat fluxes are comparatively less affected although they also play a role.

Overall, we confirm the major role played by horizontal advection in the SSUS upper ocean heat balance and its changes on synoptic time scales (Capet et al., 2017). Conversely, we find a very limited role played by vertical mixing. Our analyses also demonstrate the existence of modest intensification/relaxation asymmetries at the upwelling sector scale, i.e., the mean state dynamics and circulation of the SSUS are only weakly altered by the presence of synoptic scales in the atmospheric forcings. Of all dynamical variables considered, meridional velocities are subjected to the most important rectification effect. But, contrary to general expectations that could be derived from past studies (Gan and Allen, 2002b,a, 2005b) no associated alongshore pressure gradient asymmetry could be identified in our simulations.

All these findings are for a particular class of synoptic perturbations whose magnitude is one standard deviation above or below climatology. This is sufficient to draw the ocean outside of its intrinsic variability range and produce major biogeochemical disturbances as we will report in a forthcoming study including substantial biogeochemical asymmetries. But stronger perturbations would presumably have stronger effects, and possibly increase the degree of asymmetry between upwelling intensification and relaxation phases. During the monsoon to upwelling transition season in fall, offshore wind carrying dry air from the Sahara and warm ocean temperatures lead to intense air-sea heat losses that make for very different synoptic situations, and perhaps more surface heat flux forcing asymmetry. Exploring the whole variety of synoptic circumstances may be tedious. Gaining a priori insight into which ones are most impactful on the biogeochemical and ecosystemic functioning (e.g., because they produce hypoxic or harmful algae bloom events) of the SSUS would be useful.

⁵Away from shore, the existence of such events can also be purely due to mesoscale turbulence which modulates the flow and biogeochemical properties over a similar time scale range (Stukel et al., 2017; Chabert et al., 2021)

Acknowledgments

This work benefited from Agence nationale de la recherche fundings (SOLAB ANR-18-CE32-0009). P. C. was supported by a PhD grant from IPSL EUR. CROCO is provided by <http://www.croco-ocean.org>. Fundings for the Melax mooring were provided by FP7 PREFACE and IRD laboratoire mixte international ECLAIRS2.

Data availability statement

The ERA5 dataset provided by the ECMWF is available on <https://cds.climate.copernicus.eu/cdsapp#!/dataset/reanalysis-era5-single-levels?tab=overview>. Melax data can be requested on <https://sites.google.com/site/jointinternationallabeclairs/melax>. Given the large size of the modeling experiment outputs (~1.6 TB), the dataset is not stored online and can be shared upon request to the corresponding authors.

3 Complementary diagnostics and analyses

3.1 Spatial structure anomalies: JPO Supplementary Material

The evolution of SSH and SST fields during the simulations, SF^\pm and SF^0 are shown in Figs. II.6 and II.7. Anomalies in SF^\pm relative to SF^0 are also instructive. They are shown in Figs. II.18 and II.19.

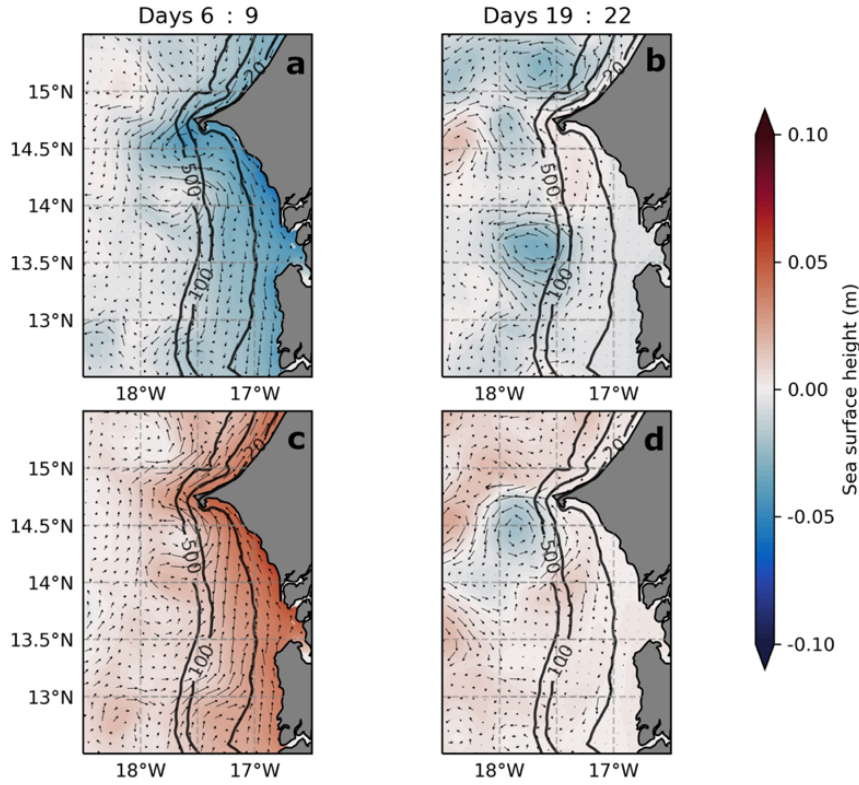


Figure II.18: Similar as Fig. II.6 but in anomalies to the climatology instead of in absolute. The climatological values are removed to the synoptic values (II.18a is II.6a minus II.6d; II.18b is II.6b minus II.6e; II.18c is II.6f minus II.6d; II.18d is II.6g minus II.6e) in colors (SSH) and arrows (surface currents).

Although they are strongly correlated, the SSH and SST anomalous fields differ in terms of fine-scale content which are much weaker in the former. SSH anomalies reveal the main mesoscale features described in section 2.4.1. A few explanations are given to help interpret the fine-scale details of the anomalous SST fields visible at day 6-9. SST fine-scales features are more intense with increased (SF^+) than reduced (SF^-) upwelling. Interestingly, SF^+ features of the SST field do not match those of w (compare Fig. II.18a and Fig. II.8). We relate this to the fact that SST anomalies are predominantly produced by lateral rather than vertical advection (see section heat budget). In particular, notice how the intensification of the prevalent anticyclonic circulation just south of Cape Verde is associated with a low SST anomaly.

Temperature anomalies have greater magnitude in a coastal strip situated inshore of the 10 m isobath and this strip tends to expand northward (resp. contract southward) during SF^- (resp. SF^+). Temperature in this coastal strip is primarily controlled by air-sea heat fluxes (Ndoye et al., 2017) and reflects their synoptic modulation.

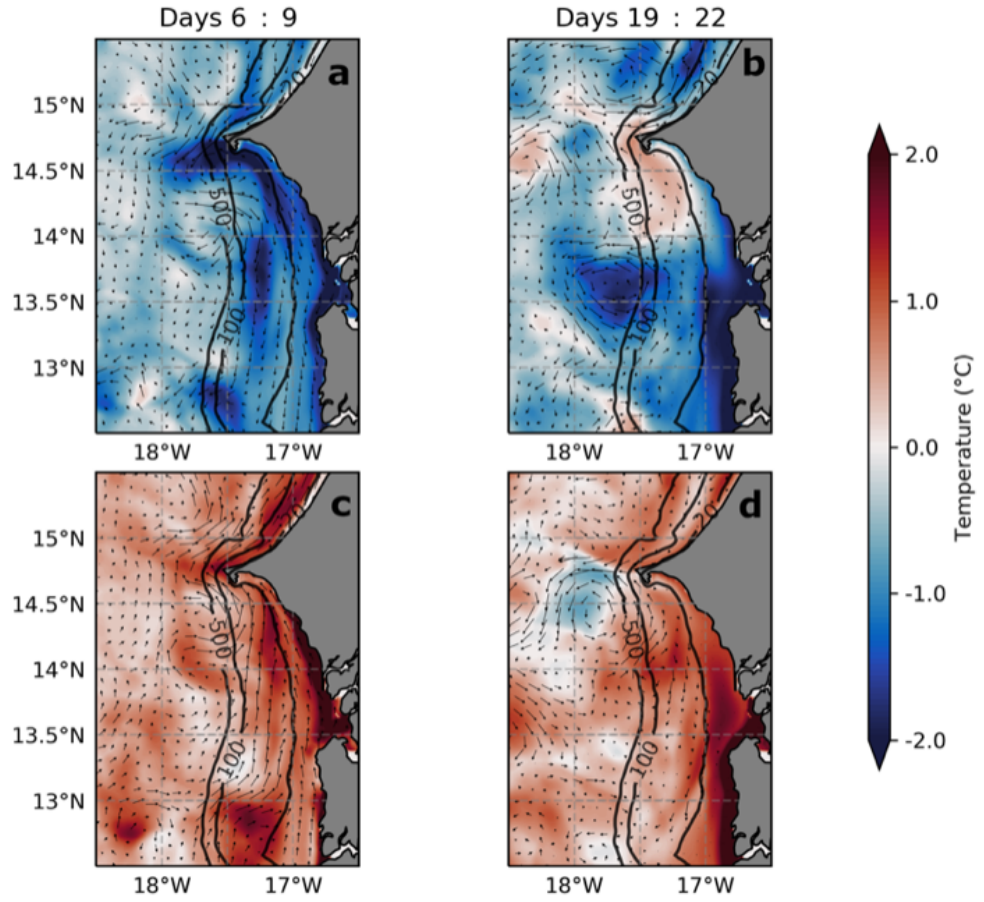


Figure II.19: Same as Fig. II.18 with SST.

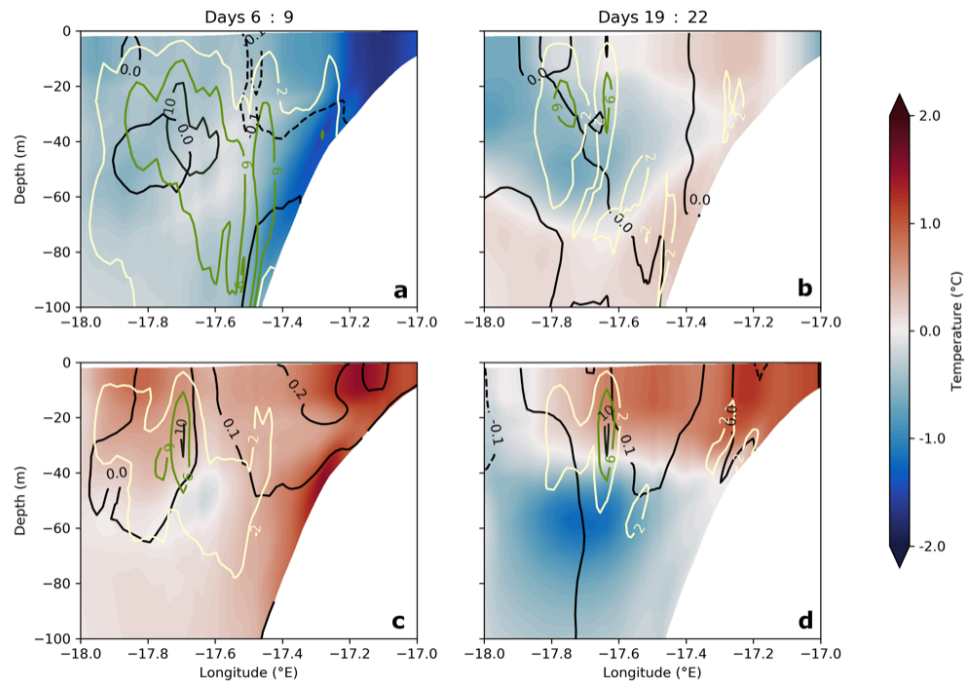


Figure II.20: Same as Fig. II.18 with corresponding Fig. II.9 transect. Anomalies in colors (temperature), green and white lines (vertical velocities) and black lines (meridional currents).

3.2 Details on a minor pre-processing error

In retrospect, we realized that net heat fluxes in SF^+ and SF^- at day 11 do not match exactly the climatology at day 11 (see Figs. II.1e and II.21). This discrepancy is due to a minor pre-processing error that we have missed. We have hesitated to redoing all numerical experiments but refrained from doing that given: electricity shortages in Europe; and most importantly the following estimate of the upper ocean temperature increment induced by this error. First we computed the heat flux error as a function of time (dots are the difference between solid and dashed in Fig. II.21). We then integrated this quantity over BoxN between days 3 and 8 (see Eq. II.1 and title of Fig. II.21 for the formulae).

$$\delta T_{boxSML} = \frac{1}{V_{boxSML}\rho_0 C_p} \iiint_{S,t}^{day0:15} \delta Q'_{SF^\pm}|_{boxSML}(x, y, t) dx dy dt \approx -0.073^\circ C \quad (II.1)$$

Assuming that this erroneous heat flux would be distributed into the surface mixed layer (whose depth we take equal to the climatological March average in BoxN i.e., 19 m), the temperature increment/error would reach $+0.03^\circ C$ at day 8 or $0.07^\circ C$ at day 15. Given the values of $\{X_{SF^0}; X_{SF^+}; X_{SF^-}\}$, this would result in a negligible modification of the residual diagnostic $\mathcal{R}_{SF}(X)$ of 0.1%. Also note that the heat flux error magnitude in BoxN is just above 5 W m^{-2} when averaged between days 1 and 15. This is to compare with the sensitivity test we performed in the JPO manuscript (section 2.6) in which we show a moderate impact of a doubling of net heat fluxes ($\pm 80 \text{ W m}^{-2}$ anomalies).

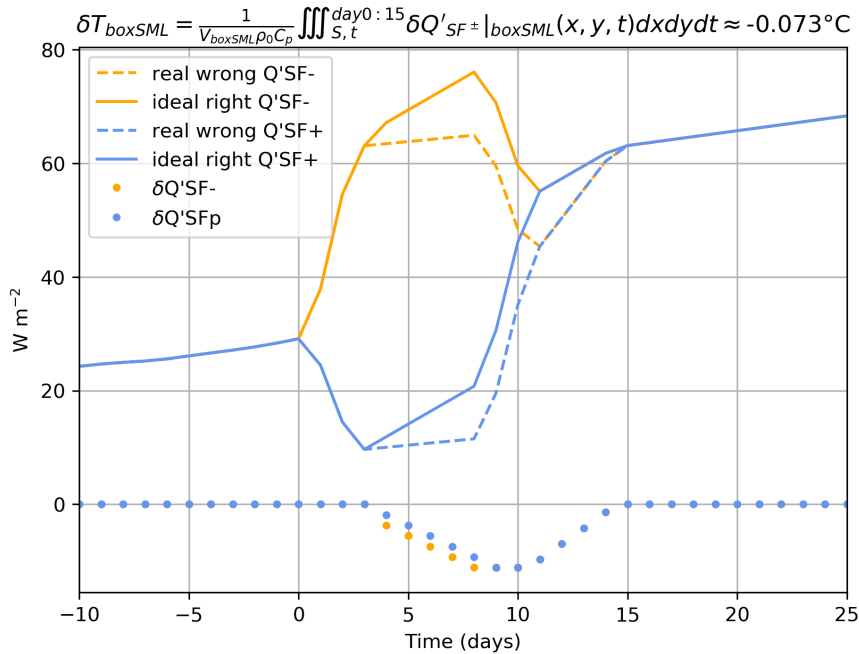


Figure II.21: Time series of SF^\pm (blue and orange) heat fluxes forcings effective on our simulations (dashed lines) and the intended, corrected forcings (continuous lines). Average over the SSUS.

3.3 Spatial and temporal dependence of the deterministic response

Here we complement the Ensemble Approach section 2.2.5 of the JPO manuscript. We compute the Root Mean Square Error (RMSE): we subtract the variable averaged over the domain before computing the RMS, as shown in Eq. II.2 for X =SST and for the forced response of SF^+ compared to SF^0 (i.e. $\Delta X^{(e)}$). This is shown in Fig. II.22b,d. We also compute RMS and RMSE diagnostics over the entire SSUS domain (see Fig. II.1) in order to assess the domain dependence of these results (see Fig. II.22c,d SSUS averages).

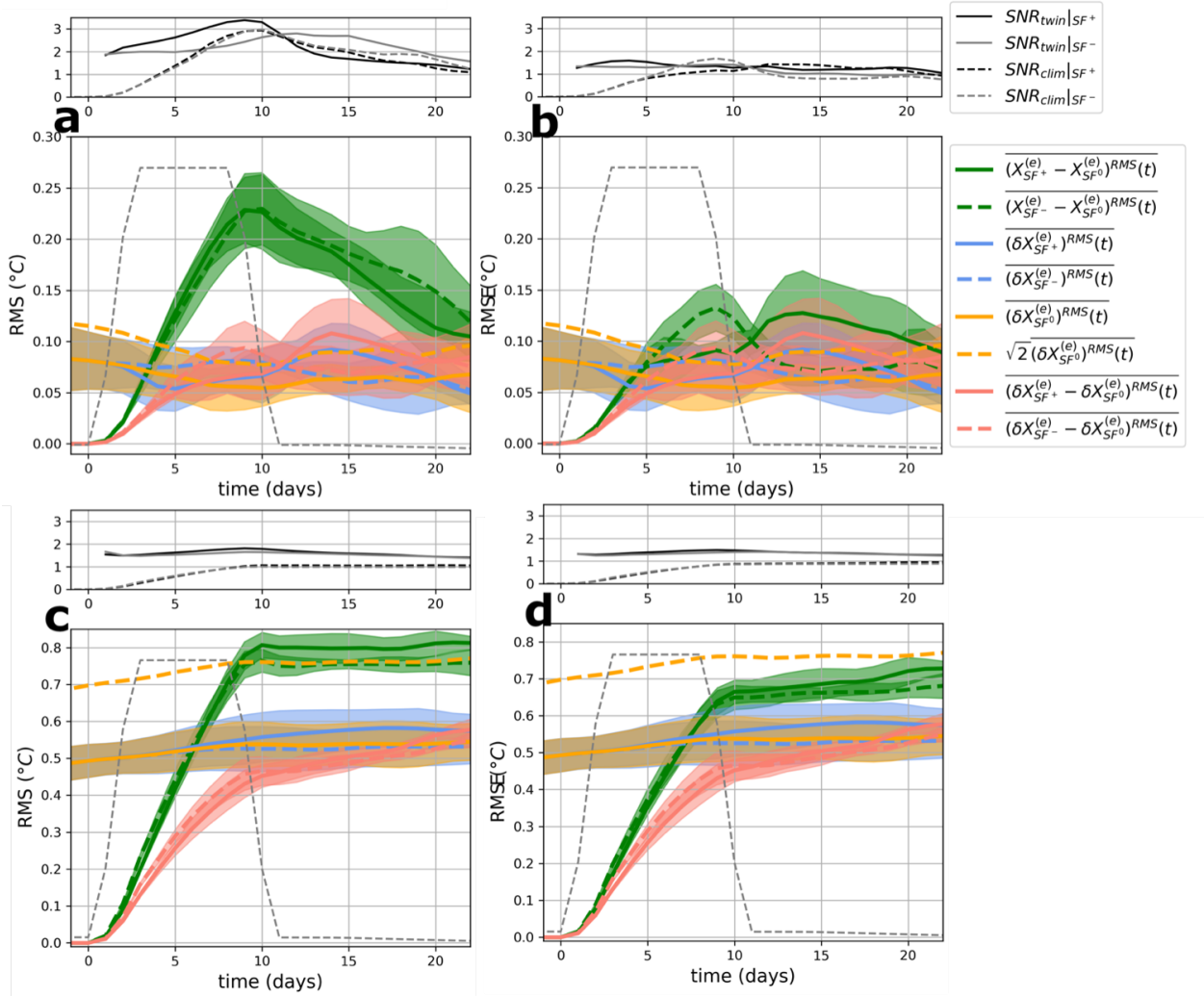


Figure II.22: Panel a is similar to Fig. II.3 (diagnostics averaged in BoxN) and the panel c indicate the average over the entire SSUS domain. Panels b and d indicate Root Mean Square Error (RMSE; over BoxN and SSUS domain, respectively). Note that we denote the ensemble averages with an overline in the legend because it is not straightforward here: we compute the diagnostics for each member and then average over the ensemble. We remind that $\Delta X_{SF^\pm}^{(e)} = (X_{SF^\pm}^{(e)} - X_{SF^0}^{(e)})$ and $\delta X_{SF}^{(e)} = X_{SF} - X_{SF^0}^{(e)}$, as defined in section 2.2.5.

$$\begin{aligned}
 \Delta X^{(e)} &= (X_{SF^+}^{(e)} - X_{SF^0}^{(e)}); \overline{\Delta X^{(e)}} = \frac{1}{L_x L_y} \sum_{i,j}^{L_x, L_y} \Delta X_{i,j}^{(e)} \\
 RMS(\Delta X) &= \sqrt{\frac{1}{L_x L_y} \sum_{i,j}^{L_x, L_y} (\Delta X_{i,j}^{(e)})^2} \\
 RMSE(\Delta X) &= \sqrt{\frac{1}{L_x L_y} \sum_{i,j}^{L_x, L_y} (\Delta X_{i,j}^{(e)} - \overline{\Delta X^{(e)}})^2}
 \end{aligned} \tag{II.2}$$

Over the shelf (BoxN), the average SST is representative of the forced response. This is shown by the fact that when we compute the RMSE, unlike the RMS, the deterministic part of the response (green lines in Fig. II.22a,b) coincides with the intrinsic part (pink lines in Fig. II.22a,b), i.e. $\Delta X_f^{RMSE}(t) \approx \delta X_i^{RMS}(t)$.

This is less true over a wider domain (SSUS), where the RMSE forced response $\Delta X_f^{RMSE}(t)$ is less different than the RMS forced response $\Delta X_f^{RMS}(t)$ (compare panels c and d in Fig. II.22) and is not confused with the intrinsic signal $\delta X_i^{RMS}(t)$. The domain is too wide for the average SST to be representative of the forced response which supports the fact that the forced response is weaker over a wider domain. Another way of seeing this is on the SNR that drops from >2.5 over the shelf to <2 over the entire domain (compare Fig. II.22 panels a and c). The forced upwelling response in SST is moderate when averaged over the entire domain and happens mostly over the shelf. To a larger extent, in agreement with this domain dependence of the deterministic response versus the intrinsic variability, we hypothesize that asymmetrical behaviors decrease with the domain size.

The memory time scale of the SF anomaly is greater over a wider domain than a smaller domain, i.e. $\Delta X_f^{RMS}(t)$ does not decrease to $\delta X_i^{RMS}(t)$ in ~ 20 days in Fig. II.22c, unlike Fig. II.22a.

To follow up on arguments advanced in section 2.2.5, we can wonder how would these diagnostics behave with a larger ensemble. Especially, the time at which the intrinsic part $\delta X_i^{RMS}(t)$ (pink lines in Fig. II.22) of our simulations reaches the intrinsic variability threshold δX_{SF^0} (orange lines in Fig. II.22) could be later.

3.4 Additional dynamical aspects of the SSUS dynamics

Synoptic variability at Melax

Measurements of atmospheric variables (wind speed, wind direction) allow to detect wind intensification and relaxation events (see Fig. II.23) and thus to attempt to build observed composites. However, these specific attempts to quantitatively compare simulated SML synoptic evolutions with composite behaviors of the observed SML were unsuccessful. This is because there are too few such events in our limited observational period, with great variability between the events (in terms of wind intensity change, duration, wind history prior to the event ...) and none closely resembling our idealized numerical posing. Thus, we limit our analysis to the examination of individual intensification and relaxation events (see JPO manuscript Fig. II.5).

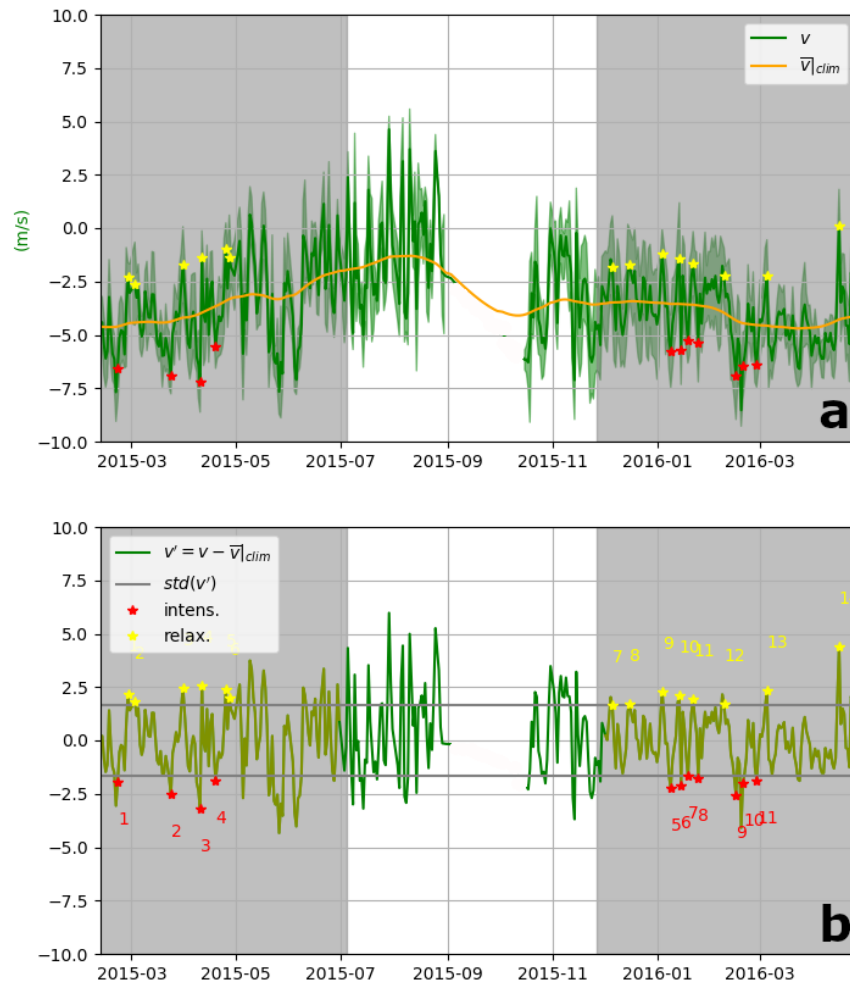


Figure II.23: Time series of meridional wind speed at Melax. Panel a shows the absolute signal and panel b the signal detrended from its seasonal cycle. Identification of intensification and relaxation events out of the standard deviation range are indicated in red and yellow stars.

Despite the difficulty to build composites on observed temperature vertical profiles, we investigated the vertical currents structure during intensification and relaxation. Thus, in addition to the depth integrated analysis presented on the JPO manuscript (Fig. II.5), we explored

building composites of the vertical structure of currents. We select Melax and CROCO vertical currents (u, v) during wind intensification and relaxation (continuous lines in Fig. II.24) and we rotate them by the angle between the major axis of the ellipse of Fig. II.5 and the north; such that we obtain a decomposition in along and across shelf terms (dotted lines in Fig. II.24; method similar to McCabe et al., 2015). This rotation improves the agreement between modeled and observed $u(z)$, despite the lack of vertical gradient in the model (Fig. II.24a). Despite a general good agreement in the direction and difference between intensification and relaxation, the $v(z)$ profiles are biased of about 0.1 m s^{-1} (Fig. II.24b). Because the standard deviation of the observed vertical profiles of currents is large ($>0.15 \text{ m s}^{-1}$), this attempt of compositing Melax observations is also limited.

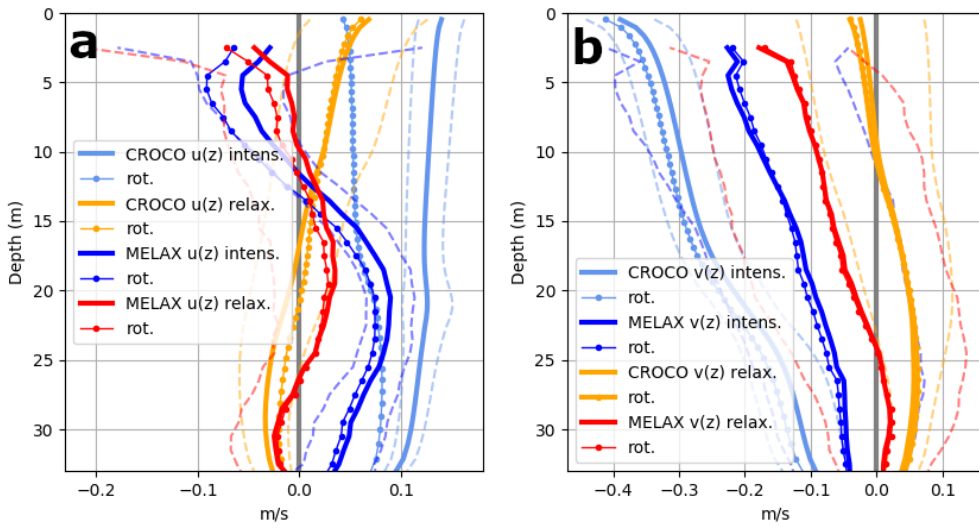


Figure II.24: Vertical structure of Melax and CROCO currents (u, v) (panels a,b) during wind intensification and relaxation. The vertical profiles rotated by the angle between the major axis of the ellipse (of depth integrated currents) and the north (see Fig. II.4 of the JPO manuscript) are indicated in dotted lines.

Coastal Trapped Waves

Before realizing that the weak wind variability in the southern part of the domain is unlikely to trigger remote forcing over the SSUS (see section 3.5 of chapter I and Fig. I.9), we investigated the potential propagation of Coastal Trapped Waves (CTW). We diagnose this by looking at the time evolution of the SSH along the coast in response to wind perturbations, precisely over the 20 m isobath (see Figs. II.25, II.26 over the northwest Africa and Senegalese domains, respectively panels a,b). Over the large domain, between days 5 and 15, the SSH structure is modified between $\sim 12^\circ\text{N}$ and $\sim 21^\circ\text{N}$, but it is not possible to attribute this to remote forcing. To diagnose the part due to remote forcing, we compute the temporal anomaly: we remove the temporal average over the 25 days period at each latitudinal point over the 20m isobath (as Eq. II.3 writes).

$$\eta'(y_j|_{20m}, t_i) = \eta(y_j|_{20m}, t_i) - \overline{\eta(y_j|_{20m}, t_i)}|_{\Sigma t_i} \quad (\text{II.3})$$

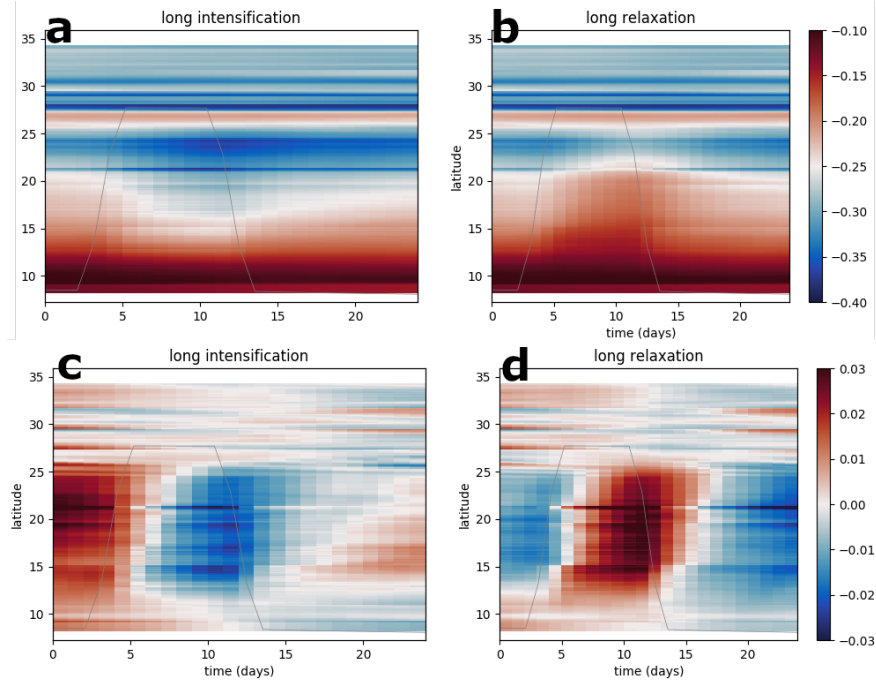


Figure II.25: Temporal evolution of the along 20 m isobath SSH (along the northwest coast of Africa) for SF^+ (a,c) and SF^- (b,d), in absolute (a,b) and temporal anomaly (c,d).

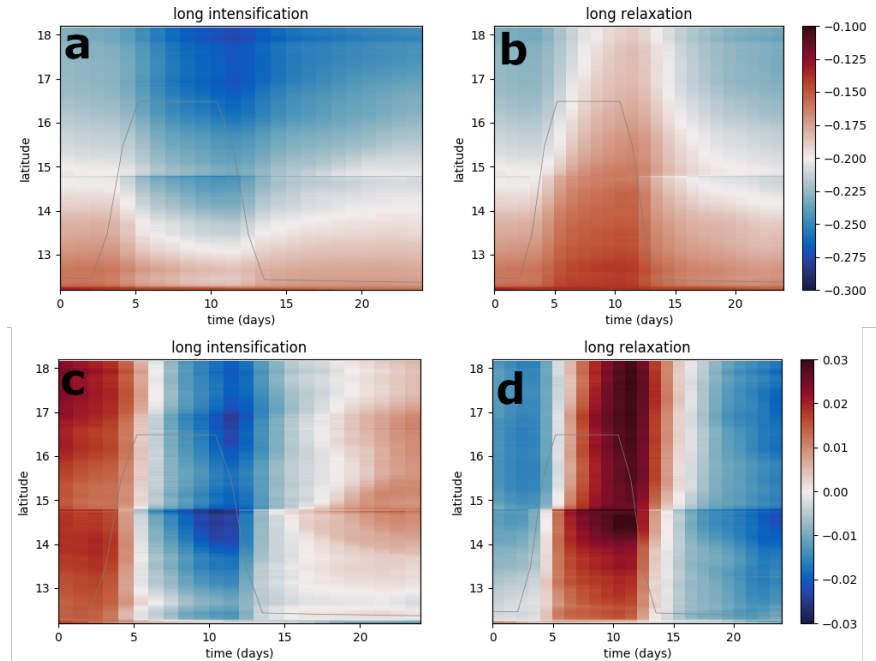


Figure II.26: Same as Fig. II.25 over the SSUS domain.

Panels c,d of Fig. II.25 exhibit a SSH anomaly between days 5 and 15 that seem to propagate along the coast poleward, with a phase speed estimated of the order of 1 m s^{-1} (about 500 km in 5 days), that we believe is remote forcing. This is of the same order of magnitude as previous observations with SSH altimeter of coastal trapped waves along the northwest coast of Africa (Polo et al., 2008). Over the smaller SSUS domain, a similar propagation is observed

in Fig. II.26. At the Cape Verde latitude, the coastline break induces a discontinuity in the hypothesized propagation but do not seem to damp it, despite theoretical indications about their limited propagation north of a cape because of dispersive effects (Crépon et al., 1984). Given their weak intensity ($< \pm 2$ cm) compared to greater locally forced SSH variations ($> \pm 10$ cm, see Fig. II.7a,f), we did not investigate further into this direction.

Pressure gradient

Previous studies (e.g. Gan and Allen, 2002a) emphasize the importance of the alongshore pressure gradient in potentially driving alongshore poleward flow in response to upwelling favorable wind relaxation. Especially, the authors point out its spatial asymmetry between the northern and southern sectors of a Cape during a relaxation. In our simulations, we find that the asymmetry between intensification and relaxation in the alongshore pressure gradient (diagnosed with the difference of SSH between points B and A in Fig. II.27) is very small ($\mathcal{R}_{SF}(SSH_B - SSH_A) = 3\%$) and thus irrelevant.

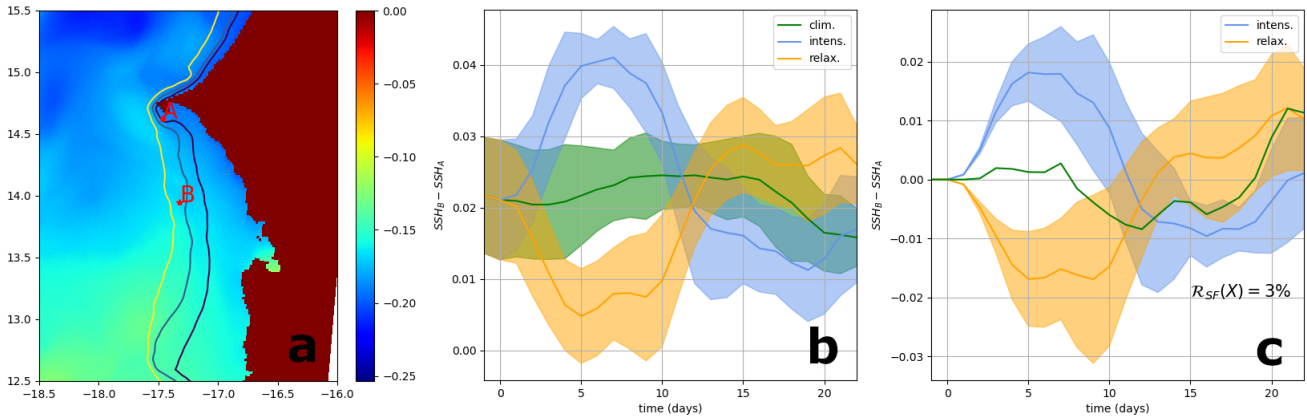


Figure II.27: Location of points (A, B) (panel a), time series ensemble averages of the difference of sea surface height (SSH) between B and A for SF^{0+-} (panels b,c). The time series is absolute on panel b and in anomaly in panel c, with the sum of the anomalies plotted in green and the \mathcal{R}_{SF} value.

Vorticity

In complement to SSH, we show the vorticity (scaled by the Coriolis parameter f) field that supports our observations on the development of robust mesoscale features (see Fig. II.28). Vorticity responses are consistent with the mesoscale circulation discussed in the manuscript. For example, negative vorticity patches around $(-17.5^\circ\text{E}; 14-14.5^\circ\text{N})$, e.g. during SF^0 (Fig. II.28a), reflect the anticyclonic circulation south of Cape Verde that can be seen in Fig. II.7 of the manuscript and is discussed in section 2.4.1.

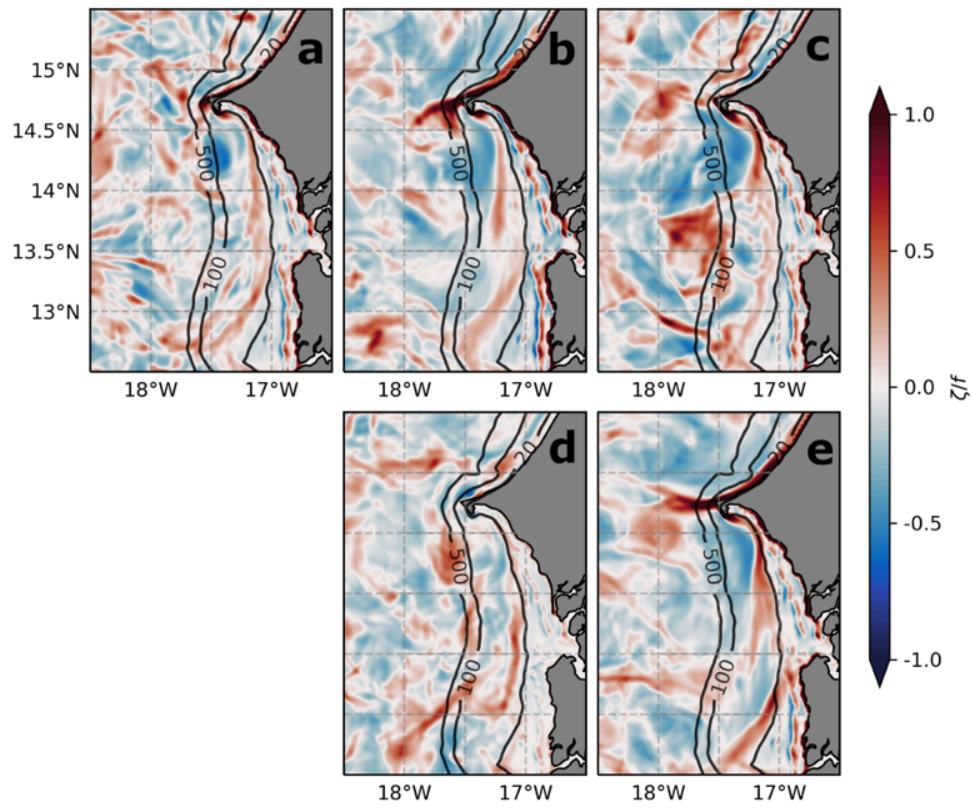


Figure II.28: Maps of surface vorticity scaled by the Coriolis parameter f : panel a) SF^0 days -1:0, b) SF^+ 6:9, c) SF^+ days 19:22, d) SF^- 6:9, e) SF^- days 19:22.

Additional comments on the physical structure

Given the little influence of vertical advection found on the SML heat budget over the shelf (see section 2.5), we initially investigated the temperature vertical structure. If the vertical temperature gradient is weak, vertical velocities, even intensified, would affect only weakly the SML heat budget. As we analyzed it during the exploration phase of the study, we show the difference of temperature between the level above and below the SML depth in Fig. II.29. The fact that this difference increases during SF^+ is not sufficient to explain the reduced role of vertical advection in the SML heat budget. However, the increase of the offshore extension of the fully mixed water column (null vertical temperature gradient in Fig. II.29) over a wide area supports the heat budget findings about the very localized role of vertical advection. This is in agreement with SML changes, in a way that this fully mixed area is pushed offshore during SF^+ and relaxed inshore during SF^- . This is also in agreement with the offshore migration of the cold upwelling tongue found in the SST structure (Fig. II.9) and with Ndoye et al. (2014) findings (their Fig. 7; cross-shore temperature gradient at the climatological scale, but consistent in terms of wind conditions).

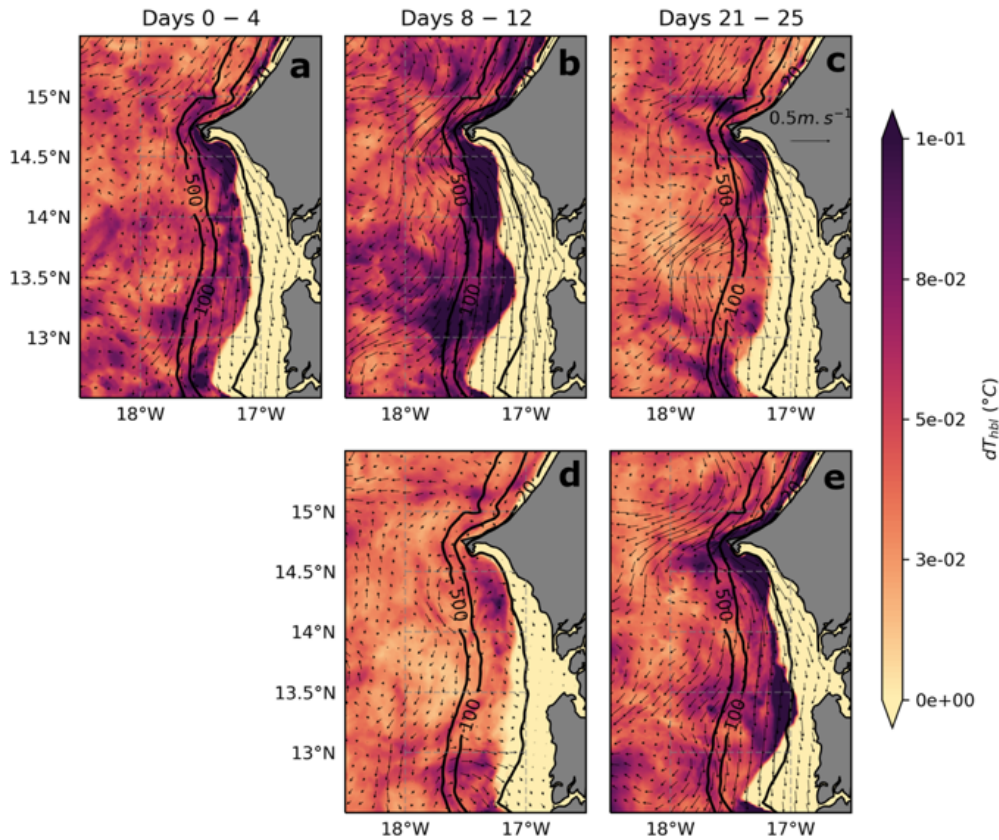


Figure II.29: Maps as Fig. II.28 with the difference of temperature between the level above and below the SML depth.

3.5 Heat transport along the box boundaries

The heat budget technique integrated in BoxN misses the information of heat changes due to entries or exits along the box boundaries, as stated in section 3.9. To address this, we compute the temporal evolution of the heat transport anomaly integrated over the SML along the sections (see Fig. II.30 upper row). We also show the corresponding currents, which indicates the orientation of the transport, towards the inside or the outside of BoxN. The combination of these two diagnostics allows to conclude about the entry/exit of colder/warmer waters than BoxN waters. Note that in Fig. II.30 the Northern, Western and Southern sections (shown in Fig. I.12) are separated by thick dashed purple lines.

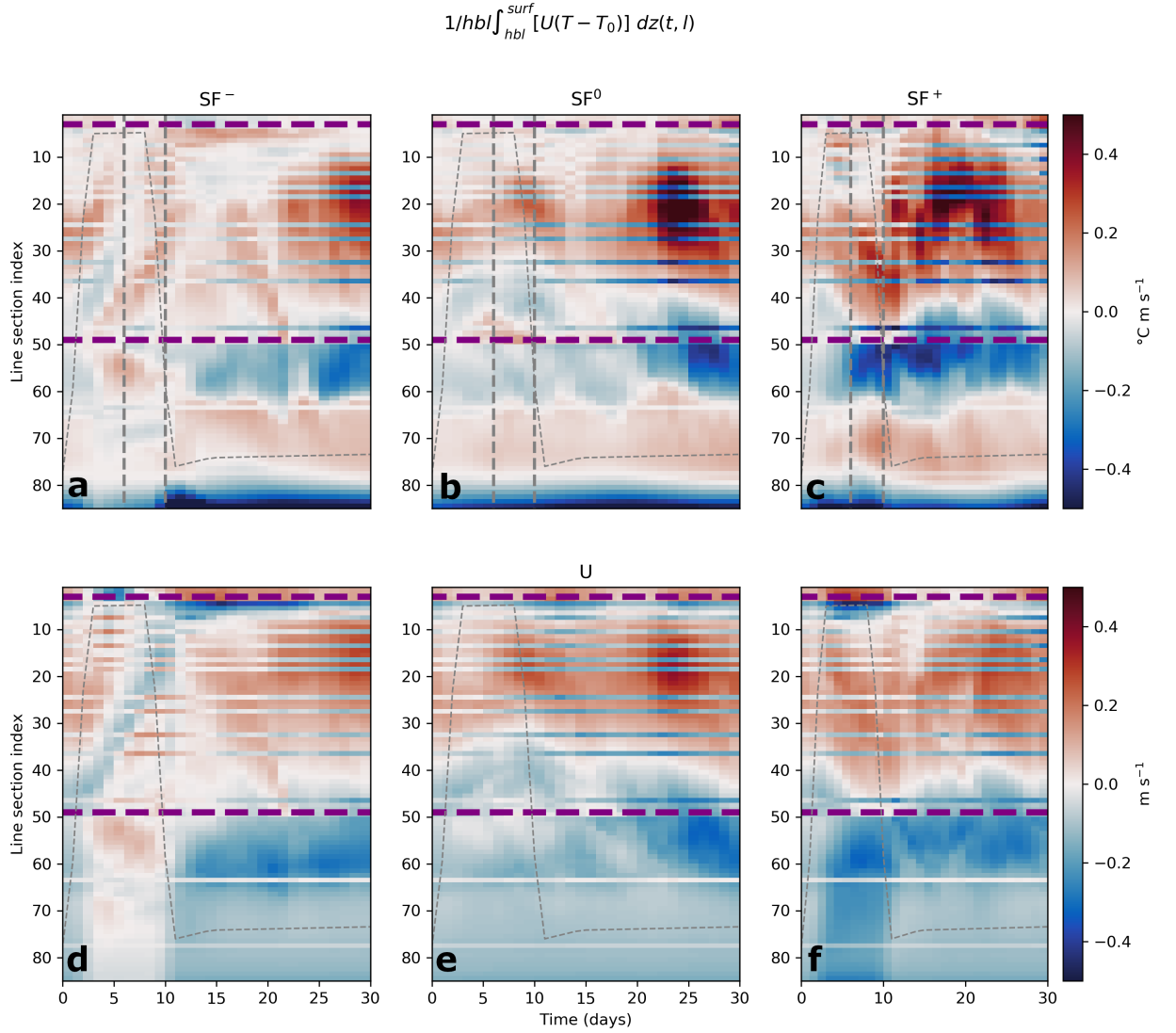


Figure II.30: Heat transport integrated over the SML depth along the sections (upper row). The lower row shows the associated velocity. The three rows indicate SF⁻⁰⁺ ensemble averages responses. The two purple dashed lines indicate the separation between Northern, Western and Southern faces of the box of Fig. I.12.

On a climatological state, the heat transport along the Northern section (line section index < 4) is negligible. Along the northern and middle parts of the Western section (lines section indices 4-~40 in Fig. II.30b), the positive heat transport and the currents oriented towards the box indicate that lateral transport brings water warmer than the average box temperature in the box. Similarly, on the southern part of the Western section and the western side of the Southern section (lines section indices ~40-60), negative heat transport and currents oriented outside of the box indicate that lateral transport expels outside of the box water warmer than the box average temperature, i.e. probably offshore warm waters recently entered inside the box near the boundaries. Similar transport is observed on the very eastern part of the Southern section (lines section indices 80-85), where currents oriented towards the outside of the box expel waters that have been strongly warmed over the very shallow inner shelf. Even if the currents are still oriented towards the outside of the box on the middle of the Southern section (lines section indices ~60-80), a positive lateral heat transport (warms BoxN) is active because waters colder than the box average temperature are expelled outside of the box, i.e. it corresponds to the southwards advection of the cold upwelling tongue. Thanks to this analysis, the exact decomposition of lateral heat transport along the different sections of the box is demonstrated.

Variations of heat transport along boundaries can also explain changes in box average heat budget. For example, in the late response to SF^+ (day ~11), nearly all the Western section injects warmer waters inside of BoxN, while the Southern section heat transport is only slightly intensified (see Fig. II.30c,f). The balance between these two import and export of warm waters could explain the oscillatory behavior of horizontal advection (warming at day 11 and cooling at day 18 in Fig. II.16).

3.6 Sensitivity tests

To complement the description of the vertical scheme sensitivity test (described in the JPO manuscript section 2.6.1), we show an example of instantaneous spatial pattern of the SML depth in Fig. II.31. Spatial structures of $k-\epsilon$ simulations are sharper than smoother KPP structures. Despite the large range of the colorbar, the tendency of $k-\epsilon$ SML depth to be smaller than KPP can be seen just south of Cape Verde.

One important aspect of the response is whether the system reached an equilibrium state or is in a transient phase. In the JPO manuscript section 2.4.3, we mention that the SST seem in a transient phase because it is the only variable that do not exhibit a response in plateau (see Fig. II.10a). We ran a SF^+ simulation in which we changed $T_{syn} = 11$ days to $T_{syn} = 21$ days and show that the SST does not decrease more in Fig. II.32. This indicates that the synoptic period of $T_{syn} \sim 11$ days captures the time scale of the thermal response of the SSUS.

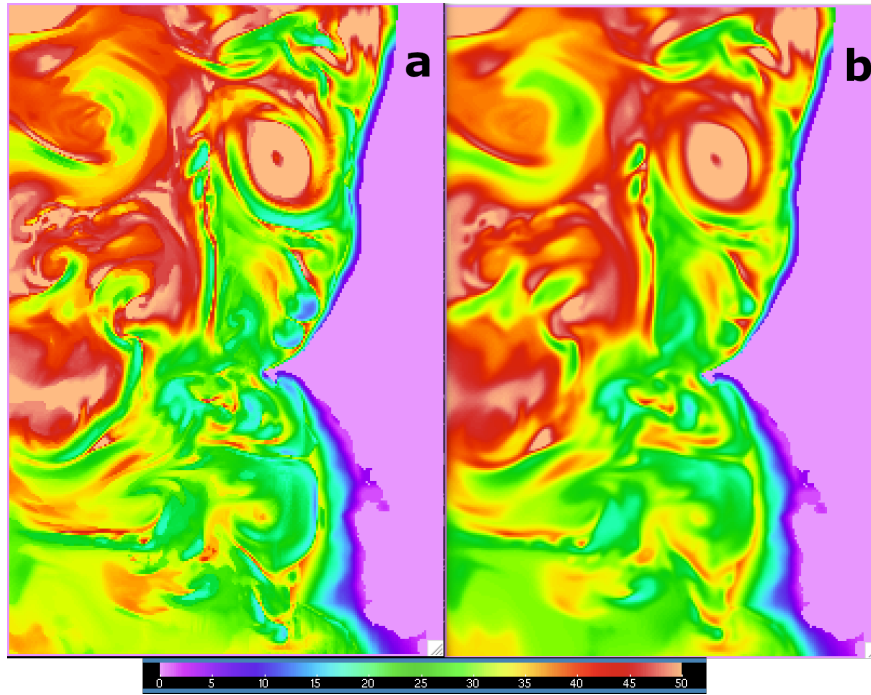


Figure II.31: Surface pattern of the SML depth (in m) on an instantaneous state of the ocean at March 1 using $k-\epsilon$ (a) and KPP (b) vertical mixing schemes. Plot made using the ncview software.

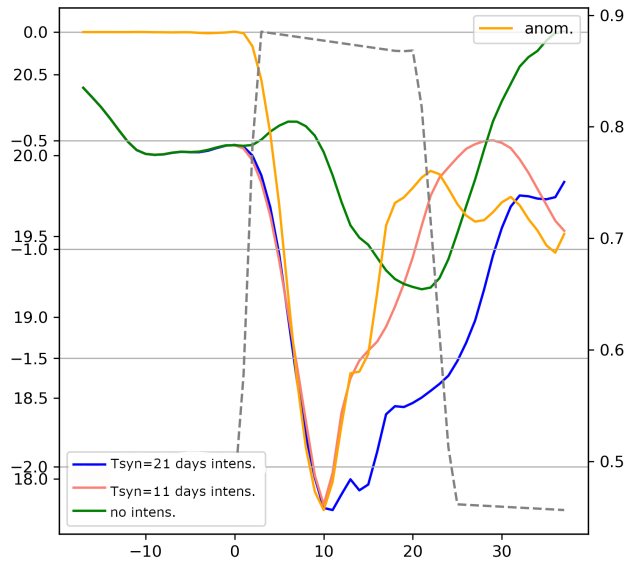


Figure II.32: Time series of the BoxN averaged SST for a $T_{syn} = 11$ days (pink line) and a $T_{syn} = 21$ days intensification (blue line). The anomaly induced by the longer intensification from the unperturbed state (green line) is indicated with the orange line.

4 Discussion

4.1 Ensemble approach

We develop an idealized framework to identify the impacts of synoptic forcings alone on the ocean. The main objective is to reduce the enhanced intrinsic variability (Marchesiello et al., 2003). To do so, we apply the same idealized synoptic wind event and average over the ensemble. Experiments based on an ensemble of climate models or an ensemble of initial conditions are common in climate sciences (Frankignoul and Hasselmann, 1977; Penduff et al., 2014; Lehner et al., 2017; Silvy et al., 2020). Also, it is subtle to extract the impact of the synoptic events because of similar mesoscale and synoptic time scales. Here we justify our experiment choices by comparing them theoretically to other possible experiments and by presenting the advantages of our design.

Our ensemble approach allows the separation of the intrinsic variability and the deterministic (i.e. forced) response of the ocean to a perturbation of the physical forcing. In the JPO manuscript section 2.2.5, we show that one to one comparison of synoptic simulations with the equivalent baseline (climatological simulations having the same initial condition) improves the Signal to Noise Ratio in the estimation of the forced response.

Another possible experiment could have been to estimate the differences between climatological and interannual simulations and would have shown the overall impact of high frequency wind variability. This approach would have been delicate for several reasons. First, assessing the impact of synoptic variability alone is tricky as interannual simulations include other temporal scales of variability, such as interannual variability. Applying interannual wind variability makes it difficult to focus on one specific period of the year (e.g. March); does not assure the same number of intensification and relaxation events; neither their exact symmetry in terms of spatial pattern and time evolution (an average on larger period/space would have been necessary). Our idealized approach guarantees these points by construction. Also, the extraction of the exact forced response of the ocean to an idealized intensification and an idealized relaxation would not have been possible. By comparing these forced responses to climatological simulations, our design allows to compute the residual effects on every physical variable. Also, our design allows a high Signal (deterministic response of the ocean to synoptic forcing) to Noise (intrinsic variability of the ocean) Ratio (SNR, defined in chapter II section 2.2.5) that would have been difficult to achieve with a different experimental setting at a comparable computation cost (see the carbon footprint of the PhD in Appendix V for an order of magnitude of the simulations cost in kgCO₂e).

In agreement with the real ocean complexity, more advanced wind events combinations could have been applied, i.e. including wind history. For example the succession of one intensification and then one relaxation. In this approach, we would have faced many choices of duration of events, time without anomaly between events, magnitude, variability or not of these events properties, etc. If we consider a succession of wind anomalies, the estimation of the exact oceanic anomaly becomes tricky. At the time of a potential second anomaly, the control simulation has a different initial state and, from then, can no longer be used as a control

simulation anymore. Thus, assessing the exact oceanic anomaly induced by wind anomaly n^o2 requires to run a simulation that has felt anomaly n^o1 as a control simulation. But there are endless combinations of wind events with a broad range of time scales (for the length of events and the interval between them) and wind amplitudes that are relevant to the functioning of the real ocean. Our choice to apply only one ideal intensification and one ideal relaxation was made to extract simply the leading order structure and processes in response to wind events.

4.2 General discussion

In addition to the discussion led in the JPO manuscript, we would like to draw the attention of the reader on additional points of general discussion. Circulations of wind-driven flows constrained by shore and bottom topography have been recently reviewed by [Largier \(2020\)](#). Here we wonder how our findings relate to other upwelling bays, and to a larger extent, what are the typical circulation properties of the SSUS.

Two main properties of the flow resulting from the airflow structure and the shoreline shape differentiate upwelling bays and circulations around a Cape. The first typical property is the ability of the flow to detach from shore (flow separation) and the second property is its ability to recirculate in the bay. First, in our case, given the shape of the northern coast, the radius of curvature of the Cape and the Rossby radius, the flow coming from the north of Cape Verde detaches and expels coastal waters offshore. [Ndoye et al. \(2017\)](#) and our findings support the idea that the source waters of the flow south of the Cape do not originate from the jet north of the Cape. Second, south of the Cape, i.e. within the upwelling bay, the circulation is anticyclonic and no recirculation occurs. We compare this circulation to [Largier \(2020\)](#) categories in [Fig. II.33](#). The SSUS circulation would stand between panel a and panel b categories, with the addition of the separation of the northern flow and no recirculation ([Fig. II.33d](#)).

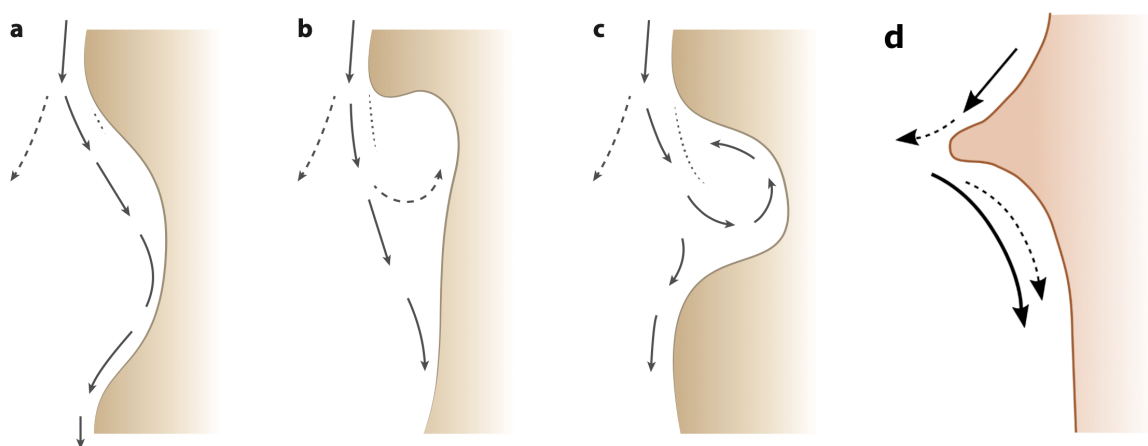


Figure II.33: Different types of circulations around bays in upwelling systems, adapted from [Largier et al. 2019](#) (a-c) and our analysis (d). Continuous lines indicate flow patterns and dashed lines indicate flow separation.

Other upwelling bays properties resemble to those of the SSUS but its exact circulation seem to be infrequent. Here we present a few sectors that we believe have comparable properties, but do not pretend to list them exhaustively. In the Valparaíso bay along the west coast of south

America, the circulation is sheltered north of Topocalma Point (equatorward winds in Southern hemisphere). The circulation is anticyclonic, follows the bay coastline and there is no recirculation inside the bay (Aiken et al., 2008) like in the SSUS. However the coastline break is not as sharp as Cape Verde and there is no flow separation. Valparaiso bay and also Agadir bay, south of Cape Ghir along the northwest coast of Africa, that presents similar properties (Van Camp et al., 1991; Mittelstaedt, 1991), can be both categorized to the typical water flow patterns of panel a in Fig. II.33a (Largier, 2020). Despite the irregular upwelling favorable wind conditions and few observations and studies, the system of the Walker bay off South Africa (Jury, 1988) seem to perform flow separation at Danger Point without recirculation inside the bay like the SSUS.

Many times during our analyses we were tempted to call the inner part of the shelf an upwelling shadow, but we refrained to do so for a few reasons. It is true that it is close to an active upwelling sector, is somewhat sheltered from upwelling favorable winds by the cape/coast, and acts as a refuge from turbulence, dilution and offshore export, has high retention times (Ndoye et al., 2017) and a strong SST front. However, there is no recirculation features, e.g. a cyclonic circulation like in Monterey Bay (Graham and Largier, 1997; Paduan et al., 2018), and its enrichment in new nutrients is ambiguous, as most of the high primary production is due to regenerated production (in anticipation of chapters III and IV findings). Also, important residence times over the SSUS are not necessarily related to sheltered conditions but to the elongated shape of the bay. As each bay offers different combination of circulation and environment characteristics, it is pertinent to cluster upwelling bays by common properties, but it might be reductive and misleading to present a sector only with the properties of one group.

5 Conclusion

As a concluding part, we rely on the schematic II.34 that sums up the majority of our findings. During SF^+ , atmospheric heat fluxes are reduced, the SML is deepened, the equatorward upwelling jet is intensified, vertical velocities south of CV are increased. Thus, the vertical advection cools down the SML over a very localized area. The input of warm water from the western side of the shelf is weaker than their exit in the southern area such that the horizontal advection is the main driver of the SML heat changes. During SF^- , atmospheric heat fluxes are increased, the SML is shoaled, the equatorward upwelling jet is nearly canceled and the subsurface poleward jet extends further upward. The exit of cold waters south of CV and the entry of warm offshore waters over the shelf that result from the relaxed jet also lead to a warming of the SML through horizontal advection.

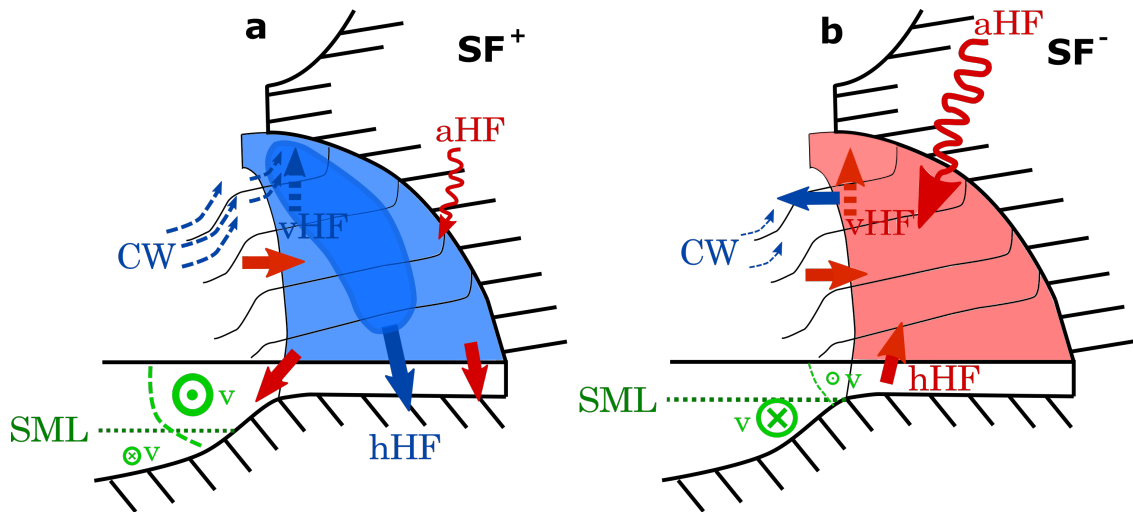


Figure II.34: Schematic of 3D shelf dynamical and heat response to SF^+ (a) and SF^- (b). Different heat fluxes are distinguished (atmospheric aHF, vertical vHF and horizontal hHF). Positive (red) and negative (blue) rates of heat in the box SML is indicated in color for each flux and for the shelf box average. Straight continuous (resp. dashed) arrows indicate horizontal (resp. vertical) currents associated to heat transport. Cold Water (CW) upwelling is indicated with along shelf slope/vertical dashed arrows. Green dotted and dashed lines indicate the SML depth and the southwards upwelling jet extent, with the associated alongshore currents v indicated with green dot and cross symbols.

In this study, we uncover in a new manner the major impact of synoptic wind intensification and relaxation on the physical structure of the SSUS and the emergence of robust mesoscale features. We identify the processes responsible for the SML heat changes and we put forward the infrequent properties of the SSUS in comparison to other sectors. We demonstrate the only modest asymmetrical response of the SSUS to SF^+ and SF^- .

The next steps to determine finest responses of generic coastal upwelling sectors under synoptic wind variability and advance the knowledge of the SSUS are several. The examination of interannual simulations would help comparing and discuss our idealized results. More generally, a focus on asymmetrical responses of other sectors to SF^+ / SF^- (in the continuity of Desbiolles et al., 2014; García-Reyes et al., 2014) would be a way to assess global properties of coastal upwelling systems. Over the SSUS, fine Lagrangian analysis (following Ndoye et al.,

2017 findings) can unravel subtleties of the origin of source waters and their impact on the SSUS dynamics. Despite their limited robustness close to shore, an analysis of long term satellite observations is an option to assess the SSUS interannual variability and explore its link to climate variability. Given the strong primary production in coastal upwelling systems (Messié and Chavez, 2015), assessing the impact of synoptic wind variability on the planktonic ecosystem and the identification of processes at play is essential. This is investigated in chapters III and IV.

Bottom-up propagation of synoptic wind intensification and relaxation in the planktonic ecosystem

Contents

1	Preamble	132
2	Bottom-up propagation of synoptic wind intensification and relaxation in the planktonic ecosystem of the South Senegalese Upwelling Sector: GRL draft . .	133
2.1	Introduction	134
2.2	Physical-biogeochemical models and numerical experiment	135
2.3	Planktonic ecosystem mean state	136
2.4	Responses to synoptic forcing perturbations	137
2.5	Propagation of atmospheric perturbations towards and up the planktonic ecosystem	139
2.6	Inner shelf specificities	140
2.7	Discussion and conclusion	141
3	Complementary comments	143
3.1	Supporting Information of the GRL draft: Response of the inner shelf to synoptic forcings	143
3.2	Temporal evolution of the along shelf structure of the ecosystem	145

1 Preamble

In this chapter, we present the main findings of our experiment of synoptic forcing over the SSUS planktonic ecosystem as a whole. It is composed of a manuscript in preparation to submit to Geophysical Research Letters (GRL, reformatted for the thesis manuscript), its supplementary material and brief complementary comments. A more general discussion on planktonic ecosystem dynamics at the synoptic scale over the Senegalese shelf is presented in chapter IV.

2 Bottom-up propagation of synoptic wind intensification and relaxation in the planktonic ecosystem of the South Senegalese Upwelling Sector: GRL draft

Pierre Chabert¹, Vincent Echevin¹, Xavier Capet¹

Keypoints

- Biogeochemical properties oscillate in space and time in response to synoptic fluctuations
- The synoptic forcing perturbation is damped as it propagates towards and up the planktonic ecosystem
- The response of the ecosystem is heterogeneous over the shelf, with a distinctive inner shelf behavior

Abstract

Synoptic intensifications or relaxations of ~10 days of upwelling favorable winds are of major importance for a better understanding of dynamical and biogeochemical properties of Eastern Boundary Upwelling Systems. This study aims to investigate their impact on the planktonic ecosystem of the South Senegalese Upwelling Sector (SSUS), located south of the sharp Cape Verde peninsula and over a particularly shallow continental shelf. Numerical experiments allow to represent the response of coastal the planktonic ecosystem to idealized synoptic wind intensification and relaxation. We find that atmospheric synoptic perturbations modify the circulation over the shelf and induce spatial and temporal oscillations of plankton concentrations. Zooplankton respond with a time and space delay with respect to phytoplankton, which corresponds to the along advection evolution of the planktonic ecosystem. We show that this perturbation tends to be damped towards the upper trophic levels of the ecosystem. These responses are heterogeneous over the shelf, with a specific inner shelf behavior, where retention is enhanced and nitrate depleted, in agreement with its sheltered environment.

Plain Language Summary

Over certain coasts of the world, wind blows alongshore and induce subsurface, cold and nutrient rich waters to rise near the surface and favor the development of plankton. Here we present the effects of ~10 days wind fluctuations, stronger or weaker than usual, on the plankton communities of the Senegalese coastal waters. We shed light on the responses of both phytoplankton and zooplankton that are strongly perturbed in a non linear way. We also find that these responses vary with the area of interest, close or further away from to the coast.

¹Sorbonne Université, CNRS, IRD, MNHN, Laboratoire d'Océanographie et du Climat: Expérimentations et Approches Numériques (LOCEAN-IPSL), Paris, France

2.1 Introduction

Alongshore upwelling favorable winds over Eastern Boundary Upwelling Systems affect ocean currents, bring nutrient-rich waters to the euphotic layer and cause high biological productivity associated to 20% of fish global catches (Fréon et al., 2009; Chavez and Messié, 2009). In addition to the seasonal cycle of these winds, many studies have shown the importance of synoptic time scales (5-10 days) on the dynamics and biogeochemical properties of coastal upwelling ecosystems (Largier et al., 2006; Botsford et al., 2006; Desbiolles et al., 2014; Capet et al., 2017; Aguirre et al., 2021). In particular, García-Reyes et al. (2014) found a better agreement of indices based on cumulative oceanic responses (e.g. cumulative index of surface nutrient during synoptic events) with chlorophyll concentration and zooplankton populations rather than with traditional upwelling indices based only on wind intensity (Bakun, 1973). Synoptic variability consists of a succession of intensifications and relaxations of upwelling favorable winds, that can have positive or negative impacts on primary production. Several studies emphasize the need of moderate winds (Cury and Roy, 1989; Jacox et al., 2016) and especially the succession of an upwelling wind event (inducing a pulse of nutrients in the euphotic layer) followed by a relaxation period of a few days to maximize primary production (Largier et al., 2006; Wilkerson et al., 2006).

Whether or not the ecosystem response associated to a synoptic wind intensification is symmetric to that associated to a relaxation allows to evaluate rectification effects and the overall impact of synoptic variability. Concerning the physical structure, some studies shed light on irreversible processes during relaxation and associated important asymmetries (Send et al., 1987), while other studies indicate weaker rectification effects (Aguirre et al., 2014) (Chabert et al., accepted in JPO). Processes driving biogeochemical and biological tracers concentrations may have asymmetrical responses to synoptic fluctuations and induce ecosystem asymmetries (Send and Nam, 2012; Dorman et al., 2005; Morgan et al., 2018; Aguirre et al., 2021).

Synoptic wind fluctuations influence biological productivity first by altering several physical processes. Nutrient supply in the euphotic layer is directly impacted by wind variability through changes of vertical velocities due to the divergence of wind-driven surface currents at the coast and altered stratification (Jacox and Edwards, 2011). Increased wind-driven vertical mixing may dilute or bring biological material below the euphotic layer where phytoplankton growth is limited by light (Largier et al., 2006). Also, synoptic wind variability modifies retention, dilution or loss of biological material through horizontal advection changes (Botsford et al., 2003, 2006). Changes in mesoscale activity may impact the offshore transport of nutrients and organic matter, the associated reduction of nearshore productivity through eddies and filaments (Cury and Roy, 1989; Botsford et al., 2003; Gruber et al., 2011; Lachkar and Gruber, 2011), and the structure of the planktonic ecosystem and associated carbon export (Hauschildt et al., 2021; Nagai et al., 2015; Stukel et al., 2017; Chabert et al., 2021). These processes occur in a complex coastal environment where coastline irregularities, shelf width and capes also have a direct impact on the circulation and biogeochemical fields (Largier, 2020),

In this study we aim to develop a realistic, though idealized, biogeochemical simulation of the South Senegalese Upwelling Sector (SSUS) that is located south of the sharp Cape Verde (CV) and that has a wide and shallow continental shelf. Despite a moderately known biogeo-

chemical structure over the northwest African sector (e.g. [Lathuilière et al. \(2008\)](#); [Auger et al. \(2016\)](#)), the dynamics of the shelf planktonic ecosystem at synoptic time scales remains poorly known. We aim to describe the general properties of a planktonic ecosystem model viewed as a non linear dynamical system ([Franks, 2002](#)) kicked by synoptic wind intensification and relaxation perturbations. We focus on the impact on nutrient, phytoplankton and zooplankton concentrations; spatial and temporal responses; propagation of the perturbations towards and up the planktonic ecosystem and spatial heterogeneities.

2.2 Physical-biogeochemical models and numerical experiment

We develop a numerical experiment that involves applying idealized synoptic wind perturbations on an ensemble of climatological initial states to obtain a robust response. We use the Coastal and Regional Ocean COmmunity model (CROCO, from <https://www.croco-ocean.org/>, [Hilt et al. \(2020\)](#)), derived from Regional Ocean Modeling System (ROMS, [Shchepetkin and McWilliams \(2005, 2009\)](#)). The model configuration is inherited from [Ndoye et al. \(2017\)](#) and Chabert et al., accepted in JPO) (details on models settings and numerical experiment are available in the supplementary information). We couple CROCO to the marine biogeochemistry model Pelagic Interactions Scheme for Carbon and Ecosystem Studies (PISCES, from <https://www.pisces-community.org/>, [Aumont et al., 2015](#); [Auger et al., 2016](#)). It represents the main nutrients (nitrates, phosphates, silicate and iron) and has four living compartments: nanophytoplankton, diatoms, microzooplankton and mesozooplankton. We also take into account the modification of light propagation in the water column induced by chlorophyll shading ([Echevin et al., 2021](#)).

We first run simulations with monthly climatological forcings to obtain an ensemble of initial states. Then, we build idealized synoptic surface wind stress and air-sea heat fluxes anomalies using ERA5 reanalyses ([Hersbach et al., 2018](#)). The amplitude of the anomalies spatial patterns is modulated in time over a period of 10 days, as shown by the grey dashed line in Fig. III.3a. We apply these idealized symmetric atmospheric perturbations (anomalies), i.e. the synoptic upwelling favorable wind intensification (positive Synoptic Forcing perturbation: SF^+) and relaxation (negative Synoptic Forcing perturbation: SF^-) over the ensemble of initial states on 1 March (day 0 in our analysis). The climatological reference simulations without perturbation are denoted SF^0 . Ensemble averaging allows to extract the forced response from intrinsic variability (all the fields shown in the following are ensemble averages). Additional information on experimental settings can be found in the supplementary information. The evaluation of the model climatological simulations against available biogeochemical observations (satellite Chl-a from [Gohin et al. \(2002\)](#) and World Ocean Database [Garcia et al., 2018](#)) is presented in the supplementary information.

During the upwelling season, the physical structure of the SSUS can be described as follows. Surface currents south of CV follow the shelf widening isobaths ([Pringle, 2002](#); [Ndoye et al., 2017](#)) forming an anticyclonic circulation south of CV and a cold upwelling tongue flowing southwards along the entire shelf (Figure III.1a). A pattern of minimum SST is found south of CV along the 20 m isobath, where vertical velocities transport subsurface waters into the upper layer (Figure III.1a,d; $\sim 17.2^\circ W; 14.3^\circ N$, see also [Ndoye et al. \(2017\)](#) and Chabert et al., accepted

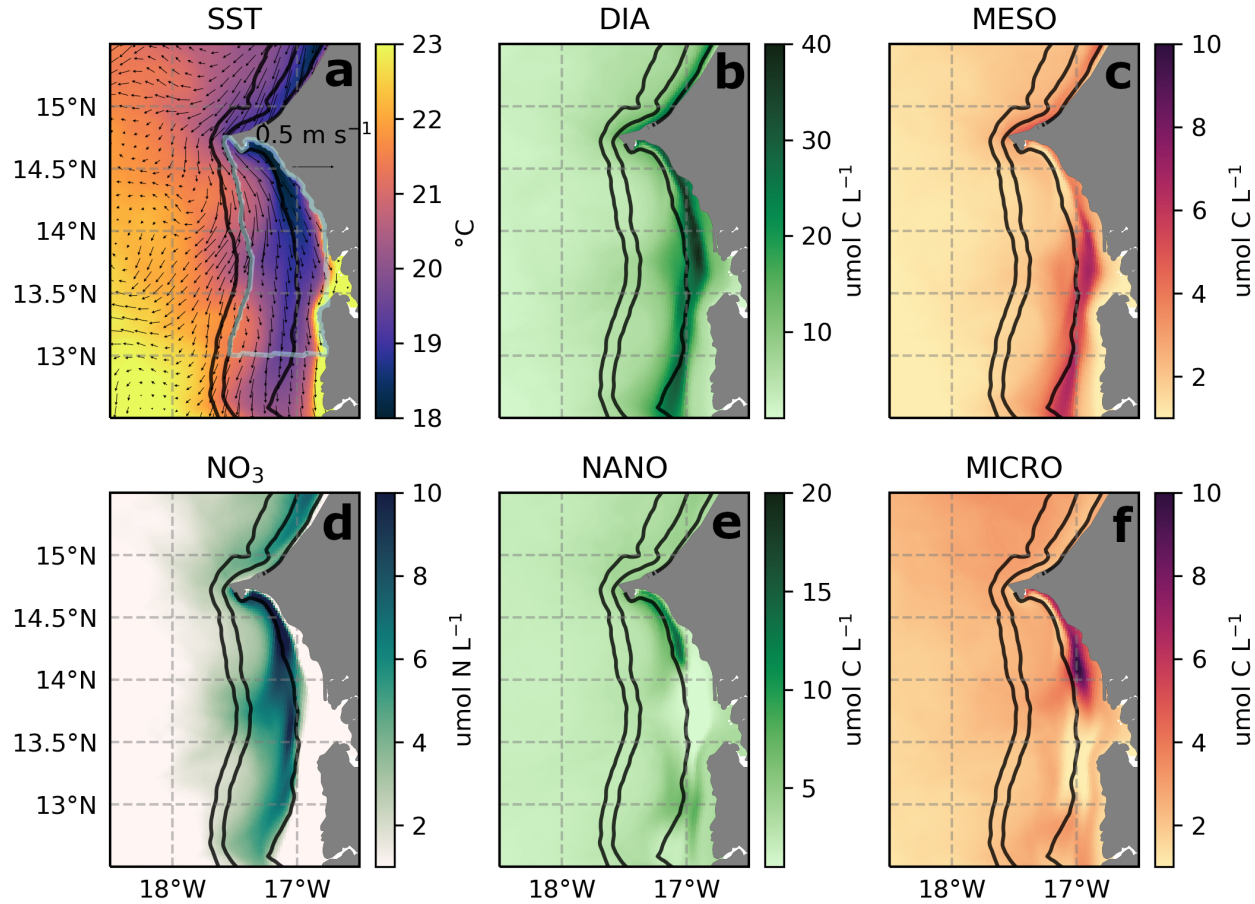


Figure III.1: Surface patterns of Sea Surface Temperature (SST, a), NO_3 (d), diatoms (b), nanophytoplankton (e), microzooplankton (f) and mesozooplankton (c) concentrations averaged over the ensemble for SF^0 between days 0 and 30. The average box is indicated with the light grey contour on panel a. The black lines indicate the 20, 100 and 500 m isobaths. Note that colorbar ranges are different for diatoms and nanophytoplankton. The Cape Verde (CV) is the land promontory extending westward at 14.7°N .

in JPO). The inner shelf, over which the bottom and surface boundary layers merge (Estrade et al., 2008) is the strip of water inshore of the ~ 20 m isobath where the euphotic layer reaches the bottom.

2.3 Planktonic ecosystem mean state

The nitrate maximum and the SST minimum collocate south of the Cape while the inner shelf is nitrate-depleted. Diatoms are more competitive than nanophytoplankton and dominate in nutrient rich coastal areas (Figure III.1b,e, Hutchings et al., 1995; Irigoien et al., 2005). The maximum diatoms concentration is found over the inner shelf between 13.5 - 14.5°N (Figure III.1b).

The ecosystem structure evolves after upwelling along its horizontal advection pathways (Messié and Chavez, 2017; Chabert et al., 2021), along shelf in our case. To characterize this evolution, we average variables over vertical sections between the 100 m isobath and the coast and first present these quantities for SF^0 (Fig. III.2, green lines; temporal average described below).

The spatial patterns (Fig. III.1b,e,c,f) and depth and cross-shore averages (Fig. III.2b,c,d,e; green lines) of planktonic species illustrate their oscillatory behaviors along their southwards advection over the shelf. Nitrate values are high in the northern part of the shelf ($\sim 14.7^\circ\text{N}$) and decrease as the water mass is advected southward.

Nanophytoplankton concentration oscillates between high values in the northern (due to their rapid growth) and southern parts of the shelf (between 14 - 14.5°N and around 13°N) and a minimum at 13.75°N . Microzooplankton graze on nanophytoplankton along the advection and peaks around 13.75 - 14°N and below 13°N . Around 13.75°N and in the southern part of the shelf (12.5 - 13°N), diatoms and mesozooplankton successively reach their maximum.

2.4 Responses to synoptic forcing perturbations

2.4.1 Perturbed spatial oscillations

SF^\pm perturbations modify the spatial oscillations of plankton concentrations by altering intensities and locations of their extrema (Fig. III.2). We focus on the time period (9-11 days, i.e. near the end of SF^\pm) when the ecosystem is the most perturbed spatially. The description of the temporal variations of these spatial oscillations that represent transitions between the mean and the most perturbed states is beyond the scope of this study.

For SF^+ (resp. SF^-), the maximum values of all variables are increased (resp. decreased) and displaced southwards (resp. northwards) along the mean flow pathways (Fig. III.2). During SF^+ , small plankton species are remarkably perturbed: nanophytoplankton maximum shifts from 14.25 to 13.8°N (~ 50 km) and triples in amplitude, and microzooplankton shifts from 14 to 13.6°N , increasing by $\sim 50\%$ at its peak with respect to SF^0 . Larger plankton (diatoms and mesozooplankton) concentrations increase mostly in the southern part of the shelf. Both zooplankton concentrations decrease importantly in the northern part of the shelf.

During SF^- , all spatial oscillations are damped such that plankton concentrations are more homogeneous over the shelf compared to SF^0 . Relaxed currents lead to the collocation of nearly all the remaining extrema of the plankton concentrations in the northern part of the shelf. Accordingly, the maximum of mesozooplankton is remarkably shifted northwards. This indicates the reduction of the spatial decoupling between trophic levels during upwelling-favorable wind relaxations, in agreement with findings from a modeling study in the California current ecosystem (Spitz et al., 2005).

2.4.2 Temporal oscillations

Plankton responses also exhibit large oscillations in time. The properties of the temporal responses (amplitude and time scales) are identified by averaging of the quantities over the shelf, i.e. between latitudes 13 - 14.75°N and 0 - 100 m isobaths (see grey box in Fig. III.1a). Nitrate and plankton concentrations tend to increase during SF^+ and decrease during SF^- with different time scales and extrema intensities (Fig. III.3). For SF^+ , the maximum value of nitrate is reached at day 9, nanophytoplankton at day 11, diatoms at day 13, microzooplankton at day 15 and mesozooplankton at day 17 (each planktonic extremum is reached broadly ~ 2 days earlier for SF^-).

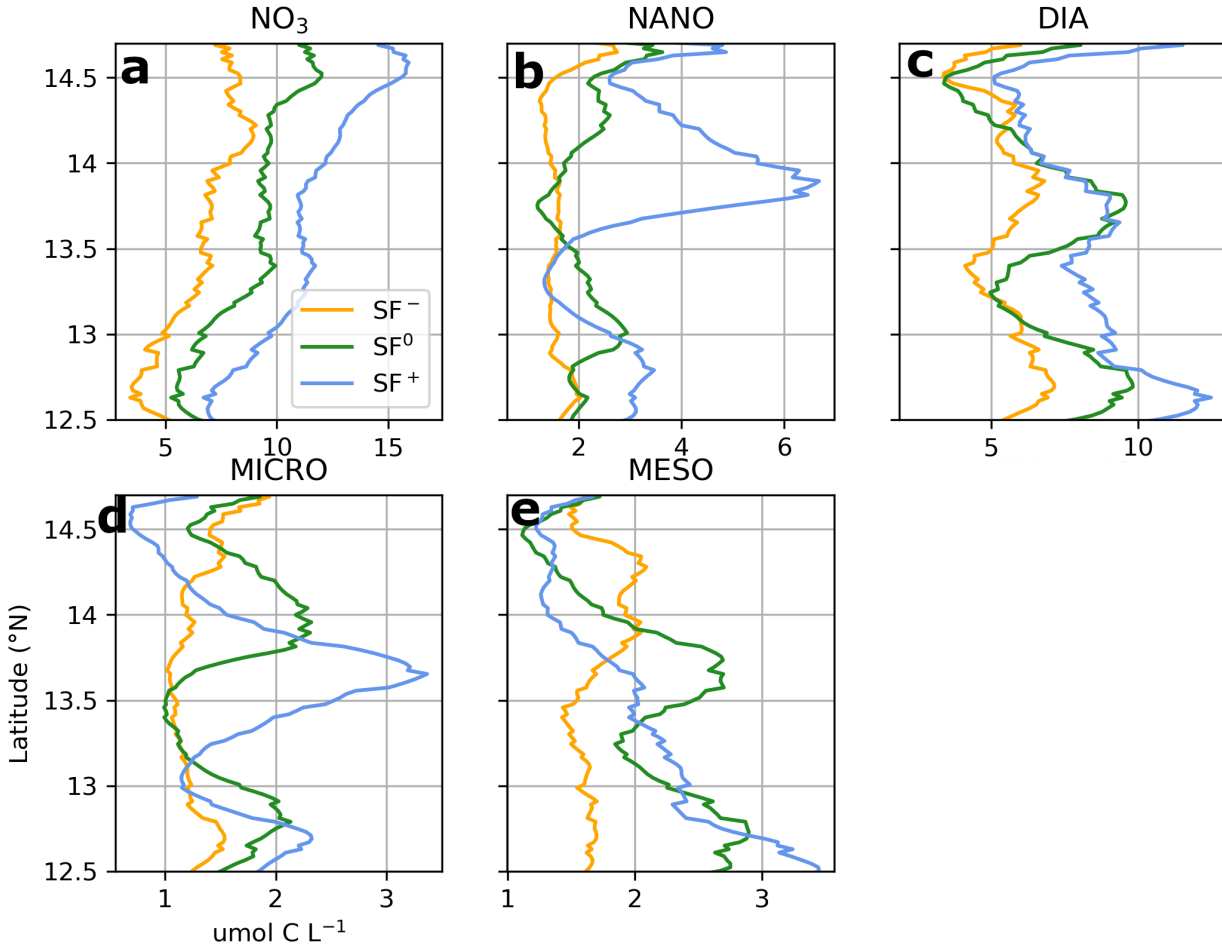


Figure III.2: Nutrient and biological quantities averaged within the 100-0 m isobaths and from the bottom of the water column to the surface between days 9-11, and over the ensemble. SF^- , SF^0 and SF^+ are indicated in orange, green and blue lines.

All plankton concentrations oscillate in time in response to SF^\pm . Except nanophytoplankton, all plankton concentrations present first a weak decrease (resp. increase) in the first days of SF^+ (resp. SF^-), followed by a strong increase (resp. decrease) after the end of the SF perturbation. Oscillations of large plankton species (Fig. III.3b,e) have longer time scales and weaker amplitudes than those of small plankton (Fig. III.3c,d). In accordance with their robust spatial patterns (evaluated by examination of individual members, not shown), small plankton responses are more deterministic than large plankton (see the weaker standard deviations in Fig. III.3c,d). Prey-predator relationships induce a time delay between phytoplankton and zooplankton oscillations. During their transition back to climatological values after SF^- , nanophytoplankton and microzooplankton biomass undergo an additional oscillation, likely due to prey-predator relationships stabilization.

Asymmetric responses of oceanic variables to symmetric synoptic atmospheric anomalies indicate the impact, and potential residual effects, of synoptic variability on the climatological mean state. We estimate this residual with $\mathcal{R}_{\text{SF}}(X) = \frac{\text{RES}_{\text{SF}}(X)}{X_{\text{SF}^0}} = \frac{\frac{1}{2}(X_{\text{SF}^+} + X_{\text{SF}^-})}{X_{\text{SF}^0}} - 1$, computed

2. Bottom-up propagation of synoptic wind intensification and relaxation in the planktonic ecosystem of the South Senegalese Upwelling Sector: GRL draft

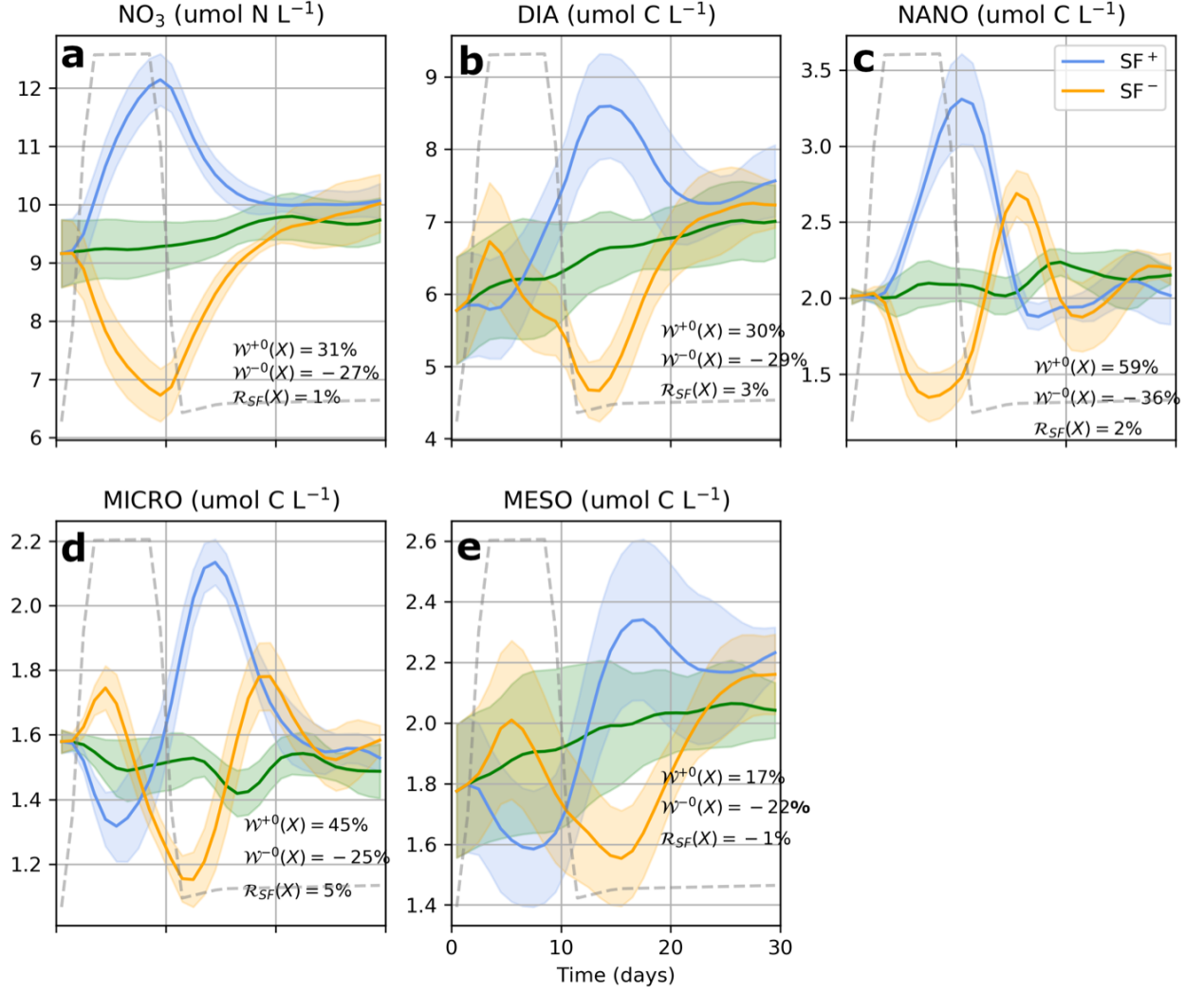


Figure III.3: Nutrient and biological quantities averaged over the shelf in the whole water column, and over the ensemble. Green, orange and blue lines indicate SF^0 , SF^- and SF^+ . Shaded areas indicate the ensemble standard deviation. $\mathcal{W}^{\pm 0}$ and \mathcal{R}_{SF} diagnose maximum of relative perturbations and asymmetries. The box of integration is shown on Fig. III.1a grey line (between 13-14.75°N and 0-100 m isobaths). The trend in all time series corresponds to the seasonal cycle.

from averages between days 9 and 14 included. We find only modest residual effect of biogeochemical variables (5-15%) associated to modest asymmetries, of the same order of magnitude as the physical ones (Chabert et al., accepted in JPO).

2.5 Propagation of atmospheric perturbations towards and up the planktonic ecosystem

The temporal modifications of biomass are robustly out of the range of their intrinsic variability (Fig. III.3). We now examine the weight of these perturbations compared to their mean state in each variable and how the atmospheric perturbation propagates towards the upper trophic lev-

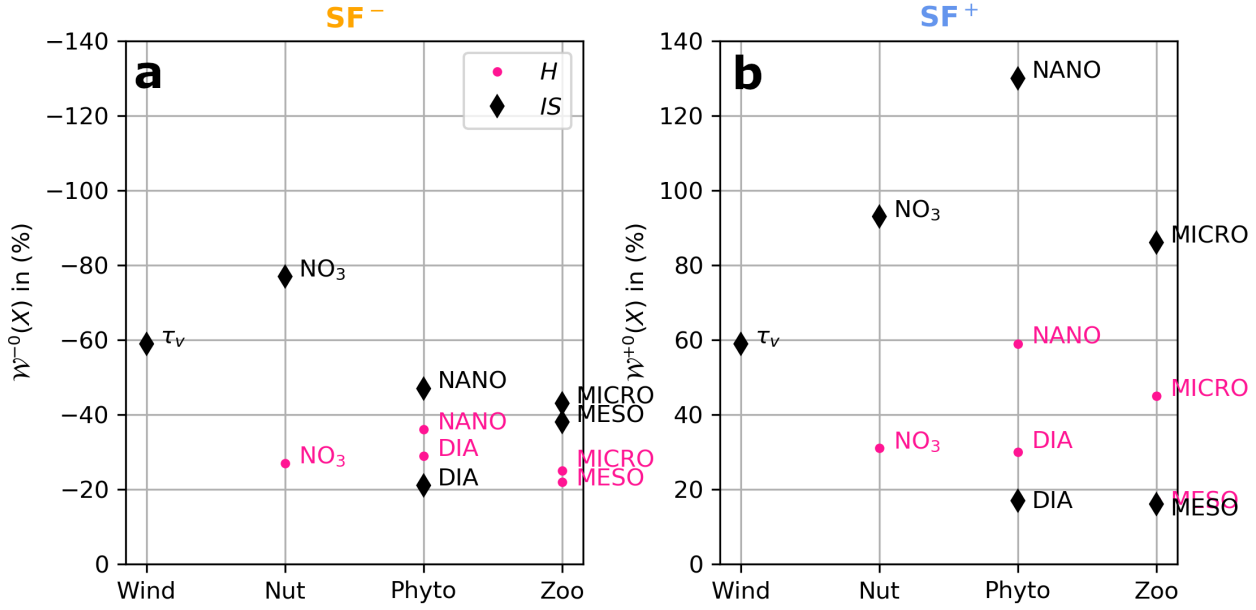


Figure III.4: Weight of SF^- (a) and SF^+ (b) perturbations along biogeochemical and biological levels over the entire shelf (H) and inner shelf (IS).

els of the ecosystem. We quantify this bottom-up propagation of atmospheric SF perturbations by computing the maximum weight of the perturbations relative to their mean state over the 30 days of the experiment: $W^{\pm 0}(X) = \max_t \left(\frac{X_{SF^{\pm}} - X_{SF^0}}{X_{SF^0}} \right)$.

A wind perturbation of $\sim 60\%$ results in a maximum change of $\sim \pm 30\%$ of nitrate concentration during SF^{\pm} compared to SF^0 (see pink dots in Fig. III.4). The propagation is more complex towards the upper biological levels. Largest size plankton in each level are subject to similar or weaker relative perturbations (diatoms: $\sim 30\%$; mesozooplankton: $\sim 20\%$). Small plankton size globally undergo higher perturbations that reach up to $\sim 60\%$ for nanophytoplankton under SF^+ conditions. Except this amplification, all the perturbations of nutrient and biological levels are below the initial atmospheric perturbation. Thus, in both small and large size classes, the perturbation is damped from phytoplankton to zooplankton. Overall, the atmospheric SF perturbation is damped towards and up the planktonic ecosystem.

2.6 Inner shelf specificities

The damping of the atmospheric perturbation described previously is specific to the entire shelf. However, the planktonic ecosystem response is spatially heterogeneous, with different patterns emerging over the inner shelf.

The lower nitrate concentration over the inner shelf ($\sim 3 \mu\text{mol N L}^{-1}$ compared to $9 \mu\text{mol N L}^{-1}$ over the entire shelf, see Figure S4) is more impacted by SF perturbations. Its perturbation is nearly three times larger than over the entire shelf ($\sim 80\text{-}90\%$, see black diamonds in Fig. III.4). Also, the responses of small plankton to SF perturbations are drastically increased over the inner shelf. This is particularly true during SF^+ when the perturbation is amplified from the physical forcing towards the nitrate concentration, small sizes phytoplankton and zooplankton (Figure II.5). On the contrary, large plankton are even more damped over the inner shelf rather than

over the entire shelf (Fig. III.4, note that this is less true for mesozooplankton during SF⁻). Thus, the response is more non linear over the inner shelf, showing that the amplification or damping of the atmospheric SF perturbation strongly depends on the event and domain.

In contrast to the nitrate depletion south of 13.5-14°N (see Fig. III.5 of the supplementary information), all plankton concentrations are higher over the inner shelf than averaged over the entire shelf. Spatial oscillations are weaker over the inner shelf (there are less local extrema; compare Fig. III.2 and Fig. III.5 of the supplementary information). Planktonic concentrations also present weaker oscillations in time over the inner shelf, especially for zooplankton species that do not present a first local extrema (compare Fig. III.3 and Fig. ?? of the supplementary information).

2.7 Discussion and conclusion

These results are in agreement with the patterns and time scales of previous studies (Menkes et al., 2002; Messié and Chavez, 2017). Especially, we identify zooplankton high concentrations patches along surface advection pathways downstream of the nutrient supply in the upper layer by upwelling. Concerning the robust high and low concentration patches of nanophytoplankton and microzooplankton, we hypothesize that they are due to the combination of robust circulation pathways, phytoplankton growth and prey-predator relationship time scales that induce a deterministic ecosystem structure. We hypothesize that the small size plankton species respond more deterministically than the large size plankton because of their rapid growth rates that induce a faster response to an environmental anomaly.

This study supports the hypothesis that asymmetries to intensification and relaxation are modest in nutrients and plankton biomass responses (in agreement with dynamical responses of Chabert et al., accepted in JPO) and brings evidence of the domain-dependence of biogeochemical asymmetrical responses. Nevertheless, our ecosystem model may underestimate rectification due to unrepresented mechanisms, such as diel vertical migration that could lead to a misrepresentation of nearshore zooplankton structure (Batchelder et al., 2002; Carr et al., 2008; Messié and Chavez, 2017).

The oscillatory responses of plankton biomass suggest us to design additional modeling and in situ experiments. First, applying a second SF anomaly in the simulations when the planktonic ecosystem is already perturbed would be indicative of its response to an additional perturbation from a non-steady initial state, and if it amplifies or damps its oscillations. Second, interesting information about ecosystem responses to extreme events could be assessed by increasing the amplitude of the SF anomaly. Third, increasing the number of measurements over the Senegalese shelf is necessary to evaluate the spatial and temporal structure of biogeochemical fields. These observations are needed to confront the oscillatory ecosystem patterns of our model, as they may be shaped by model mathematical non linear relationships (Flynn, 2005), resulting from Michaelis-Menten representations (Michaelis and Menten, 1913) that may be unadapted for plankton dynamics (Franks, 2009). This evaluation could be done by measuring chlorophyll-a as a proxy for phytoplankton biomass at several fixed locations along the shelf (e.g. on buoy just south of CV, in the spirit of Melax buoy Tall et al., 2021).

Identifying precisely the mechanisms driving the ecosystem response was not the objective of this study. However, results of a budget of diatoms, the dominant plankton species over the shelf, provide hints to identify the processes mainly responsible for changes in their concentration over the shelf. For example, the first local minimum of diatoms concentrations during SF⁺ (Figure III.3b) is mainly explained by intensified horizontal advection that induce a loss of biological material over the shelf and by a reduction of primary production (not shown). Also, an analysis of the cumulative primary production of diatoms sheds light on favorable conditions for growth. Unexpectedly, upwelling relaxation enhances primary production more strongly than upwelling intensification over the course of the event and induce a strong asymmetrical response. This, along with dynamical arguments in [Ndoye et al. \(2017\)](#) (i.e. the persistent strip of warm water nearshore) and [Wilkerson et al. \(2006\)](#) findings promote the idea that the shelf primary production benefits more from retention and reduced light limitation rather than nutrient enrichment. However, we find an opposite response between primary production and biomass, such that upwelling intensification is beneficial for plankton biomass. This contrasts with previous findings on the benefits of relaxed conditions after upwelling for plankton biomass ([Dorman et al., 2005](#); [Largier et al., 2006](#); [Evans et al., 2015](#); [Aguirre et al., 2021](#)). In our diatoms budget, this is explained by zooplankton grazing that counter balance primary production anomalies, leading to biomass anomalies of opposite sign.

Predicting primary production variability and the associated consequences on upper trophic levels is a great challenge given the variability of atmospheric forcing and oceanic responses ([Botsford et al., 2006](#); [García-Reyes et al., 2014](#); [Cury and Roy, 1989](#); [Aguirre et al., 2021](#)). In spite of the observed wind variability, we aimed to simplify the forcing the most to extract first order properties of the response of a typical planktonic ecosystem model. We uncovered noticeable properties like the spatial and temporal oscillations of plankton biomass, the bottom-up propagation and damping of the perturbation towards the upper trophic levels and the domain dependence of the response. In this study, we have provided first baseline simulations of the planktonic ecosystem at the synoptic scale of the South Senegalese Upwelling Sector, which is poorly known, has important socio-economic implications and is vulnerable to climate change ([Sylla et al., 2019](#); [Bograd et al., 2023](#)).

3 Complementary comments

3.1 Supporting Information of the GRL draft: Response of the inner shelf to synoptic forcings

The supporting information prepared for submission of the GRL draft consists first of information on the model settings and numerical experiment and then of model climatological fields evaluation with observations. We do not present it here as this has already been presented in chapter I. However, we show the spatial and temporal variability of planktonic ecosystem fields over the inner shelf in Figs. III.5, III.6, which supports the discussion section of the GRL draft.

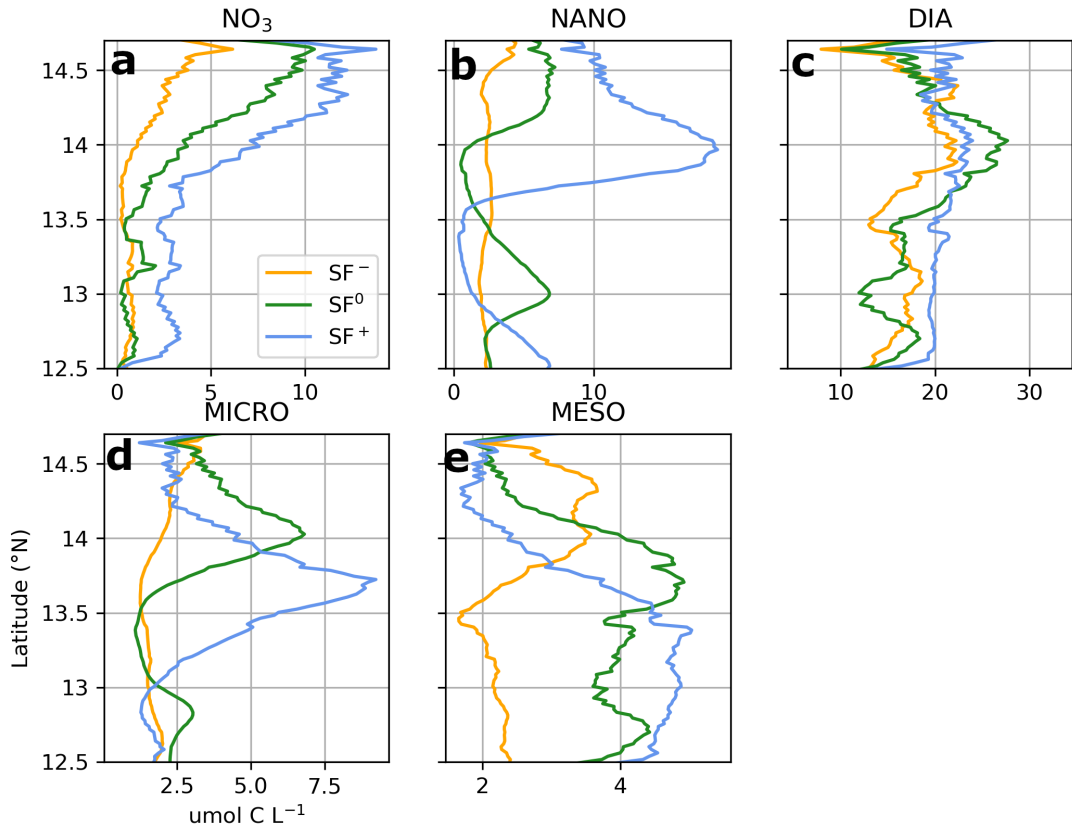


Figure III.5: Same as Figure 2 of the manuscript for the inner shelf: 20 m isobath offshore limit.

III. BOTTOM-UP PROPAGATION OF SYNOPTIC WIND INTENSIFICATION AND RELAXATION IN THE PLANKTONIC ECOSYSTEM

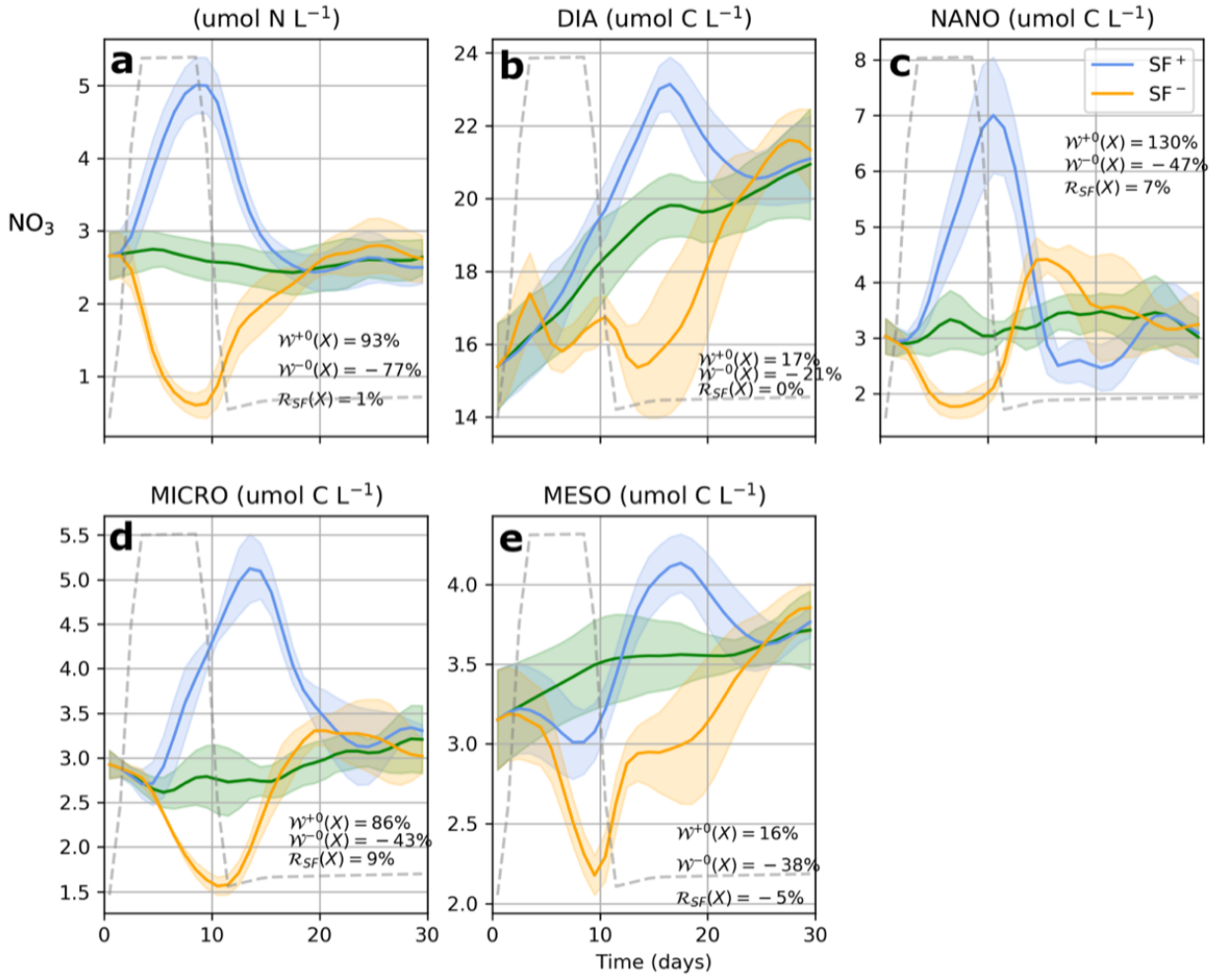


Figure III.6: Same as Figure 3 of the manuscript for the inner shelf.

3.2 Temporal evolution of the along shelf structure of the ecosystem

Here we show the temporal evolution of the along shelf structure of the ecosystem in Fig. III.7, i.e. $G(y, t) = 1/S \iint_{x,z} X dx dz(y, t)$, with X nitrate or plankton biomass. We aim to show the temporal variability of the alongshore structure shown in Fig. III.2 (see also Fig. III.5 of its supplementary information).

The propagation of the perturbations towards and up the trophic levels of the planktonic ecosystem can be seen successively in the nitrate and plankton fields with a spatial and temporal lag in Fig. III.7. For example, the anomaly pattern of nitrate anomaly during SF^+ until $\sim 14.2^\circ N$ before day 10 is found in the nanophytoplankton and microzooplankton anomaly patterns respectively at $14.8^\circ N$ and $13.5^\circ N$ around and after day 10. With this, we support our choice of averaging between days 9-11 in Fig. III.2, that aims to capture the anomalies in their most perturbed state (first and third columns of Fig. III.7).

On a mean state, horizontal structures in Fig. III.7 (middle column) indicate robust spatial patterns of the alongshore ecosystem structure. In particular, the extension of high small size plankton biomass patterns is smaller than the more diffuse larger plankton patterns (see for example microzooplankton and mesozooplankton mean states in Fig. III.7k,n. In response to SF^\pm , these very localized patches oscillate in time and space in a more deterministic manner than larger cell plankton (Fig. III.3).

Fields oscillate in space between the mean and most perturbed states. For example, the first peak of anomaly described in Fig. III.3 can be seen in Fig. III.7g (resp. Fig. III.7i) where diatoms concentration increases (resp. decreases) during SF^- (resp. SF^+ ; day ~ 4). The transitory phases of plankton biomass seem to differ between SF^+ and SF^- . When the wind intensifies (days $\sim 5-10$ at the start of SF^+ or days $\sim 10-15$ after SF^- when the wind reintensifies towards the climatological forcing), the patterns of high concentration are pushed southwards and result in rays of negative "slopes" in Fig. III.7. These slopes (i.e. the velocities of the spatial shift of the high concentration patterns) of intensification phases seem steeper than the positive ones associated to relaxation transitory phases.

III. BOTTOM-UP PROPAGATION OF SYNOPTIC WIND INTENSIFICATION AND RELAXATION IN THE PLANKTONIC ECOSYSTEM

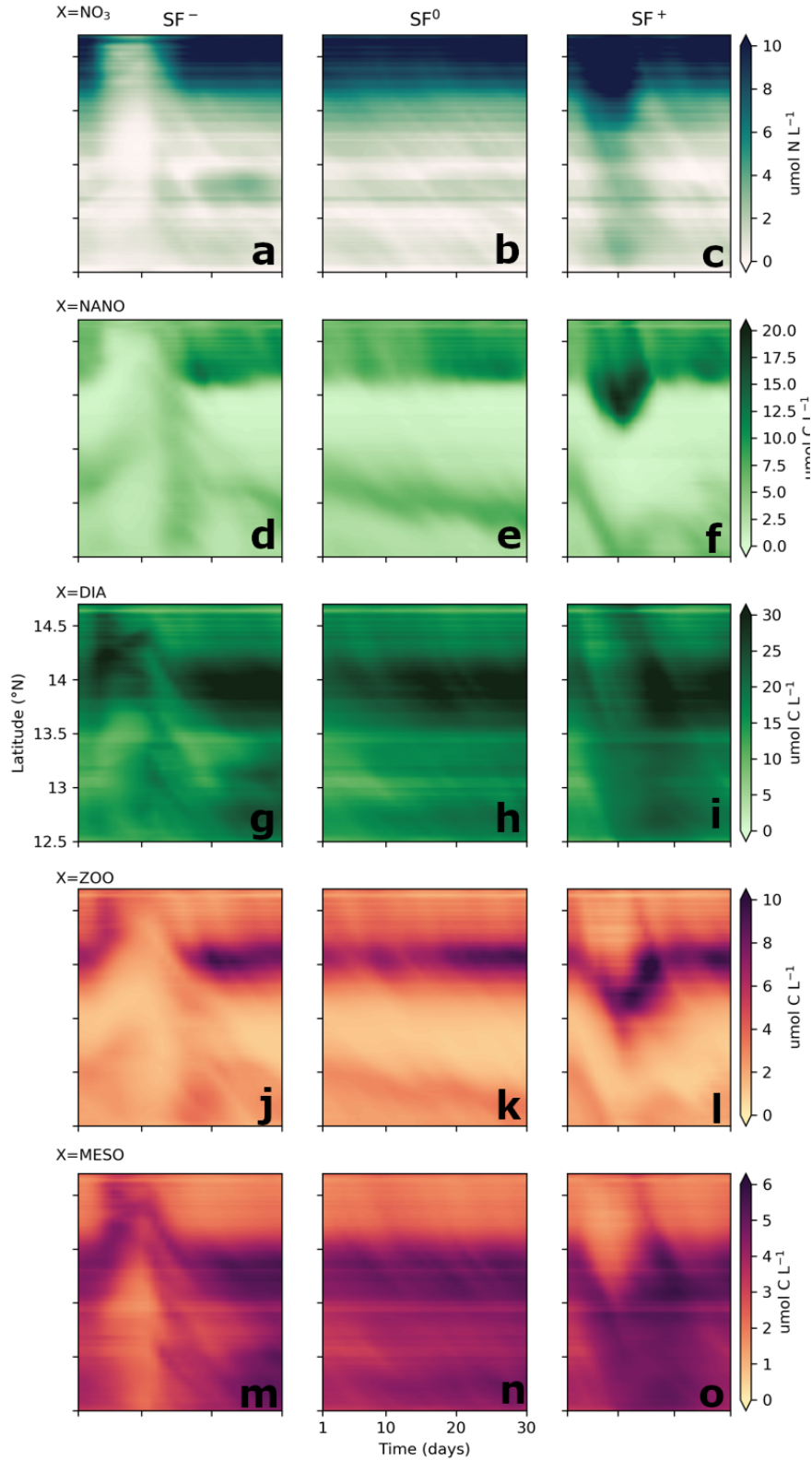


Figure III.7: Time series of the along shelf structure of nitrate (a-c), nanophytoplankton (d-f), diatoms (g-i), microzooplankton (j-l) and mesozooplankton (m-o). The left column indicates the responses to SF^- , the middle to SF^0 and the right column to SF^+ .

Insights into processes shaping the planktonic ecosystem structure

Contents

1	Preamble	148
2	Nutrients patterns, limitations and control mechanisms	149
2.1	Nutrients mean state	149
2.2	Limitation of phytoplankton growth by nutrients at synoptic time scales	151
2.3	Control of nitrate: physical versus biological mechanisms	153
3	Light availability	155
4	Control mechanisms of plankton	157
4.1	Phytoplankton primary production under climatological conditions .	157
4.2	Control mechanisms of phytoplankton biomass in response to synoptic wind perturbation	160
4.3	Zooplankton biomass	165
5	Specific inner shelf processes shaping diatoms biomass	167
5.1	Primary production	167
5.2	Detailed budget	169
6	Surface mixed layer and vertical processes	171
6.1	Detailed budget on diatoms	171
6.2	Vertical structure of large plankton biomass during a relaxation event .	174
6.3	Submesoscale eddy fluctuations	175
7	Discussion	176
8	Conclusion	178

1 Preamble

In the previous chapter, we described the impact of synoptic wind perturbations on the properties of the planktonic ecosystem as a whole. In this chapter, we aim to understand more precisely the control mechanisms of the biogeochemical and biological fields in response to synoptic wind variability, and thus explain processes responsible for the temporal evolution of fields of Fig. IV.1. To deliver a thorough characterization of all fields and help gaining a fine view of the SSUS ecosystem functioning, we develop a series of budgets on nitrate, phytoplankton and zooplankton in which we compare physical and biological processes. We first describe the nutrients fields, the associated phytoplankton nutrient limitations and we compare physical and biological terms in the nitrate budget. To complement this, we propose considerations on light exposure. Then, we analyze phytoplankton and zooplankton budgets. We develop a thorough budget in which all physical and biological terms are computed for diatoms as the dominant species in the ecosystem. Inner shelf and surface mixed layer specificities are presented.

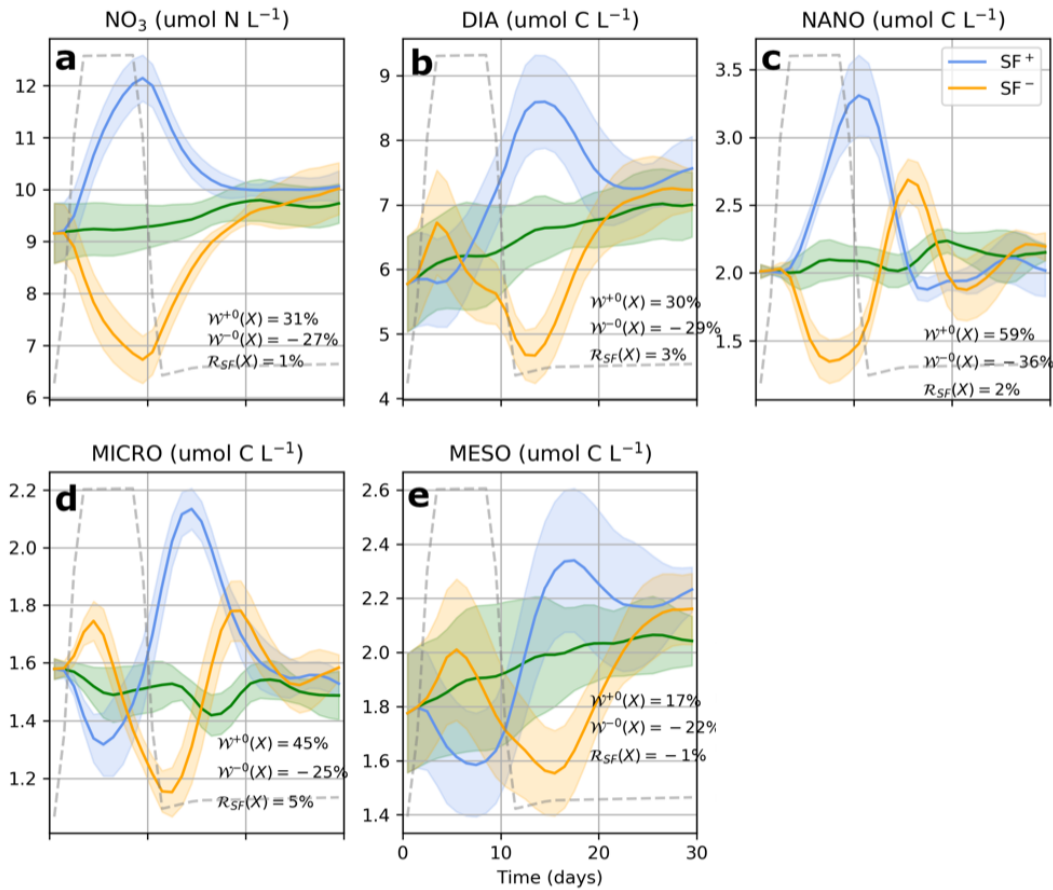


Figure IV.1: Figure similar to Fig. III.3 of the GRL manuscript chapter III. Nutrient and biological quantities averaged over the shelf in the entire water column, and over the ensemble. Green, orange and blue lines indicate SF^0 , SF^- and SF^+ . Shaded areas indicate the ensemble standard deviation. $W^{\pm 0}$ and R_{SF} diagnose maximum of relative perturbations and asymmetries. The box of integration is shown in Figure II.1a (between 13-14.75°N and 0-100 m isobaths).

2 Nutrients patterns, limitations and control mechanisms

2.1 Nutrients mean state

In addition to the fields presented in the previous chapter (GRL manuscript Fig. III.1 of chapter III), we show in Figs. IV.2 and IV.3 all the nutrients of PISCES under March climatological conditions.

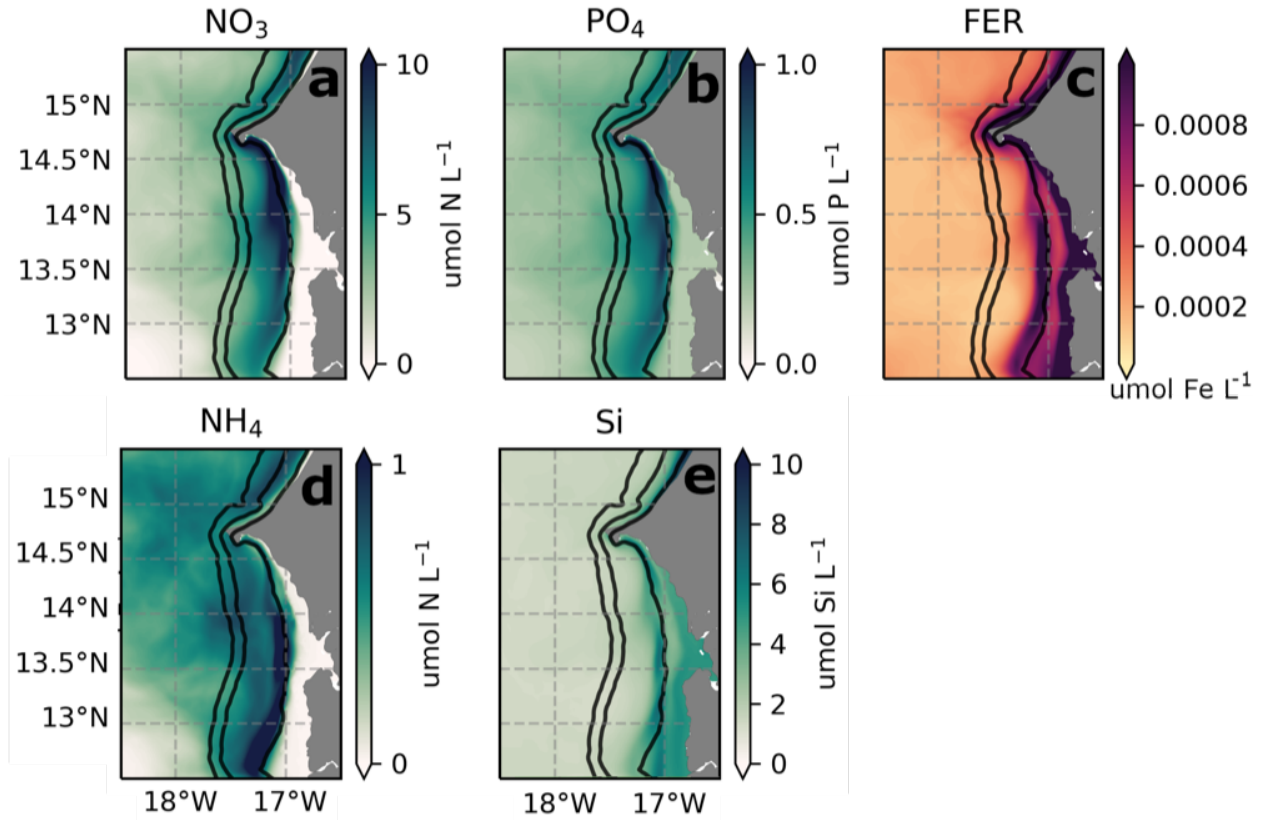


Figure IV.2: Surface patterns of NO_3 (a), PO_4 (b), Iron (c), NH_4 (d) and Si (e) concentrations averaged over the ensemble during 30 days of SF^0 .

The spatial structure of nutrients indicates that the structure of phosphate (Fig. IV.2b) resembles to that of nitrate with a collocation of their maximum concentration at $\sim(17.2^\circ\text{W}; 14.5^\circ\text{N})$, with the difference that phosphate is not depleted over the inner shelf. Nitrate and phosphate are exhausted along their southwards advection over the mid shelf (lower concentrations south of 13.5 - 14°N in Fig. IV.2a,b)

Like nitrate and phosphate, silicate is upwelled from subsurface waters to the upper layer (Fig. IV.3a,b,e). However, silicate is consumed only by diatoms, has different different bottom boundary conditions at the sediment interface compared to other elements (see chapter I section 4.1; Aumont et al., 2015) and thus exhibits a different spatial pattern with a maximum over the inner shelf.

Only nitrate and ammonium reach depletion over the inner shelf. Oppositely to nitrate, ammonium concentration is increased downstream (higher ammonium concentration south of 14°N in Fig. IV.2d), in agreement with recycling processes. Interestingly, ammonium vertical

structure exhibits two maxima (Fig. IV.3d). The maximum at the bottom of the water column is due to the degradation of fast sinking particulate organic matter accumulated on the shelf bottom, and the maximum exactly between the surface mixed layer and the euphotic layer is due to slower sinking organic matter.

High concentrations of iron are found near the coast where the shelf is shallow (Fig. IV.2c) and where effective resurgence occurs. Also, inshore of the 20 m isobath, the surface mixed layer reaches the bottom and thus iron is homogeneous from the bottom to the surface over the inner shelf (Fig. IV.2c). A latitudinal band of local minimum is found inshore of the 20 m isobath, likely due to the intake due to phytoplankton growth, because it is colocated with the highest primary production patterns (see later in Fig. IV.9b,f).

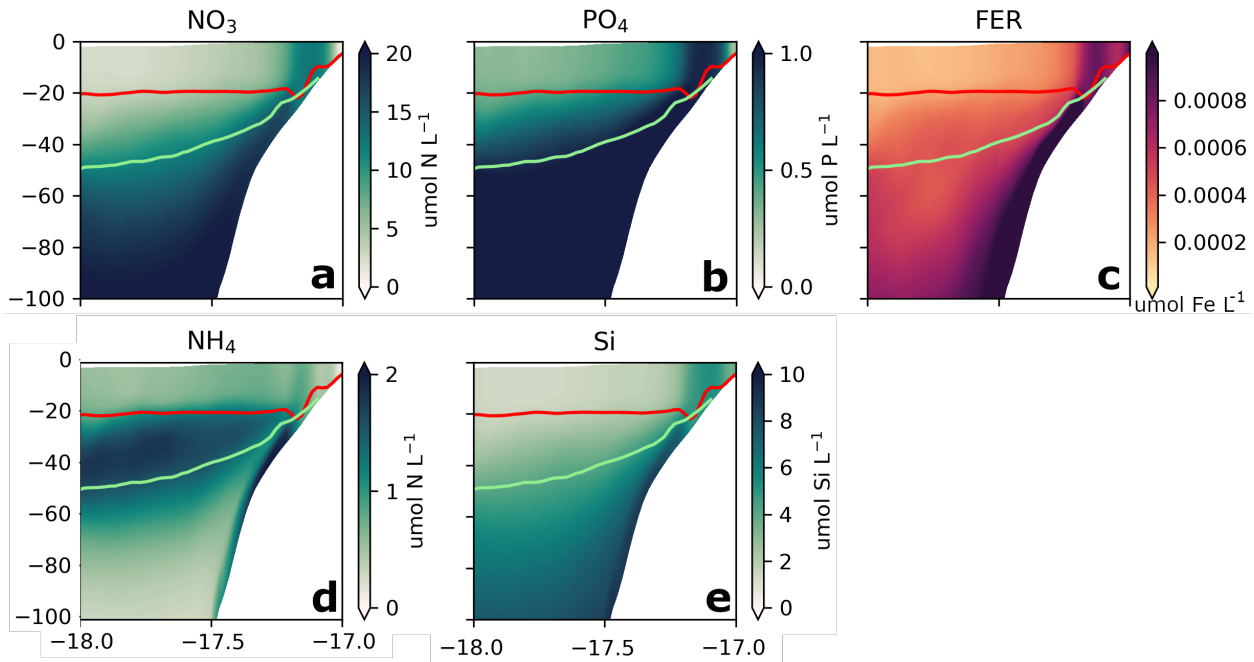


Figure IV.3: Vertical sections of NO_3 (a), PO_4 (b), Iron (c), NH_4 (d) and Si (e) concentrations averaged over the ensemble during 30 days of SF^0 . The section location is indicated in Fig. II.7 of chapter II. The red line indicates the surface mixed layer depth and the lightgreen line the euphotic layer depth.

2.2 Limitation of phytoplankton growth by nutrients at synoptic time scales

In this section, we aim to complement the previous analysis (chapter III) by delivering a detailed description of the limitation of phytoplankton growth by nutrients. To do so, we compute (in Python) the limitation factors L_{lim} of each N, P, Fe (and Si for diatoms) elements for phytoplankton growth, accordingly to their definition in PISCES, based on Monod equations for N,P (Monod, 1942) and on a quota approach for Fe. They are shown in Eqs. IV.1-IV.6 for nanophytoplankton. Note that the half saturation terms $K_{PO_4}^P$, $K_{NO_3}^P$, $K_{NH_4}^P$ for N, P are not constant and depend on the phytoplankton biomass; and that $\theta^{Fe,P}$, $\theta_{min}^{Fe,P}$, $\theta_{opt}^{Fe,P}$ are the iron quota and its minimum and optimal values. We do not show the equations for diatoms, and more details can be found in Aumont et al. (2015).

$$L_{lim}^P = \min(L_{PO_4}^P, L_N^P, L_{Fe}^P) \quad (IV.1)$$

$$L_{PO_4}^P = \frac{PO_4}{PO_4 + K_{PO_4}^P} \quad (IV.2)$$

$$L_N^P = L_{NO_3}^P + L_{PO_4}^P \quad (IV.3)$$

$$L_{NH_4}^P = \frac{K_{NO_3}^P NH_4}{K_{NO_3}^P K_{NH_4}^P + K_{NH_4}^P NO_3 + K_{NO_3}^P NH_4} \quad (IV.4)$$

$$L_{NO_3}^P = \frac{K_{NH_4}^P NO_3}{K_{NO_3}^P K_{NH_4}^P + K_{NH_4}^P NO_3 + K_{NO_3}^P NH_4} \quad (IV.5)$$

$$L_{Fe}^P = \min(1, \max(0, \frac{\theta^{Fe,P} - \theta_{min}^{Fe,P}}{\theta_{opt}^{Fe,P}})) \quad (IV.6)$$

These dimensionless factors range between 0 (total limitation) and 1 (no limitation), and the minimum between the distinct terms indicates the limiting nutrient (Aumont et al., 2015). We define arbitrarily three intervals to interpret the limiting factors: {0-0.3}: strong limitation; {0.3-0.6}: moderate limitation; and {0.6-1}: modest to no limitation by nutrients.

Under SF⁰ conditions, the surface diatoms growth is moderately limited by phosphate over the mid shelf (offshore of the 20 m isobath; Fig. IV.4b). Nanophytoplankton growth is modestly limited by phosphate (Fig. IV.4e) and moderately limited by iron around 13.5°N over the mid shelf. The only strong limitation by nutrients over the shelf occurs over the inner shelf where both phytoplankton growths are strongly limited by nitrogen, in agreement with the nitrate and ammonium depletion shown in Fig. IV.2a.

The patterns of the limitation factors are modified in response to SF[±]. To complement this and given the importance of nitrate during SF⁰, we show the surface concentration of nitrate in Fig. IV.5. During SF⁻, the pattern of strong limitation by nitrogen extends offshore and crosses the 20 m isobath at certain latitudes for both phytoplankton (Fig. IV.4a,d; see also nitrate con-

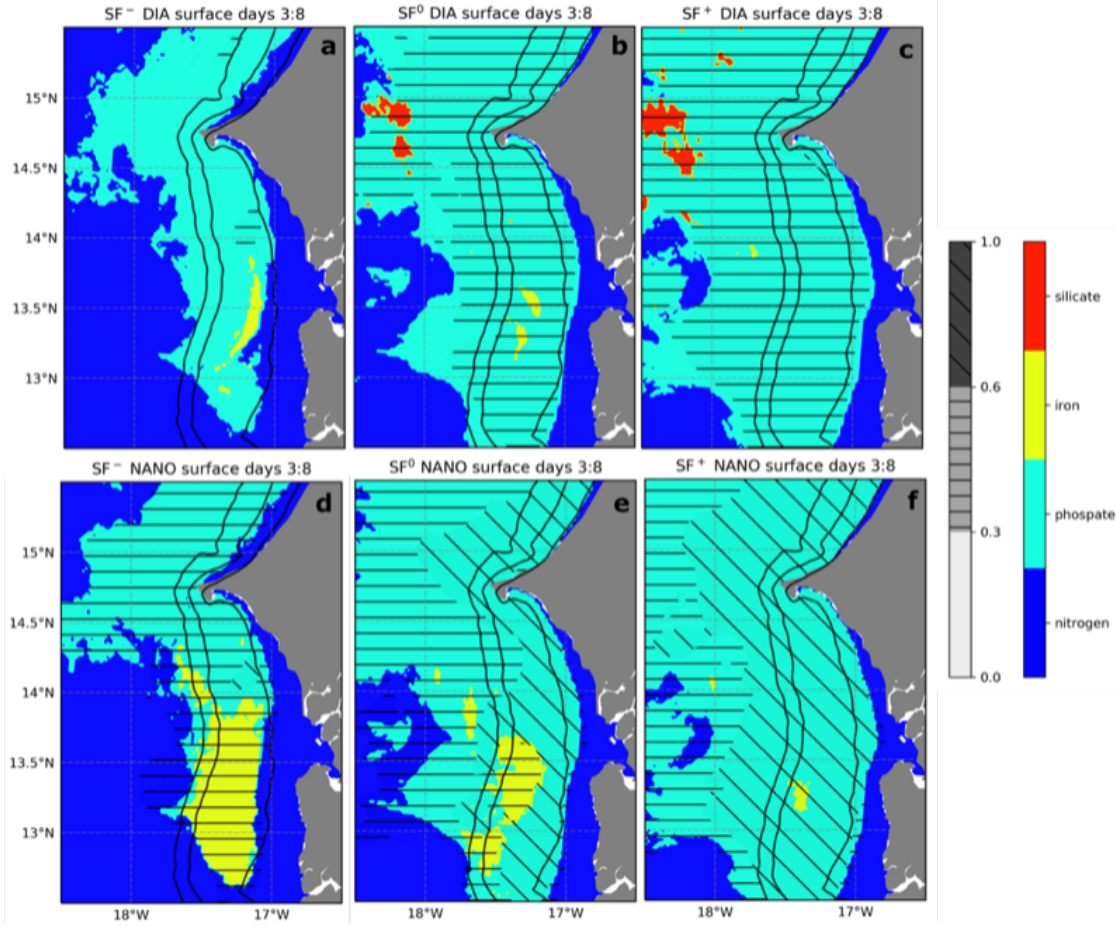


Figure IV.4: Factors of limitation by nutrients for diatoms (a,b,c) and phytoplankton (d,e,f) growths, in response to SF^- (a,d), SF^0 (b,e) and SF^+ (c,f). The limiting nutrient is indicated in color (silicate in red, iron in yellow, phosphate in light blue, nitrogen in blue). No hashing indicate strong limitation, horizontal hashing indicate a moderate limitation and inclined hashing indicate modest limitation (arbitrary intervals). The time interval for averaging is days 3:8. We show the most recurrent limiting nutrient over the ensemble in the time interval at each location.

centration decrease in Fig. IV.5a). The limitation by phosphate passes from modest to moderate for nanophytoplankton and from moderate to strong for diatoms. The pattern of modest limitation by iron is extended south of $14^\circ N$ for nanophytoplankton. During SF^+ , patterns of modest and moderate limitation by phosphate extend both offshore and inshore in a way that the pattern of strong limitation by nitrogen is closer to shore (Fig. IV.4c,f; see also nitrate increase inshore in Fig. IV.5c). The oscillation of the offshore extension of the nitrogen strong limitation pattern in response to SF^\pm agrees with previous findings discussed in the chapter II section 3.4.

Overall, we find that silicate is never limiting, iron is moderately limiting over a very reduced area only during SF^- for nanophytoplankton, and that phosphate is strongly limiting over the mid shelf during SF^- for diatoms. Only nitrogen presents a strong and robust pattern of limitation for both phytoplankton over the inner shelf. This indicates a major role of nitrate and ammonium in the planktonic ecosystem of the SSUS in our model. This needs to be evaluated against colimitation observations over the Senegalese shelf, which are currently lacking.

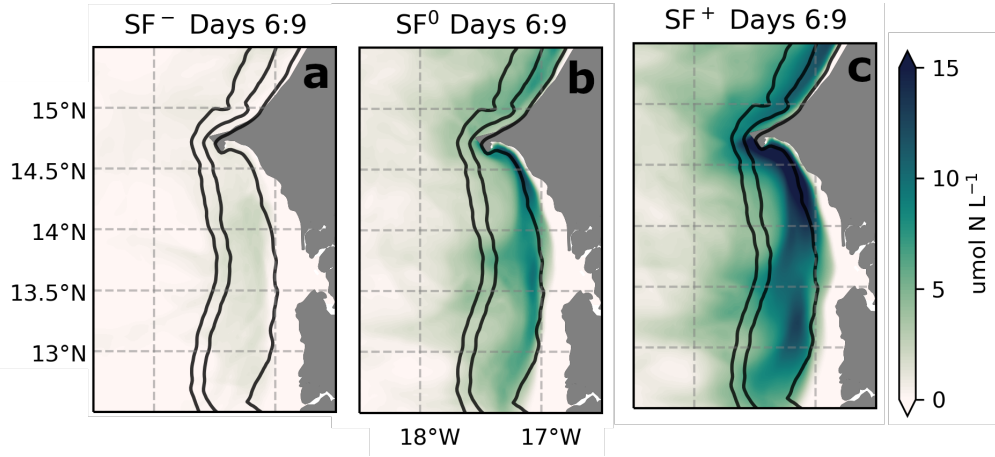


Figure IV.5: Surface NO_3 concentration averaged over the ensemble during SF^- (a), SF^0 (b) and SF^+ (c). The time interval for averaging is days 6:9 (different from Fig. IV.4).

2.3 Control of nitrate: physical versus biological mechanisms

The budget of nitrate is shown in Fig. IV.6 following Eq. IV.7, with $hadv$ denoting horizontal advection, bio biogeochemical and biological processes, the overline denotes ensemble, daily averages over the entire water column, in the box shown in Fig. III.1 (in chapter III), between 13-14.75°N and 0-100 m isobaths (this is true for all the following budgets unless specified). Because we integrate over the shelf and the entire water column, and because of the negligible role of horizontal mixing (several order of magnitude below the advection terms, not shown), the physical processes are reduced to the horizontal advection (considerations on vertical and surface mixed layer processes for diatoms are treated in section 6).

$$\overline{\partial_t \text{NO}_3} = \overline{hadv} + \overline{bio} \quad (\text{IV.7})$$

Note that in Fig. IV.6, the three upper panels indicate SF^- , SF^0 and SF^+ , and the lower panels indicate the anomaly of events $\text{SF}^- - \text{SF}^0$ and $\text{SF}^+ - \text{SF}^0$ of the same variables (the following budget Figures are structured similarly).

Under SF^0 conditions, horizontal advection transports nitrate over the shelf and balances with biogeochemical and biological sinks in way that the total rate oscillates around 0 (Fig. IV.6b). The only possible source of nitrate by biogeochemical and biological processes is by nitrification (i.e. bacterial activity convert ammonium to nitrate), and sinks are consumption by nanophytoplankton and diatoms growths and denitrification (nitrate reduced to nitrogen, Aumont et al., 2015).

At the beginning of SF^+ , the rate of change of nitrate is strongly increased and reaches a maximum at day 3, driven by intensified horizontal advection and reduced biogeochemical and biological processes (Fig. IV.6c,e). Just after the end of the event (~day 12), the cancellation of horizontal advection and a maximum of negative biogeochemical and biological processes induce a minimum negative total rate of change of nitrate.

The response of nitrate to SF^- is somewhat opposite. In the first days (\sim day 3) of the anomaly, horizontal advection is negative, which means there is more export of nitrate out of the shelf than import (Fig. IV.6a,d). Biogeochemical and biological processes also reach a negative maximum. The negative minimum peaks of physical, biogeochemical and biological processes are reached at the same time such that the negative peak of the total rate is remarkably strong. In absolute, it is nearly three times larger than the one of SF^+ . After the end of the event at day 12, all processes positive anomalies are reduced in about 10 days towards the climatological state. Overall, shapes of the responses to SF^\pm are mostly driven by horizontal advection.

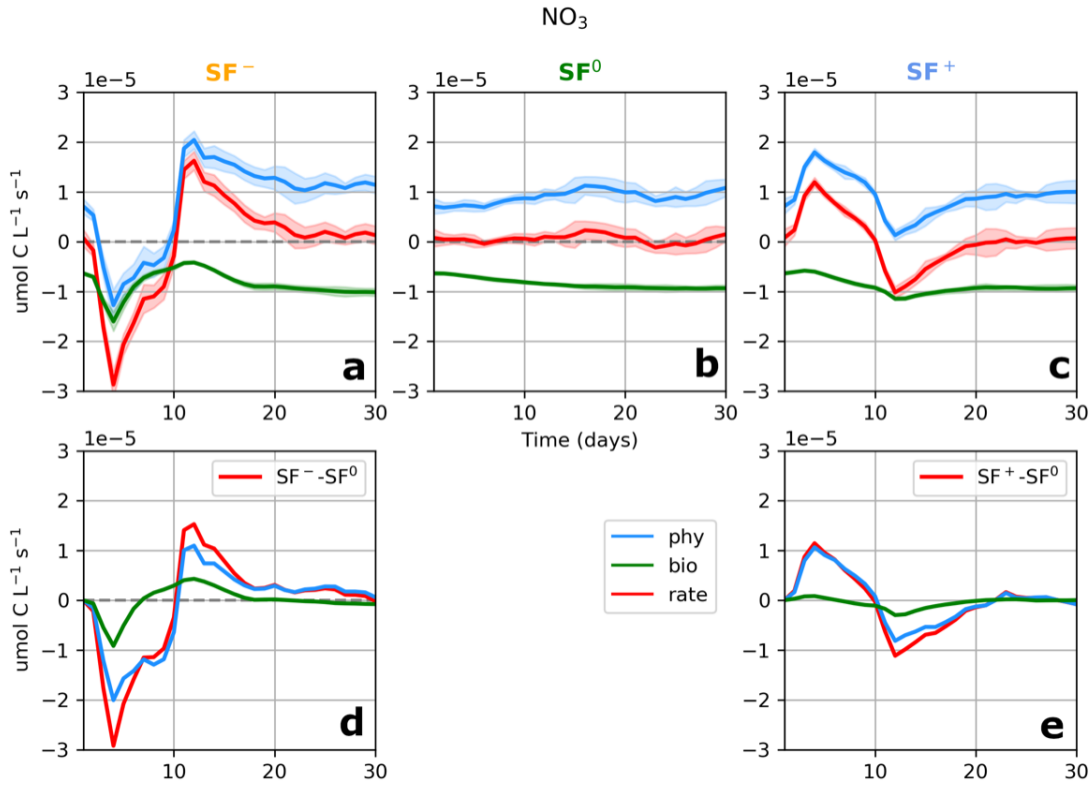


Figure IV.6: Time series of the total rate of change of nitrate concentration (red lines), physical (blue lines) and biological (green lines) terms, for SF^- (a,d), SF^0 (b) and SF^+ (c,e). Panels d,e indicate the anomalies to the climatological terms $SF^\pm - SF^0$.

3 Light availability

In order to diagnose the limitation of phytoplankton growth by light, we analyze light availability based on euphotic layer and surface mixed layer depths.

Under climatological conditions, in the offshore part of the domain, low turbidity (here low phytoplankton biomass) allows the light to penetrate relatively deep in the water column, such that the euphotic layer is way deeper than the SML and can reach 60 m for a 25 m surface mixed layer (Fig. IV.7a,b). Over the shelf, high phytoplankton biomass reduces the vertical penetration of light such that the euphotic layer is closer to the SML depth.

The SML is deeper than the euphotic layer in the offshore part of the 20 m isobath and shallower in the inshore part (red and blue patterns along the 20 m isobath in Fig. IV.7c). As the SML approaches the depth of the water column, it increases to reach the bottom and follow the bathymetry (i.e. see red line in Fig. IV.3a: increase of the SML depth at -17.5°E as it reaches the shelf). Inshore of the 20 m isobath, the SML depth is then decreased as the high phytoplankton biomass captures solar radiation and enhances stratification, such that it is shallower than the euphotic layer. Note that this was not obtained in numerical simulations without activating the chlorophyll shading parameterization (chapter II Fig. II.9).

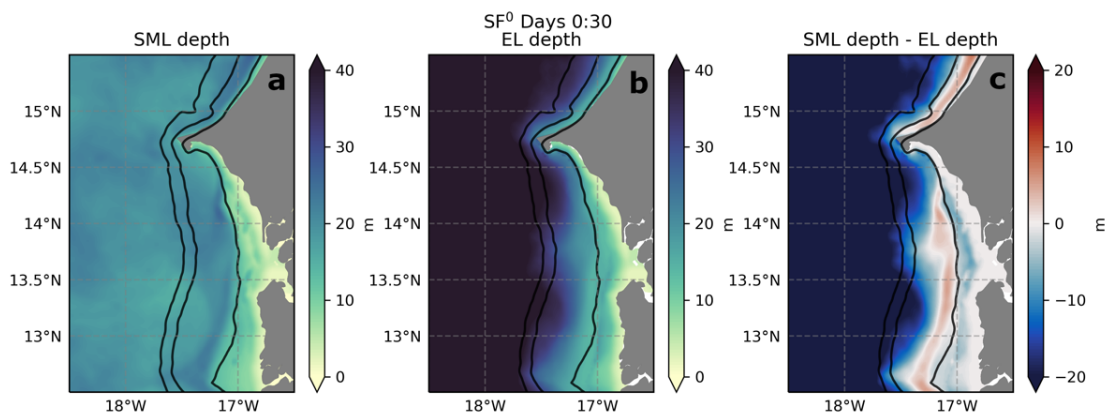


Figure IV.7: Spatial patterns of the surface mixed layer depth (SML, a), euphotic layer depth (EL, b) and their difference (c) ensemble averaged over 30 days of SF^0 . The average box is shown on the Fig. 1a of chapter 3 XX. Black lines indicate the 20, 100 and 500 m isobaths.

Over the entire shelf, the SML and euphotic layer respond oppositely to SF^+ and SF^- (Fig. IV.8). When the SML depth increases during SF^+ , the euphotic layer shoals, and oppositely during SF^- . The euphotic layer response is due to the chlorophyll shading parameterization and is in agreement with phytoplankton biomass responses (we remind that the solar radiation has not been modified and is similar between SF^+ and SF^-). The difference between the two depths is an indicator of the exposure to light of surface mixed layer material. The euphotic layer always remains deeper than the SML depth in response to SF, but this difference decreases (resp. increases) during SF^+ (resp. SF^-) which indicates a reduced (resp. increased) exposure to light (Fig. IV.8). Thus, SF^- allows an increased exposure to light (i.e. a reduced light limitation) through an increase of the euphotic layer depth and a concentration of material near the surface by SML shoaling.

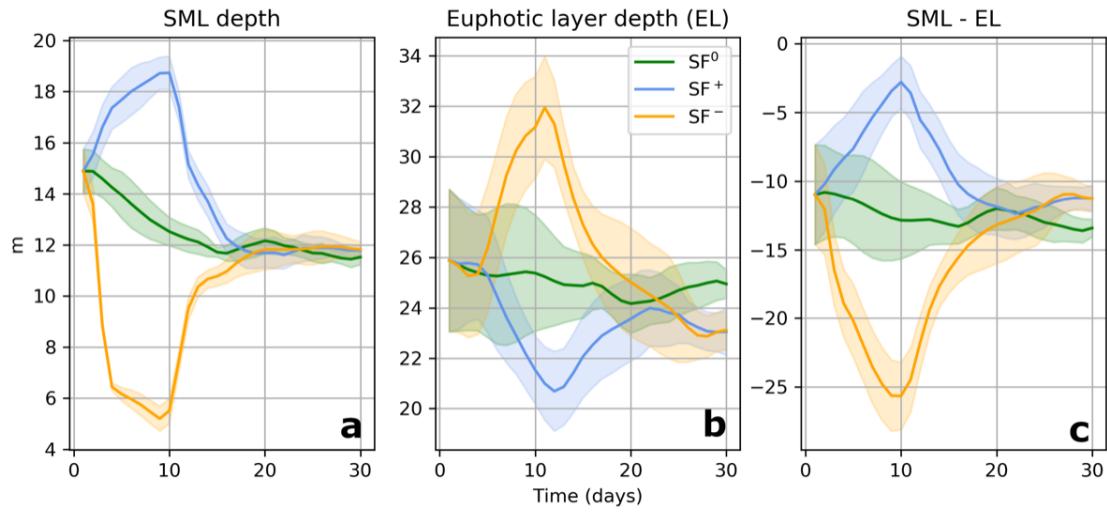


Figure IV.8: Time series of the box average SML depth (a), euphotic layer (b) and their difference (c) for SF^{0+-} .

4 Control mechanisms of plankton

After describing the nutrients and light availability, this section aims to describe processes responsible of plankton biomass changes at synoptic time scales. We first present the total, new and regenerated primary production terms for nanophytoplankton and diatoms under climatological conditions. We then analyze budgets on phytoplankton biomass where we compare physical, primary production and biological sinks terms in response to SF^0 , SF^+ and SF^- . A particular focus is drawn on diatoms where we analyze separately biological processes. Finally, zooplankton physical and biological processes are analyzed.

4.1 Phytoplankton primary production under climatological conditions

We separate the total primary production (PP) into the new (NP) and regenerated (RP) primary production terms, based respectively on nitrate and ammonium intake, as Eq. IV.1 writes.

$$PP = NP + RP \quad (IV.1)$$

We present the horizontal and vertical patterns of the production terms of nanophytoplankton and diatoms under climatological conditions in Figs. IV.9 and IV.10. Overall, the nanophytoplankton and diatoms primary production (PP) patterns coincide with their respective phytoplankton biomass patterns (Fig. IV.9a,b and Fig. IV.9e,f). For both phytoplankton, there is more NP over the northern part of the shelf and more RP over the southern part of the shelf (Fig. IV.9c,d,g,h).

On the vertical, high patches of PP are concentrated near the surface where light is the most available, and the resulting biomass is then mixed over the SML (e.g. for nanophytoplankton in Fig. IV.10a,b). Across-shore, the SML first reaches the bottom of the water column, is then shoaled where the plankton biomass is the highest (effect of shading as explained in section 3), and finally reaches the seabed when the shelf gets shallower.

Along the southwards advection of the upwelled water mass, we hypothesize that the nanophytoplankton decrease at $\sim 14^\circ N$ (see Fig. IV.9a) is not a bottom-up control by nutrient limitation because of the absence of nitrate decrease at this location in Fig. IV.2, but a top-down control by microzooplankton and then mesozooplankton given their spatial patterns in Fig. IV.9a,i,j. In the same way, we hypothesize that the local decrease of microzooplankton at $13.5^\circ N$ is due to mesozooplankton grazing (see Fig. IV.9i,j).

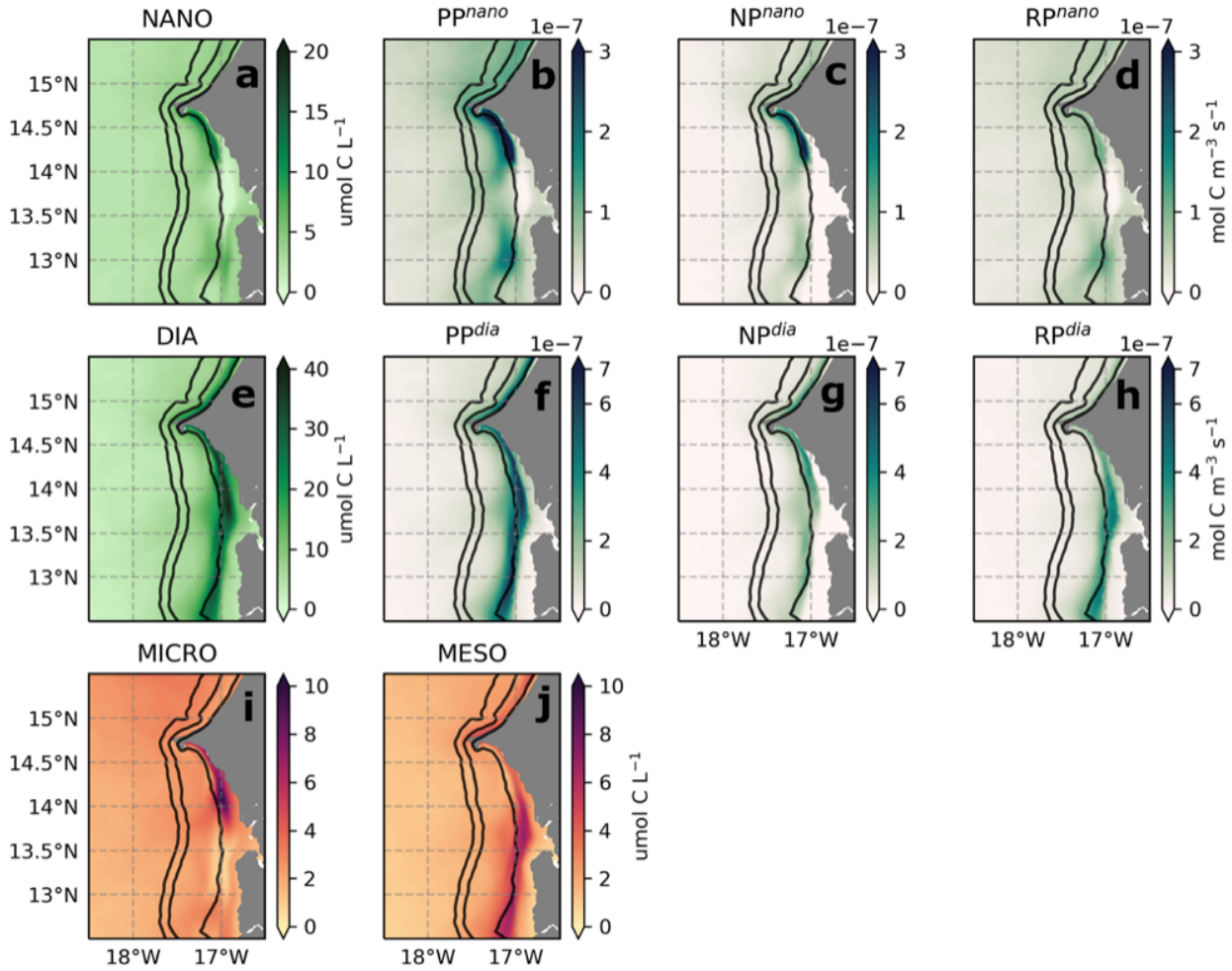


Figure IV.9: Surface patterns of nanophytoplankton (a), diatoms (e), microzooplankton (i), mesozooplankton (j) biomass. Total (PP), new (NP) and regenerated (RP) primary production terms corresponding to each plankton species are shown on panels b-d for nanophytoplankton and f-h for diatoms. Averages are made over the ensemble during 30 days of SF^0 .

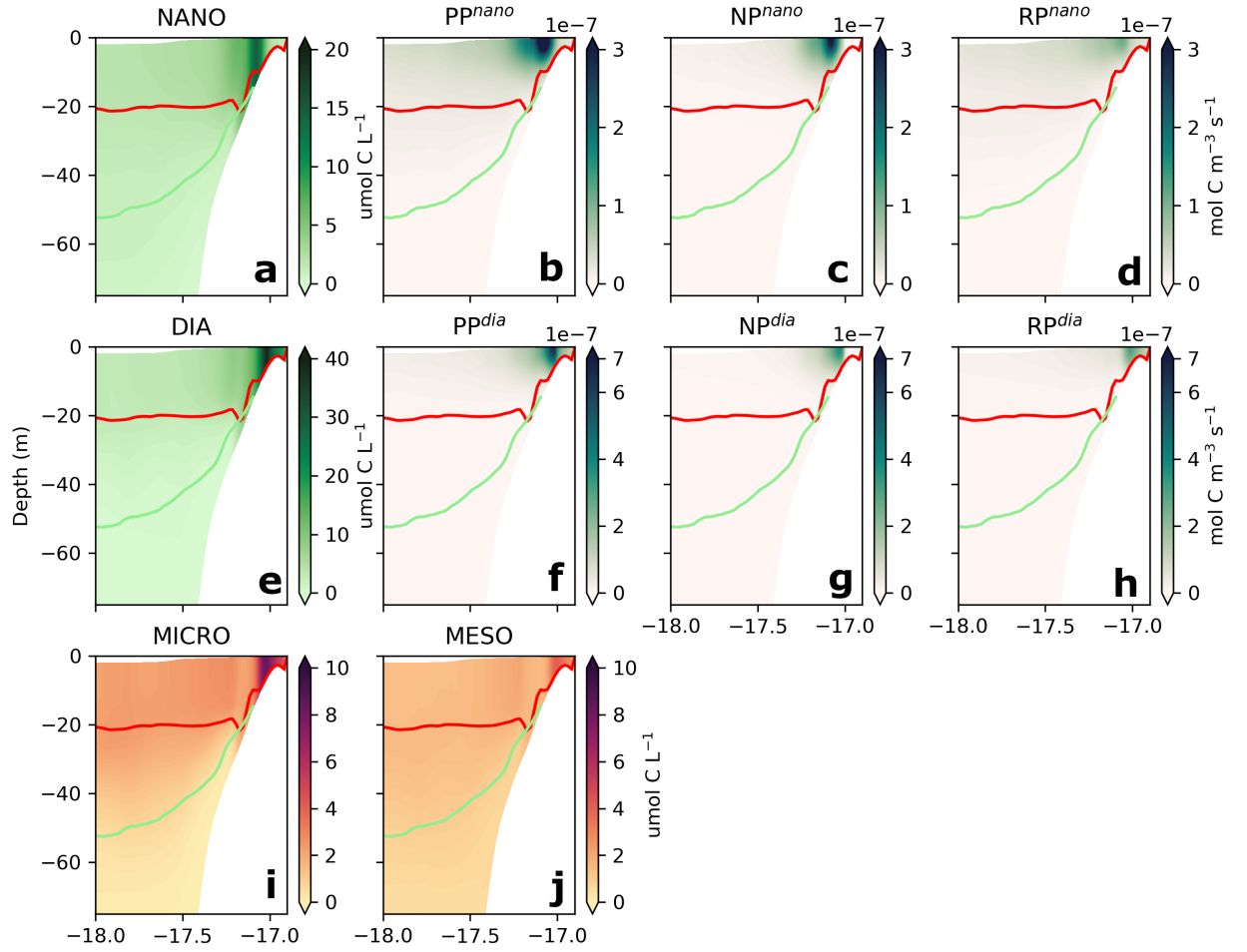


Figure IV.10: Vertical sections of nanophytoplankton (a), diatoms (e), microzooplankton (i), mesozoo-plankton (j) biomass. Total (PP), new (NP) and regenerated (RP) primary production and grazing terms corresponding to each plankton species are shown on panels b-d for nanophytoplankton and f-h for diatoms. Averages are made over the ensemble during 30 days of SF^0 . The red line indicates the surface mixed layer depth and the lightgreen line the euphotic layer depth.

4.2 Control mechanisms of phytoplankton biomass in response to synoptic wind perturbation

Here we focus on the control mechanisms of phytoplankton biomass in response to SF^\pm and compare primary production terms, biological sinks and physical mechanisms. Because of their central and dominant role in EBUS, we develop a particular effort to understand what drives the diatoms concentration evolution, and thus analyze individual biological processes in the case of diatoms.

Control mechanisms

We describe the primary production, biological sinks and physical mechanisms and identify their role in the rate of change of the phytoplankton biomass P (for nanophytoplankton, the full budget is computed for diatoms in Eq. IV.3). The biological term of the budget is computed offline by the difference between the total rate $\partial_t P$ and the sum of physical terms, i.e. $hadv$ (both computed online). In addition, we compute the biological sinks bio_{sink} by the difference between the biological term bio and the total primary production PP (separated in NP and RP), which gives Eq. IV.2. The bio_{sink} terms are the mortality, aggregation and grazing by zooplankton.

$$\begin{aligned}\overline{\partial_t P} &= \overline{hadv} + \overline{bio} \\ &= \overline{hadv} + \overline{PP} - \overline{bio_{sink}} \\ &= \overline{hadv} + \overline{NP} + \overline{RP} - \overline{bio_{sink}}\end{aligned}\tag{IV.2}$$

Diatoms

Specially for diatoms we separate the biological sinks and compute the following terms of the equation of the diatoms concentration rate of change (Eq. IV.3, see also Eqs. I.1 and I.2 of chapter I for the full equations). Note that we chose to group together mortality and aggregation (*mortaggreg*) as they are both export processes and therefore represent a direct loss out of the direct trophic chain. Grazing by microzooplankton and mesozooplankton are denoted *micrograz* and *mesograz*.

$$\overline{\partial_t D} = \underbrace{\overline{hadv} + \overline{PP}}_{phy} - \underbrace{\overline{mortaggreg} - \overline{micrograz} - \overline{mesograz}}_{bio}\tag{IV.3}$$

Time series of these budgets on diatoms and nanophytoplankton are shown respectively in Figs. IV.11 and IV.12 averaged in the entire water column and over the shelf. In addition to the balance of physical and biological terms driving the total rate (panels a-e as for the nitrate budget in Fig. IV.6), they show the evolution of the different biological source and sink terms (panels f-j). We first describe processes driving diatoms biomass changes and then mention how nanophytoplankton responses differ.

SF^0

For diatoms under SF^0 conditions over the entire shelf, oppositely to nitrate, physical processes (i.e. horizontal advection) act as a sink and balance biological source in way that the total rate oscillates around 0 (Fig. IV.11b). The primary production occurs over the shelf and is exported southwards and offshore through horizontal advection. At this quasi-equilibrium state, NP

and RP terms have a similar weight on the total PP, with a slightly more important role of RP (Fig. IV.11g; note that we have seen in the previous section that this is strongly domain dependant). Mortality/aggregation and mesozooplankton grazing are the main biological sinks, followed by microzooplankton grazing (Fig. IV.11g). PP and mortality/aggregation, individually, are one order of magnitude larger than horizontal advection.

SF⁺

At the beginning of SF⁺ (~day 3), intensified horizontal advection enhances the export of diatoms out of the shelf such that the total rate of change is negative (blue and red lines in Fig. IV.11c,e). These offshore biomass losses induce a decrease of RP and thus of PP compared to SF⁰ until the end of the anomaly (~day 12; Fig. IV.11h,j). In agreement with the nutrients limitations, SML and euphotic layer depths, we hypothesize that the reduction of PP during SF⁺ over the entire shelf is due to a reduced biomass and an increased light limitation (SML deepening and euphotic layer shoaling) rather than a lack of nutrient. At the end of SF⁺ (~day 12), the absolute intensity of all biological terms decrease. However, at ~day 12, sinks decrease more than sources (Fig. IV.11h,j), which results, along with a reduction of advection losses, in a positive total rate, and thus in an increase of the diatoms concentration around day 14 (Fig. IV.1b). This is followed by oscillations between grazing and primary production towards the climatological mean state (Fig. IV.11h,j). Similarly to the heat budget in chapter II (see Fig II.16b), horizontal advection drives a negative peak of the total rate of change of diatoms concentration at ~day 18 after SF⁺. This was explained by oscillations in horizontal transport through western and southern sections associated to the mesoscale eddy field.

SF⁻

The response to SF⁻ is more variable over time. At the beginning of SF⁻, the total rate is positive with a remarkable peak at day 3 (Fig. IV.11a,d). Weak advective processes prevent offshore loss of biological material and nitrate (Fig. IV.11a). The remarkable positive peak of NP at day 3 induces an important increase of the total PP, that we hypothesize to be related to the increased retention and reduced light limitation (through increased stratification and increase of the euphotic layer depth, Fig. IV.8). This positive peak of PP (Fig. IV.11f,i) coincides with the negative peak of the rate of change of nitrate (Fig. IV.6a). After a few days, new nutrients are exhausted by phytoplankton intake and all biological terms decrease (this is not true for RP which increases slightly). Because mortality/aggregation and mesozooplankton grazing are stronger than PP, the total biological term reaches negative values around day 4-8. The reduced offshore export by horizontal advection (between days 0-10) postpones the decrease of diatoms concentration to after the end of SF⁻ (days 12-14) when currents are reintensified (Fig. IV.1b). Towards and after the end of the anomaly, the biological term gradually reaches back positive values at day ~12.

Nanophytoplankton

Nanophytoplankton and diatoms exhibit similar balances of NP and RP and of physical and biological processes under climatological conditions (Figs. IV.12b,g). In response to SF⁻, the global succession of processes described for diatoms is also true, except that the first peak at day 3 is absent, local extrema are shifted in time and oscillations are more pronounced (the number of local extrema is increased, Figs. IV.12a,d,f,i). Compared to SF⁺, the overall evolution

of processes resemble those of diatoms, with a noticeable stronger response of NP compared to RP near the end of the event at day 12 (Fig. IV.12h,j). Another remarkable difference is the negative peak of biological processes around day 14, explained by a rapid increase (in absolute) of biological sinks (Figs. IV.12c,d,h,j).

Overall, individual biological processes dominate the control of phytoplankton over the shelf at climatological and synoptic time scales. Lumped, biological processes balance horizontal advection. In response to SF perturbations, in contrary to nitrate, the anomalies of the total rates of phytoplankton are driven by the biological term, i.e. the balance between PP, mortality/aggregation and grazing by mesozooplankton. In response to both SF^+ and SF^- , all individual biological processes anomalies to SF^0 undergo temporal oscillations (Figs. IV.11i,j and IV.12i,j), that, along with horizontal advection explain the oscillatory behavior of diatoms concentration (Fig. IV.1b).

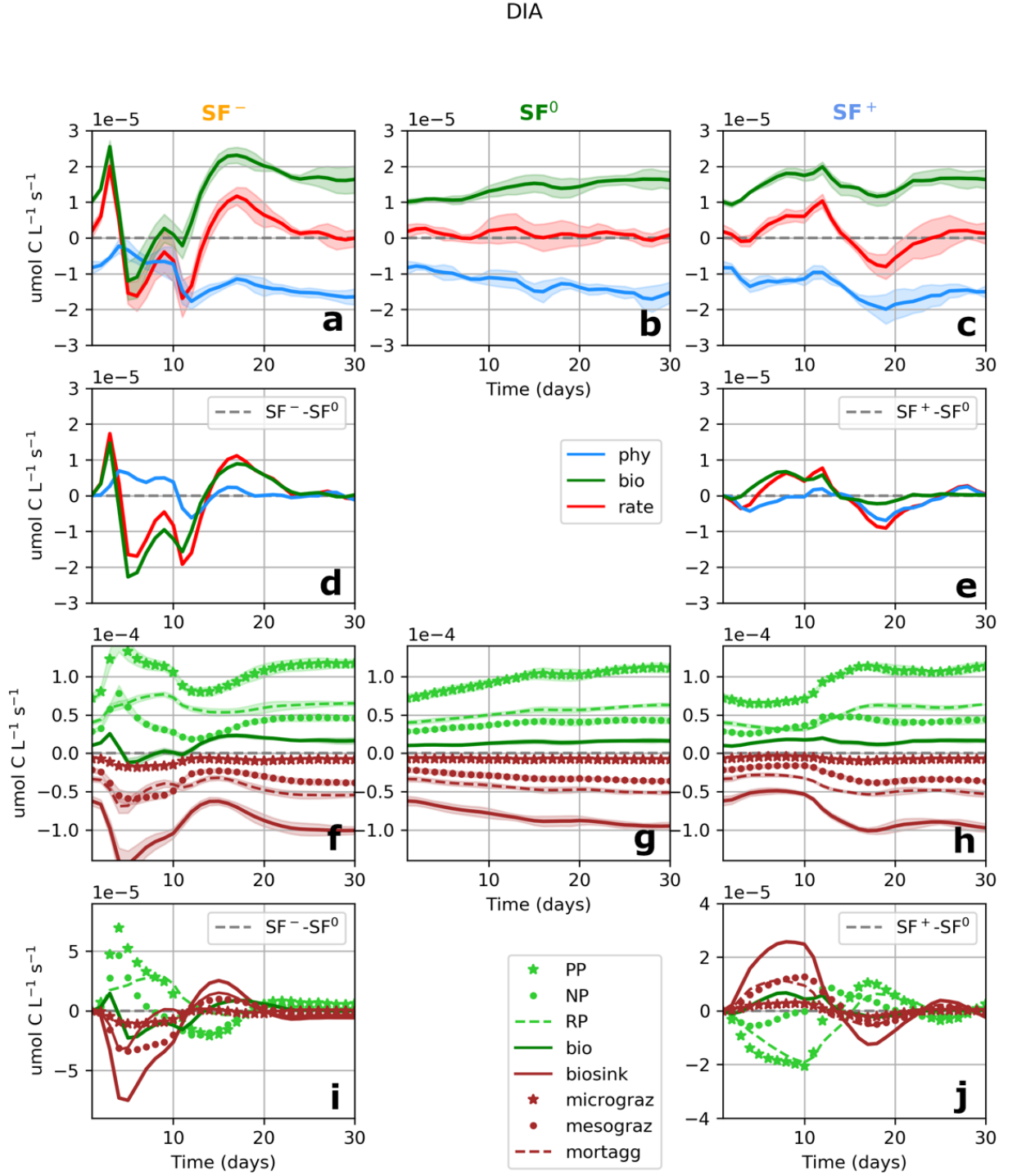


Figure IV.11: Time series of the total rate of change of diatoms concentration (red lines), physical (blue lines) and biological (green lines) terms, for SF^- (a,d), SF^0 (b) and SF^+ (c,e). Panels d,e indicate the anomalies to the climatological terms $SF^\pm - SF^0$. Panels f-j are structured similarly with individual biological terms (indicated in the legend) instead of total, physical and biological terms. The total biological term is reminded in with the darkest green continuous line on panels f-j.

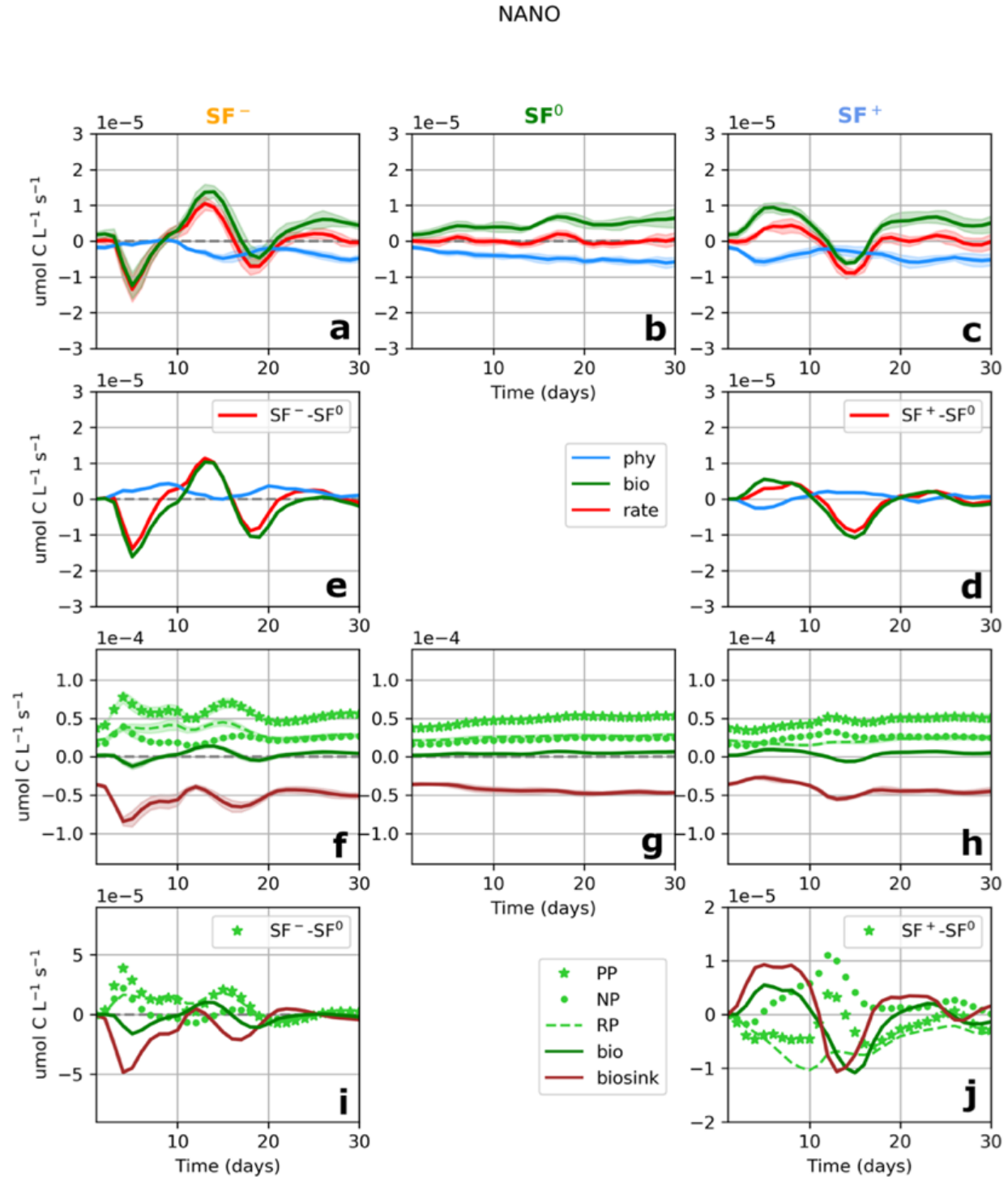


Figure IV.12: Similar to Fig. IV.11 for nanophytoplankton concentration. Biological sinks are not detailed individually.

4.3 Zooplankton biomass

The budget on zooplankton biomass Z is described simply with Eq. IV.4, where all the biogeochemical source and sink terms are lumped into the term bio as individual terms have not been stored (see more details in Eqs. 24 and 28 of Aumont et al., 2015).

$$\overline{\partial_t Z} = \overline{hadv} + \overline{bio} \quad (\text{IV.4})$$

As for phytoplankton, physical processes act as a sink and balance biological processes that are a source of zooplankton and the total rate oscillates around 0 under SF^0 conditions (Figs. IV.13b and IV.14b). Biological sources (not computed in this budget) include the grazing of phytoplankton (and organic matter for mesozooplankton) and sinks are natural (linear) mortality and (quadratic) mortality by unrepresented upper trophic levels and diseases. We first describe the response of mesozooplankton and then the differences with microzooplankton.

During the first days of SF^+ (\sim day 3), the total rate of change of mesozooplankton biomass is negative, consistently with the first local minimum of Fig. IV.1e. This is explained by the increase of the horizontal advection that exports zooplankton out of the shelf (Fig. IV.13c,e) and by the decrease of prey availability for zooplankton (i.e. decrease of the phytoplankton biomass, e.g. Fig. IV.1b and IV.11h). After SF^+ (\sim day 13), strong grazing and weak advection losses induce a positive total rate. This grazing induces negative rates of diatoms concentration because the peaks of positive rate of mesozooplankton (Fig. IV.13c) coincide in time with peaks of increased mesozooplankton grazing (Fig. IV.11h,j) and decreased rate of diatoms (Fig. IV.11c). Similar to the previous section concerning diatoms, the biological term of mesozooplankton oscillate in time.

For SF^- , increased grazing of diatoms induce a positive rate of change of mesozooplankton at day ~ 4 (the positive peak of the biological term in Fig. IV.13a,d coincides with the negative peaks of mesozooplankton grazing in Fig. IV.11f,i). This and the reduced horizontal advection explain the first positive peak of mesozooplankton concentration around day 4 of Fig. IV.1d,e. At the end of SF^- (\sim day 8), prey availability is reduced such that the biological sinks dominate and the rate is negative. After SF^- , processes oscillate towards their climatological mean state.

Covariability of nanophytoplankton and microzooplankton (and diatoms and mesozooplankton) terms seem to be consistent with food preferences by size. Similarly to the differences between sizes of phytoplankton, smaller zooplankton species exhibit similar responses as larger zooplankton but with stronger oscillations. This is especially true after the SF perturbations towards the climatological state, in agreement with Fig. IV.1d. We suspect the size and growth time scales to be responsible for this increased oscillatory responses of small plankton species. The remarkable asymmetrical response of microzooplankton to SF^+ and SF^- in Fig. IV.1d is also found in the oscillatory behavior of biological terms in the microzooplankton budgets. Like phytoplankton, anomalies of zooplankton concentration in response to SF perturbations are primarily driven by biological processes.

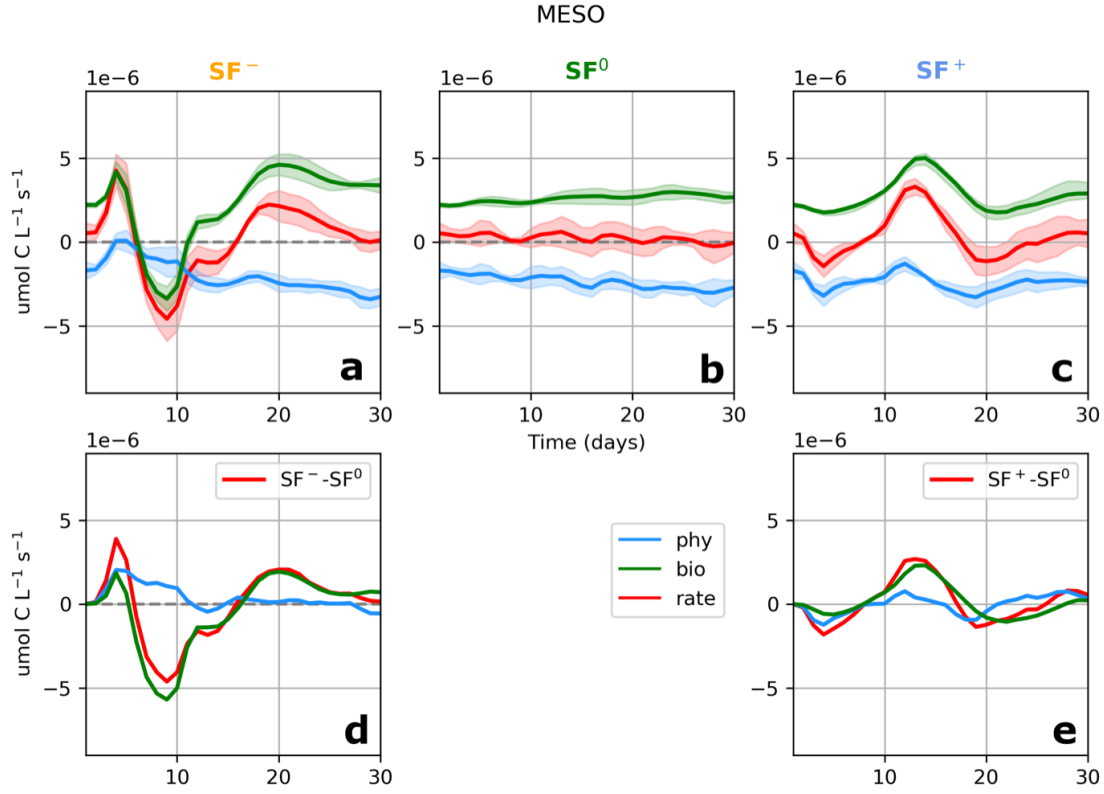


Figure IV.13: Similar as Fig. IV.6 for mesozooplankton concentration.

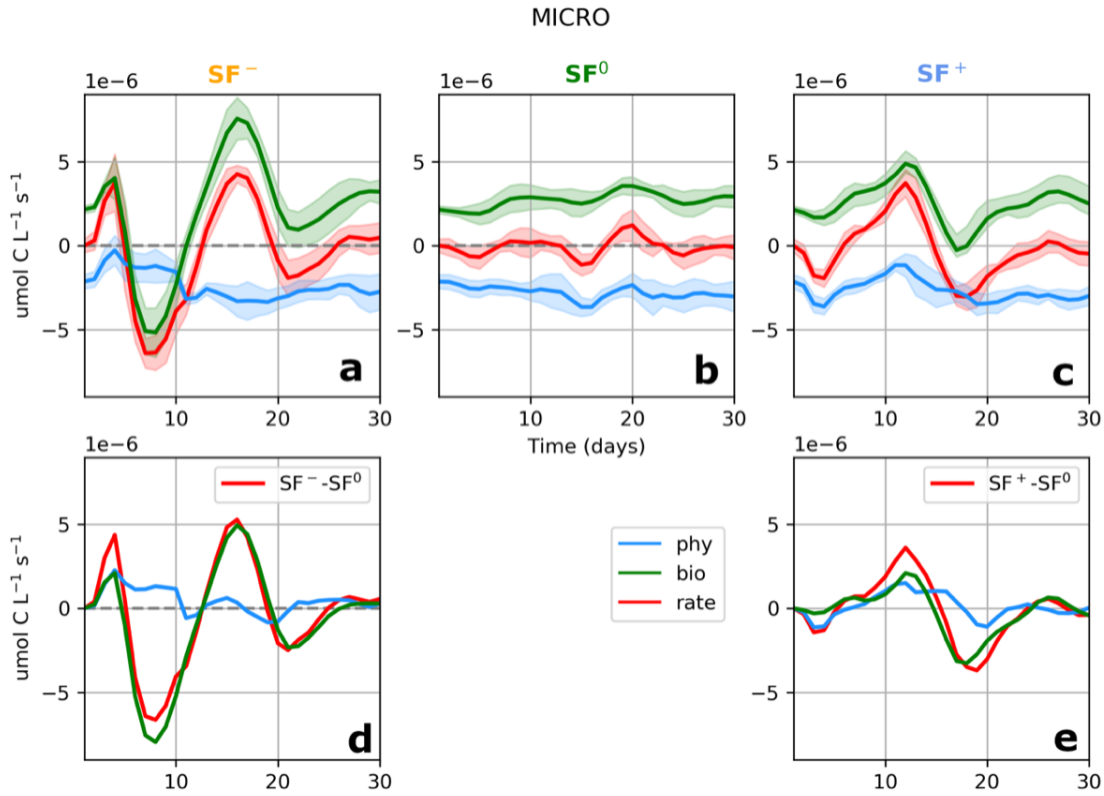


Figure IV.14: Similar as Fig. IV.6 for microzooplankton concentration.

5 Specific inner shelf processes shaping diatoms biomass

We described the processes responsible for nitrate, phytoplankton and zooplankton changes over the shelf. To complement the focus on diatoms and given the spatial heterogeneities found in chapter III, we analyze processes responsible for changes in diatoms biomass over the inner shelf. We describe the different structure of PP over the inner shelf and then describe the detailed diatoms budget over the inner shelf.

5.1 Primary production

In the same manner as Fig. III.2 of the GRL draft (chapter III), we look at the spatial structure of the PP terms along the southwards advection pathways, first over the entire shelf and then over the inner shelf. Over the entire shelf, RP is less present over the northern part of the shelf (RP ~60% of PP) and than over the southern part (>70% of PP, green lines in Fig. IV.15b, see also Fig. IV.9g,h), where new nutrients are scarce. The PP oscillates in space roughly in the same manner as diatoms (compare Fig. IV.15b and Fig. III.2c). In agreement with SF^+ high enrichment, the RP decreases to ~40% of PP in the northern part of the shelf and ~60% in the southern part of the shelf (blue lines in Fig. IV.15b). Conversely, RP dominates PP (>70% over the entire shelf, orange lines in Fig. IV.15b) during SF^- conditions with low enrichment during SF^- . Note that these spatial structures are only presented at a given time (days 9-11) of the SF perturbations.

Over the inner shelf, NP occurs only in the northern part of the shelf, with a total dominance of RP south of $13.5^\circ N$ during SF^0 conditions (green lines in Fig. IV.15a). This domination of RP is increased (RP nearly confounded with PP) and its extension is shifted northwards (south of $14^\circ N$) during SF^- (orange lines in Fig. IV.15a). A larger part of the total PP is explained by NP during SF^+ (blue lines in Fig. IV.15a).

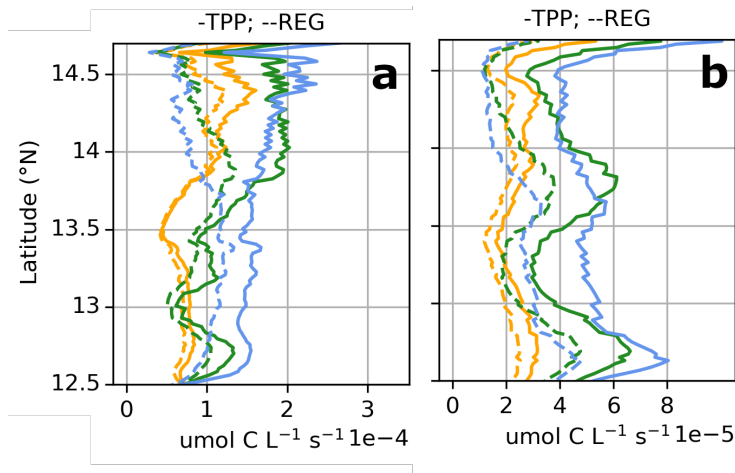


Figure IV.15: Primary production terms (for diatoms) averaged within the 20-0 m (inner shelf, panel a) and 100-0 m (entire shelf, panel b) isobaths and from the bottom of the water column to the surface between days 9-11, and over the ensemble. SF^- , SF^0 and SF^+ are indicated in orange, green and blue lines.

The temporal evolution of PP and RP are shown for the entire shelf and inner shelf in Fig. IV.16 (this information is already shown in Fig. IV.11f,g,h for the entire shelf). Over the inner shelf, RP explains most of the PP responses to SF^{\pm} except the first peak at day 3 for SF^{-} (orange lines in Fig. IV.16a; like over the entire shelf in Fig. IV.16b). Also, the null anomaly of PP between days 3-10 of SF^{+} is explained by a weak but slightly positive NP anomaly. This null PP anomaly during SF^{+} over the inner shelf, which is shallower and more exposed to light, is in agreement with our hypothesis that the reduction of PP during SF^{+} over the entire shelf is due to the increased light limitation.

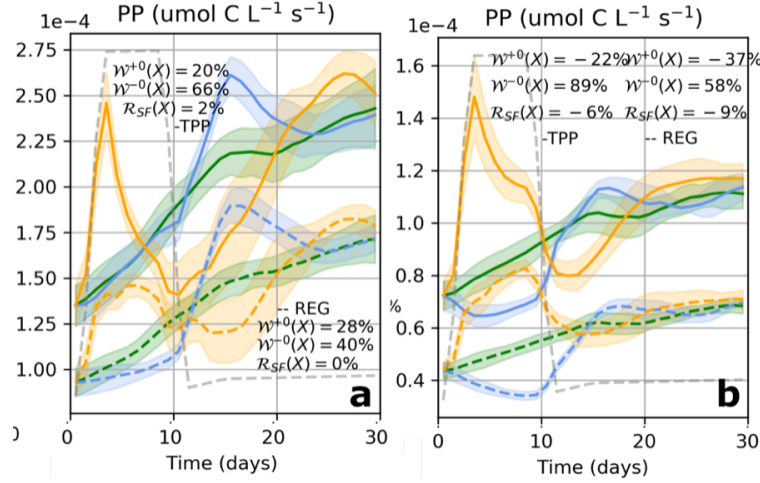


Figure IV.16: Primary production terms (for diatoms) averaged over the shelf in the entire water column, and over the ensemble. Green, orange and blue lines indicate SF^0 , SF^- and SF^+ . Shaded areas indicate the ensemble standard deviation. $W^{\pm 0}$ and R_{SF} diagnose maximum of relative perturbations and asymmetries. The box of integration is between 13-14.75°N and 0-20 m isobaths (inner shelf, panel a) and 0-100 m isobaths (entire shelf, panel b). The trend in all time series corresponds to the seasonal cycle.

5.2 Detailed budget

Similarly to section 4.2, we aim to explain the temporal evolution of diatoms in response to SF^\pm , over the inner shelf (Fig. IV.17). We present only briefly the differences in processes compared to the entire shelf.

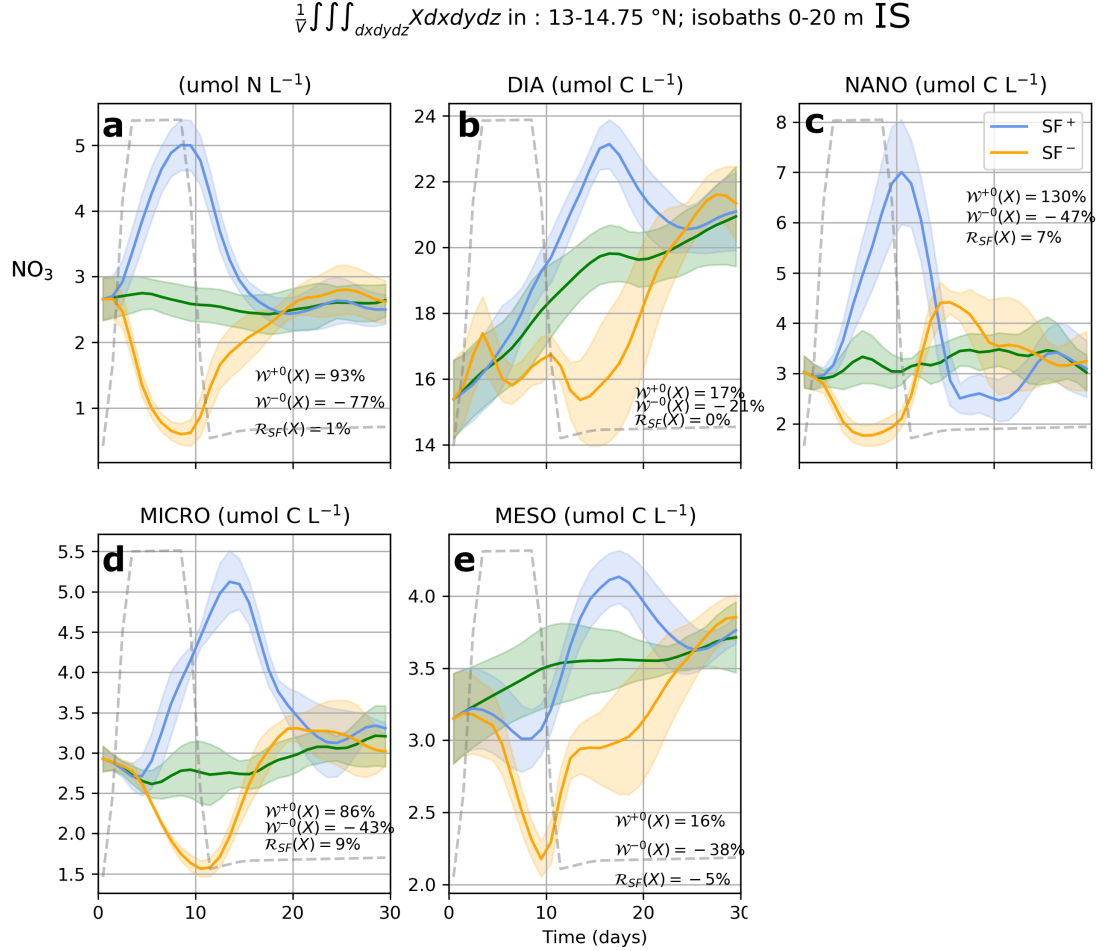


Figure IV.17: Similar as Fig. IV.1 averaged over the inner shelf, limited offshore by the 20 m isobath.

Like over the entire shelf, the inner shelf exhibits a strong peak of PP at day 3 during SF^- and not during SF^+ (Fig. IV.18f,h), induced by NP (Fig. IV.16). Over the entire shelf PP decreases during SF^+ , mostly driven by RP (Fig. IV.11h,j). This is not the case over the inner shelf, likely due to the absence of decrease of RP. At this time also, the reduced mesozooplankton grazing induces a positive diatoms rate (Fig. IV.18h,j). After both SF^+ and SF^- between days ~10-20, anomalies of PP and mesozooplankton grazing are stronger than over the entire shelf (Fig. IV.18f,i).

Overall, oscillations (number of local extrema and their intensities) are increased over the inner shelf, which may be due to the fact we average over a smaller area. The inner shelf exhibits different responses in terms of PP (i.e. increased RP) because the enrichment is weaker and the retention is higher than over the entire shelf.

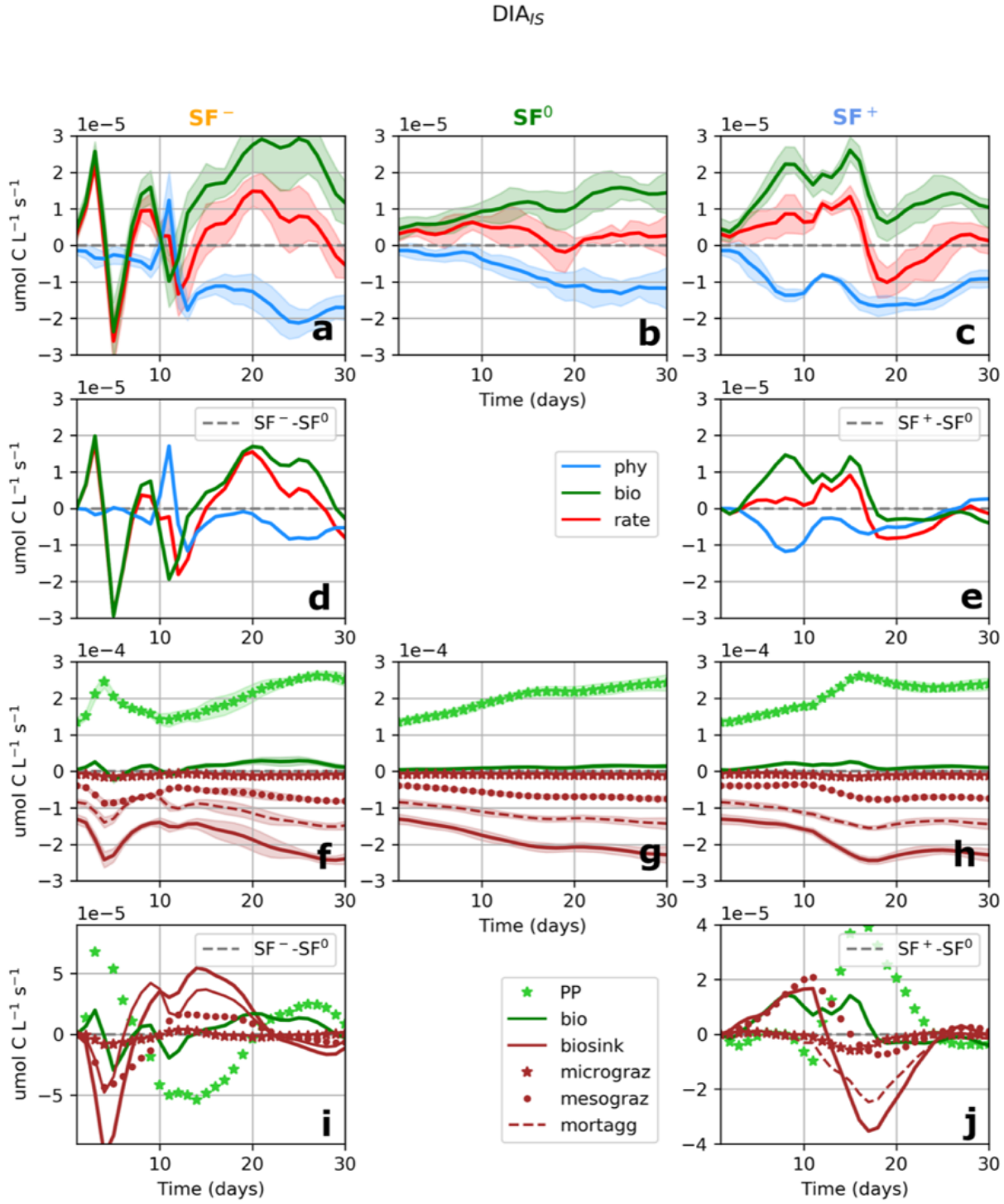


Figure IV.18: Same as Fig. IV.11 but averaged over the inner shelf.

6 Surface mixed layer and vertical processes

6.1 Detailed budget on diatoms

To go further in our understanding of processes driving changes of diatoms biomass, we analyze a budget averaged in the SML. Especially, we aim to evaluate the weight of vertical advection, mixing and entrainment/detrainment with respect to horizontal advection and biological processes described in the previous section. Fields averaged in the SML over the shelf exhibit differences compared to over the entire water column (compare Fig. IV.1 and Fig. IV.19). Nitrate concentration is lower in the SML than in the entire water column and responds with larger anomalies amplitudes to SF^\pm (Fig. IV.19a). A major part of the plankton biomass is concentrated in the SML, with higher plankton biomass in the SML than over the entire water column (Fig. IV.19b-e). Also, their oscillatory responses are enhanced (the number of extrema is increased), supporting the importance of SML processes. One noticeable difference is the lack of first local extrema for mesozooplankton biomass.

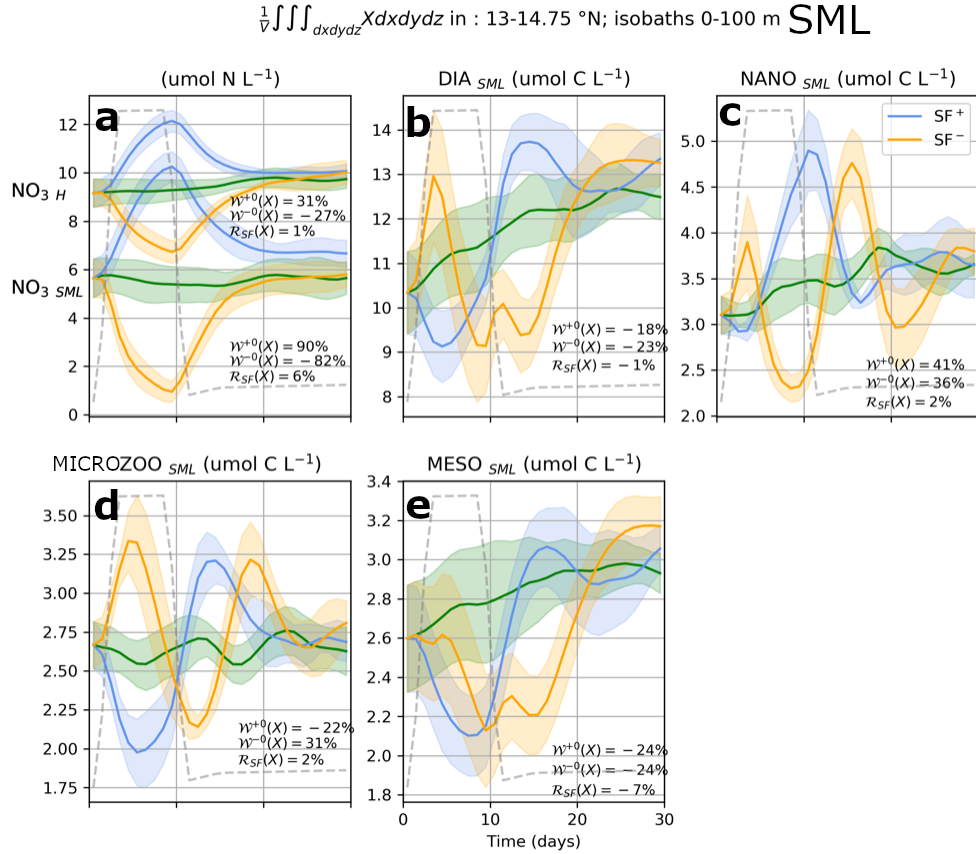


Figure IV.19: Similar as Fig. IV.1 averaged over the surface mixed layer.

In order to understand these differences and processes driving SML changes where most of the biomass is concentrated, we analyze the budget of diatoms averaged in the SML as Eq. IV.1 indicates; with $D = DIA(x, y, z, t)$ in $\mu \text{ mol C L}^{-1}$, horizontal and vertical advection and mixing, entrainment/detrainment and biological terms. The $|_{SML}$ denotes the integration in the shelf SML. The overline denotes the daily and ensemble averages.

$$\begin{aligned}
 \overline{\partial_t D|_{SML}} = & \underbrace{\overbrace{\partial_x u D|_{SML} + \partial_y v D|_{SML} + \partial_z w D|_{SML}}^{adv} + \overbrace{h_{mix}|_{SML} + v_{mix}|_{SML} + entr/detr|_{SML}}^{mix}}_{phy} \\
 & \underbrace{+ PP|_{SML} - mortaggreg|_{SML} - zoograz|_{SML} - mesograz|_{SML}}_{bio}
 \end{aligned}
 \tag{IV.1}$$

SF⁰

On a climatological quasi-equilibrium state, physical and biological processes balance to maintain a quasi-null rate of diatoms concentration (Fig. IV.20b). More precisely, vertical advection brings diatoms from below the SML with positive vertical velocities, vertical mixing and horizontal advection export diatoms out of the shelf SML (Fig. IV.20l). Horizontal mixing has negligible impacts and is not shown. Entrainment tends to be a sink of diatoms but has a weak weight in climatological conditions (slow and weak SML depth changes). In total, physical processes have a negative impact on the total rate. Concerning biological processes, the PP source balances with mortality/aggregation and mesozooplankton grazing sinks and in a weaker way microzooplankton grazing (Fig. IV.20g), like in the entire water column. Also like in the entire water column, individual physical processes are one order of magnitude below biological processes.

SF⁺

During SF⁺, physical and biological processes total rates are overall similar to the ones in the entire water column (Fig. IV.20c). The negative rate of the two first days of the event is partly related to entrainment and dilution of the initial biomass in a deeper SML. Compared to the entire water column, the total physical processes sink is reduced between days 2-10 by a reduction of the vertical mixing intensity (Fig. IV.20m,o). We interpret this as resulting of the increase of the SML depth and thus a decrease of the diatoms concentration at the base of the SML.

SF⁻

Concerning SF⁻, differences in processes between the entire water column and SML averaged are more pronounced. Just after the peak of high PP peak around days 3-4, the export of diatoms out of the shelf SML by physical processes is increased, mostly explained by entrainment (Fig. IV.20k,n). Then, physical processes gradually reach a positive peak around day 11 that is not present in the entire water column average. This is due to the near cancellation of horizontal advection and more importantly to the increase of vertical mixing, associated to SML shoaling that sets the base of the SML at a depth where diatoms concentration is strong. Around day 11 when the wind re-intensifies after SF⁻, vertical velocities are increased in a diatoms rich environment because the SML depth is still below its climatological conditions (Fig. IV.8a). This leads to an enrichment of diatoms in the SML due to vertical advection and the total physical term becomes a source. This is balanced by biological sinks (mainly driven by a PP negative anomaly, Fig. IV.20f,i; consistent with a drastic decrease of nitrate in Fig. IV.19a) that remain negative until day ~11, contrary to the entire water column averages. After day ~12, processes resemble those of the entire water column.

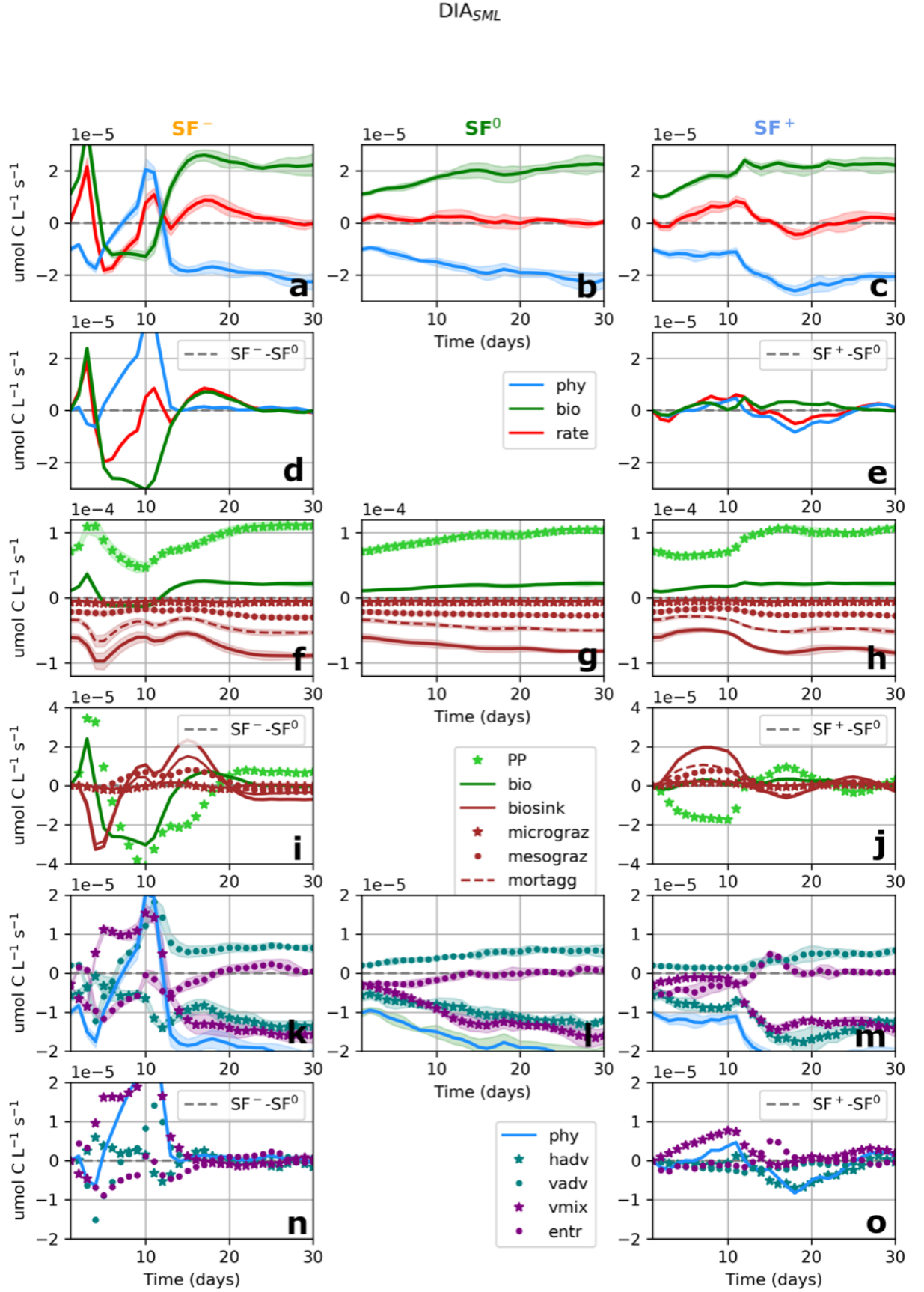


Figure IV.20: Same as Fig. IV.11 but averaged over the inner shelf. Panels k-o are structured similarly with individual physical terms (indicated in the legend). The total physical term is reminded in with the blue continuous line on panels k-o.

6.2 Vertical structure of large plankton biomass during a relaxation event

The weight of vertical processes around day 9 of SF^- (Fig. IV.20k,n) led us to investigate on the vertical structure of plankton biomass. We have already shown that under climatological conditions, the SML fields are totally mixed and the SML contains most of the biomass (Fig. IV.10). Fig. IV.21 shows an example of vertical sections of diatoms concentration of a member of the ensemble at day 9 of SF^- . At this time, we observe a deep maximum of diatoms concentration below the SML and, where the shelf is very shallow, at the bottom of the water column due to vertical sinking (Fig. IV.21a,b). The vertical structure of the diatoms concentration at day 9 is consistent with the entrainment that has removed diatoms from the SML by shoaling.

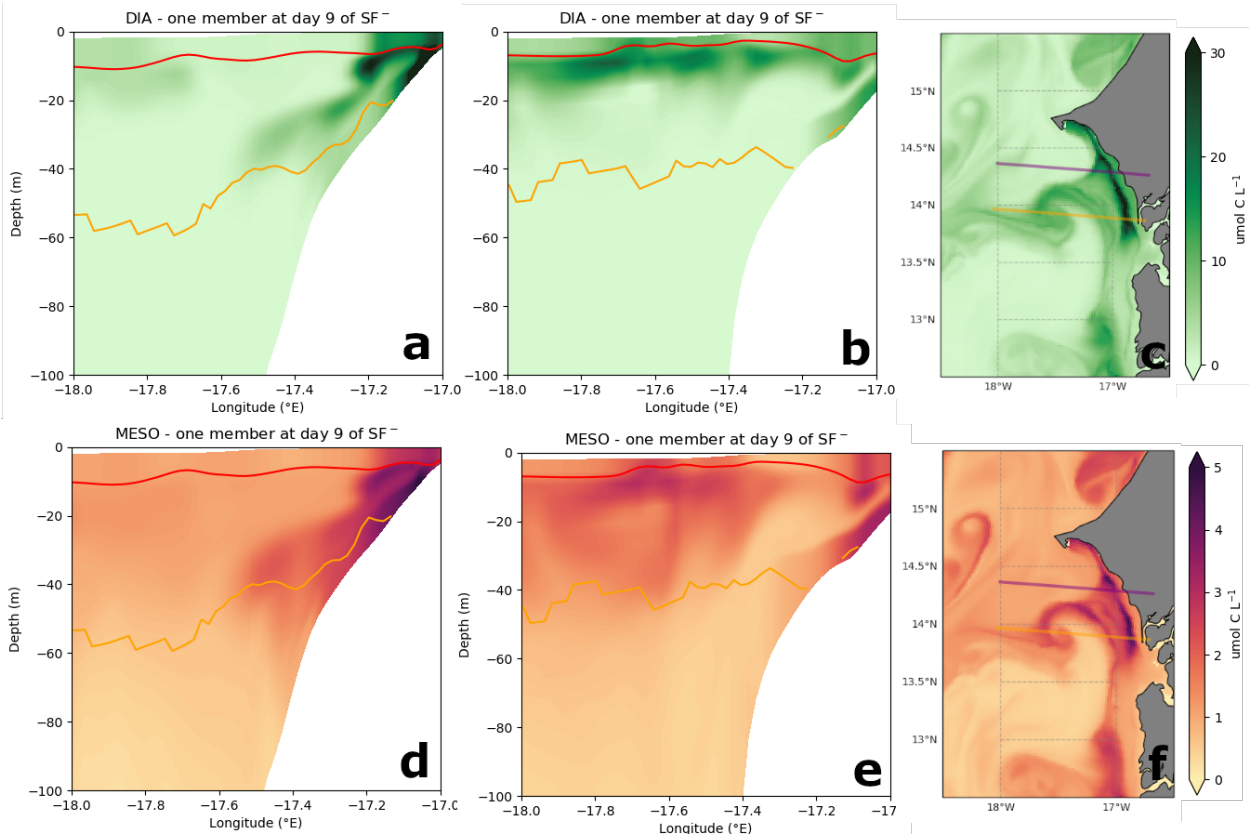


Figure IV.21: Diatoms (a-c) and mesozooplankton (d-f) concentrations for a given member of the ensemble at day 9 of SF^- . The purple and yellow cross-shore sections shown on the horizontal patterns of panels c,f are shown on panels a,d and b,e. SML and euphotic layer depths are indicated in red and orange lines.

Mesozooplankton patches seem more diffuse and somewhat shifted in space compared to diatoms patches. Given their vertical structure, averages in the entire water column (Fig. IV.1e) and in the SML (Fig. IV.19e), we hypothesize that the absence of positive local maximum at day 4 during SF^- is due to the transport of mesozooplankton below the shoaling SML. This could be due to the development of zooplankton where preys are available such that they follow sinking diatoms. This could also be due to subduction at fronts of mesoscale features, which would require further investigation. This is less true for small size zooplankton whose highest concentrations are found in the upper layer (not shown).

The vertical sink of large plankton below the SML follows particular patterns, as for example the subduction feature in the northern cross-shore section shown in Fig. IV.21a,d,c,f. Further south, in association with a cyclonic mesoscale eddy, large size plankton do not follow subduction patterns and highest concentrations are found at subsurface below the SML (shown on the southern cross-shore section of Fig. IV.21b,e,c,f; note that mesoscale features have been discussed in section 2.4.1 of chapter II). It is also worth noting the reduction of the euphotic layer depth at the locations of high plankton concentration patches.

In this section, we emphasize on the particular response of large size plankton to an upwelling relaxation through their transport to the subsurface. Overall, this sheds light on the importance of the vertical structure of diatoms in the weight of vertical processes during SF⁻.

6.3 Submesoscale eddy fluctuations

To complement the SML and vertical processes analyzed in this section, we present briefly an avenue that might be worth exploring. We suspect that submesoscale processes may have a moderate impact on the changes of diatoms concentration in the SML. In addition to the mean vertical velocities, coherent eddy fluctuations of vertical velocity and diatoms concentration anomalies could participate to the total vertical advection term (inspired by the submesoscale diagnostic on temperature of Capet et al., 2008b). In our analysis, this could be verified by computing $\partial_z(w'D')$ of Eq. IV.2 by the difference between a 5 day running average of $\overline{\partial_z(wD)}^{5day}$ computed online and a 5 day running average of $\partial_z(\overline{wD}^{5day})$ computed offline from averaged \overline{w} and \overline{D} fields.

$$\partial_z(w'D') = \overline{\partial_z(wD)}^{5day}_{online} - \partial_z(\overline{wD}^{5day})_{offline} \quad (IV.2)$$

We hypothesize that this may have a moderate role in the vertical advection negative role around day 3 of SF⁻ (Fig. IV.20k,n), where mean vertical velocities are nearly cancelled (Fig. II.8 of chapter II). This analysis was not developed due to time constraints.

7 Discussion

In this chapter, we show that the control of nitrate over the south Senegalese shelf is mostly driven by horizontal advection. In a larger domain including the SSUS and extending further offshore, [Auger et al. \(2016\)](#) find a dominant role of southerly horizontal advection in the supply of nutrients. This difference could be explained by their larger spatial domain, and especially because our shelf average does not include their offshore area containing a fraction of the Mauritania poleward current.

In order to discuss the impact of SF^\pm on biological processes, we show in Fig. IV.22 processes averaged between days 3-8 over the entire shelf and inner shelf (panel a) and the time integrated relative anomaly of PP induced by SF perturbations $\mathcal{P}_{box;day}^{SF}$ (panel b), as defined by Eq. IV.1.

$$\mathcal{P}_{box;day}^{SF^\pm} = \left(\frac{\int PP dt_{box}^{SF^\pm} - \int PP dt_{box}^{SF^0}}{\int PP dt_{box}^{SF^0}} \right) |_{day} \quad (IV.1)$$

Consistently with previous findings based on dynamical arguments (persistent warm waters inshore; [Ndoye et al., 2017](#)), we demonstrate that the shelf (and even more the inner shelf) PP benefits more of relaxed conditions during SF^- (Fig. IV.22b; through increased retention and reduced light limitation) but, through the counter balancing effects of biological sinks, the actual increase of phytoplankton concentration is favored under intensification conditions during SF^+ (Fig. IV.22a; decreased mortality/aggregation and mesozooplankton grazing). Fig. IV.22b also exhibits a major asymmetry in the response of PP ($\mathcal{R}_{SF}(PP) \sim 30\%$, also true over the inner shelf), in contrast to modest asymmetries of biological concentrations and processes.

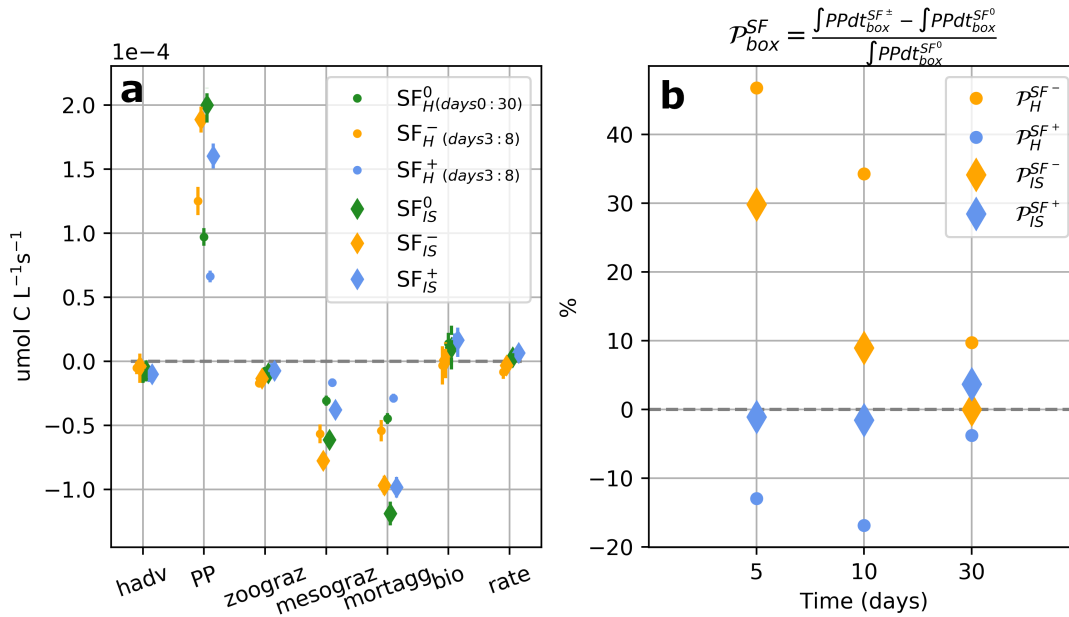


Figure IV.22: Physical and biological terms of the diatoms budget integrated on the shelf whole water column between days 3:8 (and 0:30 for SF^0 ; panel a). Relative perturbations of total PP integrated until days 5, 10 and 30. Colors (green, blue, orange) indicate SF^{0+-} ; dots indicate the entire shelf and diamonds the inner shelf.

In agreement with findings of [Botsford et al. \(2003\)](#), we find that the intensity of PP is related to the retention of biological material over the shelf (retention and PP are enhanced during SF^- and reduced during SF^+ ; see *hadv* and PP averaged between days 3-8 in Fig. [IV.22a](#), and cumulative PP in Fig. [IV.22b](#)). Our modeling study exhibits similar favorable environmental conditions for increased PP as [Largier et al. \(2006\)](#) findings: a relaxed period after upwelling favors PP through nearshore retention and exposure to light. The time scale of new nutrients intake for primary production during relaxed conditions of our study (NP anomaly in Fig. [IV.11i](#) between days 2-6) agrees with the optimal window of 3-7 days for chlorophyll-a increase found by [Wilkerson et al. \(2006\)](#). However, in our case, high PP is overcompensated by grazing and leads to a decrease of biomass during upwelling relaxation.

Not many studies focused on biological individual processes that control plankton biomass, especially at the shelf scale. At the seasonal time scale and over the Canary upwelling system, previous studies identified grazing as the dominant biological sink of phytoplankton ([Lachkar and Gruber, 2011](#)). Our results contrast their findings by putting forward the importance of mortality/aggregation term before grazing (see Fig. [IV.22a](#)). Another interpretation of the mortality/aggregation importance can be the inability of the prey-predator relationships to reach a stable equilibrium such that there is an over production of phytoplankton with respect to zooplankton grazing. This could be due to a slow growth of large plankton species ([Sarmiento and Gruber, 2013](#)), or to the reduced time and spatial scales, but also by particular circulation around peculiar geomorphological features. In particular, the high retention over the shelf and weak enrichment implied by the Cape and shallow shelf, along with the pulsed nature of enrichment, can prevent the prey-predator relationship to stabilize.

In addition to these considerations, our results rise a set of interrogations about phytoplankton-zooplankton relationships. The top-down control of phytoplankton biomass by zooplankton grazing needs to be confronted with in-situ observations over the Senegalese shelf. We also wonder about the sensitivity of phytoplankton biomass to the model parameterization of grazing. To investigate this further, a sensitivity test on grazing parameterization could be designed inspired of [Chenillat et al. \(2021\)](#), and is discussed in chapter [V](#). Also, we wonder about the impact of a major exit of biomass (by phytoplankton mortality/aggregation) out of the direct food chain on the biogeochemical cycles and food web of the planktonic ecosystem. Especially, the organic matter resulting from this mortality is exported vertically in the water column and might have important consequences on sediment dynamics in such a shallow environment.

8 Conclusion

The process oriented numerical analysis led in this chapter aimed to bring additional knowledge of the planktonic ecosystem of the south Senegalese upwelling sector in response to synoptic wind intensification and relaxation. We computed budgets of several fields to assess the role of physical and biological processes and revealed a few specific properties. A particular focus on diatoms has been developed to understand thoroughly individual and biological mechanisms driving their biomass changes over the entire shelf, over the inner shelf and in the surface mixed layer. To conclude, we rely on the schematic in Fig. IV.23 summarizing the structure of the planktonic ecosystem and control processes of diatoms concentration.

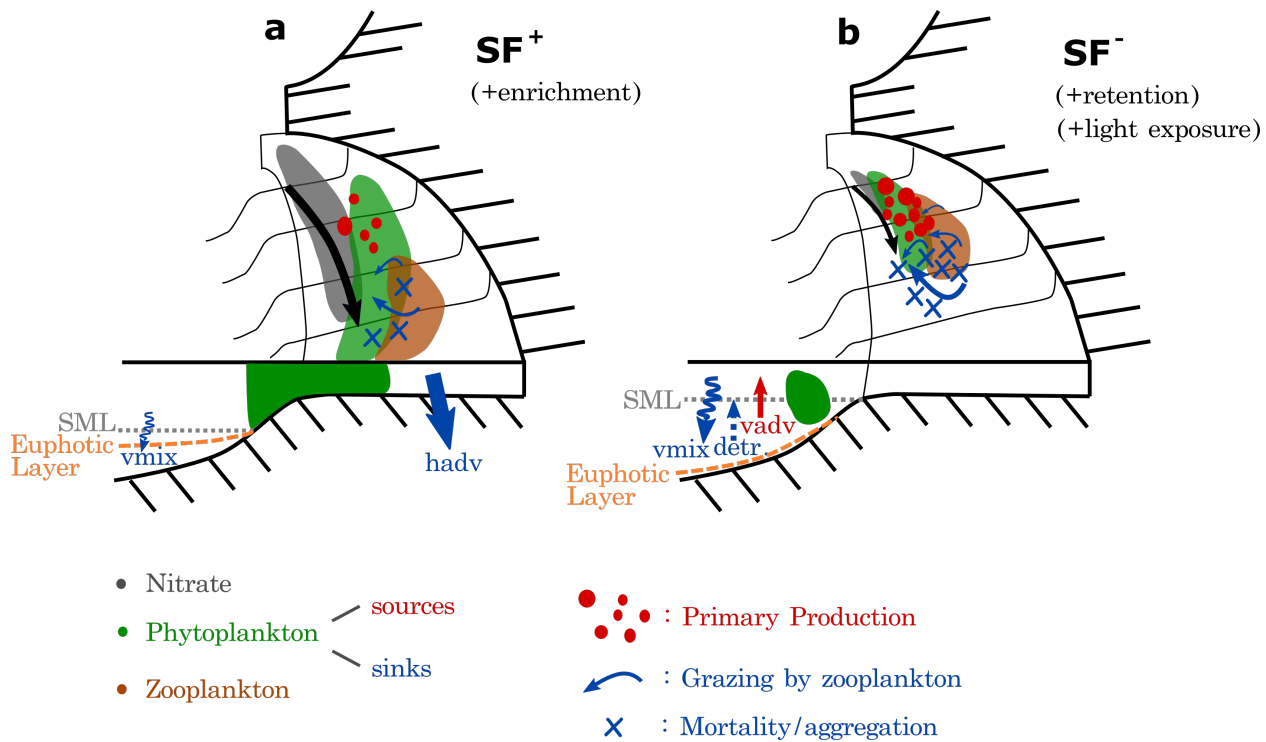


Figure IV.23: Schematic of 3D shelf nitrate and plankton response to SF^+ (a) and SF^- (b). Nitrate, phytoplankton and zooplankton concentration patterns are indicated in colored areas (respectively grey, green and brown). The continuous black arrow indicate the strength and orientation of the circulation of the flow. Grey and orange dashed lines indicate the SML and euphotic layer depths. Processes driving the rate of change of diatoms concentration in the box SML are shown as follows. Colors red and blue indicate the source and sink terms. Straight continuous arrows indicate advection terms associated to diatoms transport. Entrainment is indicated with the dashed arrow and vertical mixing by sinuous lines. Primary production, grazing by zooplankton and mortality/aggregation processes strength are indicated with the dots, curved arrows and crosses markers. Noticeable modifications of environment conditions are indicated in parenthesis below SF^\pm titles. Note that the bathymetry and inner shelf scales are unrealistic, the location of grazing by zooplankton and mortality/aggregation processes are arbitrary over the shelf and that it represents the state of the planktonic ecosystem in the late part of the SF perturbation, when we consider the system to be the most perturbed.

At the climatological time scale, we have shown that diatoms are produced over the northern part of the shelf in agreement with the nitrate input in the upper layer, and are either grazed by zooplankton or die/aggregate along their southwards alongshore advection. Especially, we find that these individual processes are one order of magnitude above other biological and physical processes (Fig. IV.22a).

In addition, we focused on the modification of processes associated to synoptic wind fluctuations. Processes driving diatoms concentration changes at the climatological scale balance each other differently in response to SF^\pm . Except for nitrate, all plankton biomass rates of change are primarily driven by biological processes. In response to SF^+ , the concentration of diatoms increases despite the decrease of primary production because of reduced grazing pressure and mortality/aggregation (Fig. IV.23a). The opposite is true during SF^- when weaker ocean dynamics are associated to an increased biological pressure through zooplankton grazing (Fig. IV.23b). Thus, we shed light on the major counter balancing role of mortality/aggregation and mesozooplankton grazing in response to perturbed primary production. At the shelf scale, SF^- primary production is several times stronger than during SF^+ , and, through counter balancing effects, so are biological sinks. This represents a major asymmetry between responses of an individual biological process, which is overall reduced by counter balancing terms. Counter balancing effects of biological terms are responsible for plankton biomass oscillations described in chapter III. Overall, the shelf primary production benefits more of relaxed upwelling conditions but the phytoplankton concentration effectively benefits more of intensified upwelling conditions.

Physical processes play an overall second order role in changes of plankton biomass that are mostly driven by biological processes in the entire water column over the shelf. However, individual physical processes can have a large impact on the budget in the surface mixed layer. Under climatological conditions, vertical mixing is about the same order of magnitude as horizontal advection and removes diatoms from the surface mixed layer. At synoptic scales, this can be enhanced along with vertical advection and entrainment (Fig. IV.23b), that can reach the absolute amplitude of individual biological sink terms, especially during SF^- shallow surface mixed layer conditions.

Conclusions and perspectives

Conclusions

In this thesis, the main objectives were to (i) describe the properties of a wind-driven planktonic coastal (eco)system kicked by synoptic wind intensification and relaxation perturbations and to (ii) bring additional knowledge on the important and little studied Senegalese coastal upwelling system. We used an original approach based on ensemble numerical experiment and on idealized synoptic wind intensification and relaxation events. Dynamical and planktonic ecosystem properties responses of the system to synoptic wind fluctuations were analyzed. Particular attention was paid to identify the processes responsible of temperature and plankton ecosystem changes over the shelf. In this section, we present the main conclusions of this thesis, develop perspectives and further implications of this work.

In chapter II we identify air-sea heat fluxes and horizontal advection as the main processes driving heat changes over the shelf surface mixed layer (SML). Vertical advection cools the SML only over a reduced area just south of Cape Verde where resurgence occurs. Synoptic wind fluctuations alter the physical structure of the system with temperature, SML depth and currents reaching values outside of their range of intrinsic variability. Synoptic wind intensification increases the SML depth, intensifies currents, decreases the SST and enhances the role of advection in the heat budget. Relaxation effects are opposite for the physical structure and modify the role of advection into a warming process by bringing warm offshore water onto the shelf. Only modest asymmetries between intensification and relaxation are found and imply only modest residual effects on the mean state.

Chapter III focused on the response of the planktonic ecosystem to synoptic fluctuations as a whole. All planktonic ecosystem fields were found to be outside of their range of intrinsic variability and altered differently with respect to physical variables. We identified oscillatory responses of planktonic concentrations in time and space, with delays and shifts depending on the event and the species. The initial atmospheric perturbation propagated in the coastal ocean dynamics, nutrients, phytoplankton and zooplankton fields. The relative anomaly of the perturbation is damped towards the upper trophic levels of the ecosystem. Responses were found to be different over the inner shelf, which exhibits enhanced retention and low enrichment properties.

In chapter IV, we complemented the analysis of the planktonic ecosystem response by focusing on control mechanisms of nitrate, phytoplankton and zooplankton evolution. Control mechanisms of the diatoms biomass, as the dominant plankton species in the ecosystem, was of particular interest. We found that primary production balances mesozooplankton grazing and mortality/aggregation sinks. These individual biological terms are found to be one order of magnitude larger than physical processes over the shelf, i.e. the horizontal advection. In response to synoptic forcing anomalies (SF^{\pm}), the rate of change of nitrate is mostly driven by

horizontal advection. Conversely, changes in plankton biomass are mostly driven by biological processes, and biological source and sinks balance each other and oscillate in time. An analysis of surface mixed layer processes highlighted the role of vertical mixing during all events and of vertical advection and detrainment during shallow surface mixed layer conditions associated to a synoptic wind relaxation (SF^-).

The benefit of relaxed conditions for the shelf primary production (enhanced retention and exposure to light) changes into unfavorable conditions with enhanced pressure by zooplankton grazing and mortality/aggregation. The opposite effects during SF^+ shed light on the actual benefit of phytoplankton biomass of intensification conditions (nutrient enrichment and lower pressure by biological sinks).

Overall, properties of a coastal upwelling planktonic (eco)system have been uncovered in an analysis of its response to synoptic wind fluctuations. Additional knowledge has been brought on synoptic scale dynamics, heat balance, nutrient and plankton evolution in the south Senegalese sector, along with the associated processes. Our analyses support the hypothesis that synoptic rectification has a modest impact on the mean state. This thesis raises a series of additional questions about our understanding of coastal upwelling ecosystems. Below we list a series of questions we believe worth exploring and the associated experiments necessary for their investigation.

Complementary investigations

Succession of wind anomalies

To go further in our understanding of the impact of synoptic wind fluctuations on the planktonic ecosystem, several additional numerical experiments could be designed. A first set of experiments could explore the variety of wind events by modifying the intensity, period and number of wind anomalies.

In the methods section, we justified our choice to apply only one idealized wind perturbation to extract the first order response of the system. Mainly based on the physical simulations, we argued that applying several successive wind events was challenging to design because of problematic choices of the duration of events, magnitudes and time between anomalies; and we concluded that this was beyond the scope of this study (see chapter II section 4.1). However, the results of the biogeochemical simulations highlight the value of studying ecosystem responses with the wind history in mind and help designing the successive events. Because of the oscillatory responses of the planktonic ecosystem variables, we wonder about their responses to a second atmospheric perturbation. The second perturbation could be initiated at the time of the peak anomaly of a given variable. For example, how would respond the diatoms biomass to a second intensification a few days after the end of the first intensification, when it reaches its maximum biomass? What if we inject an opposite anomaly, i.e. a relaxation after the maximum of diatoms biomass following the wind intensification? Would that result in a faster return to the climatological mean state? Would the oscillations be amplified or damped in the two cases?

Also, it would be interesting to study the ecosystem responses to extreme perturbations. This could be investigated by compositing rare and intense wind events detected by two standard deviations from the mean wind. This could help understand the potential proliferation

of harmful algae in coastal areas in response to specific wind conditions (Kudela et al., 2005; Gobler, 2020), but also the responses of coastal upwelling ecosystems to a changing climate in which extreme events become more frequent (Jentsch et al., 2007), and assess their resilience.

Physical model improvement

Several ways forward can be mentioned concerning the improvement of the representation of physical processes over the SSUS. Improvement of the quality of forcing fields is an evident way forward, including for example more realistic cross-shore wind profiles (Capet et al., 2004). Also, increasing the spatial resolution (e.g. from ~2.5 km to ~100 m) would allow the resolution of the internal gravity waves activity, which is of interest to assess the impact of their breaking on the shelf on the physical structure of the shelf, as suspected by observations of Capet et al. (2017), and the associated consequences on the shelf mixing properties, nutrient supply and planktonic ecosystem structure. Further thinking is needed to design properly these improvements.

Phytoplankton sensitivity to the parameterization of bottom-up and top-down control mechanisms

The difficulty to evaluate our model with observations suggests further research on the sensitivity of phytoplankton to the parameterization of its bottom-up and top-down control mechanisms. Especially, important biases may result from our lack of adjustments of the model parameters to fit the observations. Although modifying phytoplankton growth parameters is questionable (Franks, 2009), it can induce important changes in our results, in terms of mean plankton biomass but also of oscillatory responses. Thus, sensitivity tests on the parameterization of bottom-up controls may deserve further investigation.

Phytoplankton and zooplankton relationships are complex (Irigoien et al., 2005; Evans et al., 2015) and the phytoplankton top-down control by zooplankton grazing is of first order in our simulations. This makes us wonder about the sensitivity of the phytoplankton biomass to the grazing parameterization. Chenillat et al. (2021) have shown the major sensitivity of the phytoplankton biomass to top-down processes, currently less well parameterized in planktonic ecosystem models than bottom-up effects. Inspired by their study, we can imagine a set of numerical experiments modifying grazing parameterization. The Michaelis-Menten like grazing function depends on prey density X and has a density threshold below which there is no grazing, the grazing refuge T . We can design three sets of simulations, in which (i) we set the grazing refuge T to 0, (ii) we modify T depending on the plankton size and obtain a size dependent refuge parameter, and (iii) we modify the half saturation constant. This would assess the importance of the grazing parameterization in PISCES, potentially support Chenillat et al. (2021) findings about the importance of top-down effects on phytoplankton biomass control and expand our findings over the Senegalese shelf.

Adding biological processes

Another aspect worth investigating is the evaluation of parameterizing additional biological processes in the model. Some unrepresented processes may have rectification effects and thus induce additional asymmetries in the responses to intensification and relaxation, which can be identified by additional numerical experiments. This would be a way to assess the respective

importance of additional processes in a coastal upwelling system over a shallow shelf. Also, this is a step forward marine biogeochemical model development, and their application in coastal domains.

Improvement of the nitrogen cycle is a potential good candidate to make our simulations more realistic. Especially, improving the modeling of the atmospheric nitrogen fixation by diazotrophs in marine biogeochemistry models has been shown to have key impacts on primary production estimates (Bopp et al., 2022). Despite the potentially limited impact on the nearshore area of our coastal system, this improvement of nitrogen fixation modeling may reduce the offshore bias of chlorophyll in our simulations compared to satellite observations. Another aspect of the nitrogen cycle, that is specific to coastal and shallow shelf environments, is the rate of permanent burial of nitrogen in the sediments. In PISCES, this has been parameterized for offshore studies (Aumont et al., 2015) and could have an important impact on the nutrient structure over the shelf and particularly over the inner shelf where nitrate is depleted.

Diel vertical migration can modify the structure of zooplankton (Peterson et al., 1990; Messié and Chavez, 2017; Marta-Almeida et al., 2006), enhance nearshore retention if their vertical migration amplitude is sufficient to reach the subsurface onshore flow at depth (Batchelder et al., 2002) and is believed to impact remarkably the vertical structure of large particles in highly productive areas (Gorgues et al., 2019). In our simulations of the south Senegalese shelf, most of the zooplankton biomass is located nearshore and especially over the inner shelf where the water column is fully mixed. Taking into account the diel vertical migration would mostly affect zooplankton over the mid-outer shelf and offshore domains, that represent only a small fraction of the zooplankton biomass, and thus impact modestly their global structure over the shelf. However, this might be worth exploring to assess the impact of vertical migration in a coastal environment and potential rectification effects.

Another interrogation is about the impact of planktonic stoichiometric variability on ecosystem properties. Stoichiometric variability allows changes of the C:N:P ratio in phytoplankton, which is constant in our simulations. This phytoplankton plasticity depends on environmental conditions, such as nutrient availability (for example phytoplankton N/C ratios are low in regions depleted in nitrogen), light, temperature, and phytoplankton lineage (Kwiatkowski et al., 2018). As a consequence, zooplankton ratios vary with those of their prey, indicating their food quality. Additional numerical experiments with variable stoichiometric ratios allowed (possible in PISCES, Kwiatkowski et al., 2018) would help to answer several open questions. The first aspect is to assess how much stoichiometric variability modifies the planktonic ecosystem structure. If the stoichiometric variability impacts strongly the ecosystem structure, investigating how the phytoplankton nutrient intake ratio changes in response to synoptic fluctuations could reveal essential ecosystem properties. For example, during a relaxed period of low nutrient availability, would the ratios (e.g. N/C) decrease? This is of particular interest in nitrogen depleted areas, e.g. over the inner shelf. If so, how would zooplankton react to this decrease of food quality? How would growth rates be modified? Would the zooplankton biomass increase in poor food quality conditions or decrease because of deleterious quality? In other words, how much of the response is driven by stoichiometric variability? To what extent does the planktonic ecosystem adapt and is resilient through this plasticity to perturbations of environmental conditions?

Higher trophic levels

Another possible further investigation is to broaden the scope of the ecosystem to higher trophic levels, and especially to small pelagic fishes. Inspired by [Brochier et al. \(2018\)](#), a numerical experiment could be designed by coupling for example a round sardinella model to our physical-biogeochemical simulations. Given fish growth time scale, adjusting parameters of our experiments would be needed, and perhaps longer simulations with several wind events should be considered. Properties of small pelagic growth, stocks, ages, sizes, food availability, migration behaviors, habitats in response to synoptic wind fluctuations could be assessed.

It is known that mesoscale features tend to structure phytoplankton communities ([McGillicuddy and Robinson, 1997](#); [d'Ovidio et al., 2010](#)) and thus pelagic fish where food availability is enhanced ([Potier et al., 2014](#); [Benoit-Bird and Lawson, 2016](#)), and their predators (for example in mesoscale eddies, [Gaube et al., 2018](#); [Della Penna and Gaube, 2020](#)). Coastal geomorphological features can also impact fish structure as for example shelf break areas, considered as optimal locations for a trade-off between predation and starvation ([Shropshire et al., 2022](#)), but also upwelling bays with enhanced food availability that favors pelagic fish development ([Hutchings et al., 2006](#); [Largier, 2020](#)), which support the interest of investigating the impact of synoptic wind events on the structure of coastal pelagic fish.

To follow up with the questions raised by the stoichiometric variability, one can imagine questions related to the impact of plankton food quality on pelagic fish. Also, over the Senegalese shelf, two main types of sardinella are found: the sardinella aurita that is more abundant (~72%, from [Brochier et al., 2018](#)) and the sardinella maderensis. Food quality might be one driver of the distribution of these two sardinella species.

Synoptic wind fluctuations can impact the larval dispersion over a coastal upwelling system and the associated recruitment. Relaxation of upwelling impact the larvae dispersal through enhanced retention and thus larvae nearshore accumulation ([Largier, 2020](#)). Intense upwelling enhances advective offshore losses, even though this has been challenged by observations of cross-shelf postlarvae inshore migration ([Morgan et al., 2018](#)). Thus, we suspect intensification and relaxation to have major asymmetrical effects on recruitment behaviors, location and extent of pelagic habitats.

In the same idea as the top-down control of phytoplankton by zooplankton, one can imagine the importance of the top-down control of zooplankton by small pelagic fishes ([Cury et al., 2000](#)), that is parameterized by a quadratic mortality term in PISCES (that represent top-down pressure by unrepresented term, predators and viral diseases, [Aumont et al., 2015](#)), and might deserve further attention as well (for example modifying the mortality function).

Challenges of in-situ measurements

One major implication of our findings is whether the modeled oscillatory behavior of the planktonic biomass realistic or caused by unrealistic mathematical relationships. In order to evaluate this, we can sketch strategies of in situ measurements cruises. The Lagrangian solution is to follow the upwelled water parcel along its trajectory with a ship and measure planktonic biomass at a few stations along the way. However this is rare over the Senegalese shelf (recent intensive oceanographic cruises are: "*Upwelling du Sénégal 2 - UPSEN2*" in 2014 ([Capet et al., 2017](#)) and "*Structuration des COMMUnautés PlanctoniquEs en réponse à la dynamique de l'upwelling sud-Sénégalais - SCOPES*" in December 2022 - January 2023).

Another Eulerian solution is to measure at one, and ideally more, fixed stations to observe spatial and temporal variability of biogeochemical fields. Over the Senegalese shelf, only the buoy Melax was deployed and provides high frequency time series but is limited in temporal continuity and types of sensors (see chapter I section 3.10). Also, a buoy located further south over the shelf would be needed to assess the potential oscillations of biogeochemical fields. To obtain a sufficient long time series, chlorophyll measurements (with fluorometers) as a proxy for phytoplankton biomass might be an effective sampling strategy.

In a similar manner, analysis of long time series of chlorophyll satellite observations might be helpful to evaluate potential primary production oscillations, but also its spatial and inter-annual variability. However, chlorophyll satellite images over Northwest Africa are tricky to analyze because of cloud coverage and the influence of Saharan dust (Correa et al., 2021). In a larger context, this could also be used to identify potential long term trends (e.g. Kahru et al., 2009 in the CCE), and provide keys to understand the long term variability by correlation with large scale or climate indices. Despite the important lack of in situ observations to evaluate remote sensing observations, another objective could be to develop regional indices of biological active upwelling intensities (like in the CCE, e.g. Jacox et al., 2018).

Upwelling systems in a changing climate

The impact of climate change on upwelling systems is of major interest given their productivity and socio-economic importance (Bograd et al., 2023). Over most upwelling systems, upwelling favorable winds have been observed to intensify and are projected to continue (Bakun, 1990; Sydeaman et al., 2014; Bakun et al., 2015). These wind changes are due to atmospheric circulation changes, and especially a poleward extension of Hadley cells (Lu et al., 2007) and thus of upwelling favorable winds (Rykaczewski et al., 2015). However, effects on temperature and biogeochemistry remain unclear (García-Reyes et al., 2015). Future changes in increased winds and thus vertical velocities do not necessarily have a positive impact on nutrient supply in the euphotic layer because of increased stratification from climate warming (Lorenzo et al., 2005; Jacox and Edwards, 2011). In the CCE, uncertainties on nitrate supply changes seem to be driven by the nitrate vertical structure rather than stratification and vertical velocities (Pozo Buil et al., 2021). Source waters are suspected to reach the CCE with higher nitrate concentration because of changes in the large scale circulation (Rykaczewski and Dunne, 2010) and shallower euphotic layers (Aksnesa and Ohman, 2009).

In the Canary upwelling system, wind changes seem to vary with the sub domain of interest. Near the Iberian peninsula, winds intensify (Bograd et al., 2023; Rykaczewski et al., 2015) while this is questionable over the North-West coast of Africa (Benazzouz et al., 2015). The poleward shift of the Azores anticyclone is suspected to weaken the upwelling intensity of the Senegalese-Mauritanian system (Sylla et al., 2019). Changes over the south Senegalese shelf need further attention (e.g. down-scaling studies of projected winds).

Further perspectives of the thesis

Similar experiments in other upwelling sectors could be informative of potentially different processes at play and support or contrast our findings about modest asymmetries over the south Senegalese shelf. The necessity of increasing in situ measurements over the Senegalese shelf has been mentioned earlier to evaluate plankton ecosystem dynamics, understand better the spatial and interannual variability. In addition, increasing this effort is essential for assessing the impact of anthropogenic nutrient discharge on the coastal upwelling ecosystem (Dakar is a growing city with only 4 wastewater treatment plants for 1.1 million people), with potential major implications of eutrophication on the coastal ecosystem ([Kessouri et al., 2021](#)). Modeling studies, along with observations, are a tool to assess anthropogenic and climate change impacts on the ecosystem, fisheries and to support management policies of such vulnerable and socio-economically important coastal environments.



Appendix A: JGR Oceans publication

Key Points:

- The extension of elevated chl-a waters covaries with the intensity of offshore transport diagnosed from satellite-derived currents
- Offshore sites of elevated carbon export are associated with advection of chlorophyll-rich coastal waters
- Climate forcing by ENSO and the NPGO accounts for much of the interannual variability in offshore extent of chlorophyll-rich coastal waters

Supporting Information:

- Supporting Information S1

Correspondence to:

P. Chabert,
pierre.chabert@locean-ipsl.upmc.fr




Citation:

Chabert, P., d'Ovidio, F., Echevin, V., Stukel, M. R., & Ohman, M. D. (2021). Cross-shore flow and implications for carbon export in the California current ecosystem: A Lagrangian analysis. *Journal of Geophysical Research: Oceans*, 126, e2020JC016611. <https://doi.org/10.1029/2020JC016611>

Received 17 JUL 2020

Accepted 14 DEC 2020

Cross-Shore Flow and Implications for Carbon Export in the California Current Ecosystem: A Lagrangian Analysis

P. Chabert¹ , F. d'Ovidio¹, V. Echevin¹, M. R. Stukel² , and M. D. Ohman³ 

¹Sorbonne Université, CNRS, IRD, MNHN, Laboratoire d'Océanographie et du Climat: Expérimentations et Approches Numériques (LOCEAN-IPSL), Paris, France, ²Department of Earth, Ocean, and Atmospheric Sciences, Florida State University, Tallahassee, FL, USA, ³Integrative Oceanography Division, Scripps Institution of Oceanography, La Jolla, CA, USA

Abstract Eastern Boundary Current Upwelling Systems are regions of elevated primary production and carbon export and thus play a central role in the global carbon cycle. In these regions, nutrient upwelling occurs in a narrow region close to the coast, but primary production and carbon export are typically observed across a broader region. The fact that productive waters reach the open ocean has important consequences for the biological carbon pump, because such transport connects nutrient sources close to the coast to the deep carbon sinks of the offshore ocean. However, many aspects of this offshore transport are still not known. Here we address seasonal and interannual variability of upwelling-related cross-shore flows in the California current ecosystem (CCE) by employing Lagrangian diagnostics of horizontal transport inferred from satellite data. We define an advective age as the time a water parcel flowed offshore of the 500 m isobath. We find that the offshore extension of high Chl-a waters covaries with the age of a coastal water parcel, and is consistent with mesoscale circulation. Interannual variability in the offshore extent of older waters is primarily driven by mesoscale variability and covaries with large scale forcing by both ENSO and the NPGO. The measured ratio of in-situ new production: carbon export also covaries with water age, and tends to be $\gg 1$ in younger and more balanced in older waters. Our results may help to parameterize the role of the finescale on the export of carbon in upwelling regions for climate resolving models.

Plain Language Summary The California current ecosystem (CCE) is a region of strong coastal upwelling, elevated organic matter production and high carbon flux into the deep ocean, and potentially influential in the global carbon cycle. Previous studies have suggested that production and sinking are not balanced in the CCE: there is more production than sinking close to the coast and more sinking than production offshore. Our study uses satellite measurements to analyze cross-shore flows in the CCE and assess whether horizontal transport of water, nutrients, and plankton can reconcile this spatial imbalance. By following water parcel trajectories, we find that the time since a water parcel is transported from the coast to the offshore is a predictor of whether the water parcel is a net source of organic matter (greater new production than sinking) or a net sink (greater sinking than new production). We find that the offshore distance of water transport varies strongly from year to year and is related to known sources of climate forcing, including El Niño-Southern Oscillation and the North Pacific Gyre Oscillation. Future organic matter exchanges between the coast and the offshore can be estimated thanks to covariability with these climate indices.

1. Introduction

In Eastern boundary upwelling systems (EBUS), winds blow alongshore during the upwelling season, causing nutrient-replete deep waters to come to the euphotic zone through divergence of Ekman transport at the coast, stimulating elevated net primary production (NPP) and inorganic carbon uptake. This primary production induces secondary production, the recycling of nutrients, and export of organic carbon into the aphotic zone. EBUSs are strongly advective systems: Ekman currents, as well as intense geostrophic mesoscale eddies and filaments, transport nearshore surface water offshore. The transport of organic matter (OM) from formation sites to export sites, occurs in three-dimensional space: the location of carbon export may be offset spatially from the region of elevated PP (Gruber et al., 2011; Olivieri & Chavez, 2000; Plattner et al., 2005). Accurately representing the processes and spatial locations of carbon production and export is

key for constraining the ocean carbon cycle in coupled model intercomparison project (CMIP) Earth System and other models (Richter, 2015; Small et al., 2015). At present, such cross-shore fluxes of OM are poorly represented in these models and it is not clear whether they show predictable seasonality or any relationship to large-scale climate forcing.

EBUS modeling is challenging because of the spatial and temporal variability that occurs at multiple scales (Marchesiello et al., 2003), their sensitivity to climate forcing, and the complexity of biophysical coupled processes (K. K. Liu et al., 2010). The North Pacific EBUS along the northwest American coast is known as the California current system (CCS). Many research efforts have been carried out to better understand CCS circulation and California current ecosystem (CCE) dynamics and responses to climate forcing (Goericke & Ohman, 2015). In the CCS, for much of the year—but primarily in spring and summer (Di Lorenzo, 2003)—winds blow equatorward along the California coast. Ekman currents transport coastal waters to the open ocean, inducing an upwelling of waters typically from depths of 100–200 m, although source waters change with the state of the Pacific decadal oscillation (PDO, [Chhak & Lorenzo, 2007]).

Previous studies in the CCE have shown that new production (i.e., production based on upwelled nitrate) tends to exceed carbon exported vertically below the euphotic zone in the nearshore region, where new and primary production is maximal (Chavez et al., 1991; Kranz et al., 2020; Plattner et al., 2005; Stukel et al., 2011). This imbalance is reduced and possibly compensated further offshore (Stephens et al., 2020; Stukel et al., 2011), with lower than expected vertical carbon export close to shore and higher than expected vertical carbon export further offshore. A hypothesis that would explain this spatial imbalance is that inorganic carbon is fixed in the nearshore region and then exported by the cross-shore circulation from nearshore sites of production to offshore sites of export. Such cross-shore transport could be caused by three main mechanisms: advection by surface Ekman currents, cold filaments of coastal origin, and westward propagating mesoscale eddies (Amos et al., 2019; Barth et al., 2005; Chenillat et al., 2016; Nagai et al., 2015). An example of this situation arises in the area off Point Conception (34.4°N) in Southern California. This is a site of elevated primary production (Kahru et al., 2009) but also the triggering location of strong meanders potentially evolving into mesoscale filaments and eddies in summer (Centurioni et al., 2008; Marchesiello et al., 2003).

Although the physical processes associated with cross-shore transport are well known, surprisingly little is known about its interannual variability. In addition, there are few long-term observational datasets of production and export (Kelly et al., 2018). This lack of knowledge has wider consequences, and in particular limits our capacity to predict biogeochemical responses of the CCE to future climate variability. Therefore, in this study, we address the following questions: (i) What is the length scale, and associated seasonal variability, of cross-shore transport in the CCE? (ii) What is the magnitude of interannual variability of cross-shore transport? (iii) Is this variability related to known sources of climate forcing, that would enable it to be represented in climate-resolving models? (iv) What consequences do variations in cross-shore transport have for organic carbon production and export? These questions are addressed through the analysis of highly energetic coastal upwelling meanders in the CCE, combining multi-satellite observations and in situ carbon export measurements with a Lagrangian analysis. We first describe the seasonality of the spatial patterns of the cross-shore transport and use them to explain the spatial imbalance of new production and vertical carbon export in the CCE. Last, we analyze the interannual variability of cross-shore transport, and assess its relationship to climate variability.

2. Data Set and Methods

2.1. Satellite-Derived Currents

Transport analysis is based primarily on sea surface currents provided by the Copernicus Marine Environment Monitoring Service (CMEMS), which consists of nearly 26 years of multi-satellite merged altimeter data and wind stress data, here from January 1, 1994 to October 20, 2019. The spatial resolution is $0.25^\circ \times 0.25^\circ$ (≈ 25 km at mid latitudes) and the temporal resolution is one day for the whole data set. The CMEMS (<https://marine.copernicus.eu/>) product used is the delayed time version until December 31, 2018 and the near real-time for January to October 2019. The surface currents consist of geostrophic velocities plus Ekman currents. Geostrophic velocities (U_G) are derived from the Absolute Dynamic Topography.

Ekman currents (U_E) are derived from wind data provided by the European Centre for Medium-Range Weather Forecasts (ECMWF) with a temporal resolution of 3 h and a spatial resolution of $1/4^\circ$. This product ($U = U_G + U_E$) is more appropriate than the purely geostrophic one, as Ekman currents are particularly important in upwelling systems. We compute total kinetic energy (TKE) maps from these currents with:

$$TKE = \frac{1}{2}(u^2 + v^2)$$

in which (u, v) are the components of the current for the x and y directions.

2.2. Lagrangian Water Age Model

We conducted a Lagrangian particle trajectory analysis of surface velocities. Our aim is to understand the spatial offset between nearshore production and export induced by horizontal transport. We thus follow the approach of d'Ovidio et al. (2015) and define an “offshore water age” as the time taken by the water parcel to be advected backward in time from its current position along its trajectory until it crosses the 500 m isobath. The rationale of this diagnostic is to detect filaments of coastal water advected offshore by horizontal transport and to estimate the time for water parcels in the filament to leave the coastal area. For example, a value of “20 days” assigned to a pixel means that the water parcel in that area was in the coastal area approximately 20 days before, where it was likely enriched in nutrients. A cutoff for the trajectory integration is put at 90 days. This means that a parcel is not considered of coastal origin if the backward trajectory does not cross the 500 m isobath in the previous 90 days. This threshold is chosen heuristically based on the reliability of past studies that have compared altimetry-derived Lagrangian diagnostics and chlorophyll patches (see review in Lehahn et al. [2018]), for two reasons. First, for a temporal horizon longer than a season, we assume that the water parcel has been mixed together with the environmental water longer enough to have lost a coastal signature. Second, we consider that accumulated advection errors on the trajectories are too large to provide any meaningful result even in a statistical sense on a temporal horizon larger than a few months. This “offshore water age” diagnostic has been validated at mesoscale precision with satellite-derived Chl-*a* patches (d'Ovidio et al., 2015; Sergi et al., 2020), surface drifters (d'Ovidio et al., 2015), and lithogenic isotopes (Sanial et al., 2015). These studies, however, were conducted in the Southern Ocean. In the Results section we evaluate this diagnostic for the CCE and specifically in the context of our objectives. Although it would be desirable to begin tracking waters very close to shore, i.e. closer to the sources of upwelling at the coastal boundary, the satellite product we use provides unreliable measures in close proximity to the continental boundary. Hence, we chose the 500 m isobath as the defining limit of inshore waters for this study. We assume that the time lapse between upwelling into the mixed layer and crossing of the 500 m isobath is of the order of a few days or less, thus negligible in respect to the time scales (10–90 days) considered here for offshore transport. We computed water age snapshots every 4 days (this time step was chosen to reduce the data set size without missing any dynamics) for 26 years (92 snapshots per year) of satellite data (between 1994 and 2019). This led to 2,374 snapshots, and a typical field of water age is shown for July 4, 2007 in Figure 1b. The white areas represent the water parcels that had not crossed the 500 m isobath in the last 90 days prior to July, 4. We computed the water age maps at a spatial resolution of $0.05^\circ \approx 5.5$ km.

2.3. Satellite Chl-*a* Data

We compare Chl-*a* images (see example in Figure 1a) to the stirring patterns predicted by the Lagrangian analysis applied to the surface velocities. To achieve this, we use a multi-satellite product with daily sampling interval and 4 km of spatial resolution ([Kahru et al., 2015; Kahru et al., 2012] <https://www.wimsoft.com/CC4km.htm>). The temporal coverage of this data set is from 2002 to 2019. We processed data only during the lifetime of MODIS Aqua to avoid temporal interruptions. In order to compute anomalies of annual averages of ocean color images, we applied the following processing: we masked pixels under 1 mg.m^{-3} in order to focus on high surface Chl-*a* concentrations. In the analysis presented in Section 3.1, similar processing was applied to the water age to select only water ages younger than 30 days. We consider 30 days to be the threshold below which the strongest correlation with Chl-*a* concentration appears.

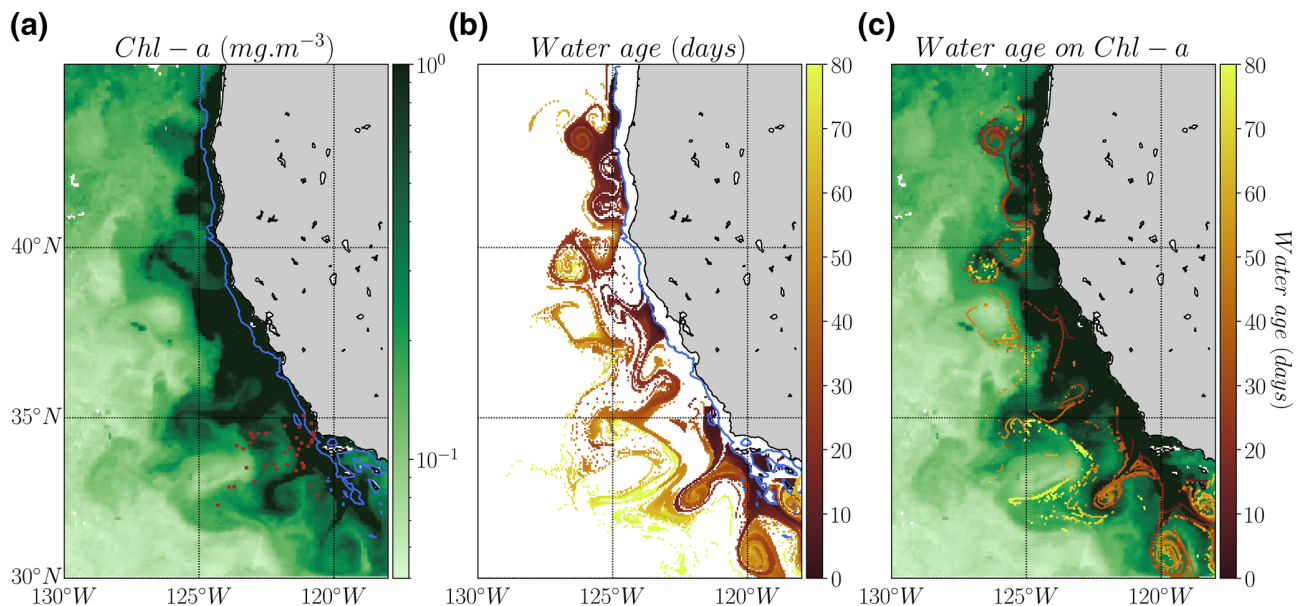


Figure 1. Snapshots of (a) the near-surface Chl-a concentration from MODIS Aqua ($\text{mg} \cdot \text{m}^{-3}$), (b) our Lagrangian diagnostic water age (days) and (c) the water age contours (levels are 10 days intervals from 0 to 80 days) superimposed on the near-surface Chl-a concentration (same colormap as panel a) over the CCE on July 4, 2007. Brown dots in (a) indicate the locations of the in-situ measurements. Light blue line in panels (a) and (b) indicates the 500 m isobath. CCE, California current ecosystem.

2.4. In situ Measurements

In situ measurements (Figure 1a, brown dots) were made during 2–5 days quasi-Lagrangian experiments on eight cruises of the CCE-LTER Program (CCE—Long Term Ecological Research, [Ohman et al., 2013; Stukel et al., 2015]). Dissolved nutrients (here $\text{Si}(\text{OH})_4$, NO_3^- , PO_4) were analyzed by continuous flow segmented autoanalyzer (<https://www.calcofi.org/about-calcofi/methods/422-nutrient-methods.html>) based on Niskin bottle samples taken from surface waters. New production (computed from $^{15}\text{NO}_3^-$ uptake) and net primary productivity (hereafter NPP, computed from $\text{H}^{14}\text{CO}_3^-$ uptake) were measured in situ on a drifting incubation array (Kranz et al., 2020; Landry et al., 2009; R. M. Morrow et al., 2018). On cruises where $^{15}\text{NO}_3^-$ uptake data were not available, equations from K. K. Liu et al. (2010) were used to estimate the f-ratio from NO_3^- , NH_4^+ , photosynthetically active radiation, and chlorophyll measurements. New production was then computed as primary productivity/ $6.625 \times \text{f-ratio}$. New production measurements based on $^{15}\text{NO}_3^-$ uptake can overestimate true nitrate uptake if substantial euphotic zone nitrification occurs, although this issue appears to be minor in the CCE (Stephens et al., 2020; Yool et al., 2007). Sinking carbon vertical fluxes were measured using $^{238}\text{U} - ^{234}\text{Th}$ disequilibrium and surface-tethered drifting sediment traps positioned at the base of the euphotic zone (Stukel & Barbeau, 2020; Stukel et al., 2019). Sinking particle flux was typically measured 20–40 m beneath the depth of the euphotic zone. It was normalized to the base of the euphotic zone using an exponential model of flux attenuation following Stukel et al. (2015). For further details, see supporting information.

2.5. Climate Indices

We compare the variability of cross-shore transport patterns with large scale physical forcing indexes. The North Pacific Gyre Oscillation (NPGO, Di Lorenzo et al. [2008], <http://www.o3d.org/npgo/>) is the second Empirical Orthogonal Function of Sea Surface Height variability in the Northeast Pacific. It represents the wind-driven, basin-scale decadal variability of the North Pacific Gyre circulation. Fluctuations in the NPGO are driven by regional and basin-scale variations in wind-driven upwelling and horizontal advection, controlling salinity and nutrient concentrations in the CCE. Detrended San Diego Sea Level Anomaly, averaged

for December-January-February (SDSLA_DJF) is an index of El Niño Southern Oscillation (ENSO) influence on the CCE (Lilly & Ohman, 2018). It is high during El Niño as elevated sea level in the equatorial band propagates along the coasts of central America, Mexico and California. High sea level is associated with a deeper than usual thermocline/nutricline and lower nearshore primary production.

2.6. Interannual Variability

In order to assess interannual variability of the water age distribution, we compute the average (between 30°N and 40°N) distance to shore of a specific water age (e.g., 60 days waters) for each snapshot. Concerning the area occupied by high Chl-a and young water age events, we compute the number of pixels concerned and multiply by the area of one pixel for each snapshot. We then compute annual means and anomalies relative to the global mean. Similar processing is applied for the TKE, SDSL_A_DJF and NPGO. Area occupied by high Chl-a and young water age events, specific water age distance-to-shore and TKE spatial averages are made between 30° and 40°N in order to obtain smooth averages. Smaller spatial averaging windows were tested and found to provide less smooth results, but with similar correlation coefficients.

3. Results

3.1. Offshore Extension of Chl-a Patterns is Largely Driven by Horizontal Stirring

Figure 1 illustrates a qualitative comparison between spatial patterns of the Lagrangian water age diagnostic and Chl-a concentration. Regions of elevated phytoplankton ($\text{Chl-a} > 1 \text{ mg.m}^{-3}$, Figure 1a) are generally associated with recently upwelled young waters (age < 30 days, Figure 1b). Mesoscale pathways are well captured by the age model. For example, at 127°W, 39°N, a high Chl-a location co-occurs with an elongated filament transporting relatively young water. Another chlorophyll-rich young coastal filament is also detectable between the coast (123°W, 37°N) and offshore (124°W, 34°N) (Figures 1a and 1b). Young water parcels are observed near the coast but also offshore, where they are rapidly advected by filaments and eddies. Older water ages are typically found offshore, sometimes around eddies as offshore older water is entrained. Patches of older waters can also be found in nearshore areas, where recirculation can trap water parcels for long (several tens of days) periods. Note also the nearshore regions without water age values (e.g. 35–37°N, Figure 1b), likely due to imperfect coastal current data which prevents the advection of particles from and to this coastal sector.

In general, elevated Chl-a concentrations can be found both nearshore and offshore but a visual comparison with patterns of water age suggests that they are more associated with younger water patches than old ones. In order to quantify this relation, we estimate the area occupied by patterns of high Chl-a and young water on a daily basis between 2002 and 2018 and compare the temporal variability of their offshore extension. This test is more robust than a filament-by-filament (pixel-by-pixel) comparison, which is notoriously resistant to quantitative validation because altimetry errors may easily displace a filament a distance of the same order as the filament width.

The results of the comparison between the areas occupied by high Chl-a patterns and filaments of young waters is depicted in Figure 2. On a seasonal time scale, these two areas are strongly correlated (Figure 2a, $r = 0.93$, $p < 0.001$). A maximal extension of chlorophyll-rich waters is reached in June, which coincides with the strongest alongshore wind stress, Ekman transport and associated coastal upwelling of nitrate-enriched water (e.g. Jacox et al. [2018]). On an interannual time scale (between 2002 and 2018), the two indices also covary significantly (Figure 2b, $r = 0.63$, $p < 0.01$). Interestingly both indices reach their lowest values in 2014 (water age) and 2015 (Chl-a) during the North Pacific warm anomaly (Di Lorenzo & Mantua, 2016).

3.2. Carbon Export Balances New Production in Regions where Offshore Water Age is Greater than 60 Days

As a second step, we test for a relationship between the offshore water age and the ratio between new production and sinking carbon export (NP and CE), after normalization of NP to carbon units assuming

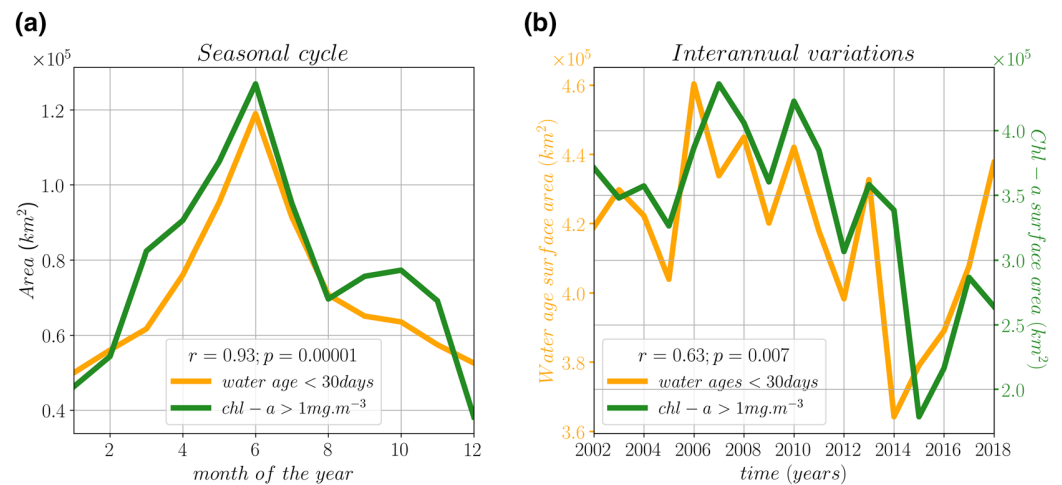


Figure 2. Area occupied by high Chl-a events ($>1 \text{ mg m}^{-3}$, green line, right axis) and area occupied by young water age events (<30 days, orange line, left axis). (a) Mean seasonal cycle ($r = 0.93$; $p < 0.01$ between the two signals) and (b) interannual variability ($r = 0.63$; $p < 0.01$ between the two signals). Averaged between 30° and 40°N .

Redfield C:N stoichiometry. Our working hypothesis is that horizontal stirring translates the temporal lag between NP and CE into a spatial offset, and that the offshore water age diagnostic can capture this spatio-temporal relation. Thanks to extensive process studies (Goericke & Ohman, 2015), in situ measurements of surface nutrients (silicic acid, nitrate and phosphate), NPP, CE and NP:CE are available in the CCE region, in particular between 32°N and 35°N (locations are marked by brown dots in Figure 1a). We thus compare in-situ measurements with satellite-derived water ages for the same day and location using negative exponential regressions. Other functions (linear and power law) were tested but show no significance or lower r -values (not shown). We find that surface nutrients (silicic acid, nitrate and phosphate, Figures 3a–3c) concentrations decay exponentially with water age. These relationships validate our hypothesis that Lagrangian trajectories are initiated in a nutrient rich environment. Accordingly, we find that NPP varies inversely with water age (Figure 3d), as expected in a system in which recent upwelling is a source of new nutrients to stimulate production. The relatively high correlation value between surface nutrients and water age is similar to the correlation value between NPP and water age ($-0.73 < r < -0.68$). As water parcels age, surface nutrients are drawn down and NPP decreases. Similarly, we found that carbon export was higher in younger age waters, although carbon export declines less rapidly with water age (Figure 3e). To assess how the balance between NP and CE changes with water parcel age, we also compared water age to the ratio of NP:CE in these water parcels (Figure 3f). We again found a statistically significant relationship, showing that younger water parcels had new production rates that substantially exceeded contemporaneous sinking particle flux. However, after 60 days, new production and export reach an equilibrium. Water parcels older than this showed approximately balanced new production and export, on average. There was, however, still substantial variability in the NP:export ratios in these older water parcels, likely because as the water age increases, processes like vertical shear, mixing and subduction complicate the interpretation of a water parcel as having a single source and age.

A steady-state one-dimensional balance between NP and CE would lead to an expected ratio of these two properties of 1 for waters of all ages, meaning that all the NP generated in the euphotic layer would be exported vertically in the water column below. In contrast, we find that NP:CE is generally higher than 1 in younger waters and declines with water age (Figure 3f, $r = -0.46$). This suggests that a significant part of the organic carbon produced in the euphotic layer is not exported below the euphotic zone locally, but is advected horizontally along the water mass trajectory. Many ratios are found below the 1:1 line between water ages of 60–80 days, which implies that in such waters the sinking organic carbon originating from other locations has been advected to the measurement sites. This situation occurs for a wide range of distances to shore (between 100 km and 400 km; Figure 3f). Except for surface nutrients and NPP (which are less correlated with distance-to-shore than the water age), distance-to-shore is not linearly correlated ($p > 0.1$) with

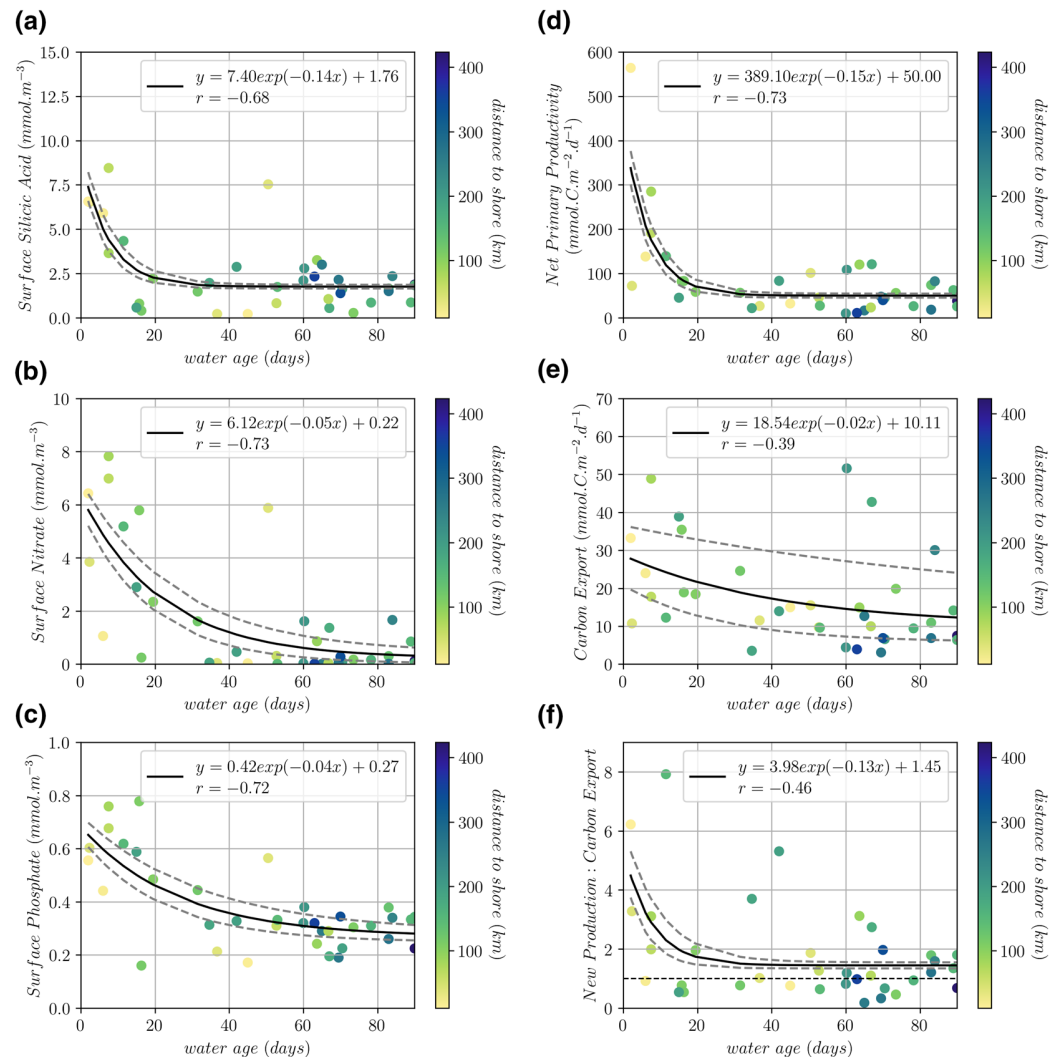


Figure 3. Relationship between water age and measured in situ: (a) surface silicic acid (mmol m^{-3}), (b) surface nitrate (mmol m^{-3}), (c) surface phosphate (mmol m^{-3}) (d) net primary production ($\text{mmol C m}^{-2} \text{d}^{-1}$), (e) vertical carbon export ($\text{mmol C m}^{-2} \text{d}^{-1}$), and (f) new production: Carbon Export ratio. Solid black lines indicate negative exponential regressions, gray dashed lines indicate 95% confidence intervals (C.I.) and horizontal dashed line in (f) indicates the equilibrium New Production: Carbon Export ratio of 1. Colors of symbols indicate the distance to shore.

variables shown in Figure 3 (distance-to-shore and: surface nitrate: $r = -0.4$, $p = 0.01$; surface silicic acid: $r = -0.3$, $p = 0.07$; surface phosphate: $r = -0.34$, $p = 0.04$; NPP: $r = -0.4$, $p = 0.02$; CE: $r = -0.25$, $p = 0.14$; NP:CE, $r = -0.2$, $p = 0.24$). Only surface Silicic Acid shows a significant negative exponential relationship with distance-to-shore, however less correlated ($r = -0.44$) than with the water age. This result shows that our simple water age index, which takes into account the history of the water mass since it has left the nutrient-rich coastal area, is strongly preferred over proximity to the coast as a predictor of biogeochemical characteristics related to organic carbon production and vertical export.

3.3. Seasonal Variability of Cross-Shore Flow and Inferred C Export

We analyze the seasonal and spatial variability of the probability of occurrence of waters of different ages, for the primary upwelling season (May–September, Figure 4). We display probabilities for occurrence of water ages of: (a) 0–20 days and (b) 60–80 days. Young ages (0–20 days, Figure 4a—upper row) are more likely

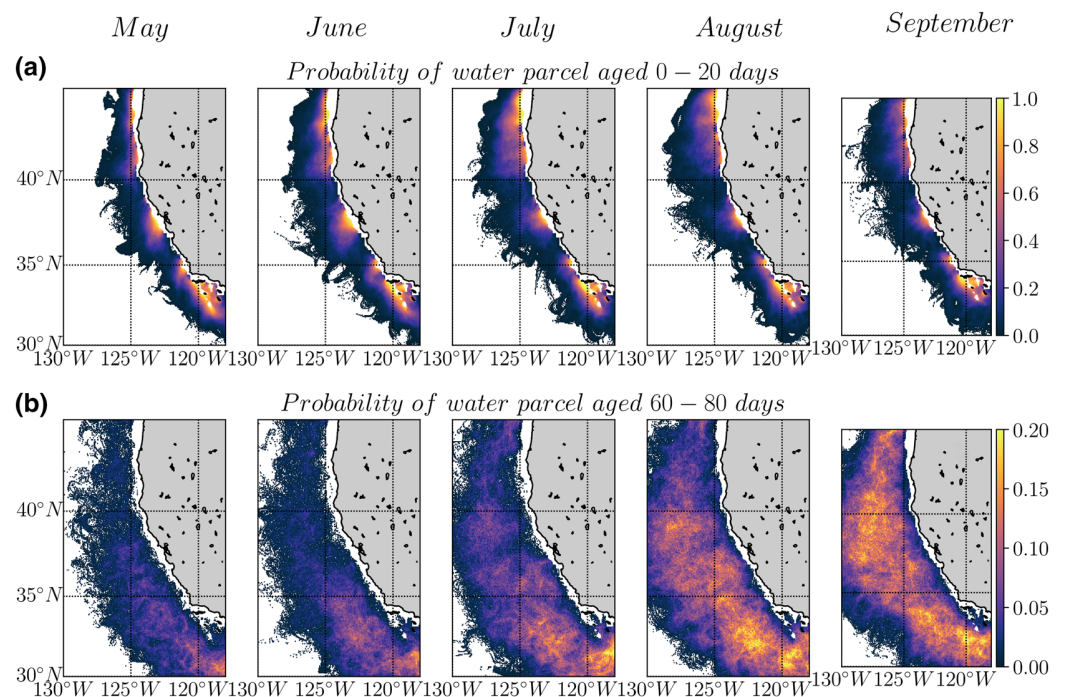


Figure 4. Climatological maps indicate the probability of occurrence of an: (a) 0–20 days and (b) 60–80 days water age event during the upwelling season (from May to September).

to occur near the coast between 32°–35°N, 37°–38°N, and north of 40°N. In the former regions, the month-to-month variability is weak while in the latter (northern) region, the seasonal cycle is more pronounced and reaches its peak in July. These locations with highest probability are limited in space, concentrated nearshore and coincide with the most intense upwelling cells along the California coast. There are locations along the coast (around 36°N) with low probability of occurrence, likely due to imperfect coastal current data (see the Discussion for details). High probabilities for occurrence of young water ages correspond to regions of elevated primary production (Figure 3). In other words, Figure 4 (upper row) also corresponds to the locations where NP is most likely to dominate.

At the beginning of the upwelling season, the probability of occurrence of old ages is higher south of 40°N than in the northern region where the upwelling season tends to start later and be shorter (Bograd et al., 2009). As the upwelling season progresses, areas of high probability of occurrence of old waters appear, corresponding to young waters upwelled earlier in the season that have been evolving. Old waters are more likely to occur in a broad region from the shore to up to 800 km offshore, in which upwelled waters have been advected and stirred. Based on the results in Figure 3, high probability for occurrence of old water ages correspond to regions where vertical carbon export tends to be close to or slightly exceed NP, i.e. where CE is most likely to dominate. To test the robustness of the seasonal patterns, we computed averages over several distinct time intervals (years [1993; 2003], [2003; 2013] and [2013; 2019]) and found similar spatial patterns (not shown). Also, removing ENSO events based on a San Diego Sea Level Anomaly criterion (>50 mm anomaly for >1 month) does not significantly affect the pattern and the seasonal cycle (not shown). Thus, we find that the climatological patterns of inferred carbon export hotspots shown in Figure 4 are reliable.

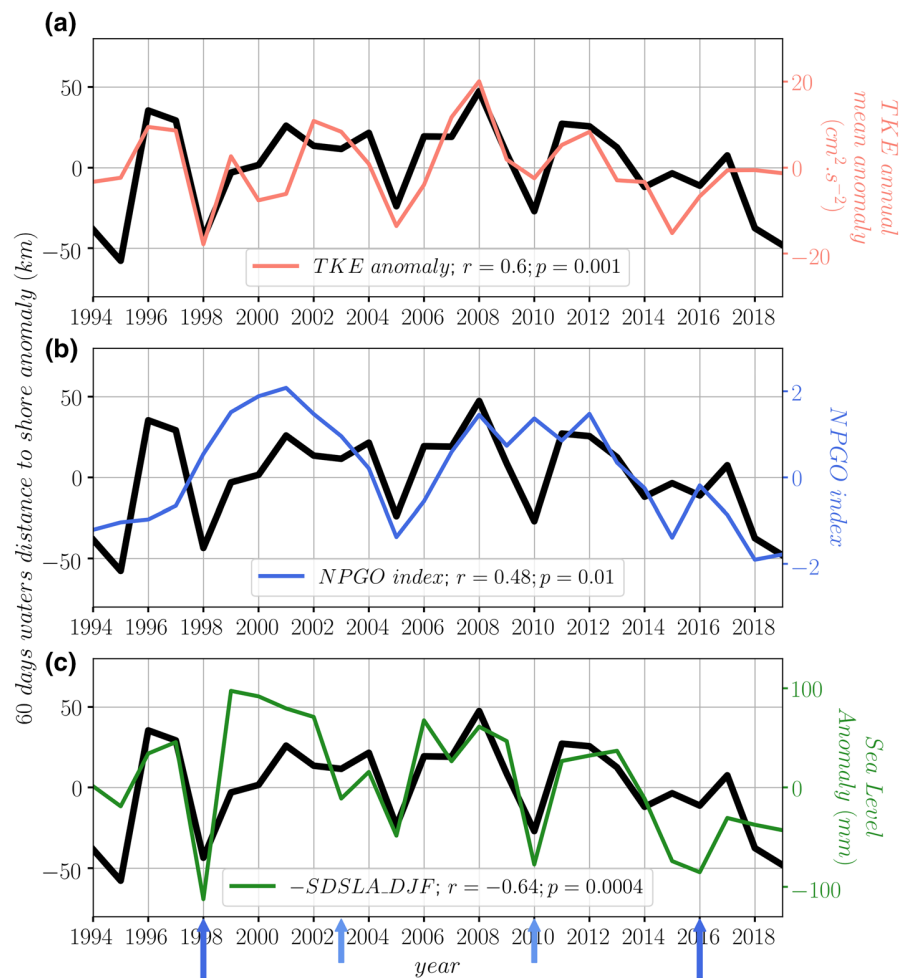


Figure 5. Interannual variability of annual averages of anomalies of distances-to-shore of 60 day old water (black line) against (a) Eddy Kinetic Energy (EKE, salmon line), (b) NPGO index (blue line) and (c) San Diego Sea Level Anomaly in December, January and February (-SDSLA_DJF, scale reversed, green line). Light blue arrows indicate California El Niño years and darker blue long arrows indicate the strongest El Niños years. NPGO, North Pacific gyre oscillation.

3.4. Interannual Variability of Offshore Extent of Flow

The 26 years satellite record enables us to compare interannual variability in water age, as a proxy for production and export, with important climate drivers. For this purpose, we consider 60 days water as a critical water age that tends to indicate balanced NP: CE (cf. Figure 3f).

We find that the annual average anomalies of the distance-to-shore of the critical water age (60 days) covaries with TKE (Figure 5a, $r = 0.66$, $p < 0.01$), the NPGO (Figure 5b, $r = 0.48$, $p = 0.01$), and with San Diego Sea Level Anomaly, as an index of ENSO in the CCE (Figure 5c, $r = -0.64$, $p < 0.001$). Moderate-to-strong El Niño events (like 1998, 2010, and 2016, blue arrows on Figure 5) tend to be associated with negative TKE anomalies and therefore with reduction in mesoscale activity, with concomitant reduction of the offshore extent of the region where NP and CE are most likely to be balanced. Conversely, this region presents greater offshore extent as La Niña events tend to be associated with positive TKE, and therefore stronger mesoscale activity.

4. Discussion

Advective processes, working at multiple spatial and temporal scales, reshape biogeochemical patterns in the pelagic ocean (Frischknecht et al., 2018; Resplandy et al., 2012). Horizontal transport leads to decoupling of net community production, new production, and export production at the mesoscale, obfuscating relationships between these and other processes (Estapa et al., 2015; Kranz et al., 2020). At the same time, mesoscale eddies, fronts, and filaments can act as sites of enhanced vertical transport leading to upwelling or downwelling with concomitant passive export of advected organic matter (Levy et al., 2013; Omand et al., 2015; Resplandy et al., 2019; Stukel et al., 2017). Understanding—and predicting—the impacts of horizontal transport on processes relevant to the biological pump is crucial to constraining different pathways of carbon transport to the ocean interior (e.g., sinking particles, diel vertical migration, active transport; [Boyd et al., 2019; Ducklow et al., 2001]). The existence of a spatial discrepancy between regions when nutrients are injected and regions where organic matter sinks is especially relevant in upwelling systems (Plattner et al., 2005). Without offshore advection of high biomass water parcels, most carbon export would remain confined at the upwelling sites. Intense offshore advection events, however, have the potential to drive export pulses in the deep ocean with important consequences for open ocean mesopelagic and benthic communities (Smith et al., 2018). The stirring process at the origin of the offshore transport however involves the interaction of fine scale features and creates patterns with a complex geometry. Understanding the variability of this offshore transport, and linking it to the large-scale dynamics—in particular to modes of climate variability—is especially relevant for climate-resolving models, which cannot explicitly resolve the subgrid details of the stirring process (Bourgeois et al., 2016), and therefore cannot properly represent where the organic matter produced in the upwelled region eventually sinks.

Explicit coupling of finescale Lagrangian water parcel transport estimates with in situ biological pump measurements is a powerful approach to elucidating how NP, NPP, and CE are related in time and space. In this study, satellite-derived Lagrangian water age diagnostics made it possible to infer the duration and lateral extent of cross-shore flows in the CCE. We found that independent measurements of NP and sinking CE are directly related to these water age diagnostics. In younger waters (i.e., those that more recently occurred closer to shore), there is an excess of NP over CE, but in older waters (60–80 days since emerging from the coast), there is a closer balance between NP and CE. Our 26-years record of water age diagnostics revealed that both seasonal and interannual scale variations in these inferred cross-shore flows are related to the areal extent of elevated Chl-a, with a broader region of high phytoplankton concentrations occurring in seasons and in years of stronger offshore transport. These seasonal and longer term variations in phytoplankton concentrations, primary production, and carbon export are modulated by variations in mesoscale TKE, and by climate forcing represented by ENSO and the NPGO.

We show that the relationship between water age and different biogeochemical properties is a result of the covariability of nutrient concentrations with water age, i.e., the time since nutrients entered the euphotic zone near the coast via coastal upwelling. As water age increases, NP decreases as macronutrients are consumed and other trophic levels (zooplankton) begin to develop. With continuing depletion of macronutrients like nitrate and silicic acid, and temporal changes in the food web (Messié & Chavez, 2017), recycled nutrients play a greater role. However, new nutrients may also enter the surface water parcels via mixing and submesoscale eddies in the offshore oligotrophic region (Kessouri et al., 2020).

Recent studies (Amos et al., 2019; Lovecchio et al., 2017) estimate organic carbon offshore transport in EBUS through lateral advection. Amos et al. (2019) describe eddy-induced offshore organic carbon enrichment, especially by cyclonic eddies, illustrating the major role played by eddies in the CCE regional carbon budget. This process is included in the present analysis because the Lagrangian water age diagnostic includes contributions by eddies, filaments, and Ekman transport. If used in association with other Lagrangian diagnostics (e.g., retention time, [d'Ovidio et al., 2015]) and with satellite-derived particulate organic carbon estimates (Amos et al., 2019), our water age diagnostics could be used to differentiate eddies and filaments and thus assess their respective roles in organic carbon offshore transport.

In order to qualitatively separate the influence of Ekman transport from geostrophic motions, we computed our same diagnostics including only the geostrophic component (purely geostrophic [PG], without considering winds; data not illustrated). We found no significant correlation between the seasonal cycle of the area

occupied by young water ages from the PG product and the area occupied by high Chl-a events, suggesting that ageostrophic motions must also be considered.

It is important to note that the cross-shore transport induced by these mesoscale eddies and filaments is not oriented solely offshore. The occurrence of old water parcels over a broad area (Figure 4) highlights not only the role of mixing in carbon export, but also the role of recirculation and retention that can in some cases lead export to occur near regions of elevated NP. This result underscores the importance of considering water age, rather than the classical distance-to-shore, as a proxy for carbon export.

This description emphasizes upwelling near the coastal boundary, without explicitly considering wind stress curl-induced upwelling (Capet et al., 2004; Chelton, 1982; Renault et al., 2016). Ekman pumping associated with positive wind stress curl can supply new nutrients to the euphotic zone offshore of the coastal boundary, with major consequences for primary production and higher trophic levels (Rykaczewski & Checkley, 2008) and potentially for carbon export. However, the region inshore of the 500 m isobath in the present study includes part of the domain of wind stress curl upwelling (Pickett & Paduan, 2003; Rykaczewski & Checkley, 2008), so this process is partially included in our analysis. Another limitation of our analysis is that in addition to macronutrients like nitrate, iron is also known to be a regionally important limiting micro-nutrient in some parts of the CCS (Brzezinski et al., 2015; Hutchins & Bruland, 1998; King & Barbeau, 2011; Messié & Chavez, 2015), and regions of severe Fe limitation may be spatially offset from regions of N limitation (King & Barbeau, 2007; Stukel et al., 2017). Furthermore, meso and submesoscale vertical dynamics which may enrich (e.g. [Kessouri et al., 2020]) or deplete (e.g., through subduction, [Gruber et al., 2011; Stukel et al., 2017]) the surface layer in the coastal transition zone are not resolved here. Last a limitation of current satellite altimetry is that horizontal mesoscale structures are much smoother (and currents weaker) than in reality because of time and space interpolation of along-track sea level observations. Submesoscale structures are not resolved by the satellite product, thus ageostrophic components and mixed-layer instabilities are not taken into account. Positional errors between Chl-a patterns and Lagrangian derived diagnostics (up to 20 km) can appear nearshore, and altimetry potentially underestimates geostrophic currents (Lehahn et al., 2018). Such errors could be estimated by a rigorous comparison of the positions of the Lagrangian structures derived from numerical trajectories with the ones obtained by analyzing real surface drifters (e.g., [Nencioli et al., 2011]). This type of error is expected to be largely reduced in the incoming years by next satellite missions like SWOT (R. Morrow et al., 2019).

5. Conclusion and Perspectives

By using satellite-derived Lagrangian water age diagnostics together with in situ measurements of surface nutrients concentrations, organic carbon production and vertical carbon export, we show that the most productive water parcels and those that are likely to vertically export the most carbon relative to local production can be differentiated. New production exceeds sinking particle export in younger waters, inferred to be recently upwelled. New production is more closely balanced by vertical export in older waters. A 26-years record of water age diagnostics identifies regions of inferred carbon export hotspots, whose spatial extent is associated with mesoscale ocean variability and modulated by large-scale sources of climate forcing that include ENSO and the NPGO. Therefore, it is possible to model at least a major part of this biogeochemically relevant cross-shore transport through its covariability with climate forcing. At the same time, the finding that some of the variability in carbon export is not related to larger scale physical forcing underscores the need for mesoscale and sub-mesoscale studies in order to fully represent carbon export in Earth System models. The Lagrangian water age diagnostic can also be used as a near real-time tool for decision making during filament-following oceanographic cruises, as it can provide locations where new production and carbon export are likely to be spatially decoupled.

Data Availability Statement

Water age maps, primary production and carbon export data are available in CCE-LTER's DataZoo (<https://oceaninformatics.ucsd.edu/datazoo/catalogs/ccelter/datasets>). Satellite data can be found at: Chla—<https://www.wimsoft.com/CC4km.htm>, surface currents—<https://marine.copernicus.eu/>; product identifier:

MULTIOBS_GLO_PHY_REP_015_004). The Lagrangian code we used is now part of the SPASSO package which can be downloaded here: <https://spasso.mio.osupytheas.fr/>.

Acknowledgments

This work has been partly supported by OCE-16-37632 from the U.S. National Science Foundation to the California Current Ecosystem LTER site, Cnes through the TOSCA project BIOSWOT-AdAC, the Gordon and Betty Moore Foundation to MDO, and benefited from the French state aid managed by the ANR under the "Investissements d'avenir" programme with the reference ANR-11-IDEX-0004 - 17-EURE-0006.

References

- Amos, C. M., Castelao, R. M., & Medeiros, P. M. (2019). Offshore transport of particulate organic carbon in the California Current System by mesoscale eddies. *Nature Communications*, 10(1), 4940. <https://doi.org/10.1038/s41467-019-12783-5>
- Barth, J. A., Pierce, S. D., & Cowles, T. J. (2005). Mesoscale structure and its seasonal evolution in the northern California current system. *Deep Sea Research Part II: Topical Studies in Oceanography*, 52(1), 5–28. <https://doi.org/10.1016/j.dsr2.2004.09.026>
- Bograd, S. J., Schroeder, I., Sarkar, N., Qiu, X., Sydemann, W. J., & Schwing, F. B. (2009). Phenology of coastal upwelling in the California Current. *Geophysical Research Letters*, 36, L01602. <https://doi.org/10.1029/2008GL035933>
- Bourgeois, T., Orr, J. C., Resplandy, L., Terhaar, J., Ethé, C., Gehlen, M., & Bopp, L. (2016). Coastal-ocean uptake of anthropogenic carbon. *Biogeosciences*, 13(14), 4167–4185. <https://doi.org/10.5194/bg-13-4167-2016>
- Boyd, P. W., Claustre, H., Levy, M., Siegel, D. A., & Weber, T. (2019). Multi-faceted particle pumps drive carbon sequestration in the ocean. *Nature*, 568(7752), 327–335. <https://doi.org/10.1038/s41586-019-1098-2>
- Brzezinski, M. A., Krause, J. W., Bundy, R. M., Barbeau, K. A., Franks, P., Goericke, R., et al. (2015). Enhanced silica ballasting from iron stress sustains carbon export in a frontal zone within the California Current. *Journal of Geophysical Research: Oceans*, 120(7), 4654–4669. <https://doi.org/10.1002/2015JC010829>
- Capet, X. J., Marchesiello, P., & McWilliams, J. C. (2004). Upwelling response to coastal wind profiles. *Geophysical Research Letters*, 31, L13311. <https://doi.org/10.1029/2004GL020123>
- Centurioni, L. R., Ohlmann, J. C., & Niiler, P. P. (2008). Permanent Meanders in the California Current System. *Journal of Physical Oceanography*, 38(8), 1690–1710. <https://doi.org/10.1175/2008JPO3746.1>
- Chavez, F. P., Barber, R. T., Kosro, P. M., Huyer, A., Ramp, S. R., Stanton, T. P., & Mendiola, B. R. d. (1991). Horizontal transport and the distribution of nutrients in the Coastal Transition Zone off northern California: Effects on primary production, phytoplankton biomass and species composition. *Journal of Geophysical Research*, 96(C8), 14833–14848. <https://doi.org/10.1029/91JC01163>
- Chelton, D. B. (1982). Large-scale response of the California Current to forcing by the wind stress curl. *California Cooperative Oceanic Fisheries Investigations Reports*, XXIII, 19.
- Chenillat, F., Franks, P. J. S., & Combes, V. (2016). Biogeochemical properties of eddies in the California Current System. *Geophysical Research Letters*, 43(11), 5812–5820. <https://doi.org/10.1002/2016GL068945>
- Chhak, K., & Lorenzo, E. D. (2007). Decadal variations in the California Current upwelling cells. *Geophysical Research Letters*, 34, L14604. <https://doi.org/10.1029/2007GL030203>
- Di Lorenzo, E. (2003). Seasonal dynamics of the surface circulation in the Southern California Current System. *Deep Sea Research Part II: Topical Studies in Oceanography*, 50(14–16), 2371–2388. [https://doi.org/10.1016/S0967-0645\(03\)00125-5](https://doi.org/10.1016/S0967-0645(03)00125-5)
- Di Lorenzo, E., & Mantua, N. (2016). Multi-year persistence of the 2014/15 North Pacific marine heatwave. *Nature Climate Change*, 6(11), 1042–1047. <https://doi.org/10.1038/nclimate3082>
- Di Lorenzo, E., Schneider, N., Cobb, K. M., Franks, P. J. S., Chhak, K., Miller, A. J., et al. (2008). North Pacific Gyre Oscillation links ocean climate and ecosystem change. *Geophysical Research Letters*, 35, L08607. <https://doi.org/10.1029/2007GL032838>
- Ducklow, H., Steinberg, D., & Buesseler, K. (2001). Upper ocean carbon export and the biological pump. *Oceanography*, 14(4), 50–58. <https://doi.org/10.5670/oceanog.2001.06>
- d'Ovidio, F., Della Penna, A., Trull, T. W., Nencioli, F., Pujol, M.-I., Rio, M.-H., et al. (2015). The biogeochemical structuring role of horizontal stirring: Lagrangian perspectives on iron delivery downstream of the Kerguelen Plateau. *Biogeosciences*, 12(19), 5567–5581. <https://doi.org/10.5194/bg-12-5567-2015>
- Estapa, M. L., Siegel, D. A., Buesseler, K. O., Stanley, R. H. R., Lomas, M. W., & Nelson, N. B. (2015). Decoupling of net community and export production on submesoscales in the Sargasso Sea. *Global Biogeochemical Cycles*, 29(8), 1266–1282. <https://doi.org/10.1002/2014GB004913>
- Frischknecht, M., Münnich, M., & Gruber, N. (2018). Origin, transformation, and fate: The three-dimensional biological pump in the California Current System. *Journal of Geophysical Research: Oceans*, 123(11), 7939–7962. <https://doi.org/10.1029/2018JC013934>
- Goericke, R., & Ohman, M. D. (2015). Introduction to CCE-LTER: Responses of the California Current Ecosystem to climate forcing. *Deep Sea Research Part II: Topical Studies in Oceanography*, 112, 1–5. <https://doi.org/10.1016/j.dsr2.2014.12.001>
- Gruber, N., Lachkar, Z., Frenzel, H., Marchesiello, P., Münnich, M., McWilliams, J. C., et al. (2011). Eddy-induced reduction of biological production in eastern boundary upwelling systems. *Nature Geoscience*, 4(11), 787–792. <https://doi.org/10.1038/ngeo1273>
- Hutchins, D. A., & Bruland, K. W. (1998). Iron-limited diatom growth and Si:N uptake ratios in a coastal upwelling regime. *Nature*, 393(6685), 561–564. <https://doi.org/10.1038/31203>
- Jacox, M. G., Edwards, C. A., Hazen, E. L., & Bograd, S. J. (2018). Coastal upwelling revisited: Ekman, Bakun, and Improved Upwelling Indices for the U.S. West Coast. *Journal of Geophysical Research: Oceans*, 123(10), 7332–7350. <https://doi.org/10.1029/2018JC014187>
- Kahru, M., Kudela, R. M., Anderson, C. R., & Mitchell, B. G. (2015). Optimized merger of Ocean chlorophyll algorithms of MODIS-Aqua and VIIRS. *IEEE Geoscience and Remote Sensing Letters*, 12(11), 2282–2285. <https://doi.org/10.1109/LGRS.2015.2470250>
- Kahru, M., Kudela, R. M., Manzano-Sarabia, M., & Greg Mitchell, B. (2012). Trends in the surface chlorophyll of the California Current: Merging data from multiple ocean color satellites. *Deep Sea Research Part II: Topical Studies in Oceanography*, 77–80, 89–98. <https://doi.org/10.1016/j.dsr2.2012.04.007>
- Kahru, M., Kudela, R., Manzano-Sarabia, M., & Mitchell, B. G. (2009). Trends in primary production in the California Current detected with satellite data. *Journal of Geophysical Research*, 114(C2). <https://doi.org/10.1029/2008JC004979>
- Kelly, T. B., Goericke, R., Kahru, M., Song, H., & Stukel, M. R. (2018). CCE II: Spatial and interannual variability in export efficiency and the biological pump in an eastern boundary current upwelling system with substantial lateral advection. *Deep Sea Research Part I: Oceanographic Research Papers*, 140, 14–25. <https://doi.org/10.1016/j.dsr.2018.08.007>
- Kessouri, F., Bianchi, D., Renault, L., McWilliams, J. C., Frenzel, H., & Deutsch, C. A. (2020). Submesoscale currents modulate the seasonal cycle of nutrients and productivity in the California current system. *Global Biogeochemical Cycles*, 34(10), e2020GB006578. <https://doi.org/10.1029/2020GB006578>
- King, A. L., & Barbeau, K. (2007). Evidence for phytoplankton iron limitation in the southern California Current System. *Marine Ecology Progress Series*, 342, 91–103. <https://doi.org/10.3354/meps342091>

- King, A. L., & Barbeau, K. A. (2011). Dissolved iron and macronutrient distributions in the southern California Current System. *Journal of Geophysical Research*, 116, C03018. <https://doi.org/10.1029/2010JC006324>
- Kranz, S. A., Wang, S., Kelly, T. B., Stukel, M. R., Goericke, R., Landry, M. R., & Cassar, N. (2020). Lagrangian studies of marine production: A multimethod assessment of productivity relationships in the California Current ecosystem upwelling region. *Journal of Geophysical Research: Oceans*, 125(6), e2019JC015984. <https://doi.org/10.1029/2019JC015984>
- Landry, M. R., Ohman, M. D., Goericke, R., Stukel, M. R., & Tsytklevich, K. (2009). Lagrangian studies of phytoplankton growth and grazing relationships in a coastal upwelling ecosystem off Southern California. *Progress in Oceanography*, 83(1–4), 208–216. <https://doi.org/10.1016/j.pocean.2009.07.026>
- Lehahn, Y., d'Ovidio, F., & Koren, I. (2018). A satellite-based Lagrangian view on phytoplankton dynamics. *Annual Review of Marine Science*, 10(1), 99–119. <https://doi.org/10.1146/annurev-marine-121916-063204>
- Levy, M., Bopp, L., Karleskind, P., Resplandy, L., Ethe, C., & Pinsard, F. (2013). Physical pathways for carbon transfers between the surface mixed layer and the ocean interior. *Global Biogeochemical Cycles*, 27(4), 1001–1012. <https://doi.org/10.1002/gbc.20092>
- Lilly, L. E., & Ohman, M. D. (2018). CCE IV: El Niño-related zooplankton variability in the southern California Current System. *Deep Sea Research Part I: Oceanographic Research Papers*, 140, 36–51. <https://doi.org/10.1016/j.dsr.2018.07.015>
- Liu, K.-K., Atkinson, L., Quiñones, R., & Talaue-McManus, L. (2010). *Carbon and nutrient fluxes in continental margins: A global synthesis*. Springer Science & Business Media.
- Lovecchio, E., Gruber, N., Münnich, M., & Lachkar, Z. (2017). On the long-range offshore transport of organic carbon from the Canary Upwelling System to the open North Atlantic. *Biogeosciences*, 14(13), 3337–3369. <https://doi.org/10.3929/ethz-b-000190480>
- Marchesiello, P., McWilliams, J. C., & Schepetkin, A. (2003). Equilibrium structure and dynamics of the California current system. *Journal of Physical Oceanography*, 33, 31.
- Messié, M., & Chavez, F. P. (2015). Seasonal regulation of primary production in eastern boundary upwelling systems. *Progress in Oceanography*, 134, 1–18. <https://doi.org/10.1016/j.pocean.2014.10.011>
- Messié, M., & Chavez, F. P. (2017). Nutrient supply, surface currents, and plankton dynamics predict zooplankton hotspots in coastal upwelling systems. *Geophysical Research Letters*, 44(17), 8979–8986. <https://doi.org/10.1002/2017GL074322>
- Morrow, R., Fu, L.-L., Arduin, F., Benkiran, M., Chapron, B., Cosme, E., et al. (2019). Global observations of fine-scale ocean surface topography with the Surface Water and Ocean Topography (SWOT) Mission. *Frontiers in Marine Science*, 6, 232. <https://doi.org/10.3389/fmars.2019.00232>
- Morrow, R. M., Ohman, M. D., Goericke, R., Kelly, T. B., Stephens, B. M., & Stukel, M. R. (2018). CCE V: Primary production, mesozooplankton grazing, and the biological pump in the California Current Ecosystem: Variability and response to El Niño. *Deep Sea Research Part I: Oceanographic Research Papers*, 140, 52–62. <https://doi.org/10.1016/j.dsr.2018.07.012>
- Nagai, T., Gruber, N., Frenzel, H., Lachkar, Z., McWilliams, J. C., & Plattner, G.-K. (2015). Dominant role of eddies and filaments in the offshore transport of carbon and nutrients in the California Current System. *Journal of Geophysical Research: Oceans*, 120(8), 5318–5341. <https://doi.org/10.1002/2015JC010889>
- Nencioli, F., d'Ovidio, F., Doglioli, A. M., & Petrenko, A. A. (2011). Surface coastal circulation patterns by in-situ detection of Lagrangian coherent structures. *Geophysical Research Letters*, 38, L17604. <https://doi.org/10.1029/2011GL048815>
- Ohman, M. D., Barbeau, K., Franks, P. J. S., Goericke, R., Landry, M. R., & Miller, A. J. (2013). Ecological Transitions in a Coastal Upwelling Ecosystem. *Oceanography*, 26(3), 210–219.
- Olivieri, R. A., & Chavez, F. P. (2000). A model of plankton dynamics for the coastal upwelling system of Monterey Bay, California. *Deep Sea Research Part II: Topical Studies in Oceanography*, 47(5), 1077–1106. [https://doi.org/10.1016/S0967-0645\(99\)00137-X](https://doi.org/10.1016/S0967-0645(99)00137-X)
- Omand, M. M., D'Asaro, E. A., Lee, C. M., Perry, M. J., Briggs, N., Cetinić, I., & Mahadevan, A. (2015). Eddy-driven subduction exports particulate organic carbon from the spring bloom. *Science*, 348(6231), 222–225. <https://doi.org/10.1126/science.1260062>
- Pickett, M. H., & Paduan, J. D. (2003). Ekman transport and pumping in the California Current based on the U.S. Navy's high-resolution atmospheric model (COAMPS). *Journal of Geophysical Research*, 108, 3327. <https://doi.org/10.1029/2003JC001902>
- Plattner, G.-K., Gruber, N., Frenzel, H., & McWilliams, J. C. (2005). Decoupling marine export production from new production. *Geophysical Research Letters*, 32, L11612. <https://doi.org/10.1029/2005GL022660>
- Renault, L., Hall, A., & McWilliams, J. C. (2016). Orographic shaping of US West Coast wind profiles during the upwelling season. *Climate Dynamics*, 46(1–2), 273–289. <https://doi.org/10.1007/s00382-015-2583-4>
- Resplandy, L., Lévy, M., & McGillicuddy, D. J. (2019). Effects of Eddy-Driven Subduction on Ocean Biological Carbon Pump. *Global Biogeochemical Cycles*, 33(8), 1071–1084. <https://doi.org/10.1029/2018GB006125>
- Resplandy, L., Martin, A. P., Le Moigne, F., Martin, P., Aquilina, A., Mémer, Y., et al. (2012). How does dynamical spatial variability impact 234Th-derived estimates of organic export? *Deep Sea Research Part I: Oceanographic Research Papers*, 68, 24–45. <https://doi.org/10.1016/j.dsr.2012.05.015>
- Richter, I. (2015). Climate model biases in the eastern tropical oceans: causes, impacts and ways forward. *WIREs Climate Change*, 6(3), 345–358. <https://doi.org/10.1002/wcc.338>
- Rykaczewski, R. R., & Checkley, D. M. (2008). Influence of ocean winds on the pelagic ecosystem in upwelling regions. *Proceedings of the National Academy of Sciences*, 105(6), 1965–1970. <https://doi.org/10.1073/pnas.0711777105>
- Sanial, V., Van Beek, P., Lansard, B., Souhaut, M., Kestenare, E., D'Ovidio, F., et al. (2015). Use of Ra isotopes to deduce rapid transfer of sediment-derived inputs off Kerguelen. *Biogeosciences*, 12(5), 1415–1430. <https://doi.org/10.5194/bg-12-1415-2015>
- Sergi, S., Baudena, A., Cotté, C., Ardyna, M., Blain, S., & d'Ovidio, F. (2020). Interaction of the Antarctic Circumpolar Current with sea-mounts fuels moderate blooms but vast foraging grounds for multiple marine predators. *Frontiers in Marine Science*, 7, 416. <https://doi.org/10.3389/fmars.2020.00416>
- Small, R. J., Curchitser, E., Hedstrom, K., Kauffman, B., & Large, W. G. (2015). The Benguela Upwelling System: Quantifying the sensitivity to resolution and coastal wind representation in a global climate model. *Journal of Climate*, 28(23), 9409–9432. <https://doi.org/10.1175/JCLI-D-15-0192.1>
- Smith, K. L., Ruhl, H. A., Huffard, C. L., Messié, M., & Kahru, M. (2018). Episodic organic carbon fluxes from surface ocean to abyssal depths during long-term monitoring in NE Pacific. *Proceedings of the National Academy of Sciences*, 115(48), 12235–12240. <https://doi.org/10.1073/pnas.1814559115>
- Stephens, B. M., Wankel, S. D., Beman, J. M., Rabines, A. J., Allen, A. E., & Aluwihare, L. I. (2020). Euphotic zone nitrification in the California Current Ecosystem. *Limnology & Oceanography*, 65(4), 790–806. <https://doi.org/10.1002/lno.11348>
- Stukel, M. R., Aluwihare, L. I., Barbeau, K. A., Chekalyuk, A. M., Goericke, R., Miller, A. J., et al. (2017). Mesoscale ocean fronts enhance carbon export due to gravitational sinking and subduction. *Proceedings of the National Academy of Sciences*, 114(6), 1252–1257. <https://doi.org/10.1073/pnas.1609435114>

Yool, A., Martin, A. P., Fernández, C., & Clark, D. R. (2007). The significance of nitrification for oceanic new production. *Nature*, 447(7147), 999–1002. <https://doi.org/10.1038/nature05885>

References From the Supporting Information

- Dugdale, R. C., & Goering, J. J. (1967). Uptake of new and regenerated forms of nitrogen in primary productivity. *Limnology & Oceanography*, 12(2), 196–206. <https://doi.org/10.4319/lo.1967.12.2.0196>
- Harrison, W. G., Platt, T., & Lewis, M. R. (1987). f-Ratio and its relationship to ambient nitrate concentration in coastal waters. *Journal of Plankton Research*, 9(1), 235–248. <https://doi.org/10.1093/plankt/9.1.235>
- Kishi, M. J., Kashiwai, M., Ware, D. M., Megrey, B. A., Eslinger, D. L., Werner, F. E., et al. (2007). NEMURO—a lower trophic level model for the North Pacific marine ecosystem. *Ecological Modelling*, 202(1–2), 12–25. <https://doi.org/10.1016/j.ecolmodel.2006.08.021>
- Knauer, G. A., Martin, J. H., & Bruland, K. W. (1979). Fluxes of particulate carbon, nitrogen, and phosphorus in the upper water column of the northeast Pacific. *Deep Sea Research Part A: Oceanographic Research Papers*, 26(1), 97–108. [https://doi.org/10.1016/0198-0149\(79\)90089-X](https://doi.org/10.1016/0198-0149(79)90089-X)
- Li, Q. P., Franks, P. J. S., Landry, M. R., Goericke, R., & Taylor, A. G. (2010). Modeling phytoplankton growth rates and chlorophyll to carbon ratios in California coastal and pelagic ecosystems. *Journal of Geophysical Research*, 115(G4), 25–29. <https://doi.org/10.1029/2009JG001111>
- Stukel, M. R., & Barbeau, K. A. (2020). Investigating the nutrient landscape in a coastal upwelling region and Its relationship to the biological carbon pump. *Geophysical Research Letters*, 47(6), e2020GL087351. <https://doi.org/10.1029/2020GL087351>
- Stukel, M. R., Benitez-Nelson, C. R., Décima, M., Taylor, A. G., Buchwald, C., & Landry, M. R. (2016). The biological pump in the Costa Rica Dome: an open-ocean upwelling system with high new production and low export. *Journal of Plankton Research*, 38(2), 348–365. <https://doi.org/10.1093/plankt/fbv097>
- Stukel, M. R., Kahru, M., Benitez-Nelson, C. R., Décima, M., Goericke, R., Landry, M. R., & Ohman, M. D. (2015). Using Lagrangian-based process studies to test satellite algorithms of vertical carbon flux in the eastern North Pacific Ocean. *Journal of Geophysical Research: Oceans*, 120(11), 7208–7222. <https://doi.org/10.1002/2015JC011264>
- Stukel, M. R., Kelly, T. B., Aluwihare, L. I., Barbeau, K. A., Goericke, R., Krause, J. W., et al. (2019). The Carbon:234Thorium ratios of sinking particles in the California current ecosystem 1: relationships with plankton ecosystem dynamics. *Marine Chemistry*, 212, 1–15. <https://doi.org/10.1016/j.marchem.2019.01.003>
- Stukel, M. R., Landry, M. R., Benitez-Nelson, C. R., & Goericke, R. (2011). Trophic cycling and carbon export relationships in the California Current Ecosystem. *Limnology & Oceanography*, 56(5), 1866–1878. <https://doi.org/10.4319/lo.2011.56.5.1866>

Observed and modeled responses of planktonic ecosystems to an upwelling pulse

In this section, we open a quick parenthesis in order to compare modeled and observed upwelling pulses in planktonic ecosystems. In particular, we compare planktonic ecosystem fields along Lagrangian pathways (obtained with satellite observations) after upwelling in the CCE (Fig. 3 of the JGR manuscript in appendix V) and averages from the simulations in the SSUS (Fig. 3 of the GRL draft in chapter III). A few properties can be compared, despite the strong differences in terms of location, time and spatial scales, average along advection at the surface (for observations) or average in depth over the shelf (for simulations).

If we hypothesize that day 0 of the observations of Fig. 3 (JGR) is the start of a nitrate pulse in the euphotic layer after an upwelling pulse, we can draw a parallel with the simulations by considering the new day 0 as the day at which the peak of nitrate is attained after SF^+ (i.e. day 9 in Fig. 3a, GRL).

In both the observations and simulations, the nitrate concentration decreases of $2 \text{ } \mu\text{mol L}^{-1}$ in ~ 10 days (from 6 to $4 \text{ } \mu\text{mol L}^{-1}$ between days 0-10 in the observations and from 12 to $10 \text{ } \mu\text{mol L}^{-1}$ between days 9-19 in the simulations). If we look at the relative anomalies reached in 10 days after an upwelling pulse, i.e. $\frac{\Delta X}{X_0} = \frac{X_{10d} - X_0}{X_0}$ with X_0 the initial value of the field at day 0 of the pulse and X_{10d} the value at day 10, we obtain -33% in the observations and -16% in the simulations. This difference is supported by the difference of magnitude of the initial concentrations: $6 \text{ } \mu\text{mol L}^{-1}$ in the observations at the surface and $12 \text{ } \mu\text{mol L}^{-1}$ for the simulations averaged in depth. However, the absolute rate of decay of nitrate concentration is similar between the observations and simulations.

In the observations, the PP decreases from 350 to $150 \text{ mmol C m}^{-2} \text{ d}^{-1}$ (JGR Fig. 3d) and in the simulations, it increases from 0.7 to $1.1 \text{ } \mu\text{mol C L}^{-1} \text{ s}^{-1}$ between days 9-19 (Fig. IV.16b). The relative anomalies reached in 10 days, reveal opposite responses of PP with -57% in the observations and +57% in the simulations. In the simulations, the PP oscillates between positive and negative anomalies and varies rapidly in time. The PP variability thus strongly depends on the spatial and temporal scale and is domain dependent. In contrary to the simulations, the observed fields do not present oscillations along the advection.

Appendix B: Carbon footprint of the PhD

At LOCEAN, the Climaction working group lead a several year long inclusive and educative approach towards the inscription of low carbon research habits in the laboratory's rules (see <https://climactions.ipsl.fr/groupe-de-travail/locean-climactions/> and <https://labos1point5.org>). This has resulted in the development of a yearly carbon quota (progressively reaching 2 tCO₂e, with surrounding subtle rules) such that every agent has to declare the carbon cost of its travels. It contributed to a general reflection towards a new low carbon culture of academic research practices, and the needed transition processes. This is especially true among young scientists who imagine their potential future of sustainable research environment. Some of us decided to limit at the most their emission and track them.

The first emission pole is related to travels, which were very few during a covid-times PhD. Participation at conferences was mainly done remotely, like OSM22 and EBUS Lima 2022 (and also OSM2020; EBUS Webinar series). A CROCO training in Brest and the participation to EGU22 in Vienna lead to (round trips by train): $2 \times 505 \text{ km} + 2 \times 1\,034 \text{ km} \approx 2 \times 2 + 2 \times 20 = 44 \text{ kgCO}_2\text{e}$ (computed with monpetitcarbone.fr, see Fig. 1). A rough estimation of daily commuting was also made; which considers a rate of emission of 3.8 g/km for the metro (source: <https://www.transilien.com/fr/page-corporate/calcul-emissions-co2>, Réseau de transport d'électricités (Rte), 2019); 3 years of about 1/3 working days of metro commuting of about 6 km (240 round trips; without pandemic related lockdown times) gives $\approx 10 \text{ kgCO}_2\text{e}$. 2/3 working days of bike commute counts about $\approx 6000 \text{ km}$ over the PhD; for a null carbon cost if the bicycle life-cycle assessment is neglected. If not, manufacturer studies estimate at $\sim 174 \text{ kgCO}_2\text{e}$ the carbon footprint of a new bike (https://www.trekbikes.com/us/en_US/sustainability/; for information they indicate that this carbon cost offset is reached after $\sim 700 \text{ km}$ of biking instead of driving a car).

The second main pole is related to numerical modeling. Considering that we use the energy expensive "Très grand centre de calcul" Joliot Curie center (TGCC; <https://www-hpc cea.fr/complexe/tgcc-JoliotCurie.htm>) for High Performance Computing, we estimate the total amount of energy/carbon required for the PhD simulations. With a rate of 4.3 gCO₂e per hour CPU (hours of Central Processing Units); Olivier Aumont/Climaction, 2019) applied to a total of $\approx 335\,000 \text{ hCPU}$, we estimate the cost of our simulations at **1440 kgCO₂e** (or 1000 with 3g/hCPU)¹.

Oceanographic cruises represent also a large pole with emissions estimated at 300 l fuel/person $\approx 1 \text{ tCO}_2\text{e}/\text{sea-day/person}$. For a 30 days cruise (SCOPES planned 10 December 2022 - 10 January 2023), plus the round-trips flights (e.g. 1 tCO₂e for Paris - Las Palmas - Paris, monpetitcarbone.fr), this represents $\approx 31 \text{ tCO}_2\text{e}$.

¹In details, 1 batch of our CROCO-PISCES Agrif experiment (i.e. 3 SF⁺⁻⁰ x 5 members x 2 months) $\approx 35\,000 \text{ h}$ ($\approx 150 \text{ kgCO}_2\text{e}$).

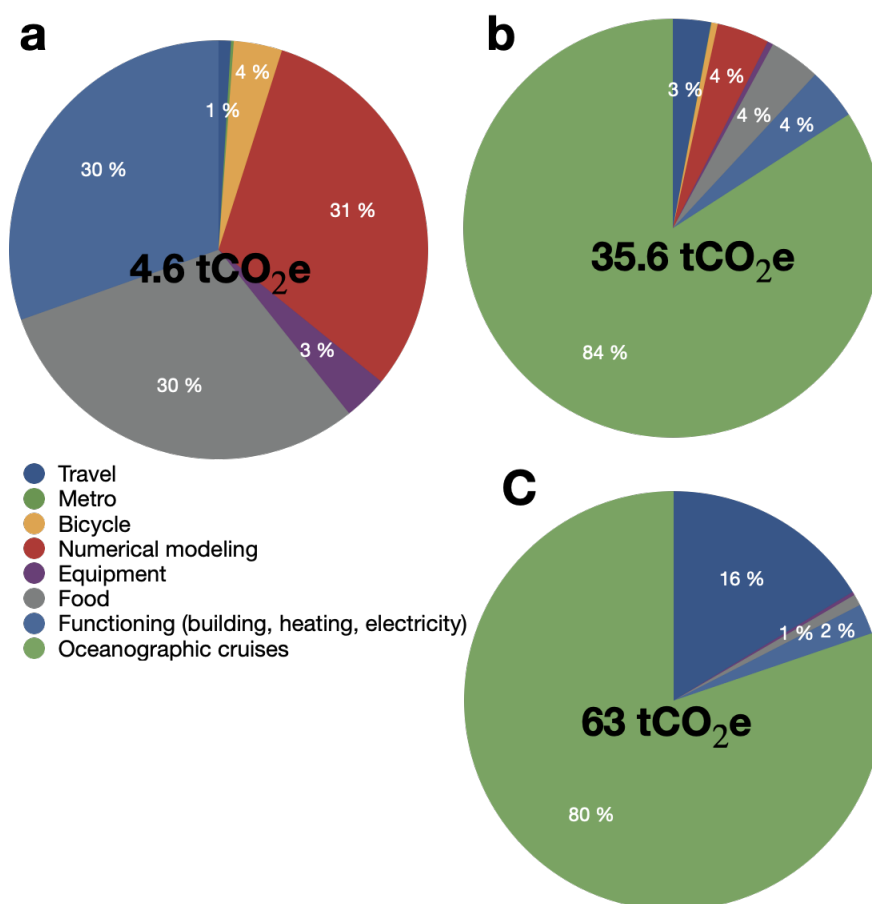


Figure 1: Pie chart of the carbon footprint of the PhD without (a) and with (b) one oceanographic cruise; of a colleague PhD student (c, Léa Olivier).

Additional poles like equipment (e.g. a laptop costs about **160 kgCO₂e**); food (average diet is 2 kgCO₂e, 5 lunches a weeks over 3 years of PhD gives **1410 kgCO₂e**, i.e. ~ the cost of numerical simulations)²; building of infrastructures (**540 kgCO₂e** for 3 years), their heating (**516 kgCO₂e**) and electricity usage (**360 kgCO₂e**)³ can also strongly impact the total budget.

Overall, by taking into account traveling, commuting, lunches, equipment, functioning and numerical modeling, this represents a PhD with a **total carbon emission of 4.6 tCO₂e**, i.e. ~1.5 tCO₂e per year (see Fig. 1a). If we take into account the participation to the cruise to this budget (measurements will not be part of this project), this would change to budget to **35.6 tCO₂e** (see Fig. 1b).

Cruises bring invaluable information that is at the heart of the oceanographer's work and climate scientists, but their weight in the total budget indicate that this pole can be a leverage for action. Alternative ways of leading oceanographic cruises can include for example coastal smaller ships or sailing. Sailing cruises could be an option for the next generation of oceanographic cruises, with the example of Tara (<https://fondationtaraocean.org/>). Fig. 1c shows the carbon budget of Léa Olivier's PhD (LOCEAN colleague using in situ measurements), which indicates the weight of ~80% of the emissions due to those cruises, similar to Fig. 1b. According to Léa's experience, sailing cruises could help reducing emissions per person by a factor of 3 in the worst conditions (from ≈ 1 tCO₂e/sea-day/person to ≈ 0.3 tCO₂e/sea-

²ADEME: [https://data.ademe.fr/datasets/base-carbone\(r\)](https://data.ademe.fr/datasets/base-carbone(r))

³Olivier Aumont/Climaction, 2019

day/person), and even more in favorable conditions. Note that emissions are even more reduced in absolute, as the ships welcome less people (of course a trade-off with the efficiency of measurements has to be made). This can be complemented by parallel measurements by fleets of Autonomous Underwater Vehicles, e.g. gliders. These are innovative ways of leading oceanographic measurements and provides a basis for future designs.

Concerning the rest of the carbon footprint, the way of commuting and the absence of flying was a doable way to limit emissions. Equipment, food habits and functioning are hardly flexible poles at the individual scale. Concerning our modeling experiment, doubling the number of members of our ensemble would thus have increased the consumption twofold, i.e. costed $\approx 2880 \text{ kgCO}_2$.

List of Figures

- 0.1 Schematic of typical dynamics of a northern hemisphere coastal wind-driven upwelling system. Air-sea heat fluxes (Q , the sinuous arrow indicates the air-sea direction), surface wind stress (τ , straight arrows indicate the wind direction) and coastal trapped waves (CTW, the arrow indicates the direction of propagation) are indicated in green. Dashed green arrows symbolically indicate remote forcing and not a realistic direction. The continuous thick blue arrows indicate the offshore Ekman drift U_{Ek} , the geostrophic onshore flow U_{geo} resulting from the alongshore pressure gradient (indicated in purple by the difference of sea surface heights $\eta_+ - \eta_-$) and the vertical velocities w . The alongshore upwelling *jet* resulting from the cross-shore pressure gradient ($\eta_{++} - \eta_{--}$) is indicated in blue in the y-axis direction, oppositely to the counter current at greater depth. Sinuous thin blue arrows indicate circulation patterns associated to coastline irregularities and to flow fluctuations $u' = u - \bar{u}$ with \bar{u} the mean flow. The surface mixed layer *SML* depth is indicated in darker blue dashed line. The nearshore rise of isopycnals is indicated with purple lines σ_{iso} and the vertical mixing in the SML with the purple *vmix* sinuous line. The typical vertical profiles of light availability, temperature and nitrate are indicated on the left side in orange, light blue and olive green lines. 14
- 0.2 Four major Upwelling Systems location and their respective mean chlorophyll concentration, NP_{pot} and PP. From [Messié and Chavez \(2015\)](#). 15
- 0.3 Seasonal mean (November-April) of the sea level pressure (colors, in hPa) and 10 m wind speed (arrows), from ERA-Interim 1979-2014 reanalysis, from [Kounta Diop \(2019\)](#) thesis. Average locations of Azores and Saharo-Lybian anticyclones are indicated in blue circles. 17
- 0.4 Schematic of a system forcing (denoted $f_f(t)$, panels a,c) and response (denoted $f_r(t)$, panels a,c). Positive (δ_f^+) and negative (δ_f^-) symmetrical ($\delta_f^+ = -\delta_f^-$) perturbations in the forcing impact the system response, symmetrically (if $\delta_r^+ = -\delta_r^-$) or not (if $\delta_r^+ \neq -\delta_r^-$). 19
- 0.5 Canary Upwelling System circulation. From [Arístegui et al. \(2009\)](#). 21

0.6	West coast of North America (a), Northwest coast of Africa (b), Monterey Bay/ Gulf of Farallones (c) and South Senegalese coast (d). Upper panels are monthly SST averages during August (a) and March (b) 2000, from Copernicus data "Multi Observation Global Ocean ARMOR3D L4" (https://doi.org/10.48670/moi-00052) and lower panels are daily SST images of the 23 May 2022 (c) and 1 March 2022 (d), from Nasa AQUA MODIS (https://oceancolor.gsfc.nasa.gov/).	22
0.7	Northwest African domains (a) and south Senegalese domain of interest (b). Bathymetry is indicated in colors.	23
0.8	Daily averages of (a) the meridional wind speed at 10 m and (b) the net heat flux over south Senegalese waters for the year 2001 from ERA5 reanalysis.	23
0.9	Satellite (L2 MODIS) SST instantaneous image during the upwelling season. From Ndoye et al. (2017)	24
0.10	Schematics of (a) the fueling of primary production by nutrients and (b) processes regulating the export of organic matter from the euphotic layer to the deep ocean. Those panels are the Figs. 5.15 and 5.17 of Williams and Follows (2011)	26
0.11	Scheme of the cross-shore structure of wind stress (large black arrows), vertical velocities (thick blue arrow represent the strong coastal upwelling and smaller blue arrows the wind stress curl upwelling), nutricline depth (dashed red line) and plankton communities (i.e. large and small plankton; circular arrows represent the intensity of growth and grazing in the nearshore and offshore sectors) in the California Current Ecosystem. From Ohman et al. (2013)	28
0.12	Scheme of the main physical and biogeochemical processes at play in the California Current Ecosystem. Wind is indicated with the large blue arrow. The organic matter formed in upwelling waters nearshore is transported offshore by filaments and mesoscale eddies. The westward direction of propagation of both mesoscale cyclones and anticyclones is indicated in the red arrows. Subduction in mesoscale features and sinking in the water column are indicated with purple and blue arrows. From Nagai et al. (2015)	29
0.13	Monthly average of March 2010 near surface chlorophyll-a concentration, satellite observation from Copernicus (Gohin et al., 2002).	33
I.1	Grid configuration used in the study. It consists of a parent domain encompassing most of the Canary current system with a zoom at 2.5 km horizontal resolution over the the Senegalese waters (green rectangle in panel a; see text for details). The study area located south of Cape Verde (SSUS) and various averaging boxes (green and blue solid lines) are shown in panel b, as well as the Melax buoy location (orange star). . .	42
I.2	Daily averages of zonal (blue) and meridional (green) QSCAT (y-axis) and derived from ERA5 (x-axis) and their correlation.	42

I.3	Time series over the 10 years studied (2000-2010): the green line indicates the meridional wind stress from ERA5 averaged over the SSUS, the blue line indicates the seasonal cycle of the latter signal, the red line indicates the detrended signal. Upwelling intensification (yellow stars) and relaxation events (orange stars) are detected during the upwelling season (November-May), with the standard deviation threshold (grey lines). Panel (a) is the 10 years time interval and panel (b) shows a zoom on the two first years.	45
I.4	Distribution of easterlies and westerlies events along the November-May upwelling season with ERA5 reanalysis.	46
I.5	Composites of zonal and meridional wind stress (τ_U , τ_V), short and long wave radiation (SW, LW), sensible and latent (SH, LH), total cloud coverage (TCC) and total heat fluxes (Qnet). The two upper lines (a) are composites of eastern wind events, the two middle lines (b) of western events and the two lower lines (c) show the composites without zonal differentiation.	47
I.6	Same as Fig. I.5 in anomaly relative to monthly mean climatological values. The two upper lines (a) show the anomalies during intensification events and the two lower during relaxation events (b).	48
I.7	Power Spectral Density of daily meridional wind stress time series of QSCAT (red) and ASCAT (blue), using Welch's method.	49
I.8	Canary current meridional wind stress (a, c) and net heat fluxes (b, d) climatological (a,b; SF^0) and SF^+ anomaly (c,d) fields at the peak of the synoptic intensification. Anomalies for SF^- are the opposite of those for SF^+ . The experimental timeline is presented in panel e. Continuous (resp. dashed) lines indicate the evolution of the meridional wind stress (resp. net heat flux) averaged over the SSUS. Green (resp. blue and orange) lines are for climatological (resp. wind intensification and relaxation) forcings. A slight deviation from perfect SF^+ - SF^- symmetry can be seen for heat fluxes, due at a small error. Its impact on simulated upper ocean temperature is negligible (see section 3.3.)	52
I.9	Meridional wind stress spatial pattern during the anomaly at day 3 (a) and along 100 m isobath before and during the wind intensification anomaly at days 0 and 3 (b). Panels (c,d) indicate the anomalies between days 0 and 3. The 100 m isobath is indicated with the red line on panel c.	54
I.10	a) Time series of the ensemble averages of spatial RMS for various quantities computed for $X=SST$ (panel a); see text in section 3.6 and Eq. I.11). The grey dashed line represents the amplitude modulation of the synoptic anomaly $f(t)$. b) Signal to Noise Ratios (SNR) as defined in section 3.6.	56
I.11	Examples of flow geometry in which both horizontal advection terms (expressed in flux form) are identically zero (case a) or not (case b) despite the similarity of the situation from the perspective of heat budget in the control area ($x=\pm L_x, y=\pm L_y$). Schematic by Xavier Capet.	59
I.12	Sections of the lateral boundaries of the integration box.	60
I.13	Time series of Melax thermistors data from 11 February 2015 to 26 April 2016.	62

I.14	Surface Mixed Layer depth time series (only between November-May during the upwelling season) observed at Melax (blue lines), of 9 years of CROCO KPP (orange lines and the shaded orange area indicates the standard deviation), two individual years with $k-\epsilon$ vertical mixing scheme (green lines) and chlorophyll shading (red lines) simulations. Note that times when the water column is fully mixed are masked.	63
I.15	Schematic of PISCES Operational Marine Biogeochemistry Model from https://www.pisces-community.org/index.php/model-description/ ; Aumont et al. (2015).	64
I.16	Time series of the SST (a) and SML depth (b) seasonal cycle for CROCO-KPP (blue lines), $k-\epsilon$ (green) and KPP with chlorophyll shading (orange), daily averages between (-18,-17°E and 14,14.6°N). Blue shaded areas indicate the standard deviation to the mean of the variables.	66
I.17	Time series of the averaged nitrate concentration in coastal Senegalese waters (the averaging box is shown in orange on panels on the right), between depths 0-100 m (a) and 100-200 m (b). The time period is 5 years of climatological simulations.	67
I.18	Climatological seasonal averages of surface chlorophyll-a concentration of satellite CMEMS observations (a-c), CROCO-PISCES simulations (d-f) and SOMNVA observations (g-i).	68
I.19	Climatological seasonal averages of surface nitrate concentration of CROCO-PISCES (CP) simulations (a-d), World Ocean Atlas observations (e-h) and the number observations it uses (i-l); standard deviation of CROCO-PISCES simulations (m-p) and World Ocean Atlas observations (q-t).	70
I.20	Seasonal World Ocean Database (dotted lines) and model (continuous lines) locations and vertical profiles of NO_3 in the Cape Verde sector.	71
I.21	Time series of intermediate quantities to reach the weight of perturbation diagnostic $\mathcal{W}^{\pm 0}(X)$, here with $X=\text{NO}_3$.	73
II.1	Grid configuration used in the study. It consists of a parent domain encompassing most of the Canary current system with a zoom at 2.5 km horizontal resolution over the the Senegalese waters (green rectangle in panel a; see text for details). The study area located south of Cape Verde (SSUS) and various averaging boxes (green and blue solid lines) are shown in panel b, as well as the Melax buoy location (orange star).	81
II.2	Canary current meridional wind stress (a, c) and net heat fluxes (b, d) climatological (a,b; SF^0) and SF^+ anomaly (c,d) fields at the peak of the synoptic intensification. Anomalies for SF^- are the opposite of those for SF^+ . The experimental timeline is presented in panel e. Continuous (resp. dashed) lines indicate the evolution of the meridional wind stress (resp. net heat flux) averaged over the SSUS. Green (resp. blue and orange) lines are for climatological (resp. wind intensification and relaxation) forcings. A slight deviation from perfect $\text{SF}^+ - \text{SF}^-$ symmetry can be seen for heat fluxes, due at a small error. Its impact on simulated upper ocean temperature is negligible (see section 2.2.3.)	84

- II.3 a) Time series of the ensemble averages of spatial RMS for various quantities computed for $X=SST$ (panel a); see text in section 2.2.5 and Eq. II.7). The grey dashed line represents the amplitude modulation of the synoptic anomaly $f(t)$. b) Signal to Noise Ratios (SNR) as defined in section 2.2.5. 86
- II.4 (u, v) depth averaged currents in: a) CROCO climatological simulations, b) CROCO synoptic simulations and, c) Melax (2015-2016 observations). Each dot corresponds to one daily mean (5 days mean in panel a) current value for the month of March. The center of each ellipse materialized with a star indicates the mean current averaged over each available day while its semi-axes indicate the maximum and minimum variance. The angle between the ellipse major axis and North is indicated on top of each panel. In b) and c), blue (resp. red) dots correspond to daily currents at wind intensification (resp. relaxation) times. Ellipses are all repeated for comparison in panel d, with the location of Melax (black star) as the origin ($u = v = 0$). 89
- II.5 Temperature anomaly profiles (panels a, c, e, g) and wind evolution (panels b, d, f, h) during intensification (panels a, b, e, f) and relaxation events (panels c, d, g, h). The upper (resp. lower) row corresponds to Melax observations during two carefully chosen events (resp. to ensemble averaged model solutions at Melax). The color codings of temperature profiles and of the wind time series are identical, which provides a time information to the former. 90
- II.6 Ensemble averaged fields of SSH (color) and surface velocity (arrows) for SF^+ (upper row), SF^0 (middle row) and SF^- (lower row). From left to right, the three columns correspond to the three periods before (average of day -1 to day 0; see timeline and date reference in Fig. II.2e), during (days 6 to 9 included) and after (days 19 to 22 included) the synoptic event. For SF^+ and SF^- panels, light green circles indicate locations where not all ensemble members agree on the sign of the SSH anomaly relative to SF^0 (see section 2.2.5). 92
- II.7 Similar to Fig. II.6 but for SST. The grey shading in panel f represents the sector over which along-isobath averaging is performed to obtain Fig. II.9. 93
- II.8 Same as Fig. II.6 for vertical velocities at the mixed layer depth. 94
- II.9 Across-shore vertical section of temperature (color), surface mixed layer depth (red dashed line), meridional currents (blacks contours, in $m s^{-1}$) and vertical velocities (white and green lines indicate isolines 2 and 6 $m day^{-1}$). Fields are ensemble, alongshore and time averaged. Alongshore averaging is carried out in the grey box represented in Fig. II.7f using a regridding from longitude to ocean depth. SF^+ (upper row), SF^0 (middle row) and SF^- (lower row) evolutions are shown. 95

- II.10 Time series of a) SST anomaly b) SML depth anomaly c) vertical velocity at the base of the SML d) surface zonal and e) meridional velocity for SF^+ and SF^- runs. Variables are ensemble and spatially averaged (over BoxN; see Fig. II.1b). Blue (resp. red) lines correspond to SF^+ (resp. SF^-). Dark (resp. light) tones are for KPP (resp. GLS k- ϵ) ensembles. Anomalies are relative to SF^0 . Red and blue stars in panels a) and b) indicate values found at days 6, 8, and 10 for the simulations forced with double heat flux anomalies ($2 Q'_{SF}$). Green dots and bars left or right of the figure box represent respectively the averages and the intrinsic variability levels computed as plus/minus the maximum standard deviation (std) between day -1 and day 22 in the ensemble run SF^0 . Dark (resp. light) green is for simulations with KPP (resp. GLS k- ϵ) turbulence submodel. SML depth is diagnosed based on a density threshold for simulations with GLS k- ϵ . It is computed internally when using KPP but using the same threshold-based method only makes minute differences. Shaded envelopes represent the standard deviation computed each day from the different ensemble members. The grey dotted line represent the shape of synoptic forcing anomaly (i.e., $f(t)$; see section 2.2.3). Percentages in the upper right corner of each panel indicate the relative importance of the asymmetry between SF^+ and SF^- , $\mathcal{R}_{SF}(X)$ (see definition in section 2.2.6). Note that the amplitude of the y-axis range is similar in panels d and e. 97
- II.11 Surface slice (a) and vertical-across-shore section (b) of ensemble, alongshore, and time averaged meridional current residual $RES_{SF}(v)$ (see definition in section 2.4.4). Time (resp. alongshore) averaging is performed between days 6 and 9 included (resp. over the sector shaded in grey in panel a). 98
- II.12 a): Vertical velocities at the base of the SML. b): horizontal density gradient magnitude $|\nabla_h \rho|$. Both quantities are averaged over BoxS (see Fig. II.1b) and represented for SF^+ (blue), SF^0 (green) and SF^- (red). Shaded envelopes indicate the ensemble standard deviation. 99
- II.13 Ensemble averaged SF^0 advection (left column), atmospheric forcing (middle column) and heating rate (right column) terms as defined in Eq. II.11 (in $^{\circ}\text{C day}^{-1}$). Surface velocities are also shown (arrows). The three rows are for the same three time windows used in Fig. II.6 and II.7 (days -1 to 0, 6 to 9 and 19 to 22 from top to bottom). 101
- II.14 Same as Fig. II.13 for SF^+ . Averages over the time window before the synoptic anomaly (days -1 to 0) is as for SF^0 and is therefore not repeated (see Fig. II.13 upper row). 102
- II.15 Same as Fig. II.14 for SF^- 103
- II.16 Time series of ensemble and BoxN (see Fig. II.1b) spatially averaged heat budget tendency terms. Color coding of the different terms is indicated in panel c). Shaded envelopes represent the ensemble standard deviation. Panels (a,b,c) correspond respectively to SF^0 , SF^+ and SF^- . Magenta dots located at $t = 1$ day (resp. $t = 11$ days) provide entrainment (ENTR) values time averaged between day 0 and 9 (resp, day 10 and 22). The associated magenta bar represents the maximum value of the ensemble standard deviation over the corresponding time window. 105

- II.17 a) Horizontal (solid lines) and vertical (dashed lines) heat advection tendencies as a function of the location of the averaging box southern boundary (which varies from 13.50 to 14.50°N). Five averaging boxes are used (indicated with dots and stars superimposed on lines). Each tendency value is ensemble and time averaged (between days 6 and 9, i.e., at the end of the synoptic anomaly if any). Green, blue and orange lines indicate respectively SF^0 , SF^+ , and SF^- . Isolated grey stars represent the outcome of diluting the SF^+ vertical advection tendency found north of 14.50°N in the boxes with southern extension at 14.25°N and 14.00°N. b) SF^+/SF^- asymmetry (i.e., synoptic residual) $RES_{SF}(X)$ associated with the domain averaged horizontal (solid) and vertical (dashed) advection tendency terms shown in panel a. 106
- II.18 Similar as Fig. II.6 but in anomalies to the climatology instead of in absolute. The climatological values are removed to the synoptic values (II.18a is II.6a minus II.6d; II.18b is II.6b minus II.6e; II.18c is II.6f minus II.6d; II.18d is II.6g minus II.6e) in colors (SSH) and arrows (surface currents). 112
- II.19 Same as Fig. II.18 with SST. 113
- II.20 Same as Fig. II.18 with corresponding Fig. II.9 transect. Anomalies in colors (temperature), green and white lines (vertical velocities) and black lines (meridional currents). 113
- II.21 Time series of SF^\pm (blue and orange) heat fluxes forcings effective on our simulations (dashed lines) and the intended, corrected forcings (continuous lines). Average over the SSUS. 114
- II.22 Panel a is similar to Fig. II.3 (diagnostics averaged in BoxN) and the panel c indicate the average over the entire SSUS domain. Panels b and d indicate Root Mean Square Error (RMSE; over BoxN and SSUS domain, respectively). Note that we denote the ensemble averages with an overline in the legend because it is not straightforward here: we compute the diagnostics for each member and then average over the ensemble. We remind that $\Delta X_{SF^\pm}^{(e)} = (X_{SF^\pm}^{(e)} - X_{SF^0}^{(e)})$ and $\delta X_{SF}^{(e)} = X_{SF} - X_{SF}^{(e)}$, as defined in section 2.2.5. 115
- II.23 Time series of meridional wind speed at Melax. Panel a shows the absolute signal and panel b the signal detrended from its seasonal cycle. Identification of intensification and relaxation events out of the standard deviation range are indicated in red and yellow stars. 117
- II.24 Vertical structure of Melax and CROCO currents (u, v) (panels a,b) during wind intensification and relaxation. The vertical profiles rotated by the angle between the major axis of the ellipse (of depth integrated currents) and the north (see Fig. II.4 of the JPO manuscript) are indicated in dotted lines. 118
- II.25 Temporal evolution of the along 20 m isobath SSH (along the northwest coast of Africa) for SF^+ (a,c) and SF^- (b,d), in absolute (a,b) and temporal anomaly (c,d). . . . 119
- II.26 Same as Fig. II.25 over the SSUS domain. 119
- II.27 Location of points (A, B)(panel a), time series ensemble averages of the difference of sea surface height (SSH) between B and A for SF^{0+-} (panels b,c). The time series is absolute on panel b and in anomaly in panel c, with the sum of the anomalies plotted in green and the \mathcal{R}_{SF} value. 120

II.28	Maps of surface vorticity scaled by the Coriolis parameter f : panel a) SF^0 days -1:0, b) SF^+ 6:9, c) SF^+ days 19:22, d) SF^- 6:9, e) SF^- days 19:22.	121
II.29	Maps as Fig. II.28 with the difference of temperature between the level above and below the SML depth.	122
II.30	Heat transport integrated over the SML depth along the sections (upper row). The lower row shows the associated velocity. The three rows indicate SF^{-0+} ensemble averages responses. The two purple dashed lines indicate the separation between Northern, Western and Southern faces of the box of Fig. I.12.	123
II.31	Surface pattern of the SML depth (in m) on an instantaneous state of the ocean at March 1 using $k-\epsilon$ (a) and KPP (b) vertical mixing schemes. Plot made using the ncview software.	125
II.32	Time series of the BoxN averaged SST for a $T_{syn} = 11$ days (pink line) and a $T_{syn} = 21$ days intensification (blue line). The anomaly induced by the longer intensification from the unperturbed state (green line) is indicated with the orange line.	125
II.33	Different types of circulations around bays in upwelling systems, adapted from Largier et al. 2019 (a-c) and our analysis (d). Continuous lines indicate flow patterns and dashed lines indicate flow separation.	127
II.34	Schematic of 3D shelf dynamical and heat response to SF^+ (a) and SF^- (b). Different heat fluxes are distinguished (atmospheric aHF, vertical vHF and horizontal hHF). Positive (red) and negative (blue) rates of heat in the box SML is indicated in color for each flux and for the shelf box average. Straight continuous (resp. dashed) arrows indicate horizontal (resp. vertical) currents associated to heat transport. Cold Water (CW) upwelling is indicated with along shelf slope/vertical dashed arrows. Green dotted and dashed lines indicate the SML depth and the southwards upwelling jet extent, with the associated alongshore currents v indicated with green dot and cross symbols.	129
III.1	Surface patterns of Sea Surface Temperature (SST, a), NO_3 (d), diatoms (b), nanophytoplankton(e), microzooplankton (f) and mesozooplankton (c) concentrations averaged over the ensemble for SF^0 between days 0 and 30. The average box is indicated with the light grey contour on panel a. The black lines indicate the 20, 100 and 500 m isobaths. Note that colorbar ranges are different for diatoms and nanophytoplankton. The Cape Verde (CV) is the land promontory extending westward at $14.7^\circ N$	136
III.2	Nutrient and biological quantities averaged within the 100-0 m isobaths and from the bottom of the water column to the surface between days 9-11, and over the ensemble. SF^- , SF^0 and SF^+ are indicated in orange, green and blue lines.	138
III.3	Nutrient and biological quantities averaged over the shelf in the whole water column, and over the ensemble. Green, orange and blue lines indicate SF^0 , SF^- and SF^+ . Shaded areas indicate the ensemble standard deviation. $\mathcal{W}^{\pm 0}$ and \mathcal{R}_{SF} diagnose maximum of relative perturbations and asymmetries. The box of integration is shown on Fig. III.1a grey line (between $13-14.75^\circ N$ and 0-100 m isobaths). The trend in all time series corresponds to the seasonal cycle.	139

III.4	Weight of SF^- (a) and SF^+ (b) perturbations along biogeochemical and biological levels over the entire shelf (H) and inner shelf (IS).	140
III.5	Same as Figure 2 of the manuscript for the inner shelf: 20 m isobath offshore limit. . .	143
III.6	Same as Figure 3 of the manuscript for the inner shelf.	144
III.7	Time series of the along shelf structure of nitrate (a-c), nanophytoplankton (d-f), diatoms (g-i), microzooplankton (j-l) and mesozooplankton (m-o). The left column indicates the responses to SF^- , the middle to SF^0 and the right column to SF^+	146
IV.1	Figure similar to Fig. III.3 of the GRL manuscript chapter III. Nutrient and biological quantities averaged over the shelf in the entire water column, and over the ensemble. Green, orange and blue lines indicate SF^0 , SF^- and SF^+ . Shaded areas indicate the ensemble standard deviation. $\mathcal{W}^{\pm 0}$ and \mathcal{R}_{SF} diagnose maximum of relative perturbations and asymmetries. The box of integration is shown in Figure II.1a (between 13-14.75°N and 0-100 m isobaths).	148
IV.2	Surface patterns of NO_3 (a), PO_4 (b), Iron (c), NH_4 (d) and Si (e) concentrations averaged over the ensemble during 30 days of SF^0	149
IV.3	Vertical sections of NO_3 (a), PO_4 (b), Iron (c), NH_4 (d) and Si (e) concentrations averaged over the ensemble during 30 days of SF^0 . The section location is indicated in Fig. II.7 of chapter II. The red line indicates the surface mixed layer depth and the lightgreen line the euphotic layer depth.	150
IV.4	Factors of limitation by nutrients for diatoms (a,b,c) and phytoplankton (d,e,f) growths, in response to SF^- (a,d), SF^0 (b,e) and SF^+ (c,f). The limiting nutrient is indicated in color (silicate in red, iron in yellow, phosphate in light blue, nitrogen in blue). No hashing indicate strong limitation, horizontal hashing indicate a moderate limitation and inclined hashing indicate modest limitation (arbitrary intervals). The time interval for averaging is days 3:8. We show the most recurrent limiting nutrient over the ensemble in the time interval at each location.	152
IV.5	Surface NO_3 concentration averaged over the ensemble during SF^- (a), SF^0 (b) and SF^+ (c). The time interval for averaging is days 6:9 (different from Fig. IV.4).	153
IV.6	Time series of the total rate of change of nitrate concentration (red lines), physical (blue lines) and biological (green lines) terms, for SF^- (a,d), SF^0 (b) and SF^+ (c,e). Panels d,e indicate the anomalies to the climatological terms $SF^\pm - SF^0$	154
IV.7	Spatial patterns of the surface mixed layer depth (SML, a), euphotic layer depth (EL, b) and their difference (c) ensemble averaged over 30 days of SF^0 . The average box is shown on the Fig. 1a of chapter 3 XX. Black lines indicate the 20, 100 and 500 m isobaths.	155
IV.8	Time series of the box average SML depth (a), euphotic layer (b) and their difference (c) for SF^{0+-}	156
IV.9	Surface patterns of nanophytoplankton (a), diatoms (e), microzooplankton (i), mesozooplankton (j) biomass. Total (PP), new (NP) and regenerated (RP) primary production terms corresponding to each plankton species are shown on panels b-d for nanophytoplankton and f-h for diatoms. Averages are made over the ensemble during 30 days of SF^0	158

IV.10 Vertical sections of nanophytoplankton (a), diatoms (e), microzooplankton (i), mesozooplankton (j) biomass. Total (PP), new (NP) and regenerated (RP) primary production and grazing terms corresponding to each plankton species are shown on panels b-d for nanophytoplankton and f-h for diatoms. Averages are made over the ensemble during 30 days of SF^0 . The red line indicates the surface mixed layer depth and the lightgreen line the euphotic layer depth.	159
IV.11 Time series of the total rate of change of diatoms concentration (red lines), physical (blue lines) and biological (green lines) terms, for SF^- (a,d), SF^0 (b) and SF^+ (c,e). Panels d,e indicate the anomalies to the climatological terms $SF^\pm - SF^0$. Panels f-j are structured similarly with individual biological terms (indicated in the legend) instead of total, physical and biological terms. The total biological term is reminded in with the darkest green continuous line on panels f-j.	163
IV.12 Similar to Fig. IV.11 for nanophytoplankton concentration. Biological sinks are not detailed individually.	164
IV.13 Similar as Fig. IV.6 for mesozooplankton concentration.	166
IV.14 Similar as Fig. IV.6 for microzooplankton concentration.	166
IV.15 Primary production terms (for diatoms) averaged within the 20-0 m (inner shelf, panel a) and 100-0 m (entire shelf, panel b) isobaths and from the bottom of the water column to the surface between days 9-11, and over the ensemble. SF^- , SF^0 and SF^+ are indicated in orange, green and blue lines.	167
IV.16 Primary production terms (for diatoms) averaged over the shelf in the entire water column, and over the ensemble. Green, orange and blue lines indicate SF^0 , SF^- and SF^+ . Shaded areas indicate the ensemble standard deviation. $\mathcal{W}^{\pm 0}$ and \mathcal{R}_{SF} diagnose maximum of relative perturbations and asymmetries. The box of integration is between 13-14.75°N and 0-20 m isobaths (inner shelf, panel a) and 0-100 m isobaths (entire shelf, panel b). The trend in all time series corresponds to the seasonal cycle. .	168
IV.17 Similar as Fig. IV.1 averaged over the inner shelf, limited offshore by the 20 m isobath.	169
IV.18 Same as Fig. IV.11 but averaged over the inner shelf.	170
IV.19 Similar as Fig. IV.1 averaged over the surface mixed layer.	171
IV.20 Same as Fig. IV.11 but averaged over the inner shelf. Panels k-o are structured similarly with individual physical terms (indicated in the legend). The total physical term is reminded in with the blue continuous line on panels k-o.	173
IV.21 Diatoms (a-c) and mesozooplankton (d-f) concentrations for a given member of the ensemble at day 9 of SF^- . The purple and yellow cross-shore sections shown on the horizontal patterns of panels c,f are shown on panels a,d and b,e. SML and euphotic layer depths are indicated in red and orange lines.	174
IV.22 Physical and biological terms of the diatoms budget integrated on the shelf whole water column between days 3:8 (and 0:30 for SF^0 ; panel a). Relative perturbations of total PP integrated until days 5, 10 and 30. Colors (green, blue, orange) indicate SF^{0+-} ; dots indicate the entire shelf and diamonds the inner shelf.	176

- IV.23 Schematic of 3D shelf nitrate and plankton response to SF^+ (a) and SF^- (b). Nitrate, phytoplankton and zooplankton concentration patterns are indicated in colored areas (respectively grey, green and brown). The continuous black arrow indicate the strength and orientation of the circulation of the flow. Grey and orange dashed lines indicate the SML and euphotic layer depths. Processes driving the rate of change of diatoms concentration in the box SML are shown as follows. Colors red and blue indicate the source and sink terms. Straight continuous arrows indicate advection terms associated to diatoms transport. Entrainment is indicated with the dashed arrow and vertical mixing by sinuous lines. Primary production, grazing by zooplankton and mortality/aggregation processes strength are indicated with the dots, curved arrows and crosses markers. Noticeable modifications of environment conditions are indicated in parenthesis below SF^\pm titles. Note that the bathymetry and inner shelf scales are unrealistic, the location of grazing by zooplankton and mortality/aggregation processes are arbitrary over the shelf and that it represents the state of the planktonic ecosystem in the late part of the SF perturbation, when we consider the system to be the most perturbed. 178
- 1 Pie chart of the carbon footprint of the PhD without (a) and with (b) one oceanographic cruise; of a colleague PhD student (c, Léa Olivier). 206

Bibliography

- Aguirre, C., Garreaud, R., Belmar, L., Farías, L., Ramajo, L., and Barrera, F. (2021). High-Frequency Variability of the Surface Ocean Properties Off Central Chile During the Upwelling Season. *Frontiers in Marine Science*, 8.
- Aguirre, C., Garreaud, R. D., and Rutllant, J. A. (2014). Surface ocean response to synoptic-scale variability in wind stress and heat fluxes off south-central Chile. *Dynamics of Atmospheres and Oceans*, 65:64–85.
- Aguirre, C., Rojas, M., Garreaud, R. D., and Rahn, D. A. (2019). Role of synoptic activity on projected changes in upwelling-favourable winds at the ocean's eastern boundaries. *npj Climate and Atmospheric Science*, 2(1):1–7. Number: 1 Publisher: Nature Publishing Group.
- Aiken, C. M., Castillo, M. I., and Navarrete, S. A. (2008). A simulation of the Chilean Coastal Current and associated topographic upwelling near Valparaíso, Chile. *Continental Shelf Research*, 28(17):2371–2381.
- Aksnesa, D. L. and Ohman, M. D. (2009). Multi-decadal shoaling of the euphotic zone in the southern sector of the California Current System. *Limnology and Oceanography*, 54(4):1272–1281. _eprint: <https://onlinelibrary.wiley.com/doi/pdf/10.4319/lo.2009.54.4.1272>.
- Aristegui, J., Barton, E. D., Álvarez Salgado, X. A., Santos, A. M. P., Figueiras, F. G., Kifani, S., Hernández-León, S., Mason, E., Machú, E., and Demarcq, H. (2009). Sub-regional ecosystem variability in the Canary Current upwelling. *Progress in Oceanography*, 83(1):33–48.
- Auger, P.-A., Gorgues, T., Machu, E., Aumont, O., and Brehmer, P. (2016). What drives the spatial variability of primary productivity and matter fluxes in the north-west African upwelling system? A modelling approach. *Biogeosciences*, 13(23):6419–6440. Publisher: Copernicus GmbH.
- Aumont, O., Ethé, C., Tagliabue, A., Bopp, L., and Gehlen, M. (2015). PISCES-v2: an ocean biogeochemical model for carbon and ecosystem studies. *Geoscientific Model Development*, 8(8):2465–2513. Publisher: Copernicus GmbH.
- Bakun, A. (1973). Coastal Upwelling Indices, West Coast of North America, 1946–71. NOAA Technical Report NMFS SSRF 671, 103pp.:112.
- Bakun, A. (1990). Global Climate Change and Intensification of Coastal Ocean Upwelling. *Science*, 247(4939):198–201. Publisher: American Association for the Advancement of Science.

- Bakun, A., Black, B. A., Bograd, S. J., García-Reyes, M., Miller, A. J., Rykaczewski, R. R., and Sydeman, W. J. (2015). Anticipated Effects of Climate Change on Coastal Upwelling Ecosystems. *Current Climate Change Reports*, 1(2):85–93.
- Bakun, A. and Csirke, J. (1998). Environmental processes and recruitment variability. *FAO fisheries technical paper*.
- Bane, J. M., Spitz, Y. H., Letelier, R. M., and Peterson, W. T. (2007). Jet stream intraseasonal oscillations drive dominant ecosystem variations in Oregon's summertime coastal upwelling system. *Proceedings of the National Academy of Sciences*, 104(33):13262–13267. Publisher: Proceedings of the National Academy of Sciences.
- Barnier, B., Siefridt, L., and Marchesiello, P. (1995). Thermal forcing for a global ocean circulation model using a three-year climatology of ECMWF analyses. *Journal of Marine Systems*, 6(4):363–380.
- Barrier, N., Deshayes, J., Treguier, A.-M., and Cassou, C. (2015). Heat budget in the North Atlantic subpolar gyre: Impacts of atmospheric weather regimes on the 1995 warming event. *Progress in Oceanography*, 130:75–90.
- Barth, J. A., Pierce, S. D., and Castelao, R. M. (2005). Time-dependent, wind-driven flow over a shallow midshelf submarine bank. *Journal of Geophysical Research: Oceans*, 110(C10). _eprint: <https://onlinelibrary.wiley.com/doi/pdf/10.1029/2004JC002761>.
- Barth, J. A., Pierce, S. D., and Smith, R. L. (2000). A separating coastal upwelling jet at Cape Blanco, Oregon and its connection to the California Current System. *Deep Sea Research Part II: Topical Studies in Oceanography*, 47(5):783–810.
- Batchelder, H. P., Edwards, C. A., and Powell, T. M. (2002). Individual-based models of copepod populations in coastal upwelling regions: implications of physiologically and environmentally influenced diel vertical migration on demographic success and nearshore retention. *Progress in Oceanography*, 53(2):307–333.
- Beardsley, R. C., Dever, E. P., Lentz, S. J., and Dean, J. P. (1998). Surface heat flux variability over the northern California shelf. *Journal of Geophysical Research: Oceans*, 103(C10):21553–21586. _eprint: <https://onlinelibrary.wiley.com/doi/pdf/10.1029/98JC01458>.
- Beckmann, A. (1998). The Representation of Bottom Boundary Layer Processes in Numerical Ocean Circulation Models. In Chassignet, E. P. and Verron, J., editors, *Ocean Modeling and Parameterization*, NATO Science Series, pages 135–154. Springer Netherlands, Dordrecht.
- Benazzouz, A., Demarcq, H., and González-Nuevo, G. (2015). Recent changes and trends of the upwelling intensity in the Canary Current Large Marine Ecosystem. Accepted: 2016-07-28T11:49:10Z Publisher: IOC-UNESCO.
- Benoit-Bird, K. J. and Lawson, G. L. (2016). Ecological Insights from Pelagic Habitats Acquired Using Active Acoustic Techniques. *Annual Review of Marine Science*, 8(1):463–490. _eprint: <https://doi.org/10.1146/annurev-marine-122414-034001>.

- Bograd, S. J., Jacox, M. G., Hazen, E. L., Lovecchio, E., Montes, I., Pozo Buil, M., Shannon, L. J., Sydeman, W. J., and Rykaczewski, R. R. (2023). Climate Change Impacts on Eastern Boundary Upwelling Systems. *Annual Review of Marine Science*, 15(1):null. _eprint: <https://doi.org/10.1146/annurev-marine-032122-021945>.
- Bopp, L., Aumont, O., Kwiatkowski, L., Clerc, C., Dupont, L., Ethé, C., Gorgues, T., Sférian, R., and Tagliabue, A. (2022). Diazotrophy as a key driver of the response of marine net primary productivity to climate change. *Biogeosciences*, 19(17):4267–4285. Publisher: Copernicus GmbH.
- Botsford, L. W., Lawrence, C. A., Dever, E. P., Hastings, A., and Largier, J. (2003). Wind strength and biological productivity in upwelling systems: an idealized study. *Fisheries Oceanography*, 12(4-5):245–259. _eprint: <https://onlinelibrary.wiley.com/doi/pdf/10.1046/j.1365-2419.2003.00265.x>.
- Botsford, L. W., Lawrence, C. A., Dever, E. P., Hastings, A., and Largier, J. (2006). Effects of variable winds on biological productivity on continental shelves in coastal upwelling systems. *Deep Sea Research Part II: Topical Studies in Oceanography*, 53(25-26):3116–3140.
- Brink, K., Jones, B., Van Leer, J., Mooers, C., Stuart, D., Stevenson, M., Dugdale, R., and Heburn, G. (1981). Physical and Biological Structure and Variability in an Upwelling Center off Peru Near 15°S During March, 1977. In *Coastal Upwelling*, pages 473–495. American Geophysical Union (AGU). _eprint: <https://onlinelibrary.wiley.com/doi/pdf/10.1029/CO001p0473>.
- Brochier, T., Auger, P.-A., Pecquerie, L., Machu, E., Capet, X., Thiaw, M., Mbaye, B. C., Braham, C.-B., Ettahiri, O., Charouki, N., Sène, O. N., Werner, F., and Brehmer, P. (2018). Complex small pelagic fish population patterns arising from individual behavioral responses to their environment. *Progress in Oceanography*, 164:12–27.
- Cambon, G. (2008). *Etude numérique de la mer d'Iroise : dynamique, variabilité du front d'Ouessant et évaluation des échanges cross-frontaux*. phdthesis, Université de Bretagne occidentale - Brest.
- Capet, X., Campos, E. J., and Paiva, A. M. (2008a). Submesoscale activity over the Argentinian shelf. *Geophysical Research Letters*, 35(15). _eprint: <https://onlinelibrary.wiley.com/doi/pdf/10.1029/2008GL034736>.
- Capet, X., Estrade, P., Machu, E., Ndoye, S., Grelet, J., Lazar, A., Marié, L., Dausse, D., and Brehmer, P. (2017). On the Dynamics of the Southern Senegal Upwelling Center: Observed Variability from Synoptic to Superinertial Scales. *Journal of Physical Oceanography*, 47(1):155–180. Publisher: American Meteorological Society Section: Journal of Physical Oceanography.
- Capet, X., McWilliams, J. C., Molemaker, M. J., and Shchepetkin, A. F. (2008b). Mesoscale to Submesoscale Transition in the California Current System. Part I: Flow Structure, Eddy Flux, and Observational Tests. *Journal of Physical Oceanography*, 38(1):29–43. Publisher: American Meteorological Society.

- Capet, X., McWilliams, J. C., Molemaker, M. J., and Shchepetkin, A. F. (2008c). Mesoscale to Submesoscale Transition in the California Current System. Part II: Frontal Processes. *Journal of Physical Oceanography*, 38(1):44–64. Publisher: American Meteorological Society Section: Journal of Physical Oceanography.
- Capet, X. J., Marchesiello, P., and McWilliams, J. C. (2004). Upwelling response to coastal wind profiles. *Geophysical Research Letters*, 31(13). _eprint: <https://agupubs.onlinelibrary.wiley.com/doi/pdf/10.1029/2004GL020123>.
- Carr, S. D., Capet, X. J., McWilliams, J. C., Pennington, J. T., and Chavez, F. P. (2008). The influence of diel vertical migration on zooplankton transport and recruitment in an upwelling region: estimates from a coupled behavioral-physical model. *Fisheries Oceanography*, 17(1):1–15. _eprint: <https://onlinelibrary.wiley.com/doi/pdf/10.1111/j.1365-2419.2007.00447.x>.
- Carton, J. A. and Giese, B. S. (2008). A Reanalysis of Ocean Climate Using Simple Ocean Data Assimilation (SODA). *Monthly Weather Review*, 136(8):2999–3017. Publisher: American Meteorological Society Section: Monthly Weather Review.
- Cassou, C., Terray, L., Hurrell, J. W., and Deser, C. (2004). North Atlantic Winter Climate Regimes: Spatial Asymmetry, Stationarity with Time, and Oceanic Forcing. *Journal of Climate*, 17(5):1055–1068. Publisher: American Meteorological Society Section: Journal of Climate.
- Chabert, P., d'Ovidio, E., Echevin, V., Stukel, M. R., and Ohman, M. D. (2021). Cross-Shore Flow and Implications for Carbon Export in the California Current Ecosystem: A Lagrangian Analysis. *Journal of Geophysical Research: Oceans*, 126(2):e2020JC016611. _eprint: <https://onlinelibrary.wiley.com/doi/pdf/10.1029/2020JC016611>.
- Chavez, F. P. and Messié, M. (2009). A comparison of Eastern Boundary Upwelling Ecosystems. *Progress in Oceanography*, 83(1):80–96.
- Chavez, F. P., Pennington, J. T., Castro, C. G., Ryan, J. P., Michisaki, R. P., Schlining, B., Walz, P., Buck, K. R., McFadyen, A., and Collins, C. A. (2002). Biological and chemical consequences of the 1997–1998 El Niño in central California waters. *Progress in Oceanography*, 54(1):205–232.
- Checkley, D. M., Asch, R. G., and Rykaczewski, R. R. (2017). Climate, Anchovy, and Sardine. *Annual Review of Marine Science*, 9(1):469–493. _eprint: <https://doi.org/10.1146/annurev-marine-122414-033819>.
- Chelton, D. B. (1982). Large-scale Response of the California Current to Forcing by the Wind Stress Curl. *CalCOFI Rep.*, XXIII:19.
- Chenillat, F., Franks, P. J. S., and Combes, V. (2016). Biogeochemical properties of eddies in the California Current System. *Geophysical Research Letters*, 43(11):5812–5820. _eprint: <https://onlinelibrary.wiley.com/doi/pdf/10.1002/2016GL068945>.

- Chenillat, F., Rivière, P., Capet, X., Franks, P. J. S., and Blanke, B. (2013). California Coastal Upwelling Onset Variability: Cross-Shore and Bottom-Up Propagation in the Planktonic Ecosystem. *PLOS ONE*, 8(5):e62281. Publisher: Public Library of Science.
- Chenillat, F., Rivière, P., and Ohman, M. D. (2021). On the sensitivity of plankton ecosystem models to the formulation of zooplankton grazing. *PLOS ONE*, 16(5):e0252033. Publisher: Public Library of Science.
- Chiang, J. C. H. and Bitz, C. M. (2005). Influence of high latitude ice cover on the marine Intertropical Convergence Zone. *Climate Dynamics*, 25(5):477–496.
- Chisholm, S. W. (1992). Phytoplankton Size. In Falkowski, P. G., Woodhead, A. D., and Vivirito, K., editors, *Primary Productivity and Biogeochemical Cycles in the Sea*, Environmental Science Research, pages 213–237. Springer US, Boston, MA.
- Christensen, J. P., Murray, J. W., Devol, A. H., and Codispoti, L. A. (1987). Denitrification in continental shelf sediments has major impact on the oceanic nitrogen budget. *Global Biogeochemical Cycles*, 1(2):97–116. _eprint: <https://onlinelibrary.wiley.com/doi/pdf/10.1029/GB001i002p00097>.
- Chust, G., Allen, J. I., Bopp, L., Schrum, C., Holt, J., Tsiaras, K., Zavatarelli, M., Chifflet, M., Cannaby, H., Dadou, I., Daewel, U., Wakelin, S. L., Machu, E., Pushpadas, D., Butenschon, M., Artioli, Y., Petihakis, G., Smith, C., Garçon, V., Goubanova, K., Le Vu, B., Fach, B. A., Salihoglu, B., Clementi, E., and Irigoien, X. (2014). Biomass changes and trophic amplification of plankton in a warmer ocean. *Global Change Biology*, 20(7):2124–2139. _eprint: <https://onlinelibrary.wiley.com/doi/pdf/10.1111/gcb.12562>.
- Citeau, J., Finaud, L., Cammas, J. P., and Demarcq, H. (1989). Questions relative to ITCZ migrations over the tropical Atlantic ocean, sea surface temperature and Senegal River runoff. *Meteorology and Atmospheric Physics*, 41(4):181–190.
- Colas, F., Capet, X., McWilliams, J. C., and Li, Z. (2013). Mesoscale Eddy Buoyancy Flux and Eddy-Induced Circulation in Eastern Boundary Currents. *Journal of Physical Oceanography*, 43(6):1073–1095. Publisher: American Meteorological Society Section: Journal of Physical Oceanography.
- Colas, F., McWilliams, J. C., Capet, X., and Kurian, J. (2012). Heat balance and eddies in the Peru-Chile current system. *Climate Dynamics*, 39(1):509–529.
- Cordeiro, N. G. F., Dubert, J., Nolasco, R., and Barton, E. D. (2018). Transient response of the Northwestern Iberian upwelling regime. *PLOS ONE*, 13(5):e0197627. Publisher: Public Library of Science.
- Correa, K., Machu, E., Demarcq, H., and Diouf, D. (2021). Neural-variational algorithm adaptation from SeaWiFS to MODIS sensor for analysis of atmospheric and oceanic parameters. Technical Report EGU21-15934, Copernicus Meetings. Conference Name: EGU21.

- Cox, M. D. (1985). An Eddy Resolving Numerical Model of the Ventilated Thermocline. *Journal of Physical Oceanography*, 15(10):1312–1324. Publisher: American Meteorological Society Section: Journal of Physical Oceanography.
- Crépon, M., Richez, C., and Chartier, M. (1984). Effects of Coastline Geometry on Upwellings. *Journal of Physical Oceanography*, 14(8):1365–1382. Publisher: American Meteorological Society Section: Journal of Physical Oceanography.
- Curcic, M., Chen, S. S., and Özgökmen, T. M. (2016). Hurricane-induced ocean waves and stokes drift and their impacts on surface transport and dispersion in the Gulf of Mexico. *Geophysical Research Letters*, 43(6):2773–2781. _eprint: <https://onlinelibrary.wiley.com/doi/pdf/10.1002/2015GL067619>.
- Cury, P., Bakun, A., Crawford, R. J. M., Jarre, A., Quiñones, R. A., Shannon, L. J., and Verheye, H. M. (2000). Small pelagics in upwelling systems: patterns of interaction and structural changes in “wasp-waist” ecosystems. *ICES Journal of Marine Science*, 57(3):603–618.
- Cury, P. and Roy, C. (1989). Optimal Environmental Window and Pelagic Fish Recruitment Success in Upwelling Areas. *Canadian Journal of Fisheries and Aquatic Sciences*, 46(4):670–680.
- Cushing, D. H. (1971). Upwelling and the Production of Fish. In Russell, F. S. and Yonge, M., editors, *Advances in Marine Biology*, volume 9, pages 255–334. Academic Press.
- Cushman-Roisin, B. and Beckers, J.-M. (2011). *Introduction to Geophysical Fluid Dynamics: Physical and Numerical Aspects*. Academic Press.
- de Boyer Montégut, C., Madec, G., Fischer, A. S., Lazar, A., and Iudicone, D. (2004). Mixed layer depth over the global ocean: An examination of profile data and a profile-based climatology. *Journal of Geophysical Research: Oceans*, 109(C12). _eprint: <https://onlinelibrary.wiley.com/doi/pdf/10.1029/2004JC002378>.
- Debreu, L. and Blayo, E. (2008). Two-way embedding algorithms: a review. *Ocean Dynamics*, 58(5):415–428.
- Debreu, L., Marchesiello, P., Penven, P., and Cambon, G. (2012). Two-way nesting in split-explicit ocean models: Algorithms, implementation and validation. *Ocean Modelling*, 49:1–21.
- Debreu, L., Vouland, C., and Blayo, E. (2008). AGRIF: Adaptive grid refinement in Fortran. *Computers & Geosciences*, 34(1):8–13.
- Della Penna, A. and Gaube, P. (2020). Mesoscale Eddies Structure Mesopelagic Communities. *Frontiers in Marine Science*, 7.
- Desbiolles, F., Blanke, B., and Bentamy, A. (2014). Short-term upwelling events at the western African coast related to synoptic atmospheric structures as derived from satellite observations. *Journal of Geophysical Research: Oceans*, 119(1):461–483. _eprint: <https://onlinelibrary.wiley.com/doi/pdf/10.1002/2013JC009278>.

- Deshayes, J., Curry, R., and Msadek, R. (2014). CMIP5 Model Intercomparison of Freshwater Budget and Circulation in the North Atlantic. *Journal of Climate*, 27(9):3298–3317. Publisher: American Meteorological Society Section: Journal of Climate.
- Deutsch, C., Frenzel, H., McWilliams, J. C., Renault, L., Kessouri, F., Howard, E., Liang, J.-H., Bianchi, D., and Yang, S. (2021). Biogeochemical variability in the California Current System. *Progress in Oceanography*, 196:102565.
- Di Lorenzo, E. and Ohman, M. D. (2013). A double-integration hypothesis to explain ocean ecosystem response to climate forcing. *Proceedings of the National Academy of Sciences*, 110(7):2496–2499. Publisher: Proceedings of the National Academy of Sciences.
- Dong, J., Fox-Kemper, B., Zhang, H., and Dong, C. (2020). The Scale of Submesoscale Baroclinic Instability Globally. *Journal of Physical Oceanography*, 50(9):2649–2667. Publisher: American Meteorological Society Section: Journal of Physical Oceanography.
- Dorman, J., Bollens, S., and Slaughter, A. (2005). Population biology of euphausiids off northern California and effects of short time-scale wind events on *Euphausia pacifica*. *Marine Ecology Progress Series*, 288:183–198.
- Dugdale, R. C. and Goering, J. J. (1967). Uptake of New and Regenerated forms of Nitrogen in Primary Productivity. *Limnology and Oceanography*, 12(2):196–206.
- d'Ovidio, F., De Monte, S., Alvain, S., Dandonneau, Y., and Lévy, M. (2010). Fluid dynamical niches of phytoplankton types. *Proceedings of the National Academy of Sciences*, 107(43):18366–18370. Publisher: Proceedings of the National Academy of Sciences.
- Echevin, V., Colas, F., Espinoza-Morriberon, D., Vasquez, L., Anculle, T., and Gutierrez, D. (2018). Forcings and Evolution of the 2017 Coastal El Niño Off Northern Peru and Ecuador. *Frontiers in Marine Science*, 5:367.
- Echevin, V., Hauschildt, J., Colas, F., Thomsen, S., and Aumont, O. (2021). Impact of Chlorophyll Shading on the Peruvian Upwelling System. *Geophysical Research Letters*, 48(19):e2021GL094429. _eprint: <https://onlinelibrary.wiley.com/doi/pdf/10.1029/2021GL094429>.
- Eppley, R. W. and Peterson, B. J. (1979). Particulate organic matter flux and planktonic new production in the deep ocean. *Nature*, 282(5740):677–680. Number: 5740 Publisher: Nature Publishing Group.
- Estrade, P., Marchesiello, P., De Verdière, A. C., and Roy, C. (2008). Cross-shelf structure of coastal upwelling: A two dimensional extension of Ekman's theory and a mechanism for inner shelf upwelling shut down. *Journal of Marine Research*, 66(5):589–616.
- Evans, W., Hales, B., Strutton, P. G., Shearman, R. K., and Barth, J. A. (2015). Failure to bloom: Intense upwelling results in negligible phytoplankton response and prolonged CO₂ outgassing over the Oregon shelf. *Journal of Geophysical Research: Oceans*, 120(3):1446–1461. _eprint: <https://onlinelibrary.wiley.com/doi/pdf/10.1002/2014JC010580>.

- Falkowski, P. G., Laws, E. A., Barber, R. T., and Murray, J. W. (2003). Phytoplankton and Their Role in Primary, New, and Export Production. In Fasham, M. J. R., editor, *Ocean Biogeochemistry: The Role of the Ocean Carbon Cycle in Global Change*, Global Change The IGBP Series (closed), pages 99–121. Springer, Berlin, Heidelberg.
- Farikou, O., Sawadogo, S., Niang, A., Diouf, D., Brajard, J., Mejia, C., Dandonneau, Y., Gasc, G., Crepon, M., and Thiria, S. (2015). Inferring the seasonal evolution of phytoplankton groups in the Senegalo-Mauritanian upwelling region from satellite ocean-color spectral measurements. *Journal of Geophysical Research: Oceans*, 120(9):6581–6601. _eprint: <https://onlinelibrary.wiley.com/doi/pdf/10.1002/2015JC010738>.
- Farneti, R., Delworth, T. L., Rosati, A. J., Griffies, S. M., and Zeng, F. (2010). The Role of Mesoscale Eddies in the Rectification of the Southern Ocean Response to Climate Change. *Journal of Physical Oceanography*, 40(7):1539–1557. Publisher: American Meteorological Society Section: Journal of Physical Oceanography.
- Fearon, G., Herbette, S., Veitch, J., Cambon, G., Lucas, A. J., Lemarié, F., and Vichi, M. (2020). Enhanced Vertical Mixing in Coastal Upwelling Systems Driven by Diurnal-Inertial Resonance: Numerical Experiments. *Journal of Geophysical Research: Oceans*, 125(9):e2020JC016208. _eprint: <https://onlinelibrary.wiley.com/doi/pdf/10.1029/2020JC016208>.
- Flato, G. M. and Boer, G. J. (2001). Warming asymmetry in climate change simulations. *Geophysical Research Letters*, 28(1):195–198. _eprint: <https://onlinelibrary.wiley.com/doi/pdf/10.1029/2000GL012121>.
- Flynn, K. J. (2005). Castles built on sand: dysfunctionality in plankton models and the inadequacy of dialogue between biologists and modellers. *Journal of Plankton Research*, 27(12):1205–1210.
- Fox-Kemper, B., Ferrari, R., and Hallberg, R. (2008). Parameterization of Mixed Layer Eddies. Part I: Theory and Diagnosis. *Journal of Physical Oceanography*, 38(6):1145–1165. Publisher: American Meteorological Society Section: Journal of Physical Oceanography.
- Frankignoul, C. and Hasselmann, K. (1977). Stochastic climate models, Part II Application to sea-surface temperature anomalies and thermocline variability. *Tellus*, 29(4):289–305. Publisher: Taylor & Francis _eprint: <https://doi.org/10.3402/tellusa.v29i4.11362>.
- Franks, P. J. S. (2002). NPZ Models of Plankton Dynamics: Their Construction, Coupling to Physics, and Application. *Journal of Oceanography*, 58(2):379–387.
- Franks, P. J. S. (2009). Planktonic ecosystem models: perplexing parameterizations and a failure to fail. *Journal of Plankton Research*, 31(11):1299–1306.
- Fréon, P., Barange, M., and Arístegui, J. (2009). Eastern Boundary Upwelling Ecosystems: Integrative and comparative approaches. *Progress in Oceanography*, 83(1):1–14.
- Gan, J. and Allen, J. (2005a). On open boundary conditions for a limited-area coastal model off Oregon. Part 1: Response to idealized wind forcing. *Ocean Modelling*, 8(1-2):115–133.

- Gan, J. and Allen, J. S. (2002a). A modeling study of shelf circulation off northern California in the region of the Coastal Ocean Dynamics Experiment 2. Simulations and comparisons with observations. *Journal of Geophysical Research: Oceans*, 107(C11):5–1–5–21. _eprint: <https://onlinelibrary.wiley.com/doi/pdf/10.1029/2001JC001190>.
- Gan, J. and Allen, J. S. (2002b). A modeling study of shelf circulation off northern California in the region of the Coastal Ocean Dynamics Experiment: Response to relaxation of upwelling winds. *Journal of Geophysical Research: Oceans*, 107(C9):6–1–6–31. _eprint: <https://onlinelibrary.wiley.com/doi/pdf/10.1029/2000JC000768>.
- Gan, J. and Allen, J. S. (2005b). Modeling upwelling circulation off the Oregon coast. *Journal of Geophysical Research: Oceans*, 110(C10). _eprint: <https://onlinelibrary.wiley.com/doi/pdf/10.1029/2004JC002692>.
- Garcia, H. E., Weathers, K., Paver, C. R., Smolyar, I., Boyer, T. P., Locarnini, R. A., Zweng, M. M., Mishonov, A. V., Baranova, O. K., Seidov, D., and Reagan, J. (2018). World Ocean Atlas 2018. Volume 4: Dissolved Inorganic Nutrients (phosphate, nitrate and nitrate+nitrite, silicate). *NOAA National Centers for Environmental Information. A. Mishonov Technical Ed.; NOAA Atlas NESDIS 84*. type: dataset.
- García-Reyes, M., Largier, J. L., and Sydeman, W. J. (2014). Synoptic-scale upwelling indices and predictions of phyto- and zooplankton populations. *Progress in Oceanography*, 120:177–188.
- García-Reyes, M., Sydeman, W. J., Schoeman, D. S., Rykaczewski, R. R., Black, B. A., Smit, A. J., and Bograd, S. J. (2015). Under Pressure: Climate Change, Upwelling, and Eastern Boundary Upwelling Ecosystems. *Frontiers in Marine Science*, 2.
- Garibaldi, L. (2012). The FAO global capture production database: A six-decade effort to catch the trend. *Marine Policy*, 36(3):760–768.
- Garstang, M. (1967). Sensible and latent heat exchange in low latitude synoptic scale systems. *Tellus*, 19(3):492–508. _eprint: <https://onlinelibrary.wiley.com/doi/pdf/10.1111/j.2153-3490.1967.tb01504.x>.
- Gaube, P., Braun, C. D., Lawson, G. L., McGillicuddy, D. J., Penna, A. D., Skomal, G. B., Fischer, C., and Thorrold, S. R. (2018). Mesoscale eddies influence the movements of mature female white sharks in the Gulf Stream and Sargasso Sea. *Scientific Reports*, 8(1):7363. Number: 1 Publisher: Nature Publishing Group.
- Gobler, C. J. (2020). Climate Change and Harmful Algal Blooms: Insights and perspective. *Harmful Algae*, 91:101731.
- Gohin, F., Druon, J. N., and Lampert, L. (2002). A five channel chlorophyll concentration algorithm applied to SeaWiFS data processed by SeaDAS in coastal waters. *International Journal of Remote Sensing*, 23(8):1639–1661. Publisher: Taylor & Francis _eprint: <https://doi.org/10.1080/01431160110071879>.

- Gorgues, T., Aumont, O., and Memery, L. (2019). Simulated Changes in the Particulate Carbon Export Efficiency due to Diel Vertical Migration of Zooplankton in the North Atlantic. *Geophysical Research Letters*, 46(10):5387–5395. _eprint: <https://onlinelibrary.wiley.com/doi/pdf/10.1029/2018GL081748>.
- Graham, W. M. and Largier, J. L. (1997). Upwelling shadows as nearshore retention sites: the example of northern Monterey Bay. *Continental Shelf Research*, 17(5):509–532.
- Gruber, N., Lachkar, Z., Frenzel, H., Marchesiello, P., Münnich, M., McWilliams, J. C., Nagai, T., and Plattner, G.-K. (2011). Eddy-induced reduction of biological production in eastern boundary upwelling systems. *Nature Geoscience*, 4(11):787–792.
- Harrison, W., Platt, T., and Lewis, M. R. (1987). f -Ratio and its relationship to ambient nitrate concentration in coastal waters. *Journal of Plankton Research*, 9(1):235–248.
- Hauschildt, J., Thomsen, S., Echevin, V., Oeschies, A., José, Y. S., Krahmann, G., Bristow, L. A., and Lavik, G. (2021). The fate of upwelled nitrate off Peru shaped by submesoscale filaments and fronts. *Biogeosciences*, 18(12):3605–3629. Publisher: Copernicus GmbH.
- Hersbach, H., Bell, B., Berrisford, P., Biavati, G., Horányi, A., Muñoz Sabater, J., Nicolas, J., Peubey, C., Radu, R., Rozum, I., Schepers, D., Simmons, A., Soci, C., Dee, D., and Thépaut, J.-N. (2018). ERA5 hourly data on single levels from 1979 to present. Copernicus Climate Change Service (C3S) Climate Data Store (CDS).
- Hetland, R. D. (2017). Suppression of Baroclinic Instabilities in Buoyancy-Driven Flow over Sloping Bathymetry. *Journal of Physical Oceanography*, 47(1):49–68. Publisher: American Meteorological Society Section: Journal of Physical Oceanography.
- Hickey, B. M. and Banas, N. S. (2008). Why is the Northern End of the California Current System So Productive? *Oceanography*, 21(4):90–107. Publisher: Oceanography Society.
- Hilt, M., Auclair, F., Benshila, R., Bordoïs, L., Capet, X., Debreu, L., Dumas, E., Jullien, S., Lemarié, E., Marchesiello, P., Nguyen, C., and Roblou, L. (2020). Numerical modelling of hydraulic control, solitary waves and primary instabilities in the Strait of Gibraltar. *Ocean Modelling*, 151:101642.
- Hong, C.-C., Li, T., LinHo, and Kug, J.-S. (2008). Asymmetry of the Indian Ocean Dipole. Part I: Observational Analysis. *Journal of Climate*, 21(18):4834–4848. Publisher: American Meteorological Society Section: Journal of Climate.
- Huisman, J. and Weissing, F. J. (1999). Biodiversity of plankton by species oscillations and chaos. *Nature*, 402(6760):407–410. Number: 6760 Publisher: Nature Publishing Group.
- Hutchings, L., Pitcher, G., Probyn, T., and Bailey, G. (1995). The chemical and biological consequences of coastal upwelling. pages 65–81.

- Hutchings, L., Verheye, H. M., Huggett, J. A., Demarcq, H., Cloete, R., Barlow, R. G., Louw, D., and Silva, A. d. (2006). 6 Variability of plankton with reference to fish variability in the Benguela current large marine ecosystemAn overview. In Shannon, V., Hempel, G., Malanotte-Rizzoli, P., Moloney, C., and Woods, J., editors, *Large Marine Ecosystems*, volume 14 of *Benguela*, pages 91–124. Elsevier.
- Hutchins, D. A. and Bruland, K. W. (1998). Iron-limited diatom growth and Si:N uptake ratios in a coastal upwelling regime. *Nature*, 393(6685):561–564. Number: 6685 Publisher: Nature Publishing Group.
- Hutchinson, G. E. (1961). The Paradox of the Plankton. *The American Naturalist*, 95(882):137–145. Publisher: The University of Chicago Press.
- Irigoien, X., Flynn, K. J., and Harris, R. P. (2005). Phytoplankton blooms: a ‘loophole’ in micro-zooplankton grazing impact? *Journal of Plankton Research*, 27(4):313–321.
- Jacox, M. G. and Edwards, C. A. (2011). Effects of stratification and shelf slope on nutrient supply in coastal upwelling regions. *Journal of Geophysical Research: Oceans*, 116(C3). _eprint: <https://onlinelibrary.wiley.com/doi/pdf/10.1029/2010JC006547>.
- Jacox, M. G., Edwards, C. A., Hazen, E. L., and Bograd, S. J. (2018). Coastal Upwelling Revisited: Ekman, Bakun, and Improved Upwelling Indices for the U.S. West Coast. *Journal of Geophysical Research: Oceans*, 123(10):7332–7350. _eprint: <https://agupubs.onlinelibrary.wiley.com/doi/pdf/10.1029/2018JC014187>.
- Jacox, M. G., Fiechter, J., Moore, A. M., and Edwards, C. A. (2015). ENSO and the California Current coastal upwelling response. *Journal of Geophysical Research: Oceans*, 120(3):1691–1702. _eprint: <https://onlinelibrary.wiley.com/doi/pdf/10.1002/2014JC010650>.
- Jacox, M. G., Hazen, E. L., and Bograd, S. J. (2016). Optimal Environmental Conditions and Anomalous Ecosystem Responses: Constraining Bottom-up Controls of Phytoplankton Biomass in the California Current System. *Scientific Reports*, 6(1):27612. Number: 1 Publisher: Nature Publishing Group.
- Jentsch, A., Kreyling, J., and Beierkuhnlein, C. (2007). A new generation of climate-change experiments: events, not trends. *Frontiers in Ecology and the Environment*, 5(7):365–374. _eprint: <https://onlinelibrary.wiley.com/doi/pdf/10.1890/1540-9295%282007%295%5B365%3AANGOCE%5D2.0.CO%3B2>.
- Jones, B. H., Brink, K. H., Dugdale, R. C., Stuart, D. W., Van Leer, J. C., Blasco, D., and Kelley, J. C. (1983). Observations of a Persistent Upwelling Center off Point Conception, California. In Suess, E. and Thiede, J., editors, *Coastal Upwelling Its Sediment Record: Part A: Responses of the Sedimentary Regime to Present Coastal Upwelling*, NATO Conference Series, pages 37–60. Springer US, Boston, MA.

- Jullien, S., Menkes, C. E., Marchesiello, P., Jourdain, N. C., Lengaigne, M., Koch-Larrouy, A., Lefèvre, J., Vincent, E. M., and Faure, V. (2012). Impact of Tropical Cyclones on the Heat Budget of the South Pacific Ocean. *Journal of Physical Oceanography*, 42(11):1882–1906. Publisher: American Meteorological Society Section: Journal of Physical Oceanography.
- Jury, M. R. (1988). A climatological mechanism for wind-driven upwelling near Walker Bay and Danger Point, South Africa. *South African Journal of Marine Science*, 6(1):175–181.
- Kahru, M., Kudela, R., ManzanoSarabia, M., and Mitchell, B. G. (2009). Trends in primary production in the California Current detected with satellite data. *Journal of Geophysical Research: Oceans*, 114(C2). _eprint: <https://agupubs.onlinelibrary.wiley.com/doi/pdf/10.1029/2008JC004979>.
- Kahru, M., Kudela, R. M., Anderson, C. R., and Mitchell, B. G. (2015). Optimized Merger of Ocean Chlorophyll Algorithms of MODIS-Aqua and VIIRS. *IEEE Geoscience and Remote Sensing Letters*, 12(11):2282–2285. Conference Name: IEEE Geoscience and Remote Sensing Letters.
- Karl, D., Letelier, R., Tupas, L., Dore, J., Christian, J., and Hebel, D. (1997). The role of nitrogen fixation in biogeochemical cycling in the subtropical North Pacific Ocean. *Nature*, 388(6642):533–538. Number: 6642 Publisher: Nature Publishing Group.
- Kessouri, F., Bianchi, D., Renault, L., McWilliams, J. C., Frenzel, H., and Deutsch, C. A. (2020). Submesoscale Currents Modulate the Seasonal Cycle of Nutrients and Productivity in the California Current System. *Global Biogeochemical Cycles*, 34(10):e2020GB006578. _eprint: <https://onlinelibrary.wiley.com/doi/pdf/10.1029/2020GB006578>.
- Kessouri, F., McWilliams, J. C., Bianchi, D., Sutula, M., Renault, L., Deutsch, C., Feely, R. A., McLaughlin, K., Ho, M., Howard, E. M., Bednaršek, N., Damien, P., Molemaker, J., and Weisberg, S. B. (2021). Coastal eutrophication drives acidification, oxygen loss, and ecosystem change in a major oceanic upwelling system. *Proceedings of the National Academy of Sciences*, 118(21):e2018856118. Publisher: Proceedings of the National Academy of Sciences.
- Key, R. M., Kozyr, A., Sabine, C. L., Lee, K., Wanninkhof, R., Bullister, J. L., Feely, R. A., Millero, F. J., Mordy, C., and Peng, T.-H. (2004). A global ocean carbon climatology: Results from Global Data Analysis Project (GLODAP). *Global Biogeochemical Cycles*, 18(4). _eprint: <https://onlinelibrary.wiley.com/doi/pdf/10.1029/2004GB002247>.
- Killworth, P. D. (1983). Deep convection in the World Ocean. *Reviews of Geophysics*, 21(1):1–26. _eprint: <https://onlinelibrary.wiley.com/doi/pdf/10.1029/RG021i001p00001>.
- Klenz, T., Dengler, M., and Brandt, P. (2018). Seasonal Variability of the Mauritania Current and Hydrography at 18°N. *Journal of Geophysical Research: Oceans*, 123(11):8122–8137. _eprint: <https://onlinelibrary.wiley.com/doi/pdf/10.1029/2018JC014264>.
- Kobashi, D. and Hetland, R. (2020). Reproducibility and variability of submesoscale frontal eddies on a broad, low-energy shelf of freshwater influence. *Ocean Dynamics*, 70(11):1377–1395.

- Kounta Diop, L. (2019). *Le rôle de la dynamique océanique et atmosphérique en Atlantique Nord sur le fonctionnement de l'upwelling ouest-africain*. These de doctorat, Sorbonne université.
- Kudela, R. M., Garfield, N., and Bruland, K. W. (2006). Bio-optical signatures and biogeochemistry from intense upwelling and relaxation in coastal California. *Deep Sea Research Part II: Topical Studies in Oceanography*, 53(25):2999–3022.
- Kudela, R. M., Pitcher, G. C., Probyn, T., Figueiras, F. G., Moita, M. T., and Trainer, V. (2005). Harmful algal blooms in coastal upwelling systems. Accepted: 2022-08-26T11:12:41Z Publisher: Oceanography Society.
- Kuebel Cervantes, B. T. and Allen, J. S. (2006). Numerical model simulations of continental shelf flows off northern California. *Deep Sea Research Part II: Topical Studies in Oceanography*, 53(25):2956–2984.
- Kwiatkowski, L., Aumont, O., Bopp, L., and Ciais, P. (2018). The Impact of Variable Phytoplankton Stoichiometry on Projections of Primary Production, Food Quality, and Carbon Uptake in the Global Ocean. *Global Biogeochemical Cycles*, 32(4):516–528. _eprint: <https://onlinelibrary.wiley.com/doi/pdf/10.1002/2017GB005799>.
- Lachkar, Z. and Gruber, N. (2011). What controls biological production in coastal upwelling systems? Insights from a comparative modeling study. *Biogeosciences*, 8(10):2961–2976. Publisher: Copernicus GmbH.
- Lapeyre, G. and Klein, P. (2006). Impact of the small-scale elongated filaments on the oceanic vertical pump. *Journal of Marine Research*, 64(6):835–851.
- Large, W. G., McWilliams, J. C., and Doney, S. C. (1994). Oceanic vertical mixing: A review and a model with a nonlocal boundary layer parameterization. *Reviews of Geophysics*, 32(4):363–403. _eprint: <https://onlinelibrary.wiley.com/doi/pdf/10.1029/94RG01872>.
- Largier, J. L. (2020). Upwelling Bays: How Coastal Upwelling Controls Circulation, Habitat, and Productivity in Bays. *Annual Review of Marine Science*, 12(1):415–447. _eprint: <https://doi.org/10.1146/annurev-marine-010419-011020>.
- Largier, J. L., Lawrence, C. A., Roughan, M., Kaplan, D. M., Dever, E. P., Dorman, C. E., Kudela, R. M., Bollens, S. M., Wilkerson, F. P., Dugdale, R. C., Botsford, L. W., Garfield, N., Kuebel Cervantes, B., and Koračin, D. (2006). WEST: A northern California study of the role of wind-driven transport in the productivity of coastal plankton communities. *Deep Sea Research Part II: Topical Studies in Oceanography*, 53(25):2833–2849.
- Lasker, R. and Zweifel, J. R. (1978). Growth and Survival of First-Feeding Northern Anchovy Larvae (*Engraulis mordax*) in Patches Containing Different Proportions of Large and Small Prey. In Steele, J. H., editor, *Spatial Pattern in Plankton Communities*, NATO Conference Series, pages 329–354. Springer US, Boston, MA.
- Lathuilière, C. (2008). *Echanges côtes-large et propriétés biogéochimiques dans les régions d'upwelling de bord Est*. phdthesis, Université Pierre et Marie Curie - Paris VI.

- Lathuilière, C., Echevin, V., and Lévy, M. (2008). Seasonal and intraseasonal surface chlorophyll-a variability along the northwest African coast. *Journal of Geophysical Research: Oceans*, 113(C5). _eprint: <https://onlinelibrary.wiley.com/doi/pdf/10.1029/2007JC004433>.
- Lehner, F., Deser, C., and Terray, L. (2017). Toward a New Estimate of “Time of Emergence” of Anthropogenic Warming: Insights from Dynamical Adjustment and a Large Initial-Condition Model Ensemble. *Journal of Climate*, 30(19):7739–7756. Publisher: American Meteorological Society Section: Journal of Climate.
- Lentz, S. J. (1987). A heat budget for the Northern California Shelf during CODE 2. *Journal of Geophysical Research: Oceans*, 92(C13):14491–14509. _eprint: <https://onlinelibrary.wiley.com/doi/pdf/10.1029/JC092iC13p14491>.
- Lomas, M. W. and Glibert, P. M. (1999). Temperature regulation of nitrate uptake: A novel hypothesis about nitrate uptake and reduction in cool-water diatoms. *Limnology and Oceanography*, 44(3):556–572. _eprint: <https://onlinelibrary.wiley.com/doi/pdf/10.4319/lo.1999.44.3.0556>.
- Lombard, F., Boss, E., Waite, A. M., Vogt, M., Uitz, J., Stemmann, L., Sosik, H. M., Schulz, J., Romagnan, J.-B., Picheral, M., Pearlman, J., Ohman, M. D., Niehoff, B., Möller, K. O., Miloslavich, P., Lara-Lpez, A., Kudela, R., Lopes, R. M., Kiko, R., Karp-Boss, L., Jaffe, J. S., Iversen, M. H., Irisson, J.-O., Fennel, K., Hauss, H., Guidi, L., Gorsky, G., Giering, S. L. C., Gaube, P., Gallager, S., Dubelaar, G., Cowen, R. K., Carlotti, F., Briseño-Avena, C., Berline, L., Benoit-Bird, K., Bax, N., Batten, S., Ayata, S. D., Artigas, L. F., and Appeltans, W. (2019). Globally Consistent Quantitative Observations of Planktonic Ecosystems. *Frontiers in Marine Science*, 6.
- Lopes, J. F., Ferreira, J. A., Cardoso, A. C., and Rocha, A. C. (2014). Variability of temperature and chlorophyll of the Iberian Peninsula near costal ecosystem during an upwelling event for the present climate and a future climate scenario. *Journal of Marine Systems*, 129:271–288.
- Lorenzo, E. D., Miller, A. J., Schneider, N., and McWilliams, J. C. (2005). The Warming of the California Current System: Dynamics and Ecosystem Implications. *Journal of Physical Oceanography*, 35(3):336–362. Publisher: American Meteorological Society Section: Journal of Physical Oceanography.
- Lu, J., Vecchi, G. A., and Reichler, T. (2007). Expansion of the Hadley cell under global warming. *Geophysical Research Letters*, 34(6). _eprint: <https://onlinelibrary.wiley.com/doi/pdf/10.1029/2006GL028443>.
- Lévy, M. (2008). The Modulation of Biological Production by Oceanic Mesoscale Turbulence. In Weiss, J. B. and Provenzale, A., editors, *Transport and Mixing in Geophysical Flows: Creators of Modern Physics*, Lecture Notes in Physics, pages 219–261. Springer, Berlin, Heidelberg.
- Lévy, M., Klein, P., and Treguier, A.-M. (2001). Impact of sub-mesoscale physics on production and subduction of phytoplankton in an oligotrophic regime. *Journal of Marine Research*, 59(4):535–565.

- Machu, E., Capet, X., Estrade, P. A., Ndoye, S., Brajard, J., Baurand, F., Auger, P.-A., Lazar, A., and Brehmer, P. (2019). First Evidence of Anoxia and Nitrogen Loss in the Southern Canary Upwelling System. *Geophysical Research Letters*, 46(5):2619–2627. _eprint: <https://onlinelibrary.wiley.com/doi/pdf/10.1029/2018GL079622>.
- Marchesiello, P. and Estrade, P. (2009). Eddy activity and mixing in upwelling systems: a comparative study of Northwest Africa and California regions. *International Journal of Earth Sciences*, 98(2):299–308.
- Marchesiello, P. and Estrade, P. (2010). Upwelling limitation by onshore geostrophic flow. *Journal of Marine Research*, 68(1):37–62.
- Marchesiello, P., McWilliams, J. C., and Shchepetkin, A. (2003). Equilibrium Structure and Dynamics of the California Current System. *JOURNAL OF PHYSICAL OCEANOGRAPHY*, 33:31.
- Marta-Almeida, M., Dubert, J., Peliz, , and Queiroga, H. (2006). Influence of vertical migration pattern on retention of crab larvae in a seasonal upwelling system. *Marine Ecology Progress Series*, 307:1–19.
- McCabe, R. M., Hickey, B. M., Dever, E. P., and MacCready, P. (2015). Seasonal Cross-Shelf Flow Structure, Upwelling Relaxation, and the Alongshelf Pressure Gradient in the Northern California Current System. *Journal of Physical Oceanography*, 45(1):209–227. Publisher: American Meteorological Society Section: Journal of Physical Oceanography.
- McGillicuddy, D. J. and Robinson, A. R. (1997). Eddy-induced nutrient supply and new production in the Sargasso Sea. *Deep Sea Research Part I: Oceanographic Research Papers*, 44(8):1427–1450.
- McWilliams, J. C. (2016). Submesoscale currents in the ocean. *Proceedings of the Royal Society A: Mathematical, Physical and Engineering Sciences*, 472(2189):20160117.
- Menkes, C. E., Kennan, S. C., Flament, P., Dandonneau, Y., Masson, S., Biessy, B., Marchal, E., Eldin, G., Grelet, J., Montel, Y., Morlière, A., Lebourges-Dhaussy, A., Moulin, C., Champalbert, G., and Herbland, A. (2002). A whirling ecosystem in the equatorial Atlantic. *Geophysical Research Letters*, 29(11):48–1–48–4. _eprint: <https://onlinelibrary.wiley.com/doi/pdf/10.1029/2001GL014576>.
- Messié, M. and Chavez, F. P. (2015). Seasonal regulation of primary production in eastern boundary upwelling systems. *Progress in Oceanography*, 134:1–18.
- Messié, M. and Chavez, F. P. (2017). Nutrient supply, surface currents, and plankton dynamics predict zooplankton hotspots in coastal upwelling systems. *Geophysical Research Letters*, 44(17):8979–8986. _eprint: <https://onlinelibrary.wiley.com/doi/pdf/10.1002/2017GL074322>.
- Messié, M., Ledesma, J., Kolber, D. D., Michisaki, R. P., Foley, D. G., and Chavez, F. P. (2009). Potential new production estimates in four eastern boundary upwelling ecosystems. *Progress in Oceanography*, 83(1-4):151–158.

- Michaelis, L. and Menten, M. (1913). Die Kinetik der Invertinwirkung. *Biochem. Z.*, 49:333–369.
- Mittelstaedt, E. (1991). The ocean boundary along the northwest African coast: Circulation and oceanographic properties at the sea surface. *Progress in Oceanography*, 26(4):307–355.
- Monod, J. (1942). Recherches sur la croissance des cultures bactériennes. Technical report, Hermann.
- Montgomery, R. B. (1974). Comments on 'Seasonal variability of the Florida Current', by Niiler and Richardson. 32(3):533–534.
- Morel, A. (1988). Optical modeling of the upper ocean in relation to its biogenous matter content (case I waters). *Journal of Geophysical Research: Oceans*, 93(C9):10749–10768. _eprint: <https://onlinelibrary.wiley.com/doi/pdf/10.1029/JC093iC09p10749>.
- Morgan, S. G., Miller, S. H., Robart, M. J., and Largier, J. L. (2018). Nearshore Larval Retention and Cross-Shelf Migration of Benthic Crustaceans at an Upwelling Center. *Frontiers in Marine Science*, 5.
- Moron, V., Oueslati, B., Pohl, B., and Janicot, S. (2018). Daily Weather Types in February–June (1979–2016) and Temperature Variations in Tropical North Africa. *Journal of Applied Meteorology and Climatology*, 57(5):1171–1195. Publisher: American Meteorological Society Section: Journal of Applied Meteorology and Climatology.
- Nagai, T., Gruber, N., Frenzel, H., Lachkar, Z., McWilliams, J. C., and Plattner, G.-K. (2015). Dominant role of eddies and filaments in the offshore transport of carbon and nutrients in the California Current System. *Journal of Geophysical Research: Oceans*, 120(8):5318–5341. _eprint: <https://onlinelibrary.wiley.com/doi/pdf/10.1002/2015JC010889>.
- Narimousa, S. and Maxworthy, T. (1989). Application of a laboratory model to the interpretation of satellite and field observations of coastal upwelling. *Dynamics of Atmospheres and Oceans*, 13(1):1–46.
- NASA (2014). NASA Goddard Space Flight Center, Ocean Ecology Laboratory, Ocean Biology Processing Group. Moderate-resolution Imaging Spectroradiometer (MODIS) Aqua 11µm Day/Night Sea Surface Temperature Data. NASA OB.DAAC, Greenbelt, MD, USA. type: dataset.
- Ndoye, S., Capet, X., Estrade, P., Sow, B., Dagorne, D., Lazar, A., Gaye, A., and Brehmer, P. (2014). SST patterns and dynamics of the southern Senegal-Gambia upwelling center. *Journal of Geophysical Research: Oceans*, 119(12):8315–8335. _eprint: <https://onlinelibrary.wiley.com/doi/pdf/10.1002/2014JC010242>.
- Ndoye, S., Capet, X., Estrade, P., Sow, B., Machu, E., Brochier, T., Döring, J., and Brehmer, P. (2017). Dynamics of a “low-enrichment high-retention” upwelling center over the southern Senegal shelf. *Geophysical Research Letters*, 44(10):5034–5043. _eprint: <https://onlinelibrary.wiley.com/doi/pdf/10.1002/2017GL072789>.

- Ohman, M. D. (1990). The Demographic Benefits of Diel Vertical Migration by Zooplankton. *Ecological Monographs*, 60(3):257–281. _eprint: <https://onlinelibrary.wiley.com/doi/pdf/10.2307/1943058>.
- Ohman, M. D., Barbeau, K., Franks, P. J. S., Goericke, R., Landry, M. R., and Miller, A. J. (2013). Ecological Transitions in a Coastal Upwelling Ecosystem. *Oceanography*, 26(3):210–219. Publisher: Oceanography Society.
- Okumura, Y. M., Sun, T., and Wu, X. (2017). Asymmetric Modulation of El Niño and La Niña and the Linkage to Tropical Pacific Decadal Variability. *Journal of Climate*, 30(12):4705–4733. Publisher: American Meteorological Society Section: Journal of Climate.
- Paduan, J. D., Cook, M. S., and Tapia, V. M. (2018). Patterns of upwelling and relaxation around Monterey Bay based on long-term observations of surface currents from high frequency radar. *Deep Sea Research Part II: Topical Studies in Oceanography*, 151:129–136.
- Papastephanou, K. M., Bollens, S. M., and Slaughter, A. M. (2006). Cross-shelf distribution of copepods and the role of event-scale winds in a northern California upwelling zone. *Deep Sea Research Part II: Topical Studies in Oceanography*, 53(25):3078–3098.
- Pearson, K. (1900). X. On the criterion that a given system of deviations from the probable in the case of a correlated system of variables is such that it can be reasonably supposed to have arisen from random sampling. *The London, Edinburgh, and Dublin Philosophical Magazine and Journal of Science*, 50(302):157–175. Publisher: Taylor & Francis _eprint: <https://doi.org/10.1080/14786440009463897>.
- Penduff, T., Barnier, B., Terray, L., Bessi eres, L., S erazin, G., Gregorio, S., Brankart, J.-M., Moine, M.-P., Molines, J.-M., and Brasseur, P. (2014). Ensembles of eddying ocean simulations for climate. *CLIVAR Exchanges, Special Issue on High Resolution Ocean Climate Modelling*, 19:26–29.
- Penven, P., Echevin, V., Pasapera, J., Colas, E., and Tam, J. (2005). Average circulation, seasonal cycle, and mesoscale dynamics of the Peru Current System: A modeling approach. *Journal of Geophysical Research: Oceans*, 110(C10). _eprint: <https://onlinelibrary.wiley.com/doi/pdf/10.1029/2005JC002945>.
- Peterson, W. T., Painting, S. J., and Hutchings, L. (1990). Diel variations in gut pigment content, diel vertical migration and estimates of grazing impact for copepods in the southern Benguela upwelling region in October 1987. *Journal of Plankton Research*, 12(2):259–281.
- Philander, S. G. H. and Yoon, J.-H. (1982). Eastern Boundary Currents and Coastal Upwelling. *Journal of Physical Oceanography*, 12(8):862–879. Publisher: American Meteorological Society Section: Journal of Physical Oceanography.
- Pitcher, G. C., Walker, D. R., Mitchell-Innes, B. A., and Moloney, C. L. (1991). Short-term variability during an anchor station study in the southern Benguela upwelling system: Phytoplankton dynamics. *Progress in Oceanography*, 28(1):39–64.

- Polo, I., Lazar, A., Rodriguez-Fonseca, B., and Arnault, S. (2008). Oceanic Kelvin waves and tropical Atlantic intraseasonal variability: 1. Kelvin wave characterization. *Journal of Geophysical Research: Oceans*, 113(C7). _eprint: <https://onlinelibrary.wiley.com/doi/pdf/10.1029/2007JC004495>.
- Potier, M., Bach, P., Ménard, F., and Marsac, F. (2014). Influence of mesoscale features on micronekton and large pelagic fish communities in the Mozambique Channel. *Deep Sea Research Part II: Topical Studies in Oceanography*, 100:184–199.
- Pozo Buil, M., Jacox, M. G., Fiechter, J., Alexander, M. A., Bograd, S. J., Curchitser, E. N., Edwards, C. A., Rykaczewski, R. R., and Stock, C. A. (2021). A Dynamically Downscaled Ensemble of Future Projections for the California Current System. *Frontiers in Marine Science*, 8.
- Pringle, J. M. (2002). Enhancement of Wind-Driven Upwelling and Downwelling by Along-shore Bathymetric Variability. *Journal of Physical Oceanography*, 32(11):3101–3112. Publisher: American Meteorological Society Section: Journal of Physical Oceanography.
- Ramos, A. M., Pires, A. C., Sousa, P. M., and Trigo, R. M. (2013). The use of circulation weather types to predict upwelling activity along the western Iberian Peninsula coast. *Continental Shelf Research*, 69:38–51.
- Ramp, S. R., Paduan, J. D., Shulman, I., Kindle, J., Bahr, F. L., and Chavez, F. (2005). Observations of upwelling and relaxation events in the northern Monterey Bay during August 2000. *Journal of Geophysical Research: Oceans*, 110(C7). _eprint: <https://onlinelibrary.wiley.com/doi/pdf/10.1029/2004JC002538>.
- Relvas, P. and Barton, E. D. (2005). A separated jet and coastal counterflow during upwelling relaxation off Cape São Vicente (Iberian Peninsula). *Continental Shelf Research*, 25(1):29–49.
- Renault, L., McWilliams, J. C., Kessouri, F., Jousse, A., Frenzel, H., Chen, R., and Deutsch, C. (2021). Evaluation of high-resolution atmospheric and oceanic simulations of the California Current System. *Progress in Oceanography*, 195:102564.
- Risien, C. M. and Chelton, D. B. (2008). A Global Climatology of Surface Wind and Wind Stress Fields from Eight Years of QuikSCAT Scatterometer Data. *Journal of Physical Oceanography*, 38(11):2379–2413. Publisher: American Meteorological Society Section: Journal of Physical Oceanography.
- Rodi, W. (1987). Examples of calculation methods for flow and mixing in stratified fluids. *Journal of Geophysical Research: Oceans*, 92(C5):5305–5328. _eprint: <https://onlinelibrary.wiley.com/doi/pdf/10.1029/JC092iC05p05305>.
- Roy, C. (1989). Fluctuations des vents et variabilité de l’upwelling devant les côtes du Sénégal. *Oceanologica Acta*, 1989. 12, 4, 361–369.
- Roy, C. (1998). An upwelling-induced retention area off Senegal: a mechanism to link upwelling and retention processes. *South African Journal of Marine Science*, 19(1):89–98. Publisher: Taylor & Francis _eprint: <https://doi.org/10.2989/025776198784126881>.

- Rykaczewski, R. R. and Checkley, D. M. (2008). Influence of ocean winds on the pelagic ecosystem in upwelling regions. *Proceedings of the National Academy of Sciences*, 105(6):1965–1970. Publisher: Proceedings of the National Academy of Sciences.
- Rykaczewski, R. R. and Dunne, J. P. (2010). Enhanced nutrient supply to the California Current Ecosystem with global warming and increased stratification in an earth system model. *Geophysical Research Letters*, 37(21). _eprint: <https://onlinelibrary.wiley.com/doi/pdf/10.1029/2010GL045019>.
- Rykaczewski, R. R., Dunne, J. P., Sydeman, W. J., García-Reyes, M., Black, B. A., and Bograd, S. J. (2015). Poleward displacement of coastal upwelling-favorable winds in the ocean's eastern boundary currents through the 21st century. *Geophysical Research Letters*, 42(15):6424–6431. _eprint: <https://onlinelibrary.wiley.com/doi/pdf/10.1002/2015GL064694>.
- Ryther, J. H. (1969). Photosynthesis and Fish Production in the Sea. *Science*, 166(3901):72–76. Publisher: American Association for the Advancement of Science.
- Saldías, G. S., Ramos-Musalem, K., and Allen, S. E. (2021). Circulation and Upwelling Induced by Coastal Trapped Waves Over a Submarine Canyon in an Idealized Eastern Boundary Margin. *Geophysical Research Letters*, 48(11):e2021GL093548. _eprint: <https://onlinelibrary.wiley.com/doi/pdf/10.1029/2021GL093548>.
- Sarmiento, J. L. and Gruber, N. (2013). *Ocean Biogeochemical Dynamics*. Princeton University Press. Publication Title: Ocean Biogeochemical Dynamics.
- Send, U. (1989). The origin of eddy heat fluxes in the northern California upwelling regime. *Journal of Geophysical Research: Oceans*, 94(C1):871–876. _eprint: <https://onlinelibrary.wiley.com/doi/pdf/10.1029/JC094iC01p00871>.
- Send, U., Beardsley, R. C., and Winant, C. D. (1987). Relaxation from upwelling in the Coastal Ocean Dynamics Experiment. *Journal of Geophysical Research: Oceans*, 92(C2):1683–1698. _eprint: <https://onlinelibrary.wiley.com/doi/pdf/10.1029/JC092iC02p01683>.
- Send, U. and Nam, S. (2012). Relaxation from upwelling: The effect on dissolved oxygen on the continental shelf. *Journal of Geophysical Research: Oceans*, 117(C4). _eprint: <https://onlinelibrary.wiley.com/doi/pdf/10.1029/2011JC007517>.
- Shanks, A. L., Morgan, S. G., MacMahan, J., Reniers, A. J. H. M., Jarvis, M., Brown, J., Fujimura, A., and Griesemer, C. (2014). Onshore transport of plankton by internal tides and upwelling-relaxation events. *Marine Ecology Progress Series*, 502:39–51.
- Shannon, L. V. and Pillar, S. C. (1986). The Benguela ecosystem. Part III. Plankton. *Oceanogr Mar Biol Annu Rev*.
- Shchepetkin, A. F. and McWilliams, J. C. (2005). The regional oceanic modeling system (ROMS): a split-explicit, free-surface, topography-following-coordinate oceanic model. *Ocean Modelling*, 9(4):347–404.

- Shchepetkin, A. F. and McWilliams, J. C. (2009). Correction and commentary for “Ocean forecasting in terrain-following coordinates: Formulation and skill assessment of the regional ocean modeling system” by Haidvogel et al., *J. Comp. Phys.* 227, pp. 3595–3624. *Journal of Computational Physics*, 228(24):8985–9000.
- Shropshire, T. A., Morey, S. L., Chassignet, E. P., Karnauskas, M., Coles, V. J., Malca, E., Laiz-Carrión, R., Fiksen, , Reglero, P., Shiroza, A., Quintanilla Hervas, J. M., Gerard, T., Lamkin, J. T., and Stukel, M. R. (2022). Trade-offs between risks of predation and starvation in larvae make the shelf break an optimal spawning location for Atlantic bluefin tuna. *Journal of Plankton Research*, 44(5):782–798.
- Silvy, Y., Guilyardi, E., Sallée, J.-B., and Durack, P. J. (2020). Human-induced changes to the global ocean water masses and their time of emergence. *Nature Climate Change*, 10(11):1030–1036. Number: 11 Publisher: Nature Publishing Group.
- Spitz, Y. H., Allen, J. S., and Gan, J. (2005). Modeling of ecosystem processes on the Oregon shelf during the 2001 summer upwelling. *Journal of Geophysical Research: Oceans*, 110(C10). _eprint: <https://onlinelibrary.wiley.com/doi/pdf/10.1029/2005JC002870>.
- Stouffer, R. J., Manabe, S., and Bryan, K. (1989). Interhemispheric asymmetry in climate response to a gradual increase of atmospheric CO₂. *Nature*, 342(6250):660–662. Number: 6250 Publisher: Nature Publishing Group.
- Strand, E., Klevjer, T., Knutsen, T., and Melle, W. (2020). Ecology of mesozooplankton across four North Atlantic basins. *Deep Sea Research Part II: Topical Studies in Oceanography*, 180:104844.
- Strub, P. T. and James, C. (2022). Evaluation of Nearshore QuikSCAT 4.1 and ERA-5 Wind Stress and Wind Stress Curl Fields over Eastern Boundary Currents. *Remote Sensing*, 14(9):2251. Number: 9 Publisher: Multidisciplinary Digital Publishing Institute.
- Stukel, M. R., Aluwihare, L. I., Barbeau, K. A., Chekalyuk, A. M., Goericke, R., Miller, A. J., Ohman, M. D., Ruacho, A., Song, H., Stephens, B. M., and Landry, M. R. (2017). Mesoscale ocean fronts enhance carbon export due to gravitational sinking and subduction. *Proceedings of the National Academy of Sciences*, 114(6):1252–1257. Publisher: National Academy of Sciences Section: Physical Sciences.
- Stukel, M. R. and Barbeau, K. A. (2020). Investigating the Nutrient Landscape in a Coastal Upwelling Region and Its Relationship to the Biological Carbon Pump. *Geophysical Research Letters*, 47(6):e2020GL087351. _eprint: <https://agupubs.onlinelibrary.wiley.com/doi/pdf/10.1029/2020GL087351>.
- Stukel, M. R., Landry, M. R., Benitez-Nelson, C. R., and Goericke, R. (2011). Trophic cycling and carbon export relationships in the California Current Ecosystem. *Limnology and Oceanography*, 56(5):1866–1878. _eprint: <https://onlinelibrary.wiley.com/doi/pdf/10.4319/lo.2011.56.5.1866>.

- Sultan, B. and Janicot, S. (2003). The West African Monsoon Dynamics. Part II: The “Preonset” and “Onset” of the Summer Monsoon. *Journal of Climate*, 16(21):3407–3427. Publisher: American Meteorological Society Section: Journal of Climate.
- Sydeman, W. J., García-Reyes, M., Schoeman, D. S., Rykaczewski, R. R., Thompson, S. A., Black, B. A., and Bograd, S. J. (2014). Climate change and wind intensification in coastal upwelling ecosystems. *Science*, 345(6192):77–80. Publisher: American Association for the Advancement of Science.
- Sydeman, W. J., Schoeman, D. S., Thompson, S. A., Hoover, B. A., García-Reyes, M., Daunt, F., Agnew, P., Anker-Nilssen, T., Barbraud, C., Barrett, R., Becker, P. H., Bell, E., Boersma, P. D., Bouwhuis, S., Cannell, B., Crawford, R. J. M., Dann, P., Delord, K., Elliott, G., Erikstad, K. E., Flint, E., Furness, R. W., Harris, M. P., Hatch, S., Hilwig, K., Hinke, J. T., Jahncke, J., Mills, J. A., Reiertsen, T. K., Renner, H., Sherley, R. B., Surman, C., Taylor, G., Thayer, J. A., Trathan, P. N., Velarde, E., Walker, K., Wanless, S., Warzybok, P., and Watanuki, Y. (2021). Hemispheric asymmetry in ocean change and the productivity of ecosystem sentinels. *Science*, 372(6545):980–983. Publisher: American Association for the Advancement of Science.
- Sylla, A., Mignot, J., Capet, X., and Gaye, A. T. (2019). Weakening of the Senegalo–Mauritanian upwelling system under climate change. *Climate Dynamics*, 53(7-8):4447–4473.
- Takahashi, T., Broecker, W. S., and Langer, S. (1985). Redfield ratio based on chemical data from isopycnal surfaces. *Journal of Geophysical Research: Oceans*, 90(C4):6907–6924. _eprint: <https://onlinelibrary.wiley.com/doi/pdf/10.1029/JC090iC04p06907>.
- Tall, A. W., Machu, E., Echevin, V., Capet, X., Pietri, A., Corr  a, K., Sall, S. M., and Lazar, A. (2021). Variability of Dissolved Oxygen in the Bottom Layer of the Southern Senegalese Shelf. *Journal of Geophysical Research: Oceans*, 126(5):e2020JC016854. _eprint: <https://onlinelibrary.wiley.com/doi/pdf/10.1029/2020JC016854>.
- Tegen, I. and Fung, I. (1994). Modeling of mineral dust in the atmosphere: Sources, transport, and optical thickness. *Journal of Geophysical Research: Atmospheres*, 99(D11):22897–22914. _eprint: <https://onlinelibrary.wiley.com/doi/pdf/10.1029/94JD01928>.
- Thompson, S. A., Sydeman, W. J., Santora, J. A., Black, B. A., Suryan, R. M., Calambokidis, J., Peterson, W. T., and Bograd, S. J. (2012). Linking predators to seasonality of upwelling: Using food web indicators and path analysis to infer trophic connections. *Progress in Oceanography*, 101(1):106–120.
- Thomsen, S., Capet, X., and Echevin, V. (2021). Competition between Baroclinic Instability and Ekman Transport under Varying Buoyancy Forcings in Upwelling Systems: An Idealized Analog to the Southern Ocean. *Journal of Physical Oceanography*, 51(11):3347–3364. Publisher: American Meteorological Society Section: Journal of Physical Oceanography.

- Torres, R., Turner, D., Rutllant, J., Sobarzo, M., Antezana, T., and Gonzalez, H. E. (2002). CO₂ outgassing off central Chile (31–30°S) and northern Chile (24–23°S) during austral summer 1997: the effect of wind intensity on the upwelling and ventilation of CO₂-rich waters. *Deep Sea Research Part I: Oceanographic Research Papers*, 49(8):1413–1429.
- Torres, R., Turner, D. R., Silva, N., and Rutllant, J. (1999). High short-term variability of CO₂ fluxes during an upwelling event off the Chilean coast at 30°S. *Deep Sea Research Part I: Oceanographic Research Papers*, 46(7):1161–1179.
- Umlauf, L. and Burchard, H. (2003). A generic length-scale equation for geophysical turbulence models. *Journal of Marine Research*, 61(2):235–265.
- Vallis, G. K. (2017). *Atmospheric and Oceanic Fluid Dynamics*. Cambridge University Press. Google-Books-ID: BTgoDwAAQBAJ.
- Van Camp, L., Nykjaer, L., Mittelstaedt, E., and Schlittenhardt, P. (1991). Upwelling and boundary circulation off Northwest Africa as depicted by infrared and visible satellite observations. *Progress in Oceanography*, 26(4):357–402.
- Van Roekel, L., Adcroft, A. J., Danabasoglu, G., Griffies, S. M., Kauffman, B., Large, W., Levy, M., Reichl, B. G., Ringler, T., and Schmidt, M. (2018). The KPP Boundary Layer Scheme for the Ocean: Revisiting Its Formulation and Benchmarking One-Dimensional Simulations Relative to LES. *Journal of Advances in Modeling Earth Systems*, 10(11):2647–2685. _eprint: <https://onlinelibrary.wiley.com/doi/pdf/10.1029/2018MS001336>.
- Veitch, J., Penven, P., and Shillington, F. (2010). Modeling Equilibrium Dynamics of the Benguela Current System. *Journal of Physical Oceanography*, 40(9):1942–1964. Publisher: American Meteorological Society Section: Journal of Physical Oceanography.
- Wang, D.-P. (1993). Model of frontogenesis: Subduction and upwelling. *Journal of Marine Research*, 51(3):497–513.
- Wijesekera, H. W., Allen, J. S., and Newberger, P. A. (2003). Modeling study of turbulent mixing over the continental shelf: Comparison of turbulent closure schemes. *Journal of Geophysical Research: Oceans*, 108(C3). _eprint: <https://onlinelibrary.wiley.com/doi/pdf/10.1029/2001JC001234>.
- Wilkerson, F. P., Lassiter, A. M., Dugdale, R. C., Marchi, A., and Hogue, V. E. (2006). The phytoplankton bloom response to wind events and upwelled nutrients during the CoOP WEST study. *Deep Sea Research Part II: Topical Studies in Oceanography*, 53(25):3023–3048.
- Williams, R. G. and Follows, M. J. (2011). *Ocean Dynamics and the Carbon Cycle: Principles and Mechanisms*. Cambridge University Press. Google-Books-ID: dfTJdgZg260C.
- Wing, S., Botsford, L., Largier, J., and Morgan, L. (1995). Spatial structure of relaxation events and crab settlement in the northern California upwelling system. *Marine Ecology Progress Series*, 128:199–211.

- Wolanski, E., Imberger, J., and Heron, M. L. (1984). Island wakes in shallow coastal waters. *Journal of Geophysical Research: Oceans*, 89(C6):10553–10569. _eprint: <https://onlinelibrary.wiley.com/doi/pdf/10.1029/JC089iC06p10553>.
- Worley, S. J., Woodruff, S. D., Reynolds, R. W., Lubker, S. J., and Lott, N. (2005). ICOADS release 2.1 data and products. *International Journal of Climatology*, 25(7):823–842. _eprint: <https://onlinelibrary.wiley.com/doi/pdf/10.1002/joc.1166>.
- Yokomizo, H., Botsford, L. W., Holland, M. D., Lawrence, C. A., and Hastings, A. (2010). Optimal wind patterns for biological production in shelf ecosystems driven by coastal upwelling. *Theoretical Ecology*, 3(1):53–63.
- Yool, A., Martin, A. P., Fernández, C., and Clark, D. R. (2007). The significance of nitrification for oceanic new production. *Nature*, 447(7147):999–1002.
- Zhang, Y., Bellingham, J. G., Ryan, J. P., and Godin, M. A. (2015). Evolution of a physical and biological front from upwelling to relaxation. *Continental Shelf Research*, 108:55–64.
- Zimmerman, J. T. F. (1986). The tidal whirlpool: A review of horizontal dispersion by tidal and residual currents. *Netherlands Journal of Sea Research*, 20(2):133–154.